

## Stress Evolution in Early-Age Cementitious Materials Considering Autogenous Deformation and Creep

### New experimental and modelling techniques

Liang, M.

**DOI**

[10.4233/uuid:270173e7-6ce6-4a71-ac42-79eab09cce5f](https://doi.org/10.4233/uuid:270173e7-6ce6-4a71-ac42-79eab09cce5f)

**Publication date**

2024

**Document Version**

Final published version

**Citation (APA)**

Liang, M. (2024). *Stress Evolution in Early-Age Cementitious Materials Considering Autogenous Deformation and Creep: New experimental and modelling techniques*. [Dissertation (TU Delft), Delft University of Technology]. <https://doi.org/10.4233/uuid:270173e7-6ce6-4a71-ac42-79eab09cce5f>

**Important note**

To cite this publication, please use the final published version (if applicable). Please check the document version above.

**Copyright**

Other than for strictly personal use, it is not permitted to download, forward or distribute the text or part of it, without the consent of the author(s) and/or copyright holder(s), unless the work is under an open content license such as Creative Commons.

**Takedown policy**

Please contact us and provide details if you believe this document breaches copyrights. We will remove access to the work immediately and investigate your claim.

# **Stress Evolution in Early-Age Cementitious Materials Considering Autogenous Deformation and Creep**

New experimental and modelling techniques



**Stress Evolution in Early-Age Cementitious Materials**  
**Considering Autogenous Deformation and Creep**  
New experimental and modelling techniques

**Dissertation**

for the purpose of obtaining the degree of doctor

at Delft University of Technology

by the authority of the Rector Magnificus prof.dr.ir. T.H.J.J. van der Hagen

chair of the Board for Doctorates

to be defended publicly on

Wednesday 3 April 2024 at 10:00 o'clock

by

**Minfei LIANG**

Master of Science in Bridge and Tunnel Engineering

Southwest Jiaotong University, China

Born in Fujian, China

This dissertation has been approved by the promotor

Composition of the doctoral committee

Rector Magnificus	chairperson
Prof.dr.ir. E. Schlangen	Delft University of Technology, promotor
Dr. B. Šavija	Delft University of Technology, promotor

Independent members:

Prof.dr.ir. K. van Breugel	Delft University of Technology
Prof.dr.ir. M.A.N Hendriks	Delft University of Technology
Prof.dr.ir. E.A.B. Koenders	Technical University of Darmstadt
Dr.ir. S. Staquet	Vrije Universiteit Brussel
Dr. Y. Wei	Tsinghua University



This research was financially supported by China Scholarship Council.

Keywords: Early-age cracking, autogenous deformation, creep/ relaxation, Temperature-Stress-Testing-Machine, finite element model, machine learning.

Printed by: Ipskamp, The Netherlands

Cover design: Minfei Liang

Copy right @ 2024 by Minfei Liang

ISBN: 978-94-6366-843-9

*To my parents and grandparents*  
谨以此书献给我的父母和祖父母



# CONTENTS

<b>LIST OF ABBREVIATION</b>	<b>1</b>
<b>1. GENERAL INTRODUCTION</b>	<b>3</b>
1.1 Research significance	4
1.2 Research objectives	6
1.3 Research methods	7
1.4 Thesis outline	8
<b>2. LITERATURE REVIEW</b>	<b>11</b>
2.1 Introduction	12
2.2 Autogenous deformation	12
2.3 Viscoelastic properties	23
2.4 Early-age stress	30
2.5 Conclusions	36
2.6 Outlook	38
<b>3. EARLY-AGE STRESS EVOLUTION INDUCED BY AUTOGENOUS DEFORMATION IN HIGH-VOLUME GGBFS CONCRETE</b>	<b>41</b>
3.1 Introduction	42
3.2 Experimental methods	43
3.3 Results	49
3.4 Discussion	61
3.5 Conclusions	63
<b>4. BAYESIAN INVERSE MODELLING OF AGING CREEP FOR PREDICTING THE EARLY AGE STRESS EVOLUTION</b>	<b>65</b>
4.1 Introduction	66
4.2 Forward modelling by rate-type creep law	66
4.3 Inverse modelling	78
4.4 Results and discussion	82

4.5	Conclusions	89
<b>5.</b>	<b>DEVELOPMENT OF A MINI TEMPERATURE STRESS TESTING MACHINE</b>	<b>91</b>
5.1	Introduction	92
5.2	The Mini-TSTM	92
5.3	Experimental methods and validation schemes	98
5.4	Results and discussion	104
5.5	Conclusions	122
<b>6.</b>	<b>EFFECTS OF CURING TEMPERATURE ON AD AND EARLY-AGE STRESS EVOLUTION</b>	<b>125</b>
6.1	Introduction	126
6.2	Methods	126
6.3	Results and discussion	128
6.4	Conclusions	141
<b>7.</b>	<b>MODELLING OF STRESS RELAXATION IN EARLY-AGE CEMENTITIOUS MATERIALS</b>	<b>143</b>
7.1	Introduction	144
7.2	Theory	145
7.3	EAS models	147
7.4	Results and discussion	155
7.5	Conclusions	172
<b>8.</b>	<b>A SURROGATE MODEL OF EARLY AGE STRESS EVOLUTION IN RESTRAINED CONCRETE BASED ON THERMO- CHEMO- MECHANICAL SIMULATION AND ACTIVE LEARNING</b>	<b>175</b>
8.1	Introduction	176
8.2	Thermo-Chemo-Mechanical (TCM) Model	177
8.3	Material model	183
8.4	Active ensemble learning (AEL)	187
8.5	Results and discussion	195
8.6	Conclusions	205
<b>9.</b>	<b>RETROSPECTION, CONCLUSIONS AND RECOMMENDATIONS</b>	<b>207</b>

<b>9.1 RETROSPECTION</b>	<b>208</b>
<b>9.2 CONCLUSIONS</b>	<b>209</b>
<b>9.3 RECOMMENDATIONS FOR FUTURE RESEARCH</b>	<b>212</b>
<b>REFERENCE</b>	<b>214</b>
<b>SUMMARY</b>	<b>254</b>
<b>SAMENVATTING</b>	<b>257</b>
<b>ACKNOWLEDGEMENTS</b>	<b>260</b>
<b>LIST OF PUBLICATIONS</b>	<b>263</b>
<b>CURRICULUM VITAE</b>	<b>267</b>



## LIST OF ABBREVIATION

AD	Autogenous Deformation
ADTM	Autogenous Deformation Testing Machine
AEL	Active Ensemble Learning
CH	Calcium Hydrate
CSH	Calcium Silicate Hydrate
CTC	Coefficient of Thermal Contraction
CTE	Coefficient of Thermal Expansion
DIC	Digital Image Correlation
EAC	Early Age Cracking
EAS	Early Age Stress
EFB	Exclusive Feature Bundling
ESEM	Environmental Scanning Electron Microscopy
FA	Fly Ash
FEM	Finite Element Method
FL	Feedback Loop
GGBFS	Ground Granulated Blast Furnace Slag
GOSS	Gradient-Based One-Side Sampling
GP	Gaussian Process
HPC	High Performance Concrete
HTC	Hygro-Thermo-Chemo
ITZ	Interfacial Transition Zone
LC3	Limestone Calcined Clay Cement
LGBM	Light Gradient Boosting Machine
LHS	Latin Hypercube Sampling
LVDT	Linear Variable Differential Transformers
MC2010	Model Code 2010

MC	Maturity Concept
MCS	Monte Carlo Sampling
ML	Machine Learning
MIP	Mercury Intrusion Porosimetry
MSE	Mean Squared Error
OPC	Ordinary Portland Cement
OSEL	One-Shot Ensemble Learning
PC	Principal Component
PCA	Principal Component Analysis
PID	Proportional–Integral–Derivative
RBF	Radial Basis Function
RH	Relative Humidity
RMSE	Root Mean Squared Error
SAP	Superabsorbent Polymer
SCM	Supplementary Cementitious Material
SF	Silica Fume
SP	Superplasticizer
SRA	Shrinkage Reducing Agent
TSTM	Temperature Stress Testing Machine
TCM	Thermo-Chemo-Mechanical
UHPC	Ultra-High-Performance Concrete
UPV	Ultrasonic Pulse Velocity
XRD	X-Ray Diffraction

# 1. GENERAL INTRODUCTION

*This chapter presents the research significance of autogenous deformation-induced early-age cracking issues of concrete structures. The research objectives and methods are stated afterwards, and the outline of the thesis is given at the end.*

## 1.1 Research significance

Early-age cracking (EAC) is a common issue encountered during the construction of concrete structures, which not only results in financial losses for contractors but also compromises the functionality, durability and aesthetics of the structures. As shown in **Figure 1-1**, EAC is caused by a combination of early-age behaviors and properties of cementitious materials, including restrained volumetric deformation and mechanical properties, which are influenced by mixture design and environmental factors [1,2]. When the volumetric deformation of hardening concrete is restrained, e.g., by adjacent structures, early-age stress (EAS) builds up in the young concrete, potentially resulting in EAC if the EAS exceeds the material's tensile strength. In this process, the restrained volumetric deformation is the root cause, while the mechanical properties determine the rate of EAS evolution per restrained deformation and therefore the EAC risk. Therefore, to calculate the EAS for evaluation of the EAC risk, it is necessary to use the restrained volumetric deformation and mechanical properties as inputs [3].

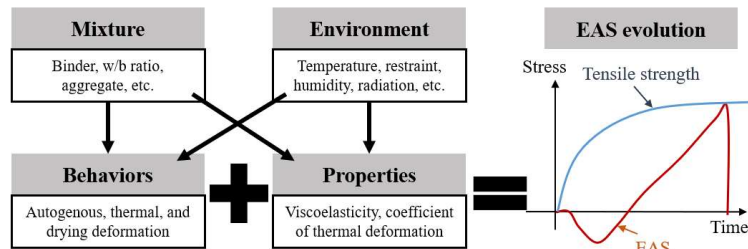


**Figure 1-1 Schematic figure for EAS evolution and EAC**

The volumetric deformation relevant to EAC mainly includes thermal, drying, and autogenous deformation. Thermal deformation is a result of heat release in the hydration reaction and the heat transfer between the concrete structure and the environment. Due to the low thermal conductivity of concrete, the heat released by the hydration reaction accumulates within the structure in the beginning and then slowly dissipates into the environment, resulting in a heating and cooling process that leads to thermal deformation [4]. Massive structures are more prone to EAC induced by thermal deformation because the heat dissipates more slowly, which results in a long cooling process and more thermal shrinkage that can induce tensile stress. Numerous strategies have been proven to effectively ease thermal deformation, such as the use of supplementary cementitious materials (SCMs) to reduce the total hydration heat [2,5].

Drying shrinkage is induced by the moisture transfer between the concrete structure and the environment. It is believed that the moisture loss causes a decrease in internal RH, produces capillary pressure to compress the microstructure, and leads to apparent drying shrinkage observed at the macroscale [6]. Other mechanisms are also involved in the drying deformation, including changes in surface free energy, disjoining pressure, and interlayer water movement [7]. Contrary to the thermal deformation, EAC induced by drying shrinkage is less pronounced in massive structures because the moisture loss mostly occurs in the surface layers of the structure, while it proceeds much more slowly in the core. Moreover, proper curing can effectively alleviate drying shrinkage at an early age by preventing moisture loss from the material to the environment [8].

The thermal and drying deformation depend not only on the material itself but also on the structural size and the environment, as heat and moisture transfer play a dominant role in inducing these deformations. In contrast, autogenous deformation (AD) is a material behavior that is not related to any substance exchange between the structure and the environment. AD mainly arises from the consumption of pore water by the hydration reaction, also known as “self-desiccation”, and directly relates to the hydration of the cementitious material [9]. The advancement of modern construction industries tends to use greener cementitious materials with high performance, which significantly affects AD and therefore the risk of EAC. For example, high-performance concrete (HPC) and ultra-high-performance concrete (UHPC) have a significantly higher risk of EAC due to AD because of lower water/binder ratios and the incorporation of silica fume [10–12]. Furthermore, concrete that uses high-volume slag or alkali-activated binders, which aim to replace Ordinary Portland Cement (OPC) and reduce its carbon emission, shows a much higher EAC risk because of higher AD [13].

Various experimental methods have been developed to quantify the AD and accordingly, various strategies have also been proposed to mitigate the high EAC risk induced by AD [9]. However, the timing at which the measurement should be started, referred to as “time-zero”, has been a debatable issue [14,15]. In view of the time-zero issue, a corrugated tube test is commonly used because it is both convenient and accurate and allows the test to start immediately after the placement of a fresh mixture [16]. In addition to experimental methods, multiple analytical models have also been proposed to predict AD [17], most of which are based on the capillary tension theory. Furthermore, several mitigation strategies have been advised to reduce AD, including internal curing (e.g., by

superabsorbent polymers, lightweight aggregate, and recycled concrete aggregate), control of hydration reaction, formation of expansive products, and use of shrinkage-reducing admixtures [11,18–23]. Nevertheless, as shown in **Figure 1-1**, restrained AD is the root cause of EAS evolution, while material properties (especially viscoelastic properties) determine the rate of EAS accumulation per AD. Therefore, only knowing the AD is not sufficient to predict the EAS; hence, the EAC risk cannot be accurately quantified from AD alone [3].

As the combined result of restrained AD and evolution of mechanical properties of hardening cementitious materials, EAS is a straightforward indicator to evaluate the EAC risk [24]. To quantify the EAS, several testing methods have been devised to measure the EAS evolution when the volumetric deformation is restrained, including the ring test, plate test, longitudinal test, and substrate restraint test [3,25]. Among these tests, the Temperature-Stress-Testing-Machine (TSTM) stands out with advantages in explicit and flexible mechanical loading schemes, active temperature control, and tunable restraint degree [26], which allow for a wide range of early-age tests for tensile and compressive creep, elastic modulus, and coefficients of thermal expansion and contraction [27]. In addition, different modeling schemes have been developed to simulate the EAS evolution using analytical or numerical methods [28,29]. These models use the measured AD and viscoelastic properties as input to run simulations following a constitutive relationship of linear viscoelasticity. While most models have proven effective for simulating EAS using linear viscoelasticity, their performance strongly relies on using the measured AD and viscoelastic properties (i.e., elastic modulus and aging creep/relaxation) as the input. The costs, reliability, and complexity of these early-age tests, including tests for AD, creep, and EAS, hinder a thorough parametric study which requires numerous experiments. Thus, a more efficient testing system for early-age properties and behaviors would be beneficial for further understanding the mechanisms of EAS evolution and establishing appropriate modeling schemes to better evaluate AD-induced EAC risk.

## 1.2 Research objectives

The objectives of this thesis are as follows:

- To develop an efficient testing system for measuring multiple early-age behaviors and properties relevant to EAC risk assessment, including the EAS, AD, elastic modulus, aging creep, and coefficient of thermal expansion/contraction (CTE/CTC).

- To develop a reliable modelling scheme for stress relaxation in EAS evolution and validate it with the experimental results of the new testing system.
- To build a theoretical model for predicting EAS under more general scenarios and apply data-driven techniques to build a surrogate of the theoretical model to form a more efficient tool for EAS prediction.

### 1.3 Research methods

To achieve the research objectives, this research comprises the following three stages:

Step 1: Preliminary understanding of the testing and modelling techniques of EAS evolution.

- Use the TSTM to study EAS evolution in restrained high-volume ground granulated blast furnace slag (GGBFS) concrete induced by AD.
- Build up a numerical modelling scheme to predict the EAS evolution in the TSTM test, using the tested AD as input.

Step 2: Develop a TSTM for more efficiently testing the early-age properties and behaviors.

- Formulate the general design of the TSTM and develop experimental methods for early-age properties and behaviors that are relevant to EAC issues.
- Validate the measurements of EAS, AD, elastic modulus, aging creep, and CTE/ CTC.
- Use a viscoelastic model to predict the EAS using the measured AD, elastic modulus, and aging creep as input.
- Study the effects of curing temperature on AD-induced EAS to show the capabilities of the newly developed TSTM experimental setup.

Step 3: Develop a reliable and efficient modelling scheme for simulating the EAS evolution.

- Examine and analyze representative viscoelastic modelling schemes for simulating the stress relaxation, propose an optimal modelling scheme for predicting the EAS evolution, and quantify the performance of these models by using the experimental results of the new TSTM.

- Build a data-driven modelling scheme as the surrogate of a Thermo-Chemo-Mechanical (TCM) model for predicting EAS evolution in general cases with higher efficiency.

## 1.4 Thesis outline

This thesis is composed of five parts (**Figure 1-2**)

Part I: A general introduction.

**Chapter 1** serves as an introduction to the research significance, research objectives and thesis outline.

**Chapter 2** presents a literature review on the experimental and modelling techniques of EAS evolution, autogenous deformation, and viscoelastic properties.

Part II: A preliminary study of experimental and modelling techniques of AD-induced EAS evolution based on TSTM tests and Bayesian inverse modelling.

**Chapter 3** shows a case study on EAS evolution in high-volume slag cement concrete using TSTM tests and provides microscale explanations for the observed macroscale behaviors.

**Chapter 4** builds a Bayesian inverse modelling scheme to predict the EAS evolution measured in the TSTM tests using the measured AD as input.

Part III: The design, development, validation, and application of a new Mini TSTM.

**Chapter 5** presents the design, experimental methods, and validation analysis of the Mini TSTM.

**Chapter 6** investigates the effects of curing temperature on AD-induced EAS evolution using the Mini-TSTM.

Part IV: A reliable numerical scheme for stress relaxation and a surrogate model for efficiently predicting EAS under general scenarios.

**Chapter 7** analyzes representative viscoelastic models for simulating stress relaxation and proposes a model for this.

**Chapter 8** builds a TCM model for simulating the EAS evolution under general scenarios and develops a data-driven surrogate for the TCM model to improve the prediction efficiency.

Part V: Conclusions and prospects.

**Chapter 9** provides the main findings of this thesis and gives recommendations for future studies.

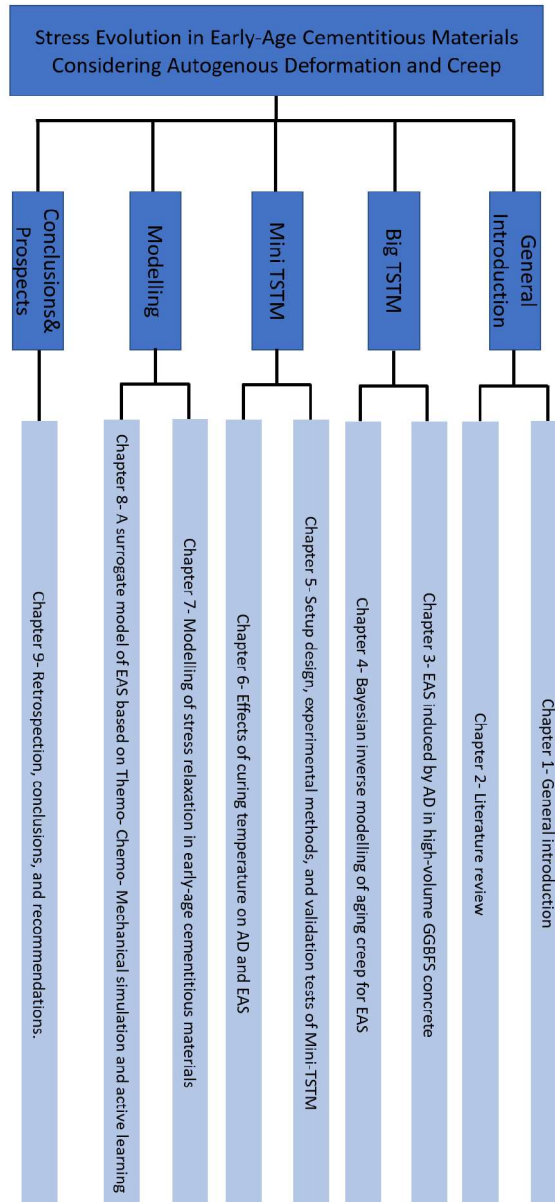


**Figure 1-2 Thesis outline**



## 2. LITERATURE REVIEW

*The risk of early-age cracking induced by (restrained) autogenous deformation is high for cementitious materials of low water-binder ratios. The autogenous deformation, viscoelastic properties, and stress evolution are three important factors for understanding and quantifying the risk of early age cracking. This chapter systematically reviews the literature related to experimental and modelling techniques for studying these three factors. It is found that the Temperature Stress Testing Machine (TSTM) is a unified experimental method for all these three factors, with a strain-controlled mode for stress evolution, hourly-repeated loading scheme for viscoelastic properties, and free condition for autogenous deformation. Such unified method provides basis for developing various models. In the end, summary of the relevant studies and outlook for future work are provided.*

*Parts of this chapter have been published in Liang, M., Xie, J., He, S., Chen, Y., Schlangen, E., & Šavija, B. (2024). Autogenous deformation-induced stress evolution in cementitious materials considering viscoelastic properties: A review of experiments and models. *Developments in the Built Environment*, 17, 100356.*

## 2.1 Introduction

As introduced in the chapter 1, the early-age stress (EAS) is the main indicator for assessing the risk of EAC. Under full restraint conditions, the EAS can be quantified by the volumetric deformation (i.e., autogenous deformation (AD) in this thesis) and viscoelastic properties. The structure of this chapter is shown in **Figure 2-1**. In this chapter, a literature review is presented related to experimental and modelling techniques of AD, viscoelastic properties, and their combined effect, i.e., the EAS evolution in early-age cementitious materials. The experimental analysis is the basis of the modelling technique, and is therefore introduced at the beginning of each section. The AD and viscoelastic properties are introduced in sections 2.2 and 2.3. In section 2.4, the studies of the EAS are summarized which should be analyzed in combination with AD and viscoelastic properties in previous two sections.

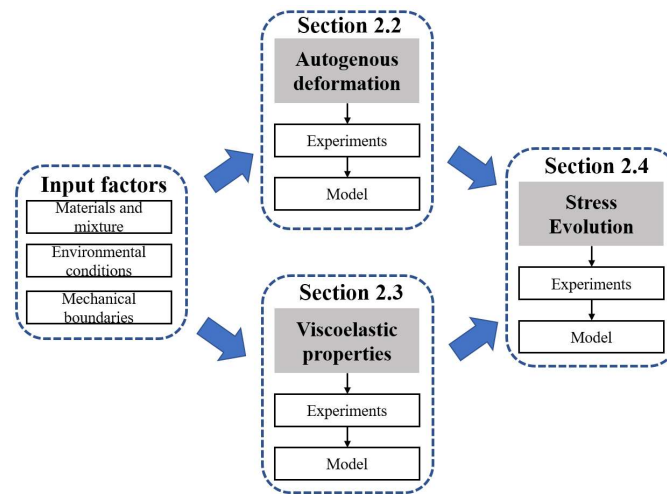


**Figure 2-1** Structure of the chapter

## 2.2 Autogenous deformation

AD ( $\epsilon_{ad}$ ) refers to volumetric deformation produced by continuous hydration of cementitious materials, excluding the effects of applied load and changes in temperature or moisture loss to the environment [30]. As shown by **Figure 2-2**, AD mainly comprises two parts: the autogenous swelling  $\epsilon_{sw}$  and self-desiccation shrinkage  $\epsilon_{sd}$ . Furthermore, if the temperature of the concrete is not constant, the apparent AD includes the

thermal deformation  $\epsilon_{th}$ , which must be deduced from the apparent AD to get the real AD. The initial deformation (mostly chemical shrinkage) happens before the solid skeleton formation, i.e., when the microstructure is not rigid enough to induce any EAS, and therefore such initial deformation can be neglected in EAC analyses [10]. On the other hand, self-desiccation refers to the pore water consumption by continuous hydration after the solid skeleton is formed. Following the theory of capillary pressure [31], water consumption causes a drop in internal relative humidity (RH), induces capillary pressure to compress the pore structure, and finally leads to overall volume contraction. If the self-desiccation shrinkage is restrained, tensile stress can be generated with a possible risk of EAC. Another part of AD, autogenous swelling, happens mainly because of the chemo-mechanical couplings between expansive hydration products (e.g., ettringite) and the pore structure [32–34]. The production of ettringite causes an initial expansion and therefore compressive stress in restrained concrete, which delays the development of tensile stress and reduces EAC risk. However, autogenous swelling is often neglected or underestimated [17], potentially because many AD tests start too late, ranging from 1 day to several days, and may overlook a part of autogenous swelling [34]. Another reason may be that the generation of expansive products depends highly on cement chemistry, such as the content of  $C_3A$  and gypsum, and only certain cements generate enough expansive products to induce apparent expansion. Furthermore, thermal deformation, which also leads to early expansion and later shrinkage, also makes it difficult to identify the “true” autogenous swelling and self-desiccation shrinkage [35].

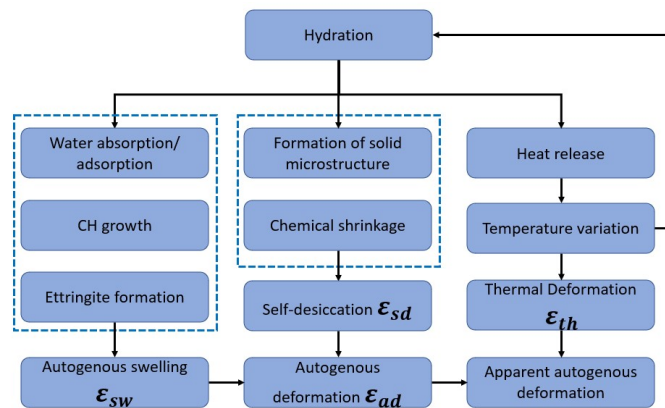


Figure 2-2 Mechanisms of autogenous deformation of cementitious materials (Adapted from [33])

## 2.2.1 Experiments for autogenous deformation

### 2.2.1.1 Methods

Following the definition of AD, the test needs to be performed with strict sealing and temperature control. The sealing condition is to prevent moisture loss of the specimen and to exclude drying deformation, while temperature control should prevent thermal deformation and changes in hydration kinetics that can be induced by temperature variation in the specimen. The most common way to test AD is to measure the length change of prismatic or cylindrical specimens with length sensors such as Linear Variable Differential Transformers (LVDT) or laser transducers attached at the side of the specimen [36,37] or strain transducers embedded in the core of the specimen [38]. The moisture loss and drying shrinkage can be easily prevented with good sealing, but the effects of temperature on the AD measurement require more complex measures. If strict temperature control in the specimen is not possible, it is often necessary to separate the real AD from the total deformation by deducing the thermal deformation indirectly based on the measurement of an embedded thermo-couple [38,39] or other sensors such as an optical fiber [40]. However, even though the thermal deformation can be well separated, regardless of the accuracy of coefficient of thermal expansion/ contraction (CTE/ CTC) that were used [41], the effects of temperature on hydration kinetics still exist and may not be neglected. Therefore, active temperature control is favorable for measuring pure AD by maintaining a strict constant temperature during the test [42]. Another problem with these tests is that the test can only start at least after setting when the cement paste is strong enough for displacement measurement. Therefore, such tests may neglect the initial part of AD and make the starting time of the AD measurement, referred to as time-zero, a debatable issue. Studies on the time-zero suggested different definitions, including the final setting time [14], the timing of the autogenous swelling peak for slag cement concrete [14], the onset of RH drop [43], the onset of capillary pressure [44], and transition point (between the fluid and solid state) determined from the autogenous strain curve [15].

Another kind of AD test, the so-called corrugated tube test, overcomes the time-zero issue by casting the cementitious material in a plastic corrugated tube and then measures the length change from the two sides [45], as shown in **Figure 2-3 (a)**. The corrugated tube is considerably stiffer in the radial than in the longitudinal direction, which enables the measurement of linear deformation by following the displacement of the corrugated tube at either end. By putting the corrugated tube in a temperature-controlled

oil bath, the effects of temperature on AD measurements can be eliminated [46]. A statistical study [16] has proven that the corrugated tube test is sufficiently sensitive to identify the AD of different levels, despite the considerably high scatter that may occur due to the inaccuracies in the initial measurement. However, because the standard corrugated tube is only 22 mm in diameter [45], corrugated tube tests were initially only used on cement pastes and fine-grained mortars. By changing the size of the corrugated tube, it has been also possible to test the AD of concrete since the placement of material [34], as shown in **Figure 2-3 (b)**.

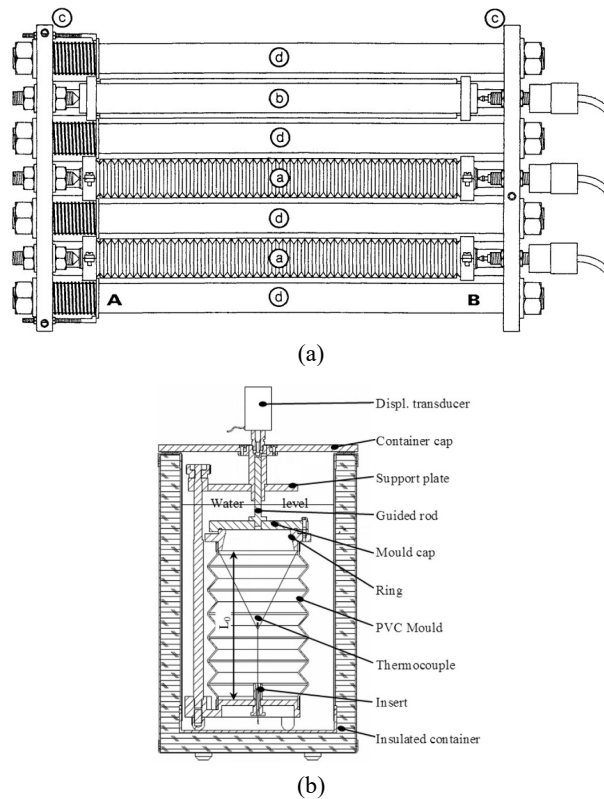


**Figure 2-3 Corrugated tube test: (a) standard designed by [45], used mostly for cement paste and mortar (a: specimen; b: invar reference specimens; c: steel plates; d: invar rods to connect the steel plates.); (b) enlarged corrugated tube test for concrete, designed by [34].**

Despite the convenience and accuracy of the corrugated tube test, the AD it measures cannot be directly related to the EAS, which is a more straightforward indicator of EAC. It was recently reported that the specimen geometry influences the AD measurement [47], which poses questions about whether the corrugated-shaped specimen is

representative of real-world structures. In view of the lack of EAS, the Temperature Stress Testing Machine (TSTM) test is developed and comprises two specimens with the same or similar geometry, one tested under free condition and one tested under restrained condition, which allows relating the measured AD to EAS. The specimens are sealed and covered by molds with embedded water channels for circulating temperature-regulated water to actively control the temperature inside the specimen. The deformation is measured by embedded bars in the specimen with LVDTs. An example of such an AD test, called the Autogenous Deformation Testing Machine (ADTM), is used in chapter 3.

Based on the testing methods described above, multiple influencing factors of AD have been investigated, mainly the effects of temperature, mix design, and the use of mitigation admixtures.

### 2.2.1.2 Temperature

AD tests are usually conducted under a constant temperature to exclude the influence of thermal deformation and different hydration kinetics. The results of such tests can only provide limited guidance on real-world applications where the temperature always varies. According to Klausen et al. [48], AD measured under a realistic temperature history differs significantly from that measured under constant temperature. In the field of cementitious materials, the maturity concept [49] has been widely used to estimate the mechanical properties under a varying temperature history based on the mechanical properties measured under a constant temperature. The assumption for the maturity concept is that temperature only influences the hydration rate, and that this influence is independent of the hydration degree. However, this assumption does not hold for AD. Specifically, except for hydration rate, the temperature also leads to changes in RH and surface tension, which reduces the applicability of the maturity concept for prediction of AD [39,50,51].

The exact influence of temperature on AD is complex because temperature not only influences the RH drop and surface tension but also results in different pore structures [52]. All these parameters are related to the formation of self-desiccation shrinkage [31]. Lura et al. [42] performed AD tests based on the ADTM machine (further discussed in chapter 3) from 10 to 40 °C and found that higher temperatures lead to earlier onset of shrinkage but not necessarily higher deformations. Similarly, Carette et al. [33] suggested an earlier onset of shrinkage when the temperature is higher. Furthermore, they also concluded that, due to the higher RH, coarser porosity, and increased solubility and decreased needle size of

ettringite, the higher temperature tends to decrease the total amplitude of both autogenous swelling and self-desiccation shrinkage. However, Orosz et al. [35] observed an opposite trend, i.e., that higher temperature leads to higher autogenous swelling, but they also mentioned the CTE may have compromised their measurement. Contradictory findings regarding the influence of temperature on self-desiccation shrinkage were also found: with increasing temperature, some studies [33,53,54] observed decreased self-desiccation shrinkage while others [41,51,55] saw an increased one. Maruyama et al. [56] conducted AD tests on ultra-high-performance concrete (UHPC) material and found that the influence of temperature is different before and after a so-called inflection point (i.e., when the maturity reaches 10~16 hours). Before the inflection point, the AD decreases with increasing temperature and then increases afterwards.

In summary, the applicability of maturity concept in predicting AD at different temperature is questionable. The increasing temperature can induce an earlier onset of self-desiccation shrinkage, which increases EAC risk. Furthermore, even with low temperatures, the rate of self-desiccation shrinkage of low-w/b ratio material is still significant, which means that EAC risk induced by AD cannot be neglected even in low-temperature environments.

### 2.2.1.3 Mixture

The influence of mixture design on AD can be summarized in 3 aspects, including the water-binder ratio (w/b), cementitious materials, and aggregate. The influence of w/b on AD is clear. A lower w/b ratio results in a denser pore structure and lower RH, which, according to the Kelvin-Laplace equation, can induce higher capillary pressure and therefore increase self-desiccation shrinkage. Sound experimental studies [38,57,58] verified that a lower w/b ratio induces faster self-desiccation shrinkage and therefore results in a higher EAC risk.

The influence of cementitious materials is a broad topic. An important factor is the particle size distribution of cementitious materials: the larger the particle size, the slower the RH decay and the larger the pore size. These two effects together lead to lower capillary stress and therefore a decrease of AD if cement with larger particle sizes is used [59,60]. Many studies also explored the influence of supplementary cementitious materials (SCMs) on AD in OPC-based blended materials. Common SCMs include Ground Granulated Blast-Furnace Slag (GGBFS), Fly Ash (FA), and Silica Fume (SF). Many researchers have observed that GGBFS [34,42,51,58,61] and SF [38,46,62] can significantly increase AD by reactive secondary hydration

leading to continuous pore refinement and internal RH drop, while the use of more inert SCMs like FA [46,51,62] and calcined dredging sediments [63] decreases AD by slowing down the hydration process. Other cementitious materials like UHPC [12,62] and limestone calcined clay cement (LC3) [64] were also reported to have significant AD. In addition, alkali-activated materials, which aim to replace all OPC with industrial byproducts like GGBFS, FA, metakaolin, etc., have been found to display a more significant AD development that is often multiple times higher than OPC-based concretes, due to the more rapid reaction and a much denser pore structure [65,66].

The influence of aggregate on AD can be summarized in 3 effects, including effects of dilution, restraint, and internal curing. The use of aggregates reduces the volume ratio of cementitious materials and directly reduces development of AD in concrete [67]. Furthermore, natural dense aggregates act as internal restraint in the cement matrix and lead to decreased AD [68]. As shown in [Figure 2-4](#), such restraining effects can result in a heterogeneous strain field which can be visualized by digital image correlation (DIC) to investigate the exact influence of aggregate size and distribution [69,70]. On the other hand, water saturated porous aggregate (e.g., lightweight aggregate, recycled concrete aggregate, etc.) acts as an internal water reservoir which gradually releases water and slows down the RH drop, alleviates the self-desiccation process, and thereby decreases the AD [19,71,72]. However, it should also be noted that the incorporation of porous aggregate leads to lower mechanical properties, and optimizations on the exact aggregate type and volume is necessary [73,74].

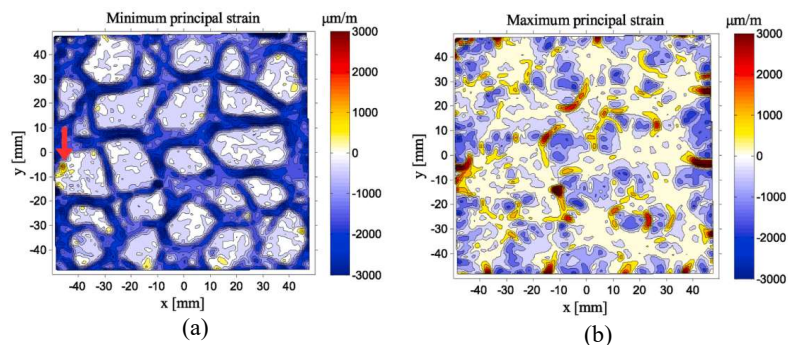


**Figure 2-4** An example of drying shrinkage captured by DIC, adapted from [70]: (a) Minimum principal strains; (b) Maximum principal strains.

#### 2.2.1.4 Mitigation strategies

Most mitigation strategies for AD prevention are based on the following mechanisms: control of hydration, reduction of surface tension of the pore solution, the addition of internal restraint, formation of expansive products, and internal curing [11].

For control of hydration, the use of SCMs is a common measure, as discussed in section 2.1.4. In addition, superplasticizers and viscosity-modifying agents that delay the hydration reaction can also decrease AD [57,75]. Shrinkage-reducing agents (SRA) decrease the surface tension of the pore solution to reduce the capillary pressure which leads to reduction of AD [13,20–23,76]. Recently, Zhang et al. [77] developed a shrinkage-reducing polycarboxylate superplasticizer which substantially reduces AD by combining the effects of delayed hydration, reduced surface tension, and formation of expansive products (i.e., portlandite). Internal restraint can be achieved by aggregate (as in section 2.1.4), reinforcement [78], and various types of fibers (e.g., steel fiber [12], cellulose fiber [79], Barchip fiber [80] etc.). The formation of expansive products by calcium sulfoaluminate cement [81,82] or CaO-based expansive agents [78,83] has been proven to effectively compensate the self-desiccation shrinkage by producing expansive products like ettringite and portlandite. Internal curing by either lightweight aggregate or superabsorbent polymers (SAP) is a straightforward countermeasure against self-desiccation and has been proven by many studies as a very effective solution [72,84]. The use of lightweight aggregate has been introduced in section 2.1.4. Despite having a negative influence on the mechanical properties, it was observed that the pre-wetted SAP partially fills with portlandite during cement hydration, delays the main hydration peak, and increases the hydration degree after a few days [84]. The success of SAP was also observed in FA and GGBFS-blended binders and LC3 pastes [85,86].

#### 2.2.2 Modelling of autogenous deformation

There are two categories of models for predicting AD: empirical models and analytical/ numerical models. Empirical models are the results of statistical analysis of experimental data and are commonly used by researchers and engineers. On the other hand, analytical or numerical models aim to predict the AD by simulating the underlying mechanisms.

### 2.2.2.1 Empirical models

Most formula-based empirical models assume that AD is the product of two components, an ultimate AD  $\varepsilon_{au,e}$ , and a time-decaying function  $f$  (mostly power function), as below.

$$\varepsilon_{au} = \varepsilon_{au,e}(mix, env) \times f(t, mix, env) \quad (2-1)$$

where the  $\varepsilon_{au,e}$  and  $f$  are both dependent mainly on the concrete mixture and environmental parameters. The form of an empirical model described by Eq (2-1) is widely adopted by different design codes [87–90]. As the autogenous swelling is seldom even mentioned in tests, the code-based formulas assume AD a monotonically decaying function as given by Eq (2-1). Contrarily, Carrete et al. [33,34] built a semi-empirical model based on the corrugated tube test for concrete (**Figure 2-3 (b)**), that considers AD as a sum of autogenous swelling and self-desiccation shrinkage which is induced by ettringite formation and capillary pressure, respectively.

A new class of empirical model have been constructed based on Machine Learning (ML) algorithms like Extreme Gradient Boosting or Artificial Neural Network, which showed significantly better performance than traditional empirical models [91,92]. The ML approach train sophisticated statistical models with massive data to obtain generalizing capabilities for predictions of AD in different scenarios and may be a promising approach to replace the traditional (i.e., formula-based) empirical models.

### 2.2.2.2 Analytical and numerical models

Analytical and numerical models aim to predict the AD from the underlying physico-chemical mechanisms, as shown in **Figure 2-5**. Constructing such a model including all (or most) relevant mechanisms involves a multiscale and multi-field analysis, and is still a challenge due to its complexity. However, some studies managed to build such unified models. Pichler et al. [93] employed a kinetic law [94] to simulate cement hydration with different chemical constituents and obtain the overall hydration kinetics and microstructural parameters (products by volume percentage). Assuming capillary pressure (induced by self-desiccation) and crystal pressure (induced by ettringite formation) as the main driving force of AD, they applied micromechanics to calculate the elastic deformation of a homogenized composite as the AD, by homogenizing the elastic modulus of different phases from the scale of Calcium-Silicate-Hydrate (C-S-H) to concrete. Pathirage et al. [95] used the Cement Hydration in Three Dimensions (CEMHYD3D) model at the microscale to obtain the material properties as input for a Hygro-Thermo-Chemo (HTC) model [96,97] at the

macroscale to simulate the RH drop (i.e., self-desiccation). Zhao et al. [98] used the Hymostruc model [99–101] for calculating the RH drop and Shimomura model [102] for calculating the pore size distribution. Based on the micromechanics, the homogenized elastic properties of concrete were obtained by an upscaling process from C-S-H to concrete, and the AD was calculated as the elastic response to the capillary pressure.

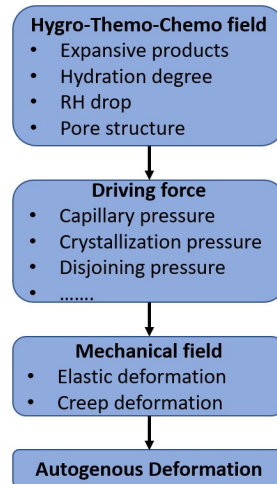


**Figure 2-5 Underlying mechanisms considered in theoretical models for AD prediction**

While the models mentioned above have already encompassed a combination of complex mechanisms, there is still room for improvement. Specifically, while the model in [95] did not extend further to mechanical field to predict the AD, the models in [93,98] only assumed AD as the elastic response of the microstructure to the capillary pressure, which is problematic because the early-age cementitious material is a viscoelastic material (if neglecting visco-elasto-plasticity at high stress condition). Based on the capillary pressure theory and micro-poromechanics, Aili et al. [103] concluded that the long-term AD evolves logarithmically, and that AD is a viscoelastic response to self-desiccation. In view of the necessity of considering creep in AD prediction, Gao et al. [104] used the Hymostruc model [99–101] to obtain the microstructure and the RH drop. Based on the simulated microstructure, they built the lattice fracture model [105] and applied internal loads (calculated by the capillary pressure) on the lattice beams to simulate the compression of the microstructure induced by self-desiccation. The creep effects were simulated by using a penalized effective modulus, which was determined by calculating the compression creep of a simple one-dimensional loaded beam.

Other models focused on the quantification of the driving force (i.e., capillary pressure in most cases) and mechanical field, left out the HTC field, and used experimental data or empirical models for the input of pore size distribution, RH drop, heat release, etc. Huang et al. [106] used a series of empirical models for the input of RH, hydration degree, saturation degree, elastic modulus, etc., and then calculated AD as the elastic response to the capillary pressure. Hu et al. [107] used a Kelvin-Voigt model to simulate the aging viscoelasticity of cement pastes and calculated the self-desiccation shrinkage based on poromechanics, using the experimental data of RH, elastic modulus, and creep as input. Lu et al. [108] considered the AD as a combination of the elastic part and the creep part and calculated the AD by a linear superposition of incremental viscoelastic deformation based on the internal capillary pressure theory. The early-age creep was obtained from the activation energy concept [109]. Furthermore, the Pickett Effect was incorporated to simulate the restraining effect of aggregate [68], which not only resulted in a good prediction for Portland cement concrete but also for alkali-activated slag and fly ash concrete [110].

These models for AD prediction are summarized and compared in [Table 2-1](#). All models considered capillary pressure as the driving force behind self-desiccation shrinkage. This is valid for early-age material because the capillary pressure is the main driving force for RH above 40-50%, while other mechanisms, including disjoining pressure, surface tension, and interlayer water, mostly occur at RH lower than 40%, which is generally not the case for early-age materials [17]. By comparison, it seems that a combination of Hystrostruc and Lattice Fracture Model [104], is until now the most complete model that encompasses the hydration reaction, self-desiccation, and the viscoelastic response to the capillary pressure from the microscale. It should still be noted that the model of Gao et al. [104] and many other models except for [93] only considered the self-desiccation shrinkage as AD and considered the capillary pressure as the driving force. This is understandable since the self-desiccation shrinkage is indeed the most relevant risk factor regarding EAC. However, the contribution of autogenous swelling should not be neglected, otherwise the EAS calculated based on the AD will be overly conservative. Another concern is that the constitutive model of the mechanical field in [104] only considered the creep effects by effective modulus, while the superposition of incremental creep strain was done with a simple one-dimensional beam, which did not consider the real strain history in the elements. Finally, one more thing worth being noted is that only the model of Pathirage et al. [95] explicitly simulated the hygral field for RH drop in self-desiccation, while the others only calculated the RH drop indirectly. However, their model [95] focused

only on the self-desiccation and RH drop, and did not extend to the mechanical field to predict the AD.

**Table 2-1 Summary of analytical models for AD prediction**

Ref.	Pore	RH	Elastic Modulus	Creep	Driving force	Mechanical model
Pichler et al. [93]	Kinetics law and others		Micromechanics	-	Capillary and crystallization pressure	Micromechanics
Pathirage et al. [95]	CEMHYD3D and HTC model		-	-	-	-
Huang [106]	Empirical formula			-	Capillary pressure	Poromechanics
Zhao et al. [98]	Shimomura model	HymoStruc model	Micromechanics	-	Capillary pressure	Micromechanics
Aili et al. [103]	Empirical formula		Micromechanics with non-aging properties		Capillary pressure	Micro-poromechanics
Gao et al. [104]	HymoStruc		Properties of each micro phase (obtained from literatures)		Capillary pressure	Lattice Fracture Model with effective modulus for creep effects
Hu et al. [107]	Test	Test	Test	Test	Capillary pressure	Poromechanics
Lu et al. [68,108]	Test	Test	Test	Activation energy concept	Capillary pressure	Poromechanics with Pickett effect

### 2.3 Viscoelastic properties

Viscoelastic properties determine the rate of EAS buildup, which can be quantified by two kinds of parameters: elastic modulus for elasticity and creep compliance or relaxation modulus for viscosity. In a loading test, elastic modulus can be calculated as the slope of the stress-strain curve of the load-increasing or -decreasing part. Creep compliance refers to the strain elapsed with time induced by a constant unit load, while the relaxation modulus refers to the stress elapsed with time induced by an

imposed constant unit strain [111]. Due to the technical difficulties of sustaining a constant strain in relaxation tests, creep tests are usually conducted [112]. Specifications for tests of elastic modulus and creep and their empirical formulas are beyond the scope of this chapter and can be found in various designing codes for concrete structures and materials [30,88,113–117]. In the following sections, the focus is on the mechanisms, testing methods, and modelling schemes for quantifying the viscoelastic properties.

### **2.3.1 Elastic modulus**

#### **2.3.1.1 Macroscale tests for elastic modulus**

Elastic modulus is positively correlated to compressive strength, as revealed by macroscale loading-unloading tests [118]. Empirical formulas are well established to infer the elastic modulus from either mixture parameters or compressive strength data [113,119]. Therefore, the influence of mixture parameters and environmental conditions on elastic modulus is generally similar to that on strength [120]. Specifically, regarding the influence of temperature, the maturity concept has also been successfully applied to predict the evolution of elastic modulus [121,122]. It is worth noting that the influence of aggregate on elastic modulus is more significant than that on strength [119,123]. Moreover, despite the good accuracy of empirical formulas in prediction of elastic modulus, they are mostly calibrated for mature concrete, which casts doubts on predictions of early-age elastic modulus. The early-age elastic modulus is difficult to measure by traditional loading-unloading methods because of the large number of tests needed for obtaining the elastic modulus at different ages and the challenges of preparing very soft specimens for testing at young ages. One way to circumvent this difficulty is through in-situ testing. Boulay et al. [124] devised a test rig called BTJADE (French acronym for BeTon au Jeune Age, mesure de la Deformation Endogene) to monitor the development of elastic modulus immediately after casting by continuously applying compression load. The BTJADE setup uses LVDTs to measure the strain and the mold uses temperature-regulated water to control the sample temperature. TSTM is also suitable for this test; furthermore, it allows testing of the elastic modulus under tension since most TSTM specimens are dog-bone shaped. However, much larger specimens are needed for TSTM testing. Elastic modulus at early ages can also be measured indirectly, e.g., by the ultrasonic pulse velocity (UPV) [125].

### 2.3.1.2 Microscale tests and modelling of elastic modulus

Microscale tests ( $10^{-6}$ ~ $10^{-4}$   $\mu\text{m}$ ) of elastic modulus aim for a more fundamental understanding and lays foundations for a reliable prediction model. OPC paste can be seen as a composite of various hydration products, including phases like C-S-H, calcium hydrate, unhydrated particles, porosity, etc. [126,127]. Assuming that the distribution of the mechanical properties of each kind of hydration product is Gaussian, statistical nanoindentation tests have been used to extract the average mechanical properties of each nanoscale ( $10^{-8}$ ~ $10^{-6}$   $\mu\text{m}$ ) phase in hydrated cement paste. Except for Gaussian-based method, other methods like k-means clustering [128] can also be used for the deconvolution process. This allowed for the effective mechanical properties of the composite to be calculated with micromechanical models using the averaged modulus and volume fraction of each phase as input [126,129–131]. The real effective elastic modulus is often obtained by microindentation test [132] to validate the results of micromechanical models. Such micromechanical models have been successfully used to predict the effective elastic modulus of different cementitious materials, including blended cement pastes [133], polymer-modified cement pastes [134], geopolymers [135,136], seawater-mixed alite pastes [137], and nature pozzolan concrete [138]. However, note that except for micromechanical models, Lattice Fracture Model [139–142] and other FEM models [143] have also been used for upscaling of mechanical properties from several phases to the effective properties of the composite. Once the homogenization scheme (either by micromechanics, Lattice Fracture Model, or other FEM methods) is chosen and validated by nano- and micro-indentation, the time-dependent elastic modulus can be obtained by using a hydration model which provides evolution of volume fractions of each micro phase, as in [94,144–146]. Although these models showed satisfactory accuracy in different cases, difficulties still exist with the quantification of ITZ properties, which was considered in [131,143,147].

### 2.3.2 Creep/ Relaxation

Viscoelastic properties can be quantified by both creep compliance and relaxation modulus. With a linear viscoelastic constitutive relationship, following the Boltzmann superposition, the creep compliance function and relaxation modulus function are fully coupled and can be calculated if either one is known [111]. Therefore, the creep compliance function and relaxation modulus function are equivalent representations of the viscoelastic properties of the material.

### 2.3.2.1 Experiments for creep/ relaxation

Measuring the relaxation modulus is much more challenging than testing the creep compliance, because the relaxation test requires not only the strain measurement but also a loading system that actively adjusts the load to maintain a constant strain, which is the principle behind the TSTM test. On the other hand, the creep test only requires one to keep the load constant and measure the strain, which is more straightforward and therefore is adopted by most studies.

#### 2.3.2.1.1 Macroscale testing

Macroscale testing directly provides input for simulating the EAS evolution. While studies have been devoted to long-term creep [148], the main interest of EAC analysis is the early-age creep, which requires multiple creep measurements during early stages of hydration. In other words, the specimen needs to be loaded multiple times to obtain the creep at different ages. However, at early age during the load-holding stage when the creep deformation is happening, which can last from hours to days, the properties of the hardening specimen also evolve very fast. As a result, the measured deformation during the load-holding stage is a combined effect of creep and hydration. In view of this, hourly repeated minute-long quasi-static tests for creep have been proposed [149–153]. The main advantage of this test is that, with a load-holding stage of only three minutes, hydration effects can be neglected, and the tested deformation then represents the creep strain obtained at corresponding loading age. Moreover, such a test allows for creep measurement in every hour and measures the elastic modulus during every loading-unloading process. Therefore, the hourly repeated minute-long quasi-static test alone is already able to provide the input of viscoelastic properties for EAS simulation. Another test that aims to exclude the effect of hydration on creep measurement is the so-called equivalent systems test [154], where part of the unhydrated cement is replaced with inert filler to emulate specific microstructural features of the real hydrating systems. However, as the results showed, real systems experienced much higher creep than the equivalent inert systems.

There are also other macroscale creep tests, such as the flexural creep test for eliminating the influence of shrinkage on creep [155–157], TSTM-based tensile creep test [158], creep test with double feedback control [159], and creep test coupled with acoustic emission measurement [160]. Macroscale creep tests can be used to investigate influence of many factors. In blended cement systems, it was found that the use of FA, quartz, and glass powder significantly increases creep [161–163], while the use of GGBFS may

decrease creep and the influence of GGBFS compositions was highlighted [164,165]. In addition, the effects of other parameters on creep, such as temperature [166], w/c ratio [167], lightweight aggregate [168], recycled concrete aggregate [169], steel fiber [168,170], MgO [171], and SAP [172] have also been extensively investigated by macroscale tests.

The temperature influences creep mainly by two mechanisms [173]: 1) a temperature increase accelerates the bond breakages and restorations causing creep, and thus increases the creep rate [166,174]; 2) a temperature increase accelerates hydration and therefore reduces the creep. For early-age concrete, the effect of hydration dominates and therefore the maturity concept can still be used for predicting the basic creep at the early age [173,175]. The increase of RH can increase the long-term creep rate [174,176], and can be quantified by the microprestress-solidification theory [173,177]. For EAS analysis, the influence of compressive or tensile creep is important, because EAS evolution usually starts with compressive stress due to the autogenous swelling (or temperature increase) and then tensile stress due to the self-desiccation shrinkage (or temperature decrease). However, a consensus regarding the influence of creep in tension and compression has not been reached yet. Atrushi [178] suggested that creep in tension is initially lower but establishes a much higher rate than in compression. Similarly, Rossi et al. [179] observed that compressive creep is more significant than tensile creep, but they also saw that compressive and tensile creep are similar under drying conditions. By contrast, many other studies suggested that compressive and tensile creep are similar, and that it is justifiable to use compressive creep to substitute tensile creep [111,166,180,181].

#### **2.3.2.1.2 Microscale testing**

Microscale creep tests aim to reveal more fundamental mechanisms of creep behavior and lay foundation of micromechanical prediction models for predicting creep properties. Minutes-long micro- or nano-indentation tests have been widely used for obtaining the creep properties of cementitious materials at the microscale [132,176,182–188]. A major advantage of such test is that it can also quantify the long-term creep properties, which is significantly faster than macroscale tests [189]. In addition, micro-cantilever tests have also been used to characterize the creep properties at microscale [190]. Microscale tests offered fundamental understandings on creep mechanisms. Hu et al. [132] identified the influence of Ca/Si ratio on creep modulus and quantified that the creep modulus of CSH is 180 GPa. Liang et al. [186] found that the long-term creep rate of cement paste appeared to be independent of loading duration,

holding duration, indentation force amplitude, and unloading duration of the microindentation tests, suggesting that it is an intrinsic material parameter. Li et al. [188] observed that the deviatoric stress-induced preferred orientation of crystallites significantly influences the creep behavior. The influence of other parameters on the creep mechanisms of cementitious materials at the microscale was also extensively investigated by microindentation tests, such as the effects of capillary water [184,185], relative humidity [191], initial viscosity [187], and porosity [192].

### 2.3.2.2 Modelling the viscoelastic properties

Models for creep predictions can be divided in two categories, empirical models and analytical/numerical models. Empirical models are often the statistical results of massive data of macroscale tests, while the analytical models are developed from the perspective of micromechanics.

#### 2.3.2.2.1 Empirical models

In empirical models, creep compliance function is usually expressed in the following form:

$$J(t_0, t) = \frac{1}{E(t_0)} + C_0 C_1(t_0) C_2(t - t_0) \quad (2-2)$$

where the  $E$  is the elastic modulus;  $t_0$  is the time when load was applied;  $t$  is the time of interest;  $t - t_0$  is the time elapsed since the load is applied;  $C_0$  is a fitting parameter related to mixture and environment;  $C_1$  is the function of  $t_0$ , which describes the aging (i.e., evolution) of creep compliance, and should also be dependent on mixture and environment;  $C_2$  is the function of  $t - t_0$ , which describes the non-aging creep, and should also be dependent on mixture and environment. Many design codes [30,88,113–117] adopted the Eq (2-2) as the form of their fitting formula of creep compliance. A major difference between different codes may be the choice of the non-aging function  $C_2$ , which is often a power function for description of short-term creep [190,193] and a logarithmic function for long-term creep [148,182,185,189,194]. Besides, improvements to the empirical formulas have been achieved by incorporating additional parameters, such as the fictitious degree of hydration [195,196], age-adjusted effective modulus [197], and hydration degree of slag [165].

Another form of empirical models is the ML-based models, such as Artificial Neural Network [198], Genetic Programming [199], Support Vector Machine [200], ensemble model [174], and Deep Convolutional Neural Networks [201]. These models were mostly trained on massive database of creep tests [202,203], and show superior performance compared to

traditional codes on predicting the creep behavior of cementitious materials.

#### 2.3.2.2.2 Analytical and numerical models

Before discussing the analytical models for creep, it is important to note that for EAS analysis, the input of creep compliance needs to be a fast-aging function. An important theory to describe the aging of creep is the solidification theory [204–206], which considers aging as resulting from the progressive solidification of a basic constituent that behaves as a non-aging viscoelastic material. Based on the solidification theory, the Microprestress-Solidification theory [111,171,177] was developed and constantly improved to describe the influence of temperature and RH. For description of the non-aging term of creep, rheological models including Kelvin chain and Maxwell chain [162,166,171,207,208] can be used, by fitting the governing equation of the rheological model with the experimental data. To describe aging, a spectrum of rheological chains is needed, which can often be calculated with the continuous retardation chain method [209–211]. Then, rheological models can be used in a Finite Element (FE) Model to calculate the creep behavior of concrete structures, using the rate-type form and exponential algorithm [111,112,212,213].

Similar to the modelling methods of elastic modulus in section 2.3.1.2, based on the microscale and macroscale tests, multiscale models were built to describe the overall creep behavior of a multiphase composite based on the input of the hydrated cement paste phases, such as C-S-H, CH, unhydrated particles at microscale and aggregate, ITZ at mesoscale. In such multiscale models [214,215], the creep compliance is often quantified as creep modulus and the input of each single phase needs to be obtained from nanoindentation tests. Based on a quasi-elastic relationship between creep and relaxation in the Carson-Laplace space [189,216], the elastic micromechanical homogenization schemes such as Mori-Tanaka scheme [217] or the Self-Consistent scheme [218] can be used to calculate the effective creep modulus from a composite of phases with different creep modulus and volume fractions. Königsberger et al. [219] compared the results of three micromechanical models with macroscopic samples of cement paste, mortar, and concrete, and demonstrated the feasibility of such upscaling method by micromechanical models. Baronet et al. [220] proposed a two-scale micromechanical model to characterize the logarithmic creep of concrete by coupling microindentation and uniaxial compression creep test. Except for micromechanical models, FEM models [221] and Lattice Fracture Models [222] can also be used for upscaling. Following the solidification theory, that aging of creep is the progressive

volume change of hydration products and unhydrated particles, the aging creep can be obtained by coupling the micromechanical models and a hydration model, as done by Lavergne et al. [223].

For analysis of EAS, time-dependent viscoelastic properties (i.e., aging creep and elastic modulus) are important input. The multiscale modelling schemes for creep and elastic modulus are similar, as introduced in section 2.3.1.2. A general description of such multiscale modelling scheme is shown in **Figure 2-6**. For elastic modulus, a direct implementation of the elastic micromechanical homogenization schemes (like in [126,129–131]), or a simulation of a loading-unloading test by a lattice model (or other FEMs, like in [139–143]) is sufficient. For creep modulus, the elastic micromechanics needs to be implemented in Carson-Laplace space (like in [214,215]), in which the relaxation and creep follow a quasi-elastic constitutive relationship. If using the Lattice model or other FE models for creep modulus (like in [221,222]), the input of creep of each phase needs to be discretized into rheological chains, and then the integral of creep needs to be calculated by either direct integration or by a more efficient algorithm, like the exponential algorithm.

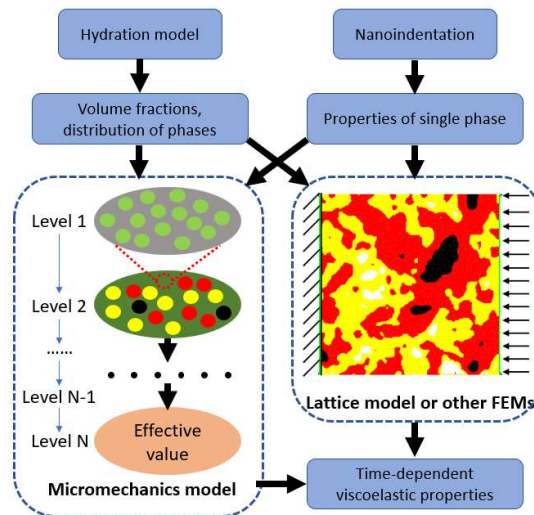


**Figure 2-6** General procedure of multiscale modelling for viscoelastic properties of cementitious materials

## 2.4 Early-age stress

EAS is the combined result of restrained AD and aging viscoelastic properties of concrete. Understanding and quantifying EAS is a significant

step to further analyze the EAC risk. Intrinsically, EAS is the result of a relaxation process, which aims to measure the stress evolution under a series of imposed deformation (i.e., restrained AD that happens constantly during hydration of restrained concrete). Therefore, the relaxation modulus and AD are important input for the calculation of EAS, which can be obtained either experimentally or numerically based on the approaches described in section 2.2 and 2.3.

### 2.4.1 Experiments

There are many methods for the quantification or characterization of EAS, such as the internal restraint test [224,225], rigid cracking frame test [226], ring test [227–230], and temperature stress testing machine (TSTM) [55,231]. Among these tests, a TSTM system appears to be the most versatile because it can not only measure the EAS, but also AD and creep if given a different boundary condition [25,28]. Moreover, a TSTM system includes strict temperature control to simulate various realistic thermal conditions. A TSTM system alone encompasses most required input parameters and output results of an EAS model, and thus provides a solid basis for a more thorough understanding of EAS buildup process and a reliable prediction model for EAS. This section will then focus on the TSTM.

#### 2.4.1.1 TSTMs

The general design of a TSTM system [27,28,55,232–236] is shown in [Figure 2-7](#). A TSTM system mainly comprises four parts: the free deformation test, the restraint test, the thermal control, and the deformation control. The free deformation test is the ADTM test used to measure the AD, as described in section 2.2.1.1. The restraint test is the main part of the TSTM system. In the restraint test, a dog-bone specimen, with a similar geometry to that of the ADTM test, is actively restrained by applying a force  $F$  at one end of the specimen. The value of  $F$  is determined by a feedback loop (FL1) to fulfill the deformation control, which keeps adjusting the  $F$  to make the deformation  $\varepsilon_r$  in the straight part of the specimen constant. Both the free and restrained specimens are connected to a cryostat, which keeps adjusting the water temperature  $T_w$  to keep the temperature in the specimen  $T_c$  following a pre-specified constant value or profile, with a specially designed feedback loop FL2.

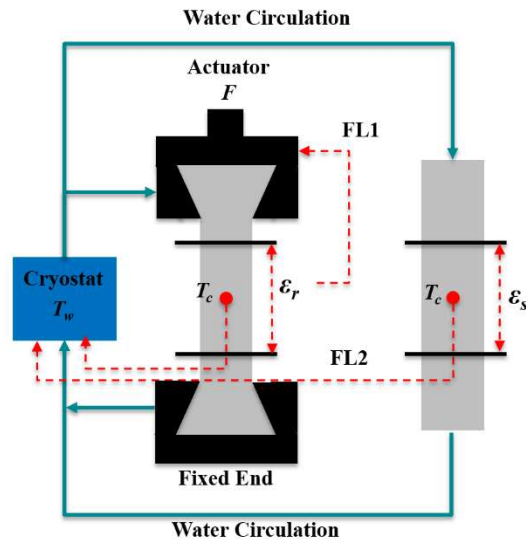


Figure 2-7 A general schematic diagram of the TSTM systems

In line with the [Figure 2-7](#), some representative TSTMs from the past four decades are summarized in [Table 2-2](#), distinguishing the specific differences between TSTMs in specimen size, strain measurement methods, strain control algorithms, and time-zero settings. All selected TSTMs use specimens longer than 1000 mm. For strain measurement, TSTMs all use different methods, but it is worth noting that the TSTM from University of Adelaide and University of Tokyo both arranged LVDT on top side of the specimen, which was reported to result in a better measurement accuracy and promote pre-installation efficiency. For the strain control (i.e., FL 1 in [Figure 2-7](#)), only the TSTM at the TU Delft uses a proportional–integral–derivative (PID) controller, which continuously adjusts the load  $F$  according to the deformation measurement  $\epsilon_r$  to fulfill the restraint condition, while others use stepping control which requires the load adjustment whenever the change of measured deformation exceeds a certain threshold. Finally, it is also interesting that different TSTMs have different time-zeros, either defined by the minimum EAS or by specifying the setting time. The problem of different definitions for the time-zero was also broadly discussed by studies of AD, as introduced in section 2.2.1.1. which can be avoided if the EAS results are available.

Table 2-2 Summary of representative TSTMs

Source	Year	L*W*H (mm)	Strain Measurement	Strain Control	Time-Zero
TU Munich [232]	1984	1500*150*150	Two-side, 2 LVDTs	Stepping	Stress 0.01 MPa
Technion [233] Hohai University [55]	1990, 2015	1500*150*150	Free-end, 1 LVDT	Stepping	Stress 0.01 MPa
NTNU [28,234]	1995, 2012	1000*88*100	Two-side, 4 LVDTs	Stepping	Initial setting
TU Delft [235]	2000	1450*150*100	Two-side, 4 LVDTs	PID	Setting time
University of Queensland [27]	2018	1200*80*80	Top-side, 4 LVDTs	Stepping	Setting time
University of Tokyo [236]	2022	1200*120*120	Top-side 2 LVDTs at two ends before 24 hours and two-side 2 LVDTs afterward	Stepping	Setting time

Despite providing valuable data about EAS, the TSTM faces certain challenges when it comes to practical implementation. Some major concerns are:

- 1) Due to the complexity of TSTM systems, the pre-test installation, casting, and post-test disassembling procedures require a substantial workforce [27]. For instance, the TSTM test conducted at TU Delft requires the collaboration of 3-4 individuals over a span of two entire working days, with each day consisting of eight hours [235].
- 2) The choice of threshold value in TSTMs employing stepping control to achieve full restraint is subjective and can impact the accuracy of the testing process [25,37].
- 3) The positioning of LVDTs for strain measurement, which provides input for the feedback loop for the actuator (i.e., FL1 in [Figure 2-7](#)), plays a crucial role in ensuring the reliability of TSTM systems [37]. Consequently, recent studies on enhanced TSTMs have placed

- significant emphasis on this aspect [27,236]. By analyzing the TSTMs outlined in **Table 2-2**, certain key points have emerged regarding the arrangement of LVDTs for strain measurement: 1) Rather than measuring deformation only on one side of the specimen, it is advisable to measure it on both sides. This approach enables the detection of potential eccentric deformations; 2) Instead of measuring deformation at the crosshead of the dog-bone specimen, it is preferable to measure it at the straight part. The absence of stress concentration in this region ensures more reliable results, which can be used as input for numerical models; 3) It is crucial to avoid directly attaching the LVDTs to the loading grip. Otherwise, any slip between the loading grip and the specimen will also be included in the strain measurement, resulting in possible errors.
- 4) In existing TSTMs, where specimens are tested horizontally, friction between the hardened specimen and the mold at the bottom can introduce errors in stress measurement. Proposed measures to reduce friction include using Teflon sheets [27] and implementing roller supports [236].

#### 2.4.1.2 Influencing factors

Despite the aforementioned concerns, TSTMs still led to important findings. Igarashi et al. [233] found that the AD-induced EAC happened when the stress-strength ratio reached 50%, and they pointed out the significant influence of relaxation on EAS evolution. Note that the strength data used in the calculation of stress-strength ratio refer to strength data obtained in traditional strength test (e.g., direct tensile strength test or tensile-splitting test), rather than the real strength of the specimen that is in the TSTM test. The importance of relaxation was also highlighted by other studies [237,238]. Zhu et al. [239] found that the EAC induced by thermal deformation happened when the stress-strength ratio reached 76% and proposed a combined stress-strain failure criterion for evaluation of EAC risk. Despite the fact that the failure mechanisms of restrained aging concrete are different from those under uniaxial tension test, a comprehensive review summarized that most EAC happens at a tensile stress-strength ratio of 0.5-0.9 [24], and therefore a maximum ratio of 0.5 is often adopted in structural designs to prevent EAC. In some other more specific failure criterions of EAC, which are mostly a variant of the stress-strength ratio, the EAS remains a necessary input [240].

Furthermore, with TSTM, the influence of temperature on AD-induced EAC was more systematically investigated. Lura et al. [42] found that the temperature increase did not induce higher AD, but led to higher EAS rate.

Similar observations were obtained by Li et al. [41]. Klausen et al. [241] conducted comprehensive TSTM tests on various influencing factors and concluded that temperature and the restraint degree are the most influential. Moreover, they also emphasized the considerable variation between different batches of the same cement, which is similarly described in corrugated tube test for AD [16]. In addition, several TSTM-based tests focused on the influence of mixture parameters, such as SCMs like GGBFS [229,242–245], FA [5,161], and SF [246], alkali-activated materials [237], recycled aggregates [247], and MgO expansive agent [248].

#### **2.4.2 Modeling the EAS using AD and viscoelastic properties as input**

Modelling the EAS basically requires three inputs: the AD, the creep/relaxation, and the elastic modulus. With the measurement or modelling results of AD and viscoelastic properties, as introduced in sections 2.2 and 2.3, the EAS can be directly calculated based on a viscoelastic model. The last key point is the conversion from the measured creep compliance to the relaxation modulus. Such conversion can be done by solving the integral relation between creep and relaxation numerically [111]. To avoid the complexity of such procedures, one can also use a semi-empirical solution given by Bažant and Kim [249]. On the other hand, Wittmann and van Breugel et al. [237,250,251] obtained an explicit conversion function based on the definition of a relaxation test, which is significantly easier than the numerical method based on the integral relationship between creep and relaxation. In recent years, both methods have shown good applicability in prediction of EAS. Wei et al. [252] converted the creep compliance given by the MPS theory using the numerical solution of the creep-relaxation integral, and successfully predicted the EAS under varying temperature in restrained concrete with good precision. On the other hand, based on the explicit conversion function, Li et al. [110,237,253] successfully predicted the EAS induced by restrained AD of alkali-activated material in multiple testing cases. In addition, it is also worth noting that some methods do not require to obtain the relaxation modulus and solve the creep-relaxation integral. Instead, it is also possible to simulate the EAS from the perspective of creep. For example, Klausen [28] first calculated the incremental creep strain based on the Boltzmann superposition, and then assuming both the AD and thermal deformation were restrained, they calculated the incremental EAS with an elastic relation, which also matched well with the experimental observation.

Note that the models mentioned above about EAS were all based on a 1D restrained case, since the validation data is from the TSTM test, which is

indeed an 1D restraint test. Modelling the EAS in real structures requires the use of FE models. It should be, however, noted that directly implementing the integral of linear viscoelastic constitutive relation in FEM is difficult, because the strain/ stress history of every previous time step would need to be stored to perform the linear superposition over the whole computation process, which is difficult for large models. Instead, the exponential algorithm [111,212,213] based on the rate-type form can circumvent such problem by changing the integral into a rate-type form and only requires storing some internal variables of the retardation chains across the calculation process. Based on the Kelvin chain model, the creep compliance function can be directly used as input to fit a continuous retardation chain [209] and then the EAS evolution of any structures can be calculated by a proper boundary condition in FEM. Note that with the Kelvin chain model, the input is directly from the creep test and therefore the conversion from creep to relaxation is not needed either. Using the exponential algorithm with Kelvin chain, numerical studies have successfully predicted the EAS results of a TSTM test [29,254,255].

## 2.5 Conclusions

For many specially designed cementitious materials, like High Performance Concrete (HPC), Ultra-High-Performance Concrete (UHPC), alkali activated materials, etc., which often has a very low internal RH and dense microstructure, AD-induced EAC risk is high. To evaluate and understand the EAC risk, the AD, viscoelastic properties, and EAS are the key points. This chapter systematically reviewed relevant experimental and modelling methods and obtained the following findings:

- 1) The corrugated tube test allows to test AD since setting time and is sensitive enough to distinguish the influence of multiple factors on AD development, including the influence of temperature, cementitious materials, and various admixtures. Changing the corrugated tube size (i.e., using a larger tube) allows for AD tests of concrete. Multiple mitigation strategies of AD including the use of more inert SCMs for controlling hydration, SRA for reducing surface tension in the pores, and internal curing either by light aggregate or SAPs, were proved to be effective in many studies.
- 2) The applicability of maturity concept for prediction of AD under varying temperature history is questionable. The influence of temperature on AD is complex because temperature not only leads to change of hydration kinetics but also the internal RH, the surface tension, and the pore structure, which all significantly influences the self-desiccation process. Temperature increase

- leads to earlier onset of self-desiccation shrinkage and faster increase of EAS. However, it should also be noted that even in low-temperature, the magnitude of AD can be high, despite a later onset, and therefore the AD-induced EAC risk cannot be neglected.
- 3) The capillary pressure theory provides a good prediction of self-desiccation shrinkage. The AD is the viscoelastic response of the microstructure to the capillary pressure, induced by RH drop in the hydration process. Therefore, incorporation of creep deformation in such models is important. In addition, another part of AD, which is induced by expansive products like ettringite, is often neglected in both modelling and experimental works, and can cause overestimation of EAS.
  - 4) The viscoelastic properties, including the elastic modulus and creep, can both be tested with an in-situ hourly-repeated loading scheme. Such method leads to high-resolution measurement of the evolution of very early-age elastic modulus and creep, which are important input for EAS analysis.
  - 5) The microscale mechanical tests, including nanoindentation and microindentation tests, offered a fundamental understanding of the elastic modulus and creep, and provides input for multi-scale modelling. By either micromechanical homogenization schemes (e.g., Mori-Tanaka or Self-Consistent) or microscale FE models (e.g., Lattice fracture model), combined with a hydration model (e.g., Hymostruc or CEMHYD3D), the time-dependent evolution of elastic modulus and creep can be calculated. The viscoelastic properties are not only an important input for EAS, but also for AD at microscale, which is considered as the viscoelastic response of the microstructure to the internal capillary pressure.
  - 6) The EAS evolution is a combined result of AD and viscoelastic properties. TSTM tests can measure EAS under different temperatures and restraint degrees. Besides, the AD of a dummy specimen with a similar geometry and temperature history to a TSTM specimen, which is called the ADTM in a TSTM system, can also be tested in free condition. Thus, the TSTM system provides a unified testing scheme of AD and EAS, which helps to build up the models of EAS.
  - 7) With the experimental or modelling results of AD, elastic modulus, and creep, the EAS can be calculated by the integral of linear superposition. Conversion of creep function to relaxation function is often an important step. To run an FE analysis on EAC, the exponential algorithm based on the rate-type form is a more efficient method to avoid directly solving the integrals which requires to store huge amounts of internal variables.
  - 8) Combining the modelling schemes reviewed in this chapter, including the hydration models for volume change of hydrates,

homogenization schemes (or FE models) for upscaling of viscoelastic properties, and the capillary pressure theory for self-desiccation shrinkage, a unified model can be constructed, which enables to predict the EAS directly based on the composition of utilized mixtures.

## 2.6 Outlook

EAS is an important indicator of the EAC risk, and it is strongly dependent on the AD and viscoelastic properties. Therefore, experimental and numerical tools for EAC analysis should emphasize AD, viscoelastic properties, and EAS to obtain a comprehensive understanding of EAC issues. Based on this review, the following should be considered for further improvement in the experimental and numerical tools for EAC analysis:

- 1) TSTM tests should not only focus on the EAS and AD evolution, but also the evolution of viscoelastic properties, which are important input for EAS analysis and modelling. Rather than the strain-controlled test in the EAS measurement, an hourly-repeated loading scheme can be incorporated into the TSTM test to measure the viscoelastic properties at every hour. Thereby, the TSTM itself can be a unified testing system for the three important early-age properties/ behaviors (AD, EAS, and viscoelastic properties) relevant to EAC.
- 2) The effects of temperature on AD should be further examined. Contradictory findings have been reported in the literature regarding the influence of temperature on AD. The complexity of this issue is that temperature not only influences the hydration kinetics, but also expansive hydration products like ettringite that leads to autogenous swelling and RH, porosity, and surface tension that significantly influences the self-desiccation process.
- 3) The efficiency of TSTM tests should be improved. To obtain the AD, EAS, and viscoelastic properties, at least two TSTM tests should be conducted for each mixture. Moreover, considering the scatter in measurements of early-age AD and EAS, several repeated tests may also be needed for each mixture. Due to the complexity of the TSTM system, the cost of such a test is high and therefore more efficient testing methods should be developed to obtain more testing data in a broad range of mixture parameters.
- 4) The modelling schemes of EAS should be further examined and developed. The lack of data for early-age viscoelastic properties is one of the main challenges in validating such models. Although a solid theoretical basis is present, a systematic validation of these modelling schemes for predicting EAS is still missing. Therefore, a thorough investigation based on comprehensive and reliable

input of viscoelastic properties is needed to validate or improve the applicability of EAS models.

- 5) Efficient and reliable data-driven models should be developed for analyzing the EAC risks. Due to the complexity of EAC issues, a unified model in this field requires to couple multiple physical and chemical mechanisms, including (but not limited to) hydration reaction, heat transfer, and viscoelastic mechanical response. The computational cost of solving such a complex multi-field model is high. Building a surrogate model by data-driven approaches to replace the complex multi-field model can promote the computational efficiency.



# 3. EARLY-AGE STRESS EVOLUTION INDUCED BY AUTOGENOUS DEFORMATION IN HIGH-VOLUME GGBFS CONCRETE

*Autogenous deformation and the stress evolution in restrained high-volume ground granulated blast furnace slag (GGBFS) concrete is investigated in this chapter. The Temperature Stress Testing Machine (TSTM) and Autogenous Deformation Testing Machine (ADTM) were used to study the macro-scale autogenous deformation and stress evolution of high-volume GGBFS concrete with w/b ratios of 0.35, 0.42, and 0.50. The early-age cracking (EAC) risk (quantified by the stress to strength ratio) and stress relaxation were analyzed extensively based on ADTM and TSTM results. Furthermore, Environmental Scanning Electron Microscopy (ESEM), X-Ray Diffraction (XRD), and Mercury Intrusion Porosimetry (MIP) were used to explain the micro-scale origin of the autogenous deformation of high-volume GGBFS concrete. It was found that the ettringite formation in the first two days results in autogenous expansion, which can delay the appearance of tensile stress. The magnitude of autogenous expansion depends on the ettringite content and pore size. The w/b ratio of 0.42 showed optimal performance because it resulted in the highest amount of ettringite and, consequently, the highest autogenous expansion. In comparison, significant autogenous shrinkage after the expansion peak is present in GGBFS concrete with the w/b ratio of 0.35, which therefore results in a high early-age cracking risk.*

*Parts of this chapter have been published in Liang, M., Chang, Z., Zhang, Y., Cheng, H., He, S., Schlangen, E., & Šavija, B. (2023). Autogenous deformation induced- stress evolution in high-volume GGBFS concrete: Macro-scale behavior and micro-scale origin. Construction and Building Materials, 370, 130663.*

### 3.1 Introduction

Ground granulated blast furnace slag (GGBFS) is a promising alternative cementitious material to replace ordinary Portland cement (OPC), which not only reduces carbon dioxide emissions but also improves workability [256] and shows comparable or even higher compressive strength [257], flexural strength [258] and elastic modulus [259] at later ages. Although GGBFS can reduce the early-age cracking (EAC) risk induced by thermal deformation by decreasing the hydration heat release [260–262], the active pozzolanic reaction of GGBFS leads to continuous pore refinement and a decrease of internal relevant humidity, which enhances the self-desiccation effects and therefore results in increased autogenous deformation (AD) [46,108,263]. As restrained AD often leads to cracks in concrete structures [225], the EAC risk in high-volume GGBFS should be prevented.

Many studies investigated the EAC risk of GGBFS-blended concrete, using a temperature stress testing machine (TSTM) [61,229,242,245,264] or a ring test [230]. Contradictory findings regarding the influence of GGBFS on the EAC risk were reported. This is understandable considering the difference in testing details, including the thermal boundaries, material differences, etc. For example, in non-isothermal conditions, the addition of GGBFS certainly decreases the EAC risk since thermal shrinkage is highly reduced. Such declaration is mostly tenable in massive concrete structures where thermal shrinkage dominates. However, for medium- or thin-concrete structures, autogenous shrinkage, which is inevitable and can induce stress continuously, is more important for EAC. Despite the disagreement, there is an agreement that GGBFS increases autogenous shrinkage, which indicates potentially higher EAC risk [10,46,58,62,91,108,263].

Published studies on EAC risks of GGBFS concrete mostly focused on a low replacement ratio of OPC (0~50%). In addition, an ideal isothermal condition at constant temperature was often unreachable, making it difficult to decouple the autogenous and thermal deformation. Meanwhile, the EAC analysis of high-volume GGBFS concrete with different water-binder ratios is scarce. In view of these limitations, TSTM tests are conducted to understand the autogenous shrinkage and early-age stress (EAS) evolution of high-volume GGBFS concrete with a 70% replacement rate of OPC and w/b ratio ranging from 0.35 to 0.5. An OPC concrete mix is tested as a reference. A thorough analysis of the coupling influence of autogenous shrinkage, elastic modulus, and stress relaxation on EAS evolution was conducted. MIP, XRD, and ESEM tests were performed to

provide an in-depth understanding of the AD of high-volume GGBFS concrete with different w/c ratios.

## 3.2 Experimental methods

### 3.2.1 Materials

Three GGBFS mixes, with CEM III/B 42.5 as the cementitious material, with the w/b ratios of 0.35, 0.42, and 0.50 were studied. Furthermore, a reference mix using CEM I 42.5 as the cementitious material and a w/b ratio of 0.42 was also tested. Both CEM III/B and CEM I was supplied by the ENCI, Netherlands. The detailed mixture proportions are given in [Table 3-1](#). The mix labels indicate the difference in cementitious materials and w/b ratio. For example, "C3-50" stands for the mix using CEM III/B with a w/b ratio of 0.50. The chemical compositions of utilized CEM III/B 42.5 and CEM I 42.5 are given in the [Table 3-2](#). Superplasticizer (SP) MasterGlenium 51 with a water-reducing rate of 35% was used for mixes with w/b = 0.42 and 0.35. The compressive strength of each mix was tested on three cubic samples with a side length of 150mm at ages 1, 3, 7, 14, and 28 days. The evolution of compressive strengths was measured and reported in [Figure 3-1](#).

**Table 3-1 Concrete mixes used in TSTM tests (kg/m<sup>3</sup>)**

Sample	Cement type	Cement	w/b	Sand (0-4 mm)	Gravel (4-16 mm)	SP	Slump (mm)	Setting time (hour)
C3-50	CEM III/B	320	0.50	811.8	1032	0	90	8
C3-42	CEM III/B	320	0.42	811.8	1032	0.48	60	7.8
C3-35	CEM III/B	320	0.35	811.8	1032	1.90	40	7.5
C1-42	CEM I	320	0.42	811.8	1032	0.48	50	7.4

**Table 3-2 Oxide composition of utilized cementitious materials (wt.%)**

Composition	CEM III/B	CEM I
CaO	47.11	64.00
SiO <sub>2</sub>	29.11	20.00
Al <sub>2</sub> O <sub>3</sub>	10.02	5.00
MgO	5.89	-
SO <sub>3</sub>	2.82	2.93
Fe <sub>2</sub> O <sub>3</sub>	1.19	3.00
Na <sub>2</sub> O	0.28	0.58

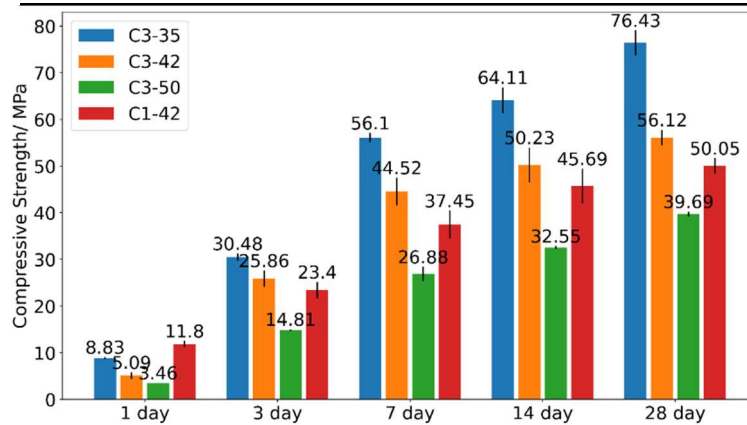


**Figure 3-1 Compressive strength measurements (The bar is the average value and the line indicates the standard deviation obtained from three cubic specimens).**

### 3.2.2 ADTM and TSTM

The Autogenous Deformation Testing Machine (ADTM) and Temperature Stress Testing Machine (TSTM) have been developed to test the AD and the stress it induces[235]. Herein, the ADTM and TSTM tests were conducted by following the workflow in [Figure 3-2](#). Two wooden molds with low heat conductivity were used for casting of prism and dog-bone specimens, which were then sealed and tested under free and restrained conditions, respectively. Isothermal conditions were ensured by circulating temperature-regulated water around the concrete specimens in wooden molds.

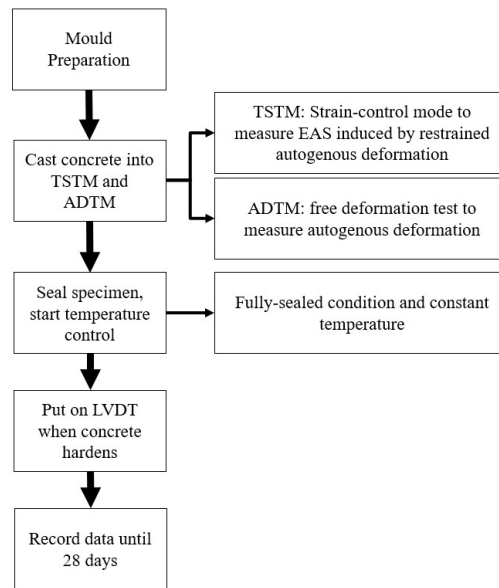


**Figure 3-2 ADTM and TSTM testing procedure**

The ADTM is used for testing the AD of concrete (Figure 3-3). Wooden plates with low thermal conductivity were assembled to form a mold for casting prismatic samples with the size  $1000 \times 150 \times 100 \text{ mm}^3$ . By wrapping the sample with plastic film, moisture exchange with the environment was prevented to exclude the effects of drying shrinkage. To exclude the influence of temperature, temperature-regulated water was circulated in the surrounding wooden mold through the embedded water channel (Figure 3-3 (c)). A steel plate was applied on the inner surface of the wooden mold to enable fast heat conduction (Figure 3-3 (d)). Three thermo-couples were embedded in the sample to monitor the temperature development, as shown by the red dots in Figure 3-3 (a). A feedback loop between the measurement of the middle thermo-couple and an externally-connected cryostat was used to regulate the water temperature and maintain the temperature of the sample at 20 degrees. Four Linear Variable Differential Transformers (LVDTs) were configured at two sides of the sample and the average of the deformation at the two sides was taken as the measurement of autogenous shrinkage. The LVDTs on the same side were connected with a quartz bar, which has a low coefficient of thermal expansion so that any potential deformation of mounting base due to heat change cannot influence the deformation measurement of the specimen. With the measures above, the influence of thermal and drying deformation can be excluded, and the AD can be measured.

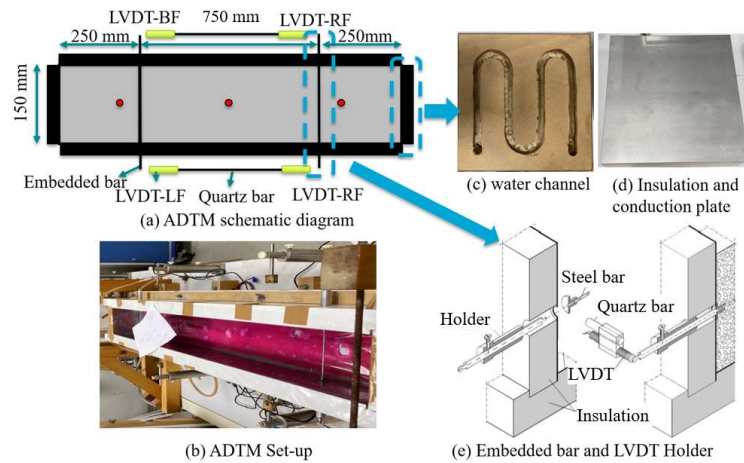


**Figure 3-3 Autogenous Deformation Testing Machine (ADTM)**

The TSTM (Figure 3-4) is used to restrain AD and measure stress development. In the TSTM, the principles of the mold assembly, water circulation, and LVDT configurations are the same as in the ADTM introduced above. The load applied by the actuator was continuously adjusted to keep the deformation of the specimens measured by four LVDTs at 0, based on a Proportion Integration Differentiation (PID) control algorithm. To ensure that all AD-induced stress is accounted for, the TSTM test has to be started before the concrete hardens [265]. Herein, the TSTM tests were started 7.0 hours after casting, which is earlier than the final setting time of the cement paste of all studied mixes. Before the LVDTs could be set up, the load was controlled by the displacement of the clamping head measured by 2 LVDTs. Afterwards, the 4 LVDTs at the two sides of TSTM were set up and used to control the load. During the first stage, when the concrete was not hardened (within the first 7 hours after casting), the stress measured was less than 0.01 MPa, and therefore only the stress after 7 hours was accounted for in the experimental results of this chapters. Due to unforeseen factors such as power-off, the testing duration for each test differs somewhat, ranging from 647 hours to 804 hours.

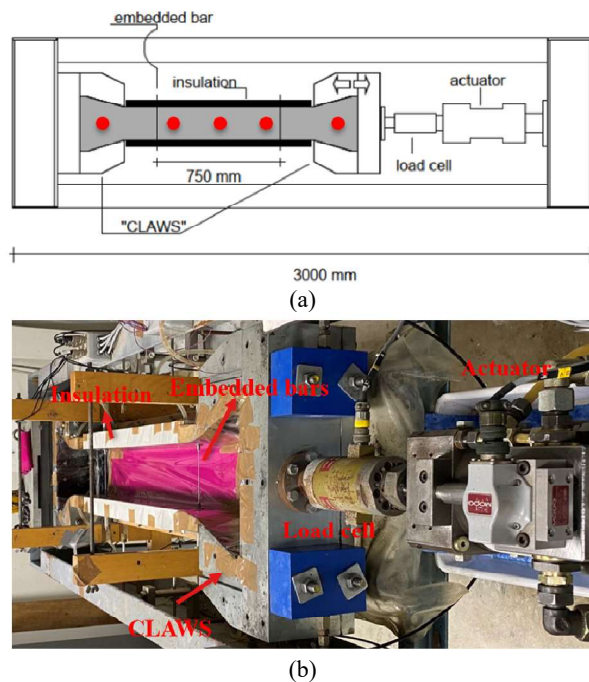


Figure 3-4 Temperature Stress Testing Machine (TSTM): (a) TSTM schematic diagram; (b) TSTM setup.

### 3.2.3 Corrugated tube test

In the process of AD, the aggregate mainly plays the role of restraint [68], while the AD mainly originates from the cement paste. Therefore, it is also important to measure the AD of cement paste. Considering that this chapter is mainly about the influence of GGBFS, only the 3 relevant mixes were incorporated into this test. Hence, the corrugated tube tests [45] were conducted to measure the autogenous shrinkage of cement paste of C3-35, C3-42, and C3-50, and the measurements were initiated immediately after casting.

### 3.2.4 Material characterization

Material characterization tests were performed to reveal microscale origins that explain the corresponding macroscale behavior (i.e., AD and EAS) of high-volume GGBFS concrete. By analyzing the consumption of  $C_3A$  and  $C_4AF$ , Darquennes et al. [242] inferred that the autogenous expansion in GGBFS concrete is a result of ettringite formation. Indeed, as the most active phase of clinker, the  $C_3A$  begins immediately to react with gypsum and forms ettringite once it dissolves in water. According to [266], the additional sulfur and alumina in GGBFS can highly promote ettringite

formation. Afterwards, ettringite tends to grow in the pores and expand, applying crystalline pressure on the pore walls, thereby inducing autogenous expansion. Hence, the magnitude of autogenous expansion depends on the volume/ amount of ettringite and the pore size distribution [267]. In other words, autogenous expansion can happen only when the volume of ettringite is sufficient to fill the pores. To investigate the effects of ettringite formation on AD, we employed ESEM to qualitatively study the distribution of ettringite and QXRD/ MIP to quantitatively analyze the change of ettringite amount and pore structure. In this section, the cement pastes of the three mixes containing GGBFS C3-35, C3-42, and C3-50 were tested. Each sample was cast and cured at a room temperature of 20 degrees and the hydration was stopped at the desired ages using the solvent exchange with isopropanol.

Since autogenous shrinkage is driven by capillary tension induced by self-desiccation and can be well explained by Kelvin's Law [31,32,268], the pore structure evolution is important for the analysis of the autogenous shrinkage process. Therefore, the mercury intrusion porosimetry (MIP) test was conducted. Paste specimens were crushed into small pieces and stored in the vacuum container to remove isopropanol after hydration was stopped. Note that, in the MIP test, it is necessary to use small pieces of specimens (with a size typically smaller than 4 mm) to avoid the influence of ink-bottle pores [269]. According to [269], it is optimal to prepare the sample with a slow cutting process. However, specimens younger than 3 days were too soft to bear the clamping force applied by the cutting machine, as well as the cutting force. Instead, the specimens were soft enough to be easily crushed into small pieces with a gentle force by a steel block. Note that, due to the damage induced in the sample preparation process and the assumption and limitations of the MIP test itself [270,271], the results herein do not necessarily represent the absolute value of the true pore size distribution. However, considering that all specimens undergo the same process, qualitative results regarding the pore structures will still be comparable, allowing for further analysis of the influence of pore structures on AD. The intrusion process of the mercury was as follows: 1) a low-pressure state from 0 to 0.170 MPa; 2) a high-pressure state from 0.170 to 210 MPa; 3) an unpressurized state from 210 MPa to 0.170 MPa. The pore radius was calculated based on the Washburn equation, with the surface tension of mercury being 0.485 N/m and the contact angle between mercury and sample being 140° [272].

As the hydration products also directly influence the AD process, ESEM and XRD were used to analyze the evolution of microstructure and chemical

compositions. For ESEM, 2mm-thick samples were ground using 4000 grit abrasive paper for 5 minutes and polished using synthetic silk polishing cloth (MD-Dac from Struers) charged with 3  $\mu\text{m}$  and 1  $\mu\text{m}$  diamond pastes for 2 consecutive 30-minute sessions. During grinding and polishing, an oil-based lubricant (DP-Lubricant Brown from Struers) was used as a cooling fluid. Between each grinding and polishing interval, the sample was immersed in an ultrasonic bath filled with pure ethanol for 30 seconds to remove debris. Afterwards, samples were carbon coated and moved into an FEI QUANTA FEG 650 ESEM. An accelerating voltage of 10 kV and a working distance of 10 mm were used throughout the research. The XRD test was carried out on a Philips PW 1830/40 powder diffractometer using the Cu K-alpha radiation. The adopted acceleration voltage was 40 kV and the X-ray beam current was 40 mA. The XRD data were collected with a step size of  $0.03^\circ$  for a  $2\theta$  range from  $5^\circ$  to  $60^\circ$ .

### 3.3 Results

#### 3.3.1 AD

The AD as measured by the ADTM are shown in

**Figure 3-5.** The results show that the AD of all 4 mixes is characterized by an autogenous expansion phase in the first 1~3 days, followed by autogenous shrinkage. For the mix C3-50, a second expansion peak can be observed, which resembles the second peak of the heat release rate of GGBFS concrete [273,274] and may therefore be attributed to the continuous hydration of slag after the first day. For the mixes C3-35, C3-42, C3-50, and C1-42, the expansion peak of 52.4, 84.8, 55.3, and 28.9  $\mu\text{-strain}$  are reached at 40, 38, 27, and 33 hours, respectively. Comparing the expansion phase of the 4 mixes, the following patterns can be observed:

- 1) Significant autogenous expansion in the first two days characterized the AD process. The magnitudes of early autogenous expansion for C1-42, C3-42, and C3-50 are higher than the subsequent autogenous shrinkage. For C3-35, the autogenous expansion is compensated by a fast shrinkage process at a later age (around 600 hours).
- 2) The high-volume GGBFS mixes show much higher expansion than the OPC mix.
- 3) From the GGBFS mixes, C3-42 shows higher expansion than the others. C3-50 and C3-35 have a similar expansion magnitude, but C3-50 shows a longer expansion phase.

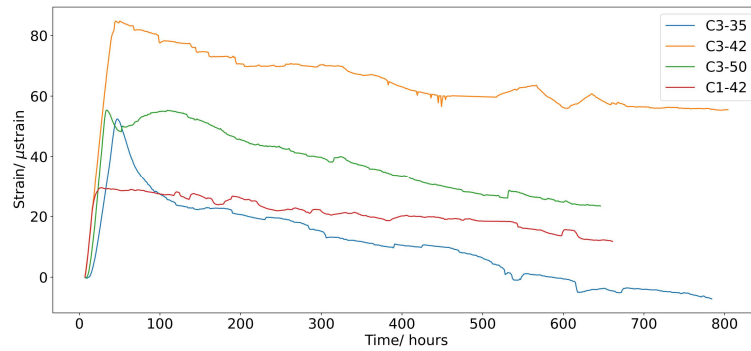


**Figure 3-5 AD measured by ADTM**

Taking the first expansion peak as time-zero, the shrinkage process of the 4 mixes is shown in **Figure 3-6**. The results show that, after the expansion peak, all high-volume GGBFS mixes show higher autogenous shrinkage than the OPC mix, which is in accordance with published literature [51,57]. Within the first 100 hours, the high-volume GGBFS concrete with a low w/b ratio (C3-35) shows drastic autogenous shrinkage, and afterwards, a similar shrinking rate can be observed for the three GGBFS concretes. With a higher w/b ratio, C3-50 shows a second expansion peak, which seems to be favorable for avoiding EAC. A slightly faster shrinking rate is also observed for C3-50 compared with the mix of a lower w/b ratio C3-42. This contradicts existing studies [38,55] which concluded that a lower w/b ratio corresponds to lower porosity and smaller pore size, and should have higher autogenous shrinkage. However, due to the limitations (e.g., temperature instability and friction) of the ADTM, the AD curve is not smooth, and considering the measurement error that may be involved, the slight difference between the shrinking phase of C3-42 and C3-50 should not be seen as significant.

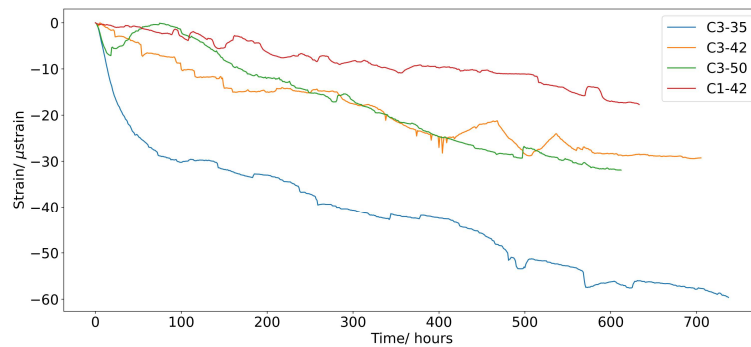


**Figure 3-6 Autogenous shrinkage zeroed at the expansion peak**

The ADs of cement pastes of C3-35, C3-42, and C3-50, measured by the corrugated tube test [45], are shown in Figure 3-7. Note that, due to the incorporation of the aggregate and much smaller sectional size of specimens used in the corrugated tube test, the absolute values of the AD measured by ADTM are significantly lower than those measured by corrugate tube tests. Figure 3-7 (a) shows the AD curve by setting the time-zero the same as the ADTM, and Figure 3-7 (b) shows the AD after the expansion peak. The results of all 3 GGBFS cement pastes resemble the behavior of their concrete counterparts: first, an expansion phase that lasts around 30 hours, followed by the shrinkage phase. Similar to the results of concrete, the C3-42 shows the highest expansion peak and the C3-50 shows a lower shrinking rate after the first expansion peak. However, due to the effects of dilution and restraint incorporated by aggregate and the interfacial transition zone, the results of paste still preserve obvious differences with concrete: 1) the expansion peak of C3-50 is notably higher than that of C3-35, and the second expansion peak seems to be less obvious; 2) the shrinking rate of C3-42 is higher than C3-50.

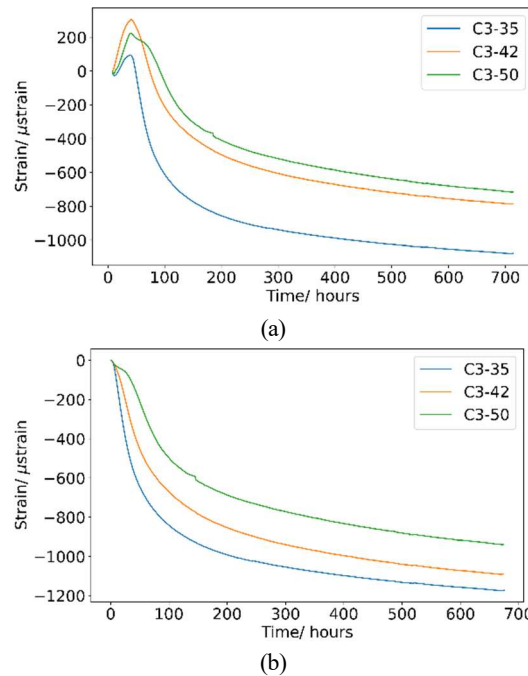


**Figure 3-7 AD measured by the corrugated tube test: (a) After the same time-zero as ADTM results; (b) After the expansion peak.**

Overall, the results show that AD of high-volume GGBFS mix is characterized by a high expansion peak, which can delay the appearance of

tensile stress at an early age and therefore reduce the EAC risk. After the expansion peak, the GGBFS mixes undergo a faster autogenous shrinkage than the OPC mix. Especially for concrete with a low w/b ratio at 50~150 hours, the drastic autogenous shrinkage indicates a high EAC risk. Comparing all the GGBFS mixes, both paste and concrete results indicate that the mix with a medium w/b ratio (i.e., 0.42) shows the highest expansion that can reduce the EAC risk.

### 3.3.2 Stress Evolution

#### 3.3.2.1 Stress results

Under isothermal conditions ensured by water circulation, wood mold insulation, and constant room temperature, the AD is restrained by the TSTM, resulting in stress development as shown in **Figure 3-8**. The stress evolution resembles the pattern observed in AD results: all mixes display an initial compression phase and then go to tension phase. The expanding and shrinking process observed in the ADTM corresponds well with the stress decrease (i.e., compression) and increase (i.e., tension) observed in the TSTM. The initial compression phase has a similar duration as the autogenous expansion measured by the ADTM, which proves the validity of combined ADTM and TSTM testing. The following can be observed from the TSTM results:

- 1) The GGBFS mix with a low w/b ratio (C3-35) shows a fast increase of stress between 50-150 hours, which indicates a high risk of EAC.
- 2) The OPC mix (C1-42) shows the shortest expansion phase and the slowest stress evolution rate, which is even slower than the GGBFS mix with a higher w/b ratio (C3-50).
- 3) The GGBFS mix with medium w/b ratio (C3-42) undergoes a compressive stress similar to C3-35. Note that, although C3-42 has much higher expansion as measured in the ADTM, the lower elastic modulus and higher relaxation (see later in section 3.2.3) limits the compressive stress level that can be induced by the restrained expansion. However, compared to C3-50, the compressive stress in C3-42 is noticeably higher, which compensates for more shrinkage-induced tensile stress after the expansion peak and finally leads to a similar tensile stress level.

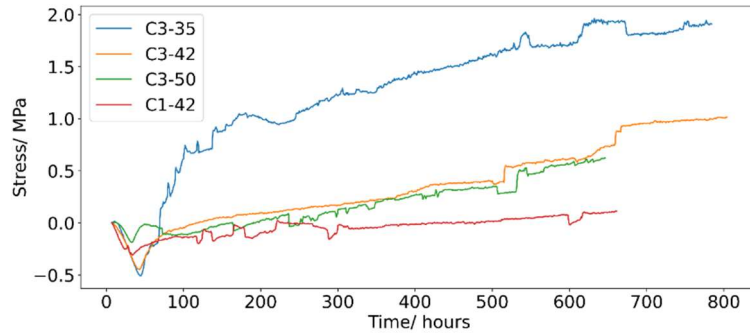


Figure 3-8 Stress evolution in restrained concrete measured by TSTM

### 3.3.2.2 Stress-strength ratio

The stress-strength ratio is a straightforward index to assess the EAC risk at different ages. The tensile strength of concrete is closely correlated with the compressive strength and can be predicted accurately by a closed-form formula [118,275,276]. To quantitatively evaluate the EAC risk, the formula proposed by the Model Code 2010 [113] is used herein to estimate the development of splitting tensile strength as follows:

$$f_{ct}(t) = \begin{cases} 0.3 \times f_c^{\frac{2}{3}}, & f_c < 50 \text{ MPa} \\ 2.12 \times \ln(1 + 0.1 \times f_c) & f_c \geq 50 \text{ MPa} \end{cases} \quad (3-1)$$

where  $f_{ct}(t)$  is the estimated tensile strength at the age of  $t$  hours;  $f_c$  is the compressive strength measured at  $t$  hours, as shown in section 3.2.1. In this chapter, the compressive strength tested at 1, 3, 7, 14, and 28 days is used to estimate the tensile strength at corresponding ages, and then a quadratic spline [277] is used to interpolate the estimated tensile strength in a continuous time range. By dividing the stress results of Figure 3-8 with the estimated tensile strength, the stress-strength ratio of the 4 mixes is obtained (Figure 3-9). Note that the negative values in Figure 3-9 mean that the specimen is in a compressive phase and therefore shows no EAC risk. The stress-strength ratio of mixes C3-35, C3-42, C3-50, and C1-42 exceeds 0 at 70, 127, 200, and 412 hours, respectively; at this point, the tensile stress starts to develop. The stress-strength ratio results show a similar but more straightforward and clearer pattern than the stress results, allowing for the following observations:

- 1) The stress-strength ratio of the mix C3-35 shows a rapidly increasing rate before 150 hours and a steady increasing stage afterward. A value of 0.417 is reached at 785 hours. It should be noted that the limit state value of the tensile stress-strength ratio commonly used in engineering design practice

is 0.5 [278]. Furthermore, the ratio of 0.417 is a result of autogenous shrinkage-induced stress under a (favorable) curing temperature of 20 degrees, while the stresses due to thermal and drying shrinkage are not considered. Therefore, the stress-strength ratio of the mix C3-35 indicates a high EAC risk.

- 2) The OPC mix develops tensile stresses at the latest age and reaches a stress-strength ratio of (only) 0.018 at 691 hours, which proves that autogenous shrinkage-induced stress has negligible influence on the EAC of OPC concrete with a medium w/b ratio (0.42).
- 3) Although the tensile stress in C3-42 develops earlier than in C3-50, their stress-strength ratio maintains at a level lower than 0.2 at the first 672 hours and shows a similar increasing rate.

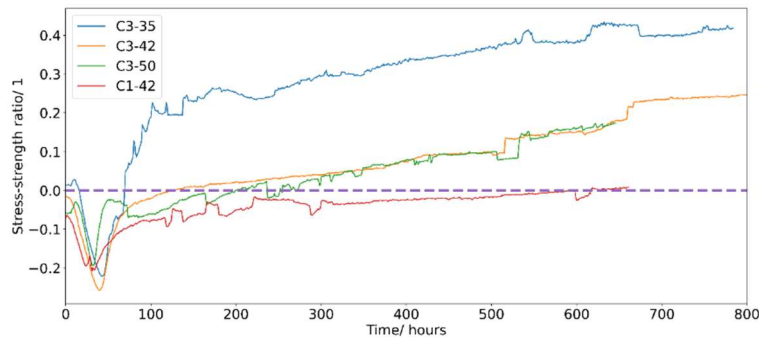


Figure 3-9 Stress-strength ratio

### 3.3.2.3 Stress relaxation

Stress relaxation is a significant factor that must be considered in the quantification of early-age stress evolution in restrained concrete since the creep/ relaxation of early-age concrete is very high [174,201,238]. This chapter aims to provide a qualitative understanding of how relaxation influences stress accumulation. Because the stress level is below 50% of tensile strength, it is reasonable to assume an ideal viscoelastic constitutive model of concrete. Thereby, the stress is formed by the elastic part  $\sigma_{el}$  and relaxed part  $\sigma_{re}$ , expressed as [253]:

$$\sigma(t) = \sigma_{el}(t) - \sigma_{re}(t) \quad (3-2)$$

where  $\sigma(t)$  is the overall stress measured by the TSTM tests. If the aging relaxation modulus or the aging creep compliance is known, following the Boltzmann superposition principle, the total stress can be expressed as the following convolution:

$$\sigma(t) = \int_0^t R(t_0, t) \dot{\varepsilon}(t_0) dt_0 \quad (3-3)$$

where  $R(t_0, t)$  represents the aging relaxation modulus at time  $t$  when the load is applied at  $t_0$ ;  $\varepsilon$  represents the enforced strain. To account for the influence of relaxed stress on the overall stress evolution, the relaxed stress is directly calculated by subtracting the elastic stress from the overall stress measured by the TSTM. The elastic stress can be calculated as:

$$\sigma_{el}(t) = \int_0^t E(t) \dot{\varepsilon}(t) dt \quad (3-4)$$

where  $E$  is the elastic modulus. Applying the mid-point rule and assuming the time step  $\Delta t$  as 1 hour, the calculation of Eq(3-4) can be expressed as:

$$\sigma_{el}(t) = \sum_0^t E(t + \frac{1}{2} \Delta t) \times \Delta \varepsilon(t) \times \Delta t \quad (3-5)$$

Substituting Eq(3-5) in Eq(2-1), the stress can be expressed as:

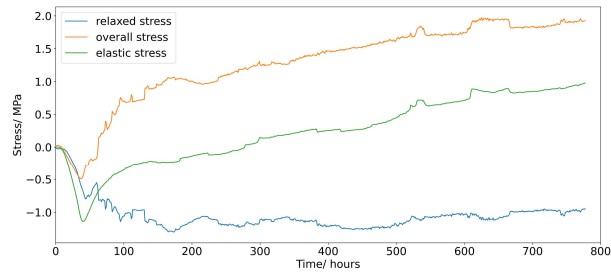
$$\sigma_{re}(t) = \sum_0^t E(t + \frac{1}{2} \Delta t) \times \Delta \varepsilon(t) \times \Delta t - \sigma(t) \quad (3-6)$$

Due to the close correlation with compressive strength [119,123,279], the elastic modulus  $E(t)$  is estimated herein by applying the formula recommended by the Model Code 2010 [113]. Note that the validity of this estimation was confirmed by comparing the influence of various formulas and the estimated results of the C3-50 with the elastic modulus tests, which will be shown in the Chapter 4. The formula used for estimating the elastic modulus is as follows:

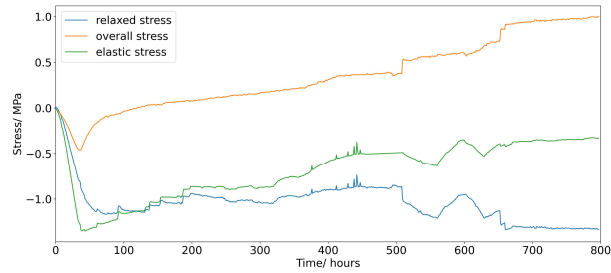
$$E(t) = E_{c0} \alpha_E \left( \frac{f_c(t)}{10} \right)^{\frac{1}{3}} \quad (3-7)$$

where  $E_{c0}$  is a coefficient and equals 21500 MPa;  $\alpha_E$  is the coefficient for different aggregates ranging from 0.7 to 1.2. Considering the aggregates used in the tests are mainly quartzite gravel,  $\alpha_E$  is taken as 1.0 in this study. Following Eq ((3-5)~(3-7)), the elastic and relaxed stress can be calculated, as shown in **Figure 3-10**. A significant influence of relaxation on stress accumulation before the expansion peak is observed, which directly results in the decrease of compressive stress and accelerates the occurrence of tensile stress. Afterwards, the relaxed stress steadily decreases and most elastic stress is preserved as the total stress. This can also be seen from the similar increase rate of the overall stress and elastic stress. The results here show that the influence of creep/ relaxation on the EAC risk of GGBFS

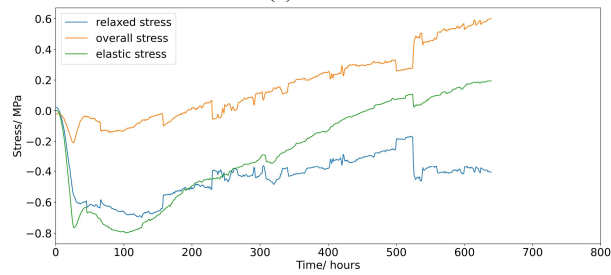
concrete is negative during the autogenous expansion. The high creep/relaxation at an early-age compromises the effect of early-age autogenous expansion and reduces the compressive stress in the first 1~3 days and exposes the restrained concrete to tensile stress earlier.



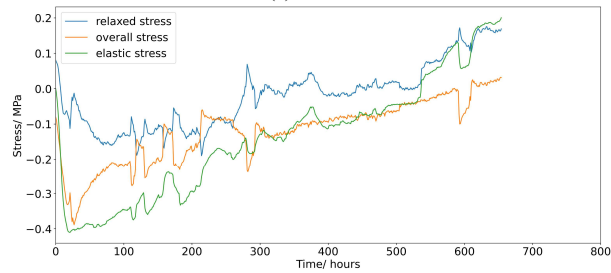
(a) C3-35



(b) C3-42



(c) C3-50



(d) C1-42

**Figure 3-10 Relaxed stress: (a) C3-35; (b) C3-42; (c) C3-50; (d) C1-42.**

### 3.3.3 AD due to ettringite formation

#### 3.3.3.1 ESEM results

Representative ESEM images of the 3 GGBFS mixes C3-35, C3-42, and C3-50 at 1 day are shown in **Figure 3-11**. The 5000x images were taken at porous areas of the samples and the 20000x images were the zoomed-in view of one of the large pores. The 5000x ESEM images show that ettringite mostly appears in porous regions where continuous hydration happens and fibrous CSH grows. The 20000x SEM images show the existence of rod-like ettringite in all mixes. The GGBFS mixes with higher w/b ratios (i.e., 0.42 and 0.50) have more porous areas and tend to obtain more ettringite with larger rod sizes. In the C3-50 mix, scattered ettringite grows in large pores, which indicates limited crystalline pressure and therefore lower autogenous expansion. On the other hand, in the mix C3-42, dense clusters of ettringite with large rod sizes fill in relatively smaller pores, which indicates considerable crystalline pressure resulting in higher autogenous expansion. These observations are consistent with the aforementioned ADTM and TSTM tests of all 4 mixes.

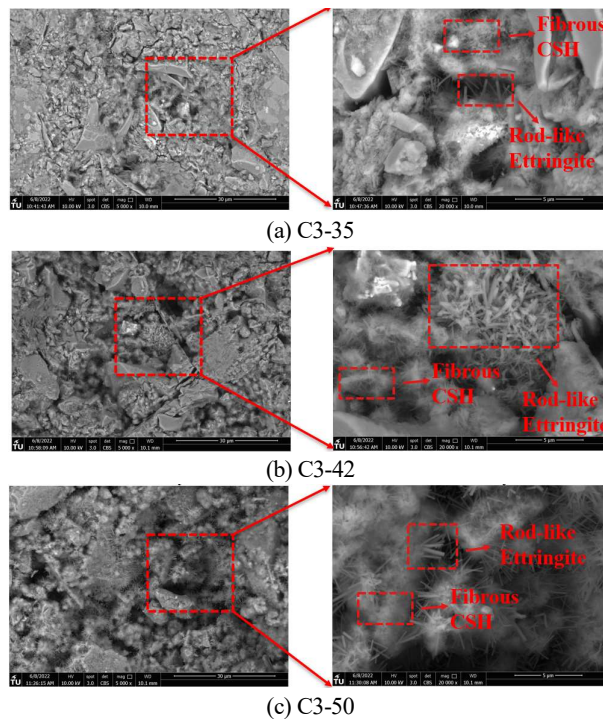


**Figure 3-11** SEM images of ettringite formation: (a) C3-35; (b) C3-42; (c) C3-50. (left: porous area; right: zoomed-in view of large pores)

### 3.3.3.2 XRD and Rietveld Refinement

The ADTM/ TSTM tests show high autogenous expansion in high-volume GGBFS concrete, indicating a high amount of ettringite. Therefore, the GGBFS mixes C3-35, C3-42 and C3-50 were selected to conduct XRD analysis at the age of 2 days, which is the approximate timing of autogenous expansion peaks observed in ADTM/ TSTM tests. Meanwhile, to distinguish the pattern of how ettringite content evolves with time, the ettringite content of the mix C3-42 at 1, 2, and 3 days were also tested. Before the XRD test, 10% silicon was added to the sample powder as an internal standard, and then Rietveld refinement [280] was conducted to decompose the raw XRD curve. By predefining the mineral types of different hydration products and clinkers that exist in early-age GGBFS paste, the decomposition is conducted based on the program BGMN [281] and the ICDD database. As shown in **Figure 3-12**, considerably good fitting performance was obtained for all XRD patterns of all samples, whose weighted profile R-factors ( $R_{wp}$ ) were all lower than 2.0%.

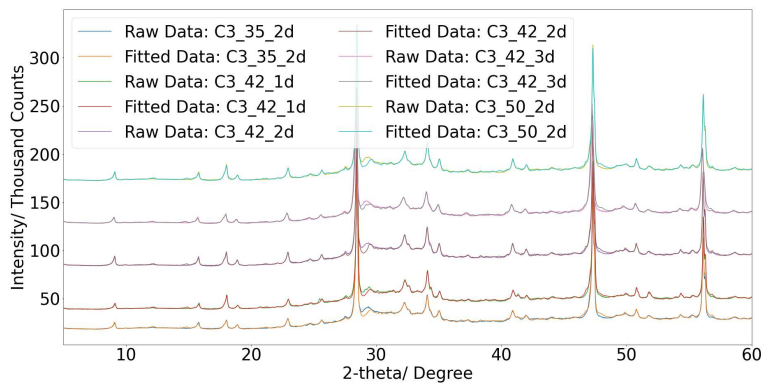


**Figure 3-12** XRD pattern and Rietveld refinement

The intensity of ettringite at around 9 degrees measured by the QXRD and the mass fraction of ettringite calculated by Rietveld refinement are shown in **Figure 3-13**. Note that the generation of calcium hydroxide (CH) can also be a reason for such autogenous expansion [282]. However, in the high-volume slag system the CH is mostly consumed by the pozzolanic reaction of slag and therefore its content is low. In the QXRD results, the CH contents of all samples are below 1% and therefore they are ruled out as the reason inducing the expansion and will not be shown and discussed here. The results are consistent with the ADTM/ TSTM results in the following 2 aspects:

- i. Comparing the GGBFS samples with different w/b ratios at 2 days

(i.e., C3-35-2d, C3-42-2d, and C3-50-2d), the sample C3-42-2d contains the highest amount of ettringite. The ADTM/ TSTM tests exhibited the consistent pattern that the C3-42 sample obtained the highest expansion peak and high compressive stress.

- ii. Comparing the GGBFS samples with the same w/b ratio at 1, 2, and 3 days (i.e., C3-42-1d, C3-42-2d, and C3-42-3d), it is found that a considerable amount of ettringite is produced in the first day, and then keep increasing until the second day. Afterward, the amount of ettringite starts to decrease and transform into calcium monosulfoaluminate. This is also consistent with the ADTM/ TSTM finding that the expansion peaks of GGBFS mixes all occur during the second day.

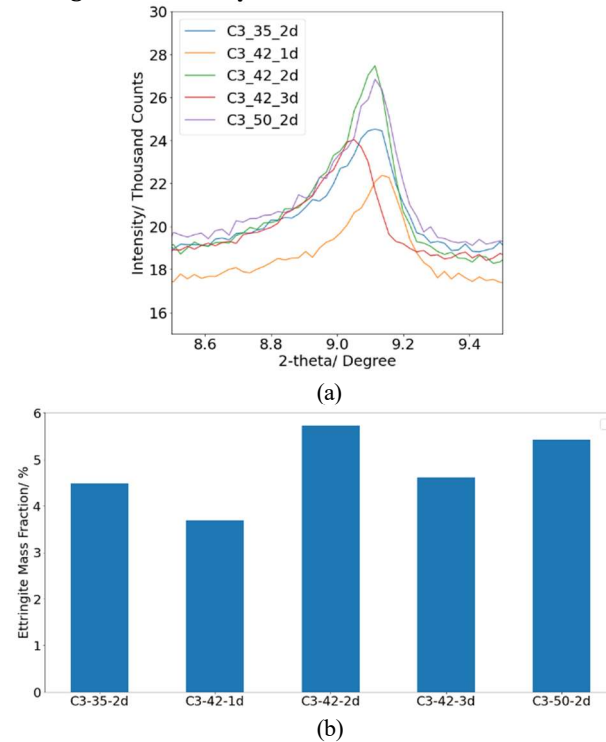


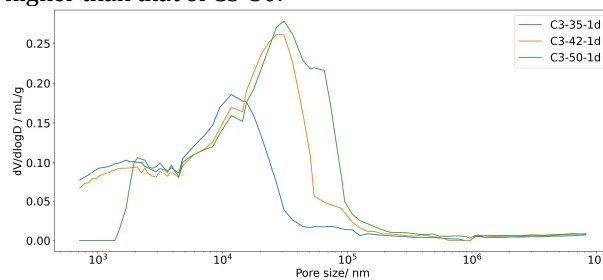
**Figure 3-13 Ettringite content measured by XRD: (a) Intensity; (b) Mass fraction calculated by Rietveld refinement**

### 3.3.3.3 MIP results

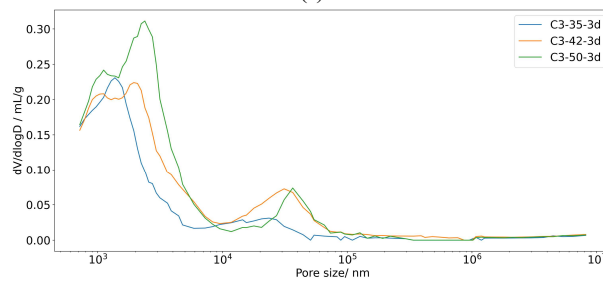
The pore structure not only influences the capillary tension that can be induced by self-desiccation, but also determines the crystalline pressure that can be generated by the ettringite formation. Given this, the MIP tests are conducted on the 3 high-volume GGBFS cement pastes at 1 and 3 days.

The results are shown in **Figure 3-14** and **Figure 3-15**. The following can be inferred from the MIP results:

- 1) The rank of the critical pore entry radius (CPER) (i.e., the point where the steepest slope of the  $dV/d\log D$  curve is observed in **Figure 3-14**) is  $C3-35 \ll C3-42 \leq C3-50$ . The “ $\ll$ ” means that the CPER of the C3-35 is much smaller than others. The “ $\leq$ ” means that the CPER of the C3-42 is lower than C3-50 after 1 day, but similar after 3 days. According to Kelvin’s equation, the capillary tension that can be induced by self-desiccation is also dependent on the pore size: smaller pores correspond to higher capillary tension and, therefore, cause higher autogenous shrinkage. In the ADTM/TSTS tests, the C3-35 showed the fastest autogenous shrinkage and therefore generated more tensile stress. Overall, based on Kelvin’s Equation, the ADTM/TSTM results of all the GGBFS mixes can be explained by the rank of CPER.
- 2) After 1 day, the CPER of the mix C3-42 is lower than that of C3-50, which means that the pore size of C3-42 is generally much smaller than C3-50. Therefore, even though with similar ettringite amounts and overall porosity, the pores of C3-42 are easier to fill, and more crystalline pressure can be applied to the pore walls. This explains why the expansion peak of the C3-42 is significantly higher than that of C3-50.



(a)



(b)

**Figure 3-14** Pore size distribution at ages of: (a) 1 day; (b) 3day

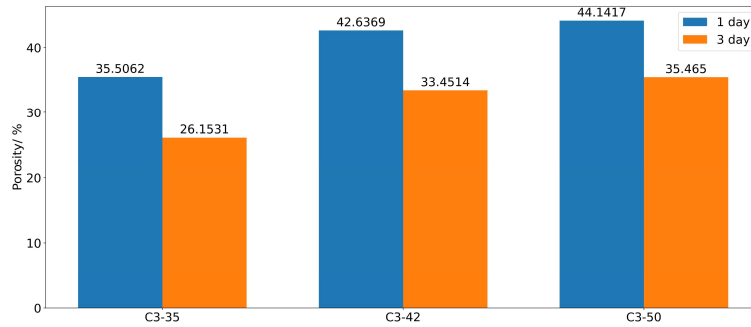


Figure 3-15 Porosity of different mixes derived from MIP results

### 3.4 Discussion

Based on the ADTM/ TSTM tests and ESEM/ XRD/ MIP tests, the influence of adding high-volume GGBFS on EAC risk is a complex result of the changes in AD and mechanical properties. In the first 2 days after casting, ettringite formation induces significant autogenous expansion. After 2 days, GGBFS either acts as filler or promotes the pozzolanic reaction, which continuously refines the pores and consumes water. As a result, the capillary pressure that can induce autogenous shrinkage is increased, according to Kelvin's equation. Therefore, in the first 2 days, the influence of GGBFS is favorable for preventing EAC risk, because high expansion introduces compressive stress and delays the occurrence of tensile stress. However, due to the high early-age creep/ relaxation, most of the compressive stress that would have accumulated by the autogenous expansion is relaxed. The advantage of the autogenous expansion cannot leverage the increased autogenous shrinkage afterward, and therefore the EAC risk induced by autogenous shrinkage of high-volume GGBFS concrete is higher than that of OPC concrete.

Among the high-volume GGBFS concrete with w/b ratios of 0.35, 0.42, and 0.50, the w/b ratio of 0.42 appears to be the most favorable choice when considering the compressive strength and the EAC risk quantified by the stress/ strength ratio. Such an advantage is achieved mainly by the compatibility of ettringite formation and pore size evolution. The highest amount of ettringite is generated in C3-42 which can fill the pores and apply crystalline pressure to induce high autogenous expansion. In the mix C3-35, less ettringite is produced, and therefore only limited autogenous expansion is observed. Afterwards, along with the fast decrease of the pore size and the internal relative humidity, the autogenous shrinkage goes fast and results in the rapid increase of tensile stress. For the mix C3-50,

although the ettringite amount is comparable with the C3-42, larger pore size limits the effective contact between ettringite and the pore walls, and therefore only limited autogenous expansion is observed. However, note that the observations are valid when it comes to AD, while when thermal and drying deformation is involved, more factors like e.g., the structural size need to be considered and thus the final EAC risk for different mixes may change.

The presented study found an agreement between the macroscale TSTM/ADTM tests and microscale ESEM/ XRD/ MIP tests. However, in the TSTM/ADTM test results, the fluctuations of measurement with time still indicate a potential error in the macroscale test. This error can be attributed to the temperature instability and the friction between the sample and the supporting plate. Because the dog-bone specimens of TSTM tests are all larger than 1 meter, almost all TSTM tests (including this study) are conducted horizontally [28,37,232,234,236]. The self-weight of concrete and the contact between the specimen and the supporting table makes the influence of friction unavoidable, which may cause jumps in the stress and deformation measurements. Based on the temperature regulating system introduced in section 3.2.2, the temperature at the middle thermocouple is fixed at 20 degrees. To show how temperature control influences the measurement, the temperature measurement of the C3-42 is given as an example, as shown in [Figure 3-16](#). It is found that the temperature in the middle part of the dog-bone specimen was well controlled at 20 degrees, with an error range of 0.05 degree. The temperature at the two ends of the specimen, where water circulation cannot reach, has a temperature close to the room temperature of around 19.5 degrees. To keep the temperature of the middle part specimen at 20 degrees, the water with a temperature of around 20.7 degrees circulates the middle part of the sample. Therefore, the measurement indicates that a temperature difference of less than 1 degree exists in both length-wise and depth-wise direction. Moreover, because the room temperature is not strictly constant, it can influence the temperature of the specimen at the two ends directly, and can also influence the feedback control to adjust its water temperature, indicating a change of temperature at the specimen surface also happens. All the factors mentioned above are potentially responsible for measurement jumps in both AD and restraint stress.

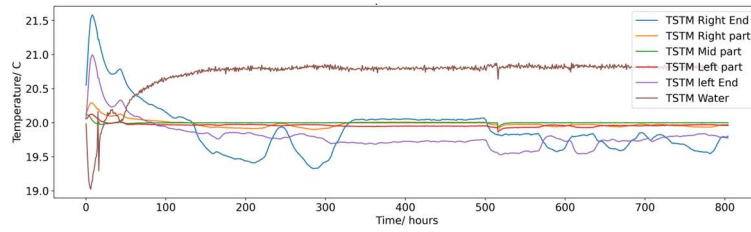


Figure 3-16 Temperature measurement of C3-42

### 3.5 Conclusions

To investigate the EAC risk of high-volume GGBFS concrete, herein ADTM and TSTM tests were performed to measure the AD and induced EAS of high-volume GGBFS concrete with w/b ratios ranging from 0.35~0.5. In addition, an OPC mix with a medium w/b ratio is also tested as a reference. ESEM/ XRD/ MIP tests were also performed to study the mechanisms of AD of GGBFS concrete at the microscale. The results of the macro-scale ADTM/ TSTM tests and micro-scale ESEM/ XRD/ MIP tests agree well. The following conclusions can be drawn:

- 1) High-volume GGBFS concrete shows higher autogenous expansion in the first two days and higher autogenous shrinkage afterwards than OPC concrete.
- 2) The EAC risk induced by AD of high-volume GGBFS concrete is higher than that of OPC concrete, because the compressive stress induced by early-age autogenous expansion is limited by high creep/ relaxation, and the higher autogenous shrinkage of GGBFS concrete plays a more significant role in tensile stress evolution.
- 3) The w/b ratio of 0.42 might be the optimal choice for high-volume GGBFS concrete because it produces the highest amount of ettringite and develops compatible pore size to ensure effective contact between ettringite and pore walls, which further leads to the highest autogenous expansion and therefore high compressive stress as observed in this study.
- 4) The w/b ratio of 0.35 appears to be risky for high-volume GGBFS concrete in terms of EAC potential. Due to the fast decrease of pore size and porosity, autogenous shrinkage of the high-volume GGBFS concrete with a w/b ratio of 0.35 happens drastically after the expansion peak, which then results in the highest stress/ strength ratio.



# 4. BAYESIAN INVERSE MODELLING OF AGING CREEP FOR PREDICTING THE EARLY AGE STRESS EVOLUTION

*This chapter presents a Bayesian inverse modelling scheme of aging creep for predicting the early-age stress (EAS) evolution induced by the AD in ground granulated blast furnace slag (GGBFS) concrete. An FE model for simulating the stress evolution in TSTM tests was established by a self-defined material subroutine based on the Rate-type creep law. By characterizing the creep compliance function with a 13-unit continuous Kelvin chain, forward modelling was first conducted to predict the stress development. Then, inverse modelling was conducted by Bayesian Optimization to efficiently modify the constant aging terms in the empirical formulas of the codes for the aging creep. The major findings of this chapter are as follows: 1) the magnitude of compressive stress that occurs as a consequence of high autogenous expansion in GGBFS concrete is low because of high relaxation and low elastic modulus; 2) the codes highly underestimated the early-age creep of GGBFS concrete. Although the codes could predict creep reasonably well after 200 hours, they significantly underestimated its magnitude in the early ages; 3) The proposed inverse modelling method with Bayesian Optimization can be used to adjust the aging terms of the code formulas to reproduce the experimental results. The adjusted creep compliance function of GGBFS showed a much faster aging speed at early ages than the one proposed by the codes.*

*Parts of this chapter have been published in Liang, M., Li, Z., He, S., Chang, Z., Gan, Y., Schlangen, E., & Šavija, B. (2022). Stress evolution in restrained GGBFS concrete due to autogenous deformation: Bayesian optimization of aging creep. *Construction and Building Materials*, 324, 126690.*

## 4.1 Introduction

Viscoelastic properties (i.e., creep/ relaxation) are necessary input that significantly influence the performance of EAS prediction models [237,238,283]. Early age creep can be modelled by a power law function [166,193,284], which can then be used as the input for EAS prediction models. However, early-age creep tests require decoupling of the effects of hydration and creep. Moreover, the potential difference between compressive and tensile creep [158,179] also poses challenges in modeling the EAS with the measured aging creep function as input. This is because the EAS development is a process from compression to tension, while the measured aging creep function is typically obtained from either compressive or tensile creep test. In addition, the aging creep function requires a continuous (or at least frequent) measurement throughout the early age of concrete, which makes the tests even more difficult. Although there are many standard codes providing prediction formulas of creep for normal concretes, the incorporation of high-volume GGBFS and difficulties of testing the very early-age creep raise questions regarding the applicability of these formulas [162,164,190,285].

In view of the difficulties of obtaining an appropriate input of aging creep function, therein a Bayesian inverse modelling scheme is proposed to infer the aging creep function and predict the EAS evolution based on the rate-type creep law. Two TSTM and ADTM testing results (i.e., C3-35 and C3-50) from Chapter 3 were used to show the efficiency of proposed modelling schemes, based on the creep functions of two representative international codes. The creep/ relaxation behavior was implemented as a 13-units Kelvin chain in 3D FE modelling based on the Rate-type creep law with a self-defined material constitutive subroutine. The proposed model was validated by forward modelling. The effects of aging creep on EAC were quantified under the framework of Euro code and ACI code by inverse modelling based on Bayesian optimization.

## 4.2 Forward modelling by rate-type creep law

The stress evolution is a direct index of EAC potential of concrete. The EAC potential  $p(t)$  can be derived by normalizing the EAS evolution  $\sigma(t)$  with the tensile strength development  $f(t)$  as follows:

$$p(t) = \frac{\sigma(t)}{f(t)} \quad (4-1)$$

An objective of the proposed model is to predict the EAS evolution  $\sigma(t)$  of GGBFS concrete in fully restrained TSTM tests.

#### 4.2.1 Stress superposition and computational dilemma

Since EAC analysis focuses on undamaged concrete, it can be assumed that the previous state of stress and deformation of concrete does not influence the mechanical response of concrete at later stages. In other words, the mechanical responses of concrete in different time steps are independent from each other. Therefore, the Boltzmann superposition principle can be applied to sum all mechanical responses of concrete at all time steps to form an overall mechanical response. In TSTM tests, the relative distance of two embedded bars is restrained (see Chapter 3), which corresponds to a typical relaxation scenario. Therefore, the EAS evolution  $\sigma(t)$  can be expressed as the following convolution:

$$\sigma(t) = \int_0^t R(t_0, t) d\varepsilon(t_0) \quad (4-2)$$

where  $t$  is the age of concrete;  $t_0$  is the age when loads are applied;  $\varepsilon$  is the imposed strain (in this study,  $\varepsilon$  refers AD);  $R$  is the relaxation function. To compute the stress superposition in TSTM tests, we first divide the continuous process of AD by a time interval  $\Delta t$ . Assuming that, in each time interval  $\Delta t$ , the AD occurs immediately at the onset and is constant until the end of the interval (as shown in **Figure 4-1 (a)**). With a fully restrained boundary condition, the AD (i.e., imposed strain) first causes an instantaneous elastic stress at the onset of each time interval which gradually decreases due to relaxation effects. **Figure 4-1 (b)** shows the stress history of each time interval corresponding to the strain history of **Figure 4-1 (a)**. The red line in **Figure 4-1 (b)** is the instantaneous elastic stress increase induced by imposed strain at the onset of each time interval, while the green line is the relaxation history of the stress.

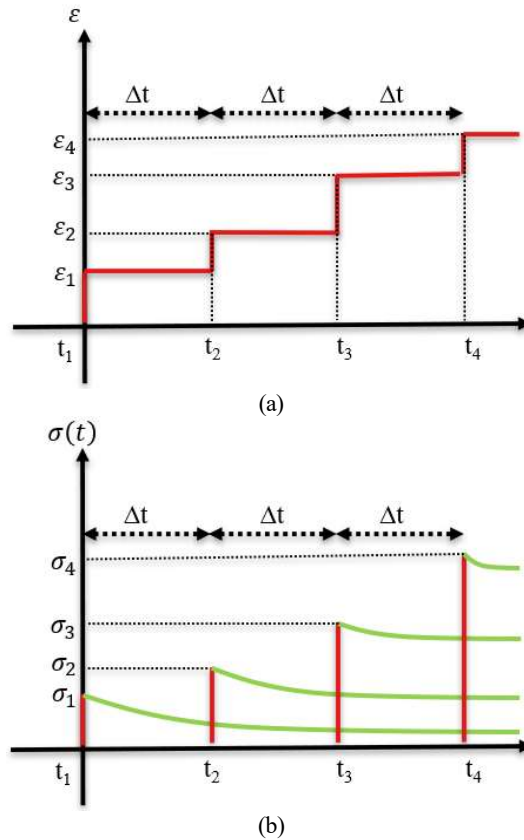


Figure 4-1 Illustration of stress superposition: (a) AD history; (b) Stress of each time interval

Following Eq (4-2), the stress evolution after  $t_4$  in **Figure 4-1** will be the sum of all the stress curves (i.e., green curves), which can be expressed as:

$$\sigma(t) = \varepsilon_1 R(t_1, t) + \varepsilon_2 R(t_2, t) + \varepsilon_3 R(t_3, t) + \varepsilon_4 R(t_4, t) \quad (4-3)$$

The case showed by **Figure 4-1** illustrates the computational dilemma of Eq (4-2), which requires to restore every stress history curve of each previous time interval and sum them up. In the simple example depicted in **Figure 4-1**, which only has 4 timesteps, 4 terms of stress histories are needed to count the whole stress evolution history. In real cases, where many timesteps are needed, direct implementation of Eq (4-2) in FEM is very difficult because storing all the stress histories of every element is very computationally demanding.

### 4.2.2 Rate-type Creep Law

The rate-type creep law [111,213] can efficiently solve the computational dilemma introduced in section 4.2.1. The relaxation function  $R(t_0, t)$  is difficult to measure because the strain must be adjusted to a constant value in every time-interval. Therefore, it is more practical to characterize the measure creep. The integration form of strain is expressed as:

$$\varepsilon(t) = \int_0^t J(t_0, t) d\sigma(t_0) \quad (4-4)$$

where  $J$  is the creep compliance function. Rearranging Eq (4-4) into the incremental form from  $t_i$  to  $t_{i+1}$  and assuming a linear stress variation in each time interval, one can obtain the quasi-elastic constitutive equations:

$$\Delta\sigma = E^* \Delta\varepsilon - \sigma^* \quad (4-5)$$

$$E^* = \frac{\Delta t}{\int_{t_i}^{t_{i+1}} J(t_0, t_{i+1}) dt_0} \quad (4-6)$$

$$\sigma^* = E^* \int_0^{t_i} [J(t_0, t_{i+1}) - J(t_0, t_i)] \dot{\sigma} dt_0 \quad (4-7)$$

where  $\Delta\sigma$  and  $\Delta\varepsilon$  are difference of stress and strain between two consecutive time steps  $t_i$  and  $t_{i+1}$ . Note that the integration in Eq (4-7) still requires to revisiting the stress history, which makes FEM modelling very difficult. By implementing the rate-type Creep Law [111,213], the integral can be transformed to a series of linear differential equations, which are the governing equations of the Kelvin chain rheological model with multiple sets of springs and dashpots. The creep compliance function can be expressed as a Dirichlet series:

$$J(t', t) = \frac{1}{E_0(t_0)} + \sum_{j=1}^N \frac{1}{E_j(t_0)} \left(1 - e^{-\frac{t-t_0}{\mu_j}}\right) \quad (4-8)$$

where  $N$  is the number of Kelvin chain units;  $E_j$  and  $\mu_j$  is the elastic modulus and retardation time of  $j$ -th Kelvin chain unit. Assuming that the variation of stress within each time interval is linear, substituting Eq (4-8) into Eq (4-6)~(4-7), and calculating the integral by mid-point rule, one can obtain the expression of  $E^*$  and  $\sigma^*$  as follows:

$$E^*(t^*) = \frac{1}{\frac{1}{E_0(t^*)} + \sum_{j=1}^N \frac{1}{E_j(t^*)} \left(1 - \left(1 - e^{-\frac{\Delta t}{\mu_j}}\right) \frac{\mu_j}{\Delta t}\right)} \quad (4-9)$$

$$\sigma^*(t_i) = E^*(t^*) \sum_{j=1}^N (1 - e^{-\frac{\Delta t}{\mu_j}}) \varepsilon_j^*(t_i) \quad (4-10)$$

$$\varepsilon_j^*(t_i) = \int_0^{t_i} \frac{1}{E_j(t_0)} e^{-\frac{t_i-t_0}{\mu_j}} \dot{\sigma} dt_0 \quad (4-11)$$

$$\varepsilon_j^*(t_{i+1}) = e^{-\frac{\Delta t}{\mu_j}} \varepsilon_j^*(t_i) + \frac{1}{E^*(t_i)} (1 - e^{-\frac{\Delta t}{\mu_j}}) \frac{\mu_j}{\Delta t} \Delta \sigma \quad (4-12)$$

where  $t^*$  is the average of two consecutive time steps  $t_i$  and  $t_{i+1}$ . Eq (4-5) and Eq ((4-9)~ (4-12)) form the incremental viscoelastic constitutive relationship for simulating the development of stress induced by AD. Note that the  $\varepsilon^*$  of each Kelvin chain unit is the internal state variable, which is a second-order strain tensor that must be updated in each integration point according to Eq (4-12) at every time step.

### 4.2.3 FEM configuration

#### 4.2.3.1 Meshes and boundary conditions

The Rate type creep law is implemented by a self-defined subroutine of material mechanical constitutive behavior in the commercial FEM software COMSOL Multiphysics. A numerical dog-bone TSTM specimen is generated as shown in **Figure 4-2**, which is discretized by evenly distributed hexahedral mesh. At the transition area from the two ends to the middle, a denser mesh is adopted to assure numerical precision. The FE model uncertainties are significant factors influencing the optimization results. Since the input parameters (except for creep aging terms) are derived from tests, the only variation lies in the FE configurations, including step size, step convergence criterion, meshing schemes, etc. These parameters were calibrated at the beginning to get reliable results. Roller boundaries are attached to the purple areas in **Figure 4-2 (b)** (i.e., bottom sides and the lateral sides of the two ends), which ensures zero displacement in the direction normal to the boundary surface.

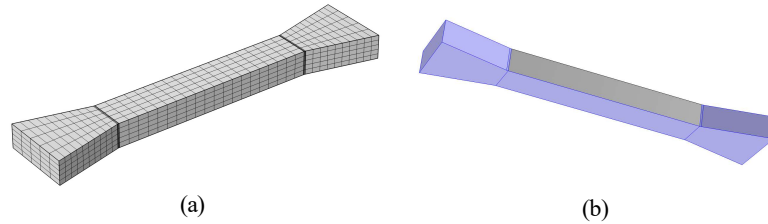
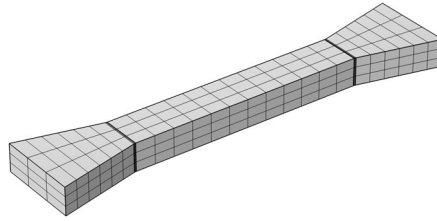
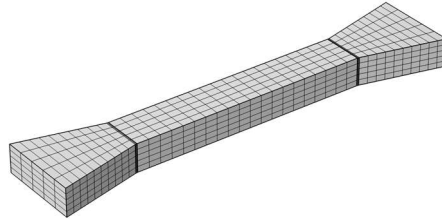


**Figure 4-2 Numerical dog-bone specimen: (a) mesh; (b) boundary conditions**

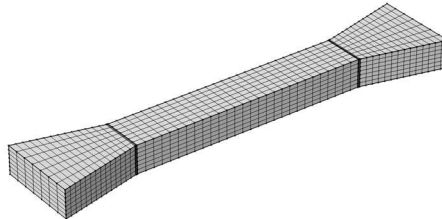
The influence of meshing sizes on modelling results is presented by comparing the results of four different meshing sizes, including original mesh size, 1 coarser mesh size (166.7% of current mesh size), and 2 finer mesh size (71.4% and 55.6% of original mesh size), as shown below.



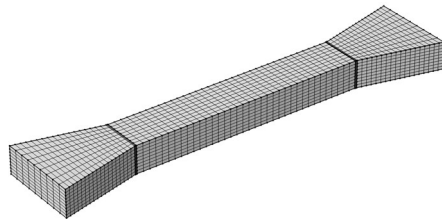
(a) 166.7% original mesh size (number of elements = 270)



(b) original mesh size (number of elements = 1150)



(c) 71.4% original mesh size (number of elements = 3038)



(d) 55.6% original mesh size (number of elements = 6318)

**Figure 4-3 Four meshing schemes (a-d): 166.7%, 100%, 71.4%, and 55.6% of the original mesh size, with the element number of 270, 1150, 3038, and 6318 respectively.**

Taking C3-50 as an example, the results of the 4 meshing schemes are shown below. It can be found that all 4 meshing schemes can produce similar results. The difference between different meshing schemes remains almost invisible from the whole-time range. Minor difference can only be

seen on amplified time range. Therefore, the current FEM configurations can efficiently guarantee the repeatability of the numerical model with the same material input.

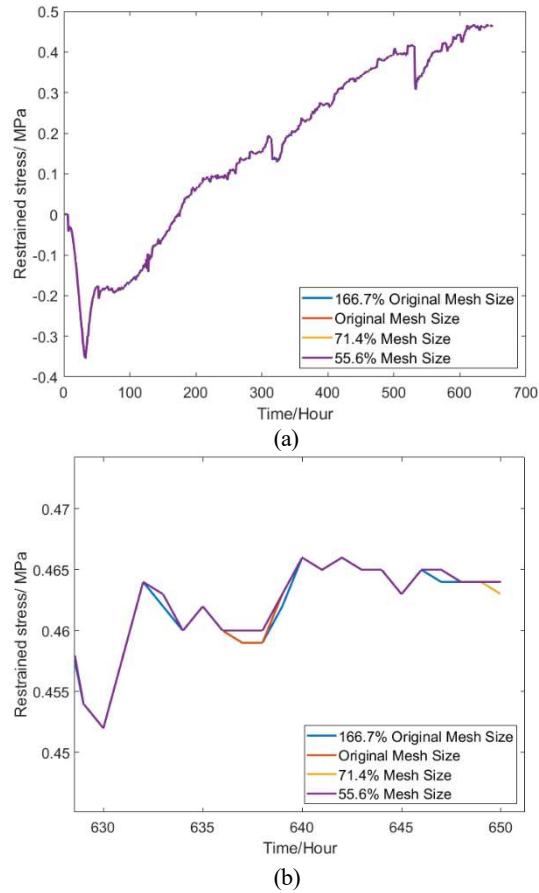


**Figure 4-4 Results of 4 different meshing schemes in (a) 0-28 days and (b) between 630-650 hours**

#### 4.2.3.2 Constitutive relationship and input parameters

Considering AD as an isotropic deformation in all directions, the quasi-elastic constitutive equation described by Eq (4-5) can be rewritten as follows:

$$\Delta\sigma = E^*(\Delta\varepsilon - \Delta\varepsilon_{ad}) - \sigma^* \quad (4-13)$$

where  $\Delta\varepsilon_{ad}$  is the autogenous strain in each time interval;  $\sigma^*$  is the state variable that stores the previous load histories and should be updated in every time step according to Eq ((4-9)~ (4-12)). In this model, there are

three kinds of input material properties and behaviors: autogenous strain  $\varepsilon_{ad}(t)$ , elastic modulus  $E(t)$ , and creep compliance function  $J(t_0, t)$ . The testing results of AD and compressive strength of C3-35 and C3-50 from tests in Chapter 3 are used as inputs of the model. The results of compressive strength are used to calculate the  $E(t)$  [286]:

$$E(t) = E_{c0} \alpha_E \left( \frac{f(t)}{10} \right)^{\frac{1}{3}} \quad (4-14)$$

where  $f(t)$  and  $E(t)$  are the compressive strength and elastic modulus at an age  $t$ , respectively;  $E_{c0}$  is a coefficient and equals to 21500 MPa;  $\alpha_E$  is the coefficient for different aggregate ranging from 0.7 to 1.2. Considering the aggregates used in the tests are mainly quartzite gravel,  $\alpha_E$  equals to 1.0 in this study. Note that the selection of a proper estimation formula for the elastic modulus can influence the modelling results. The influence of 4 international codes (i.e., Eurocode 2, Model Code 2010 and codes made by American Concrete Institute (ACI) and Canadian Standards Association (CSA)) [30,286–288] on the simulation results were investigated, by using their different formulas in the model. As an example, the simulation of  $w/b = 0.50$  was conducted. Based on the compressive strength at different ages, the elastic modulus can be calculated according to formulas in the 4 international codes, shown as follows.

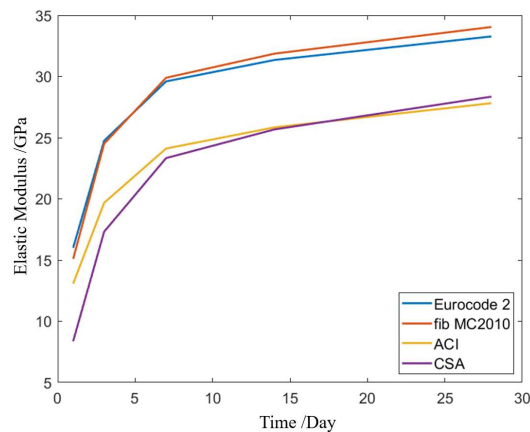
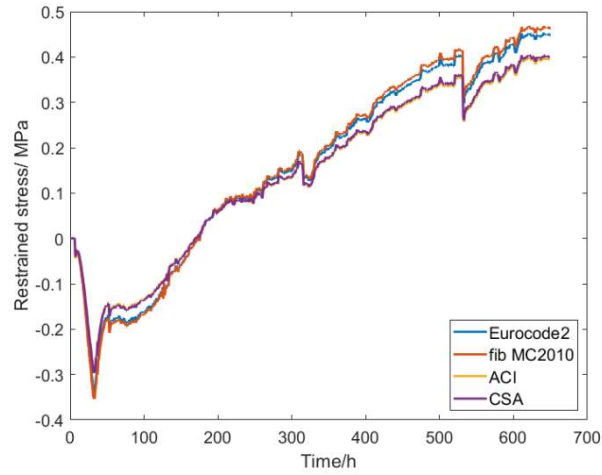


Figure 4-5 Elastic modulus of the mix  $w/b = 0.50$  based on 4 international codes

Furthermore, based on the calculated elastic modulus based on four different international codes, the stress results are shown below. The difference between the codes' estimation on elastic modulus is reflected in the stress results: 1) Because Eurocode 2 and fib MC2010 has similar estimation on elastic modulus, their stress results are also close; 2) Because

ACI and CSA tend to underestimate the elastic modulus, their stress results showed lower compressive and tensile stress among the whole-time range. The parametric study presented here also validate the reasonability of the proposed model.



**Figure 4-6 Stress results of the mix C3-50 using formulas of elastic modulus of 4 international codes**

The bottleneck of this model lies in the creep compliance function  $J(t_0, t)$ , which is difficult to test because: 1) the creep tests last for a certain period of time, which makes it difficult to decouple the influence of hydration from creep, especially for very early age concrete; 2) creep tests only allow measuring the creep compliance function at discrete loading ages, while  $J(t_0, t)$  is a continuous function characterized by a 3D surface.

#### 4.2.4 Kelvin-chain spectrum

To overcome the issue of missing creep compliance data, this study parameterizes the creep compliance function  $J(t_0, t)$  into a continuous Kelvin chain spectrum under the framework of two international standard codes: Eurocode 2 [288] and ACI-209R [30]. First, the  $J(t_0, t)$  recommended by the codes is used as input in this model to evaluate the performance of the codes; then, inverse modelling is conducted by Bayesian optimization to find the most appropriate  $J(t_0, t)$  of GGBFS concrete C3-35 and C3-50 in chapter 3. Both of these codes follow the Double Power Law [193], and their formulas can be expressed as:

$$J(t', t) = \frac{1}{E(t')} + C_0 C_1(t') C_2(\xi) \quad (4-15)$$

where  $C_0$  is a coefficient related to general concrete properties and environmental conditions, such as compressive strength at 28 days, relative humidity, etc.;  $C_1$  is a power function to describe the aging of creep compliance, which only depends on age of loading  $t_0$ ;  $C_2$  is a power function representing the non-aging term, which depends on the time length of loading  $\xi$  ( $\xi=t-t_0$ ). In the rate-type law, the creep compliance function is expressed as a Kelvin chain model (i.e., a Dirichlet series as Eq (4-8)). Therefore, to incorporate the creep compliance data of codes in the FEM model, the Kelvin chain parameters (i.e.,  $E_j, \mu_j$  for  $j = 1: N$ ) should be fitted by the function Eq (4-15).

However, directly fitting the  $E_j, \mu_j$  is problematic because of weak points such as non-unique solutions [204]. This study implements a general procedure of fitting the Kelvin chain parameters with a continuous spectrum [209], which guarantees a unique and stable solution. A 13-units Kelvin chain ( $j=13$  in Eq (4-8)) is used to describe the creep compliance function Eq (4-15) in the first 28 days. First, the retardation time  $\mu_j$  is chosen as a priori to prevent ill-conditioned equation system as follows [289]:

$$\mu_j = 10^{-6+j}, j = 1:13 \quad (4-16)$$

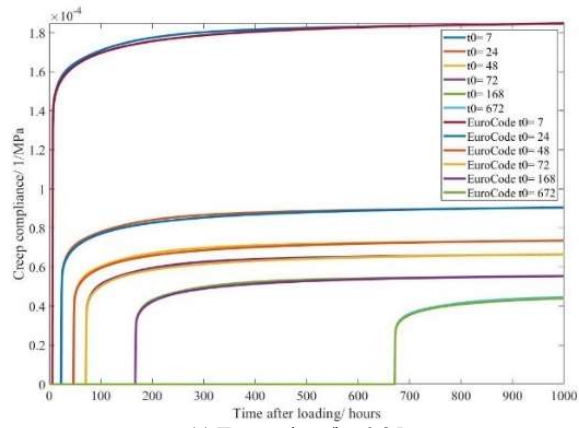
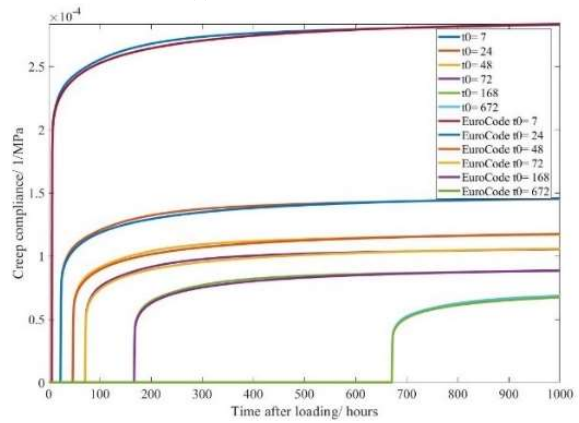
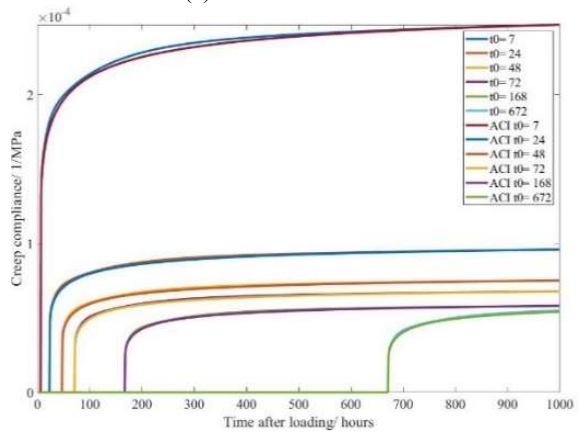
The continuous form of the non-aging term is expressed as follows [213]:

$$C_2(\xi) = \int_0^{\infty} \frac{1}{E_j} (1 - e^{-\frac{\xi}{\mu_j}}) d(\ln \mu_j) \quad (4-17)$$

Using the Laplace transform and Widder's formula, the solutions of  $E_j$  can be derived [209]:

$$\frac{1}{E_j} = -\ln 10 * \lim_{k \rightarrow \infty} \frac{(-k\mu)^k}{(k-1)!} C_2^{(k)}(k\mu) \quad (4-18)$$

In this study, the spectrum of third order ( $k=3$ ) is used. The fitting results of the mixes C3-35 and C3-50 from Chapter 3 are shown in [Figure 4-7](#), which shows that the fitted Kelvin chain can mimic the codes with good precision.

(a) Eurocode  $w/b=0.35$ (b) Euro code  $w/b=0.50$ (c) ACI  $w/b=0.35$ 

(Continue in the next page)

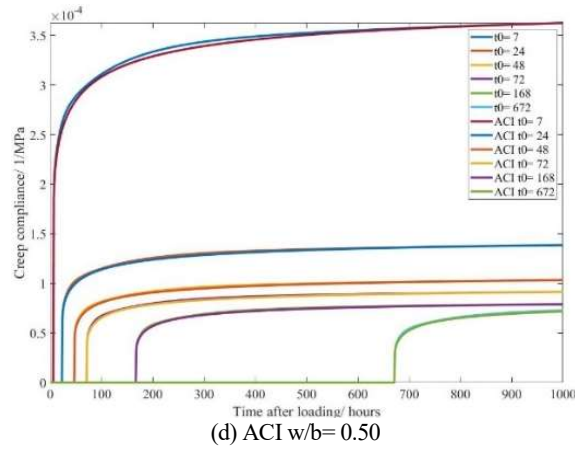


Figure 4-7 Fitting results of Kelvin chain with codes: (a) Eurocode  $w/b=0.35$ ; (b) Euro code  $w/b=0.50$ ; (c) ACI  $w/b=0.35$ ; (d) ACI  $w/b=0.50$ .

#### 4.2.5 Modelling the EAS using creep functions from codes

The procedure of forward modelling is shown in [Figure 4-8](#), based on the framework of FEM model established in section 4.2.2~4.2.4. In TSTM tests, the stress is calculated by normalizing the restraint force with the area of cross-section of the dog-bone specimen. In the FEM model, as shown in [Figure 4-9](#), the modelling result of stress evolution  $\sigma_M$  is calculated at the middle section of the specimen and expressed as follows:

$$\sigma_M(t) = \frac{\iint \sigma_{xx} dy dz}{A} \quad (4-19)$$

where  $\sigma_{xx}$  is the component of stress tensor in xx direction (i.e., axial direction of dog-bone specimen);  $A$  is the cross-section area of the yz plane at  $x=0$ . The metric Root Mean Squared Error (RMSE) is used to assess the modelling accuracy by averaging the residual error at each time step:

$$RMSE = \sqrt{\frac{\sum_t (\sigma_M(t) - \sigma_T(t))^2}{t_{total}}} \quad (4-20)$$

where  $\sigma_M(t)$  and  $\sigma_T(t)$  are the modelling and testing results of stress at time step  $t$ , respectively.

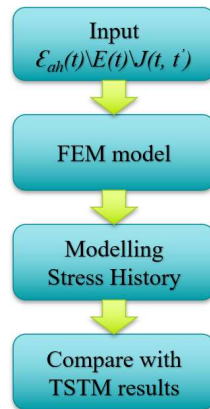


Figure 4-8 Workflow of forward modelling

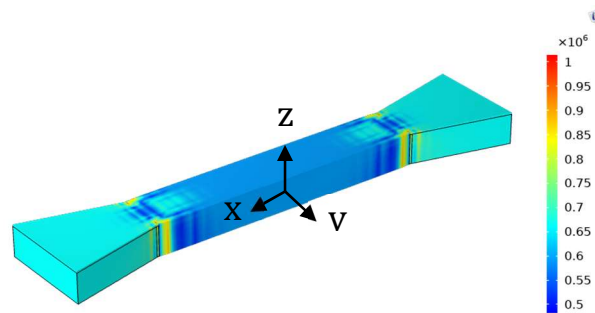


Figure 4-9 Stress contour at 640h ( $w/b=0.5$ ), the units in the legend bar is Pa.

### 4.3 Inverse modelling

Creep tests of concrete at early age are difficult to perform because the influence of hydration cannot be fully decoupled. For example, for a concrete specimen under sustained loads from an age of 12 hours to 36 hours, the measured creep compliance curve from  $J(12, 12)$  to  $J(12, 36)$  can be derived by subtracting the shrinkage strains from the measured total strains. Then with the experimental results, the creep compliance function  $J(12, t)$  will be fitted by either power function or logarithmic function, which aims to represent the creep strain development since the age of 12 hours when a unit load is applied. However, this process assumes that the concrete properties (e.g., elastic modulus, creep etc.) remain constant during 12~36 hours, while in reality the microstructure of concrete changes drastically in that period. In view of the testing difficulties of aging creep, this study uses inverse modelling to unravel the aging patterns of

creep [290–292]. An objective function is first defined to measure the agreement between modelling and experimental results. Then, Bayesian Optimization is implemented to find the best-fit parameters of aging creep and achieve a minimum in the objective function.

#### 4.3.1 Definition of the objective function

In forward modelling, the accuracy of the FEM model can be defined as:

$$RMSE = f[\varepsilon_{ad}(t), E(t), J(t', t), \sigma_T(t)] \quad (4-21)$$

where  $f$  is a complex implicit function represented by the FEM model. With the function  $f$ , inverse modelling can be defined as the following optimization process: given the input of AD  $\varepsilon_{ad}(t)$ , elastic modulus  $E(t)$  and testing results  $\sigma_T(t)$ , find the creep compliance function  $J(t', t)$  that can give best modelling results. Thus, the objective function of inverse modelling can be expressed as:

$$\arg \min f\{J(t', t) | \varepsilon_{ad}(t), E(t), \sigma_T(t)\} \quad (4-22)$$

As in Eq (4-15), the creep compliance function  $J(t', t)$  is a surface controlled by  $E(t)$ , constant term  $C_0$ , aging term  $C_1$  and non-aging term  $C_2$ . It should be noted that, in both codes, the terms  $C_0$  and  $C_2$  are dependent on mixture and environmental parameters, while the aging term  $C_1$  remains constant for all conditions. In other words, the codes assume that the aging kinetics of creep of different concretes under different environmental conditions is the same. This assumption can cause significant errors [153,174]. Therefore, the optimization process focuses on the aging term  $C_1$ . The aging term  $C_1$  of both codes is generalized as a power function controlled by coefficients  $a$ ,  $b$ , and  $c$ :

$$\text{Eurocode: } C_1(t') = \frac{c}{b+t'^a}; \quad (4-23)$$

$$\text{ACI code: } C_1(t') = \frac{c}{t'^a} \quad (4-24)$$

Then the inverse modelling process can be further described as:

$$\arg \min f\{C_1(t', a, b, c) | \varepsilon_{ad}(t), E(t), \sigma_T(t), C_0, C_2(t - t')\} \quad (4-25)$$

Note that the function  $f$  is non-differentiable and computationally expensive, since calculating the function  $f$  means running the FEM model to get the stress result of the whole time-range. Therefore, an efficient optimization algorithm is needed. Bayesian Optimization is used herein, which includes Gaussian Process (GP) [293] and a well-defined acquisition function. The workflow of this process is shown in [Figure 4-10](#).

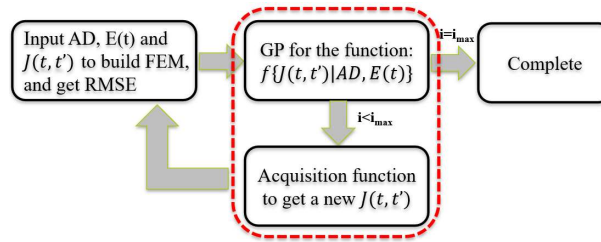


Figure 4-10 Workflow of inverse modelling

### 4.3.2 Bayesian optimization

Solving Eq (4-25) is computationally expensive because 1) running an FE model is computationally expensive; and 2) high dimensionality of parameters produces a large sample space. By fitting the objective function with a probabilistic model, Bayesian Optimization is a smart sampling and efficient global optimization algorithm for expensive black-box function [294,295]. The workflow of Bayesian Optimization in this study is shown as Figure 4-11.

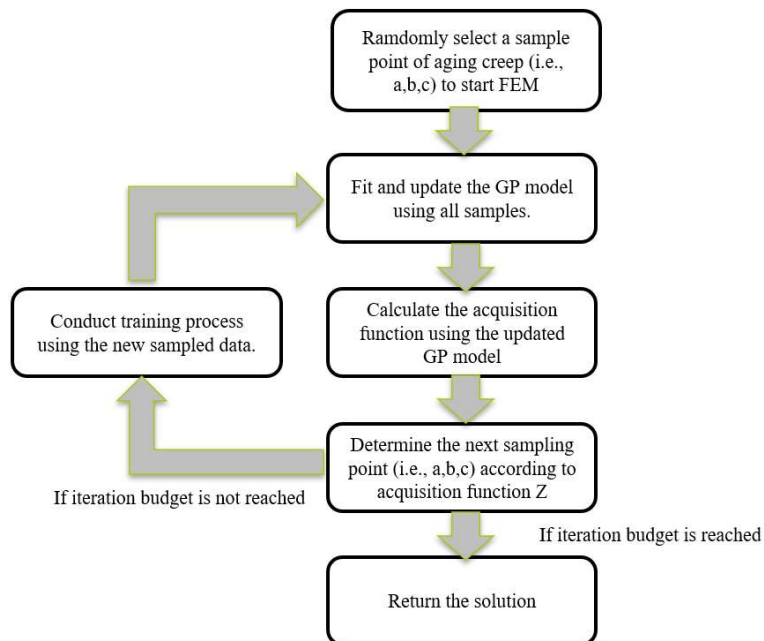


Figure 4-11 Workflow of Bayesian Optimization

By assuming that the objective function Eq(4-25) follows the multivariate Gaussian distribution, the objective function can be fitted by Gaussian Process (GP). For  $i$ -th sampling point of aging creep  $X_i = (a_i, b_i, c_i)$ , the

implementation of GP is by fitting the kernel of the covariance matrix as follows:

$$K = \begin{bmatrix} k(X_1, X_1) & \cdots & k(X_1, X_n) \\ \vdots & \ddots & \vdots \\ k(X_n, X_1) & \cdots & k(X_n, X_n) \end{bmatrix} + \sigma_{noise}^2 \mathbf{I} \quad (4-26)$$

in which  $k$  is the covariance kernel calculated by an exponential function of the second norm of the difference value between two samples [296];  $n$  is the number of sample points of aging creep that are incorporated in the GP model;  $\sigma_{noise}$  is the standard deviation of the noise, which follows a normal distribution. Denote the multivariate Gaussian distribution of  $n$  sample points of aging creep as  $D_{1:n} = (X_{1:n}, Y_{1:n})$ , and then the performance (i.e., RMSE of FEM) of the next sample point (i.e.,  $(n+1)$ -th sample point) can be predicted by Bayesian rules for multivariate Gaussian distribution as follows [293]:

$$Y_{n+1} | D_{1:n} \sim N(\mu(X_{n+1}), \sigma^2(X_{n+1}) + \sigma_{noise}^2) \quad (4-27)$$

in which

$$\mu(X_{n+1}) = \mathbf{k}^T K^{-1} Y_{1:n} \quad (4-28)$$

$$\sigma^2(X_{n+1}) = k(X_{n+1}, X_{n+1}) - \mathbf{k}^T (K + \sigma_{noise}^2 \mathbf{I})^{-1} \mathbf{k} \quad (4-29)$$

$$\mathbf{k} = [k(X_{n+1}, X_1) \ k(X_{n+1}, X_2) \ \cdots \ k(X_{n+1}, X_n)] \quad (4-30)$$

Based on GP, the inference of performance (i.e., RMSE of FEM) of any possible sample points can be drawn. Then, the acquisition function (i.e., Expect Improvement [297]) is calculated to infer the improving potential of every possible sample point, as expressed below:

$$EI(X_n) = (y_{best} - \mu(X_n)) \Phi\left(\frac{y_{best} - \mu(X_n)}{\sigma(X_n)}\right) + \sigma(X_n) \phi\left(\frac{y_{best} - \mu(X_n)}{\sigma(X_n)}\right) \quad (4-31)$$

where  $\Phi(\cdot)$  and  $\phi(\cdot)$  are the standard normal density and distribution function, respectively;  $y_{best}$  is the tentative optimal value (i.e., lowest RMSE) in current sample space. The first term measures the difference between every possible sample point and the best sample point, which aims to achieve exploitation. The second term assigns more weight to the sample points of more uncertainty to ensure there is no “blank” area in sample space, which achieves exploration. Combining the first and second term, the acquisition function  $EI$  tends to get higher values at sample points with lower posterior mean and lower credible intervals, thereby achieving a balance between exploitation and exploration.

## 4.4 Results and discussion

### 4.4.1 Forward modelling results

Fitting the Kelvin chain with ACI and Eurocode and inputting the testing results (i.e., C3-35 and C3-50) of AD and elastic modulus, the modelling results of EAS can be obtained (Figure 4-12). By comparing the RMSE, the creep compliance function given by the ACI code produces better results when  $w/b = 0.35$ , while the one given by the Eurocode performs better when  $w/b = 0.50$ . After 200 hours, the simulated stress curves are parallel with the testing results, which indicates that both codes show good conformity with TSTM testing results at a latter age. However, an obvious difference at early age shows that both codes do not perform well at an early age. In the results of  $w/b = 0.35$  (see Figure 4-12 (a-b)), although the modelling and testing curves are almost parallel after 100 hours, the big difference before 100 hours causes significant errors in the entire time range.

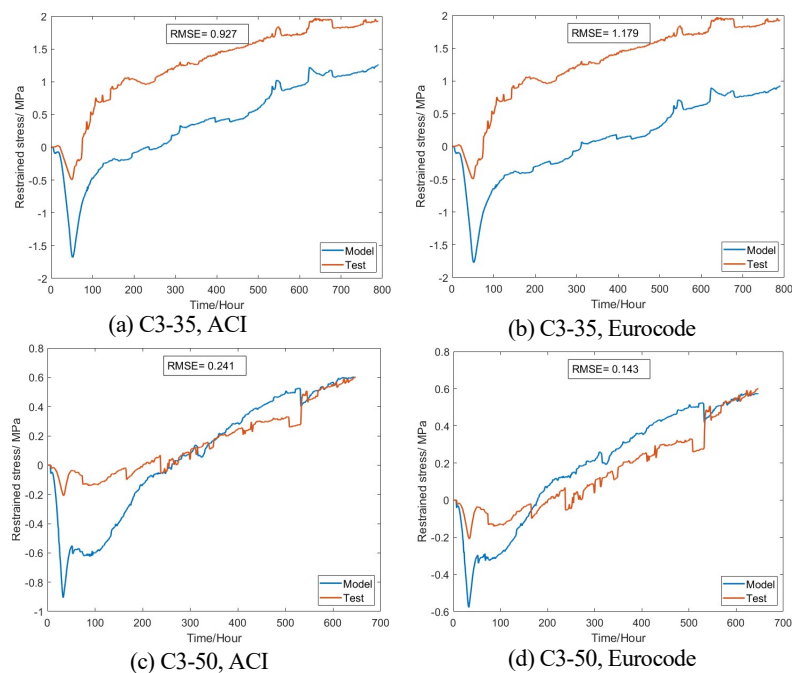


**Figure 4-12 Simulated stress evolution with different codes for creep compliance: (a-b) modelling results of C3-35 using ACI and Eurocode, respectively; (c-d) modelling results of C3-50 using ACI and Eurocode, respectively.**

The comparison results of forward modelling suggest that both codes have good performance at a latter age, but the error is non-negligible at the early

age (e.g., before 200 hours). This stems from the choice of creep compliance function in the two codes (see Eq (4-15)): both codes have specified formulas for calculating  $C_0$  and  $C_2$ , depending on different parameters of concrete properties and environmental conditions such as w/b ratios, relative humidity, etc.[30,116]. However, the aging term  $C_1$  is constant and only depends on age of loading  $t_0$  and remains unchanged for all kinds of concrete under all conditions, as shown below:

$$\text{Eurocode: } C_1(t') = \frac{1}{0.1+t_0^{0.2}}; \quad (4-32)$$

$$\text{ACI code: } C_1(t') = \frac{1.25}{t_0^{0.118}} \quad (4-33)$$

#### 4.4.2 Inverse modelling results

Bayesian Optimization can efficiently save the computational resources, as shown in **Figure 4-13**. For the FEM model with ACI code, the minimum is found within 10 iteration steps, while for the model with Eurocode, the minimum converges within 15 steps. The reason why the Eurocode takes longer than ACI is the complexity of the aging term: the aging term  $C_1$  in Eurocode is controlled by 3 parameters (i.e.,  $a$ ,  $b$ ,  $c$ ) while the ACI only has two parameters for  $C_1$  (i.e.,  $a$ ,  $c$ ).

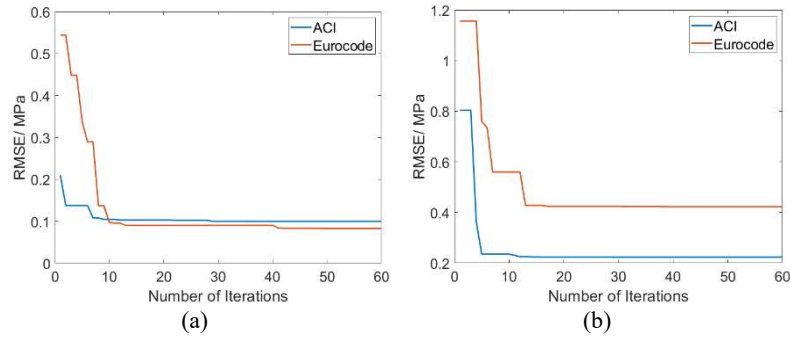


**Figure 4-13** Optimizing history of (a) C3-35 and (b) C3-50

Since the aging term  $C_1$  of ACI only depends on two parameters  $a$  and  $c$ , its objective function can be visualized as a 3D surface, as shown in **Figure 4-14**. The distribution of sampling points is much denser when approaching the minima, and more diluted when approaching the peaks, which guarantees a tradeoff between exploitation and exploration: 1) more computational resources are spent to exploit the area that is more likely to have a minimum; 2) certain computational resources are allocated to explore areas that have low confidence.

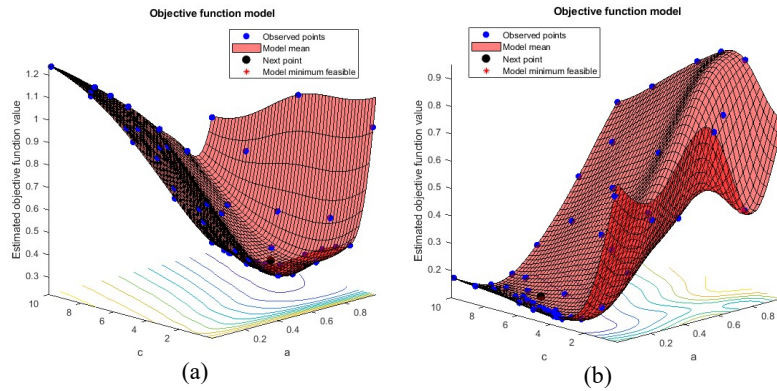


Figure 4-14 Objective function with ACI model of w/c (a) 0.35 and (b) 0.50

With the inverse modelling, the aging term  $C_1$  of creep compliance function is adjusted to obtain the optimal modelling results, as shown in Figure 4-15. The adjusted parameters for the aging term of creep compliance function/ $(t_0, t)$  is shown in Table 4-1.

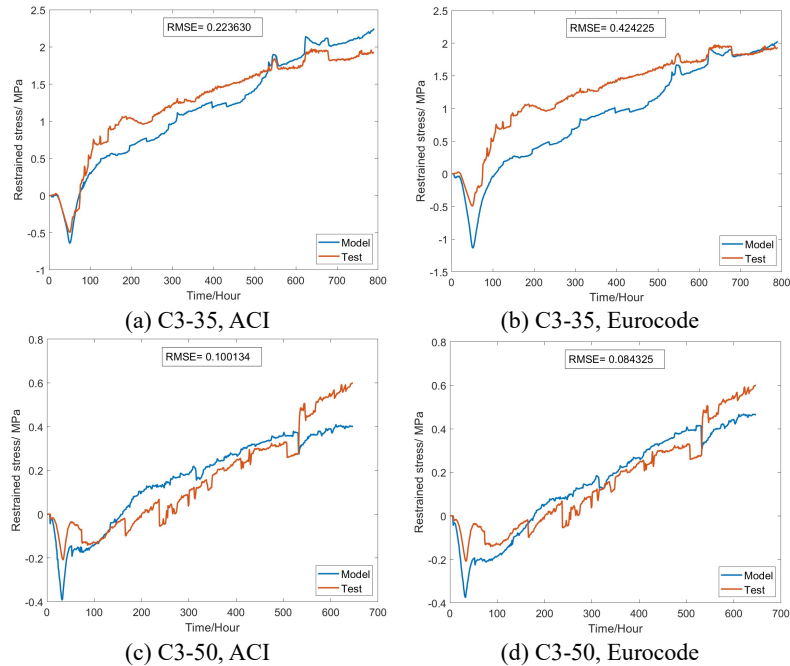
Table 4-1 Adjusted aging terms for creep function of GGBFS concrete

	ACI ( $C_1(t') = \frac{c}{t_0^a}$ )		Eurocode ( $C_1(t') = \frac{c}{b+t_0^a}$ )		
	a	c	a	b	c
Original values	0.118	1.250	0.200	0.100	1.000
C3-35	0.990	7.786	0.984	0.024	2.373
C3-50	0.139	5.228	0.903	1.020	9.940

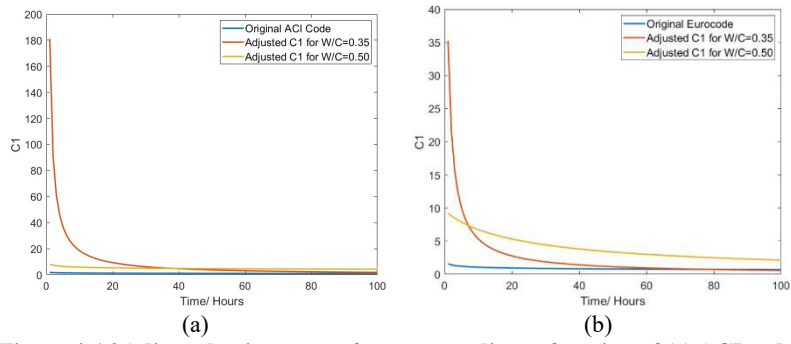
The results with adjusted aging terms show obvious improvement on results with original aging terms of codes. Moreover, it can be found that the major improvement is in early age, since the big gaps before 100 hours are effectively reduced. Such changes can also be directly seen from the aging creep term  $C_1(t_0)$  of both codes, as shown in Figure 4-16. Note that because ACI and Eurocode have different configurations for the constant term  $C_0$  and non-aging term  $C_2$ , the magnitudes of  $C_1$  are different and cannot be directly compared. However, for both codes, the curves of the adjusted aging term  $C_1$  (see Figure 4-16) show a similar trend: the aging term goes through a fast decrease in first 100 hours, and then converges to a value that is close to the original aging term given by the codes. Such trend is even more obvious when w/b ratio is 0.35. Overall, the adjusted results prove that much higher creep should be expected for GGBFS concrete at an early age. And creep of concrete with lower w/b ratio goes through a faster aging process. A comparison of adjusted creep compliance function with

the original creep compliance function of the codes are shown in [Figure 4-17](#). The 3D surfaces of the creep compliance function show the same pattern as in [Figure 4-16](#): a steep slope along the axis “age when load is applied” (i.e.,  $t_0$ ) is observed, which indicates much faster aging of concrete creep at early ages which must be considered to obtain accurate modelling results of stress evolution.

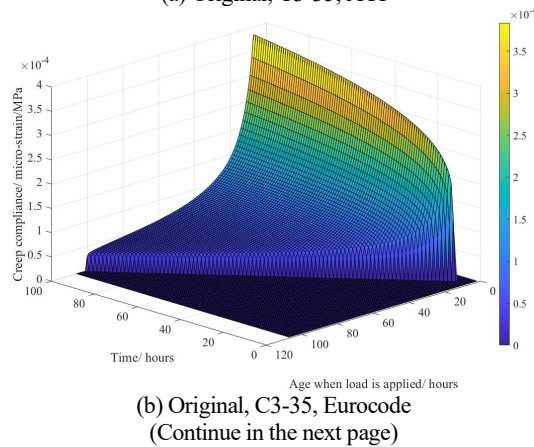
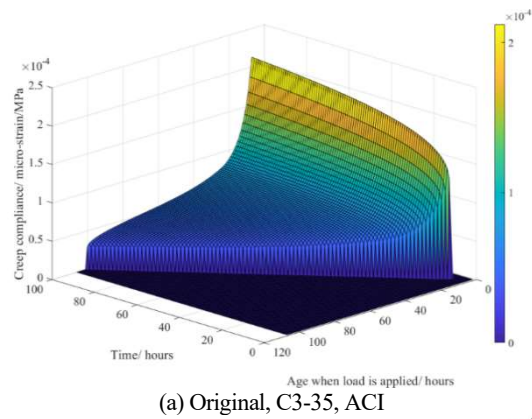
In the end, it should be noted that the Bayesian inverse modelling in this chapter is a compromise with the fact that the aging creep is difficult to test, despite its high efficiency and good prediction accuracy. In the following chapters, a new testing setup will be devised to provide a testing approach to monitoring the development of creep from a very early-age.

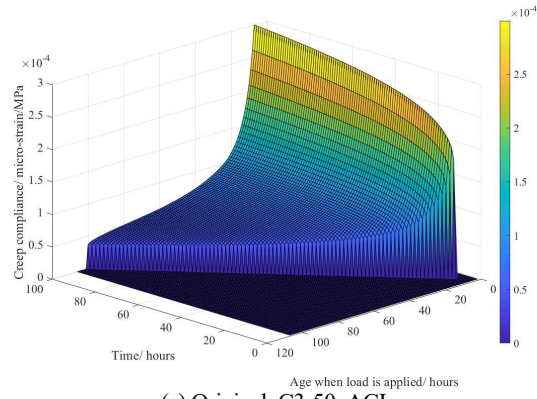


**Figure 4-15** Modelling results with adjusted aging term of creep: (a-b) results of C3-35 based on ACI and Eurocode respectively; (c-d) results of C3-50 based on ACI and Eurocode respectively.

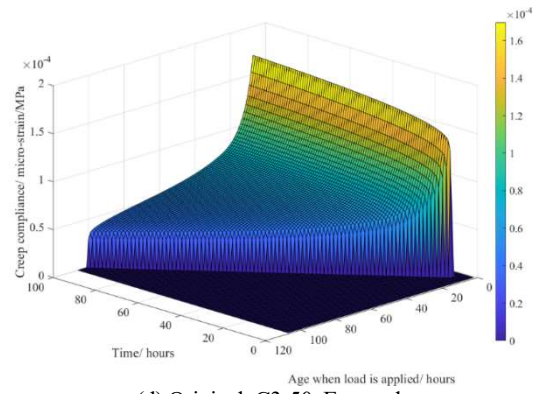


**Figure 4-16 Adjusted aging term of creep compliance function of (a) ACI code and (b) Eurocode.**

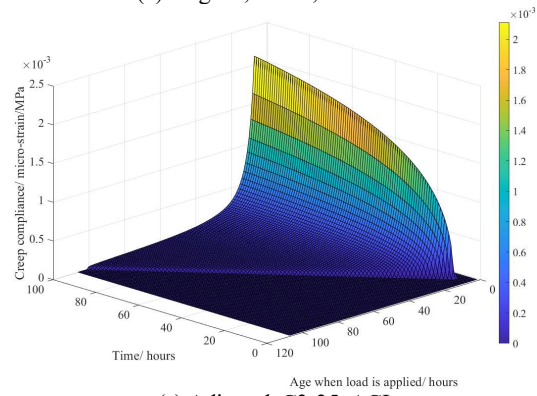


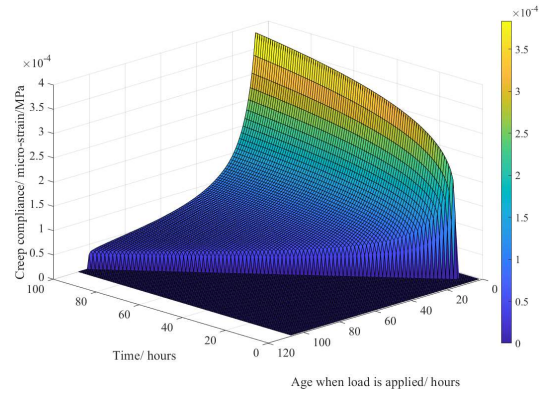


(c) Original, C3-50, ACI

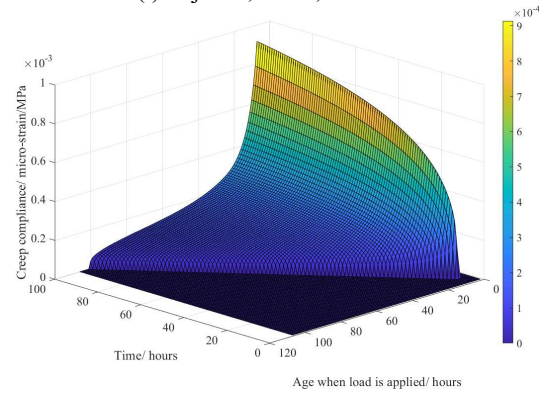


(d) Original, C3-50, Eurocode

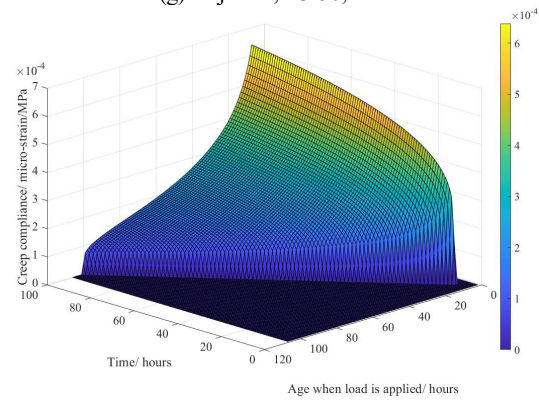
(e) Adjusted, C3-35, ACI  
(Continue in the next page)



(f) Adjusted, C3-35, Eurocode



(g) Adjusted, C3-50, ACI



(h) Adjusted, C3-50, Eurocode

**Figure 4-17 Original and adjusted creep compliance function: (a-b) original creep compliance function of C3-35 of ACI and Eurocode; (c-d) original creep compliance function of C3-50 of ACI and Eurocode; (e-f) adjusted creep compliance function of C3-35 of ACI and Eurocode; (g-h) adjusted creep compliance function of C3-50 of ACI and Eurocode;**

## 4.5 Conclusions

This chapter presents numerical modelling of the early-age stress evolution of restrained GGBFS concrete, considering the development of AD and creep. An FE model for simulating the stress development in TSTM tests was established by incorporating a self-defined material subroutine based on the Rate-type creep law. The creep compliance function was fitted with a 13-units continuous Kelvin chain, which was then inputted in the FEM to characterize the continuous relaxation. Using the creep compliance function proposed by the ACI code and Eurocode, forward modelling was performed to predict the stress development and evaluate the performance of codes. Finally, this study conducted inverse modelling with Bayesian Optimization to efficiently improve the settings of aging terms in the creep compliance functions of the two codes and shed light on the aging pattern of creep/ relaxation of GGBFS concrete. The major conclusions are as follows:

- (1) Using the 13-units continuous Kelvin chain, the creep compliance function can be fitted with good accuracy and incorporated in FE modelling by Rate-type Creep law. Using the creep compliance function recommended by the Eurocode and ACI code as input, the modelling and testing results showed good agreement after 200 hours.
- (2) Due to the arbitrary settings of constant aging terms in the formula of in the formulas of creep, both codes did not perform well in prediction of early-age stress development. The big gaps in early-age prediction result in significant errors in the stress calculations over the entire time-range.
- (3) The adjusted aging terms suggested that both Eurocode and ACI code significantly underestimate the early-age creep of GGBFS concrete. The results also indicated that GGBFS concrete with lower w/b ratios tend to cause faster aging of creep in first hours.
- (4) By Bayesian Optimization, inverse modelling was conducted to find the aging patterns of creep of GGBFS concrete. The modelling results with the adjusted aging terms show obvious improvement in the prediction of early-age stress development. However, Bayesian inverse modeling is a compromise to the difficulty of testing aging creep, despite its efficiency and accuracy, while future chapters will introduce a new testing setup for early monitoring of creep development.



# 5. DEVELOPMENT OF A MINI TEMPERATURE STRESS TESTING MACHINE

*Temperature stress testing machine (TSTM) is a universal testing tool for properties and behavior relevant to early-age cracking (EAC) of cementitious materials (see Chapter 3 and Chapter 4). However, the complexity of TSTMs requires heavy lab work and thus hinders a more thorough experimental study on EAC issues of a range of cementitious materials. This chapter presents the development and validation of a Mini-TSTM for efficiently testing the AD, viscoelastic properties, and their combined results, the early-age stress (EAS). The setup was validated through systematic tests of EAS, AD, elastic modulus, and creep. In addition, the heating/ cooling capability of the setup was examined by tests of coefficient of thermal expansion by temperature cycles. The results of EAS correspond well to that of AD, which qualitatively validates the developed setup. To quantitatively validate the setup, a classical viscoelastic model was built, based on the scenario of a 1-D uniaxial restraint test, to predict the EAS results with the tested AD, elastic modulus, and creep of the same cementitious material as the input. The predicted EAS matched the testing results of Mini-TSTM with good accuracy in six different cases. The testing and modelling results together validate the developed Mini-TSTM setup as an efficient tool for studying early-age cracking of cementitious materials.*

*Parts of this chapter have been submitted for publication in Liang, M., Chang, Z., Holthuisen, P., Chen, Y., He, S., Schlangen, E., & Šavija, B. (2023). Efficiently Assessing the Early-Age Cracking Risk of Cementitious Materials with A Mini Temperature Stress Testing Machine.*

## 5.1 Introduction

In view of the main concerns of the existing TSTMs as described in Chapter 2, a lighter and smaller version of TSTM – Mini-TSTM - that can be more efficiently implemented while maintaining good testing accuracy is presented in this chapter. The design of the Mini-TSTM and testing procedures for different early-age material behavior and properties is introduced in section 5.2. In sections 5.3 and 5.4, systematic validation tests are designed and conducted. Based on a viscoelastic model, the AD, elastic modulus, and creep compliance measured at different ages using the Mini-TSTM are used to calculate the EAS in different cases. The good match between the calculated EAS and that tested by the mini-TSTM directly validate the newly designed setup.

## 5.2 The Mini-TSTM

### 5.2.1 Setup design

The new Mini-TSTM should be simple and efficient. The overall design of the Mini-TSTM is shown in **Figure 5-1**. The total length of the specimen is 300 mm and the area of interest (i.e., the middle part of the specimen) is  $50 \times 50 \times 100 \text{ mm}^3$  (**Figure 5-1 (c)**), which is significantly smaller than that of the TSTMs described in Chapter 2. The small size of the Mini-TSTM enables direct installation of the setup into the Instron universal loading machine (see **Figure 5-1 (b)**), which is equipped with a load cell of 10 kN with an accuracy of 1 N. Therefore, the Mini-TSTM can be loaded vertically, which minimizes the influence of friction that can happen in horizontally loaded TSTMs (see Chapter 2). Note that the cross-section size of the specimen ( $50 \times 50 \text{ mm}^2$ ) will limit the maximum size of aggregate that can be used. However, this size is imposed by the utilized loading machine and can be increased if a more capable loading machine is available. The design of the AD testing machine (ADTM) is the same as the TSTM, except for the steel-made parts at two ends of the specimen. The test of AD by the Mini-ADTM is also conducted vertically, which reduces the influence of friction which may be present in the horizontal test. The design of Mini-TSTM/ ADTM is introduced in the following aspects: 1) Mold, 2) Strain measurement, 3) Temperature control, and 4) Assembly procedures.

#### 5.2.1.1 Mold

The mold of the Mini-TSTM is manufactured using Stereolithography (SLA) 3D printing with white powder-based polyamide (PA 2200), which is one

of the most versatile 3D printing materials with good strength, flexibility, and heat resistance. As shown in the middle of **Figure 5-1(a)**, the mold of the Mini-TSTM includes 3 covering plates (C1, C2, C3), 2 side plates (S1, S2), 2 crosshead plates (CH1, CH2), and 1 back plate (B1). In the Mini-TSTM, the plates CH1 and CH2 are made of steel, while in the Mini-ADTM the CH1 and CH2 are made by 3D printing with PA 2200. The assembly of all the plates is mainly by bolting. In each plate, except for CH1 and CH2, water channels were designed and the inner surface of the plates in contact with the specimen is sealed with a copper plate (see upper right of **Figure 5-1(a)**), which ensures good heat conduction and is therefore favorable for temperature regulation.

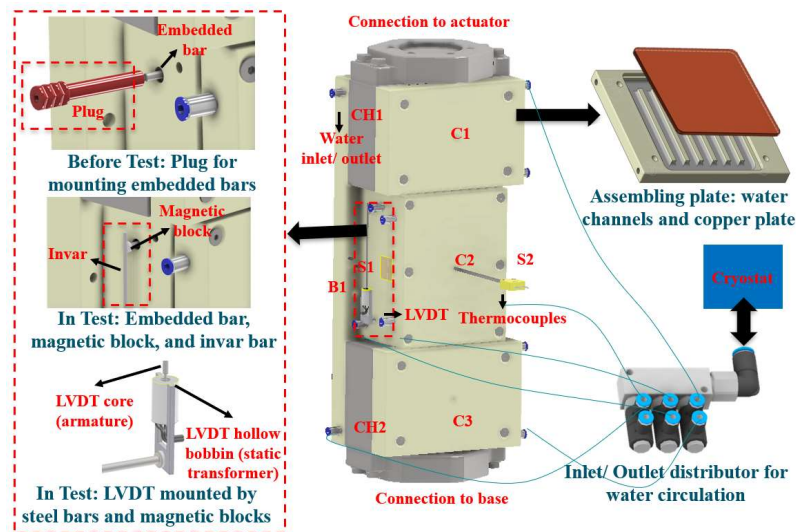
### 5.2.1.2 Strain measurement

The strain measurement of both the Mini-TSTM and the Mini-ADTM are done by embedded steel bars, plastic plugs, LVDTs, invar bars, and magnetic blocks. The embedded steel bar has a length of 13.3mm and diameter of 3mm. As shown in the left of **Figure 5-1(a)**, before casting the fresh mixture in the mold, the embedded bar should be fixed by plugs (shown in red). Afterwards, when the specimen is nearly hardened and the test is about to start, these plugs can be removed and the LVDTs can be attached to the embedded bars. The LVDT is an inductive displacement transducer that requires no contact during measurement. The LVDT is manufactured by Solartron Metrology and is composed of a hollow bobbin (static transformer) and a magnetic core (armature) (see the lower left of **Figure 5-1(a)**). As the core travels in the hollow bobbin, the voltage changes are related to the displacement. The measurement range of the adopted LVDT is  $\pm 1\text{mm}$  and the precision is  $0.01\ \mu\text{m}$ . The assembly of the strain measurement components can be seen in **Figure 5-1(c)**: first, the LVDT core should be glued to the lower side of the invar bar; then, with magnetic blocks as the connection, the upper side of the invar bar is attached to the upper embedded bar and the LVDT hollow bobbin is attached to the lower embedded bar. Thereby, the LVDT core can be set in the LVDT hollow bobbin to measure the deformation between the upper and lower embedded steel bars.

### 5.2.1.3 Temperature regulation

Temperature is regulated by circulating water in the plates C1, C2, C3, S1, S2, and B1. Each of these plates has water channels (**Figure 5-1(a) upper right**) and a water inlet/ outlet (**Figure 5-1(a) upper middle**). As shown in **Figure 5-1(d)**, a parallel connection is used to circulate the water around the specimen: heated/ cooled water is firstly pumped out from the cryostat

to the inlet distributor, transported to each of the plates, and then sent back to the cryostat via the outlet distributor. The plastic water tubes, tube joints, water inlet/outlet, and distributors were manufactured by FESTO with a diameter of 3mm and 8mm. The thermocouple has an exposed welded tip (0.2mm in diameter) and is produced by LABFACILITY with a measurement range of  $-75\sim 250$  °C and precision of 0.05 °C. Thermocouples are inserted into the middle of the specimen through the hole of plates C2 to measure the temperature inside the specimen. The temperature measured at plate C2, which is in the center of the specimen, is then set as the controlled objective of the temperature PID controller. Therefore, the water temperature of the cryostat can be continuously adjusted to ensure that the temperature at the center of the specimen follows the specified value.



(a) Overall design  
 (Continue in the next page)

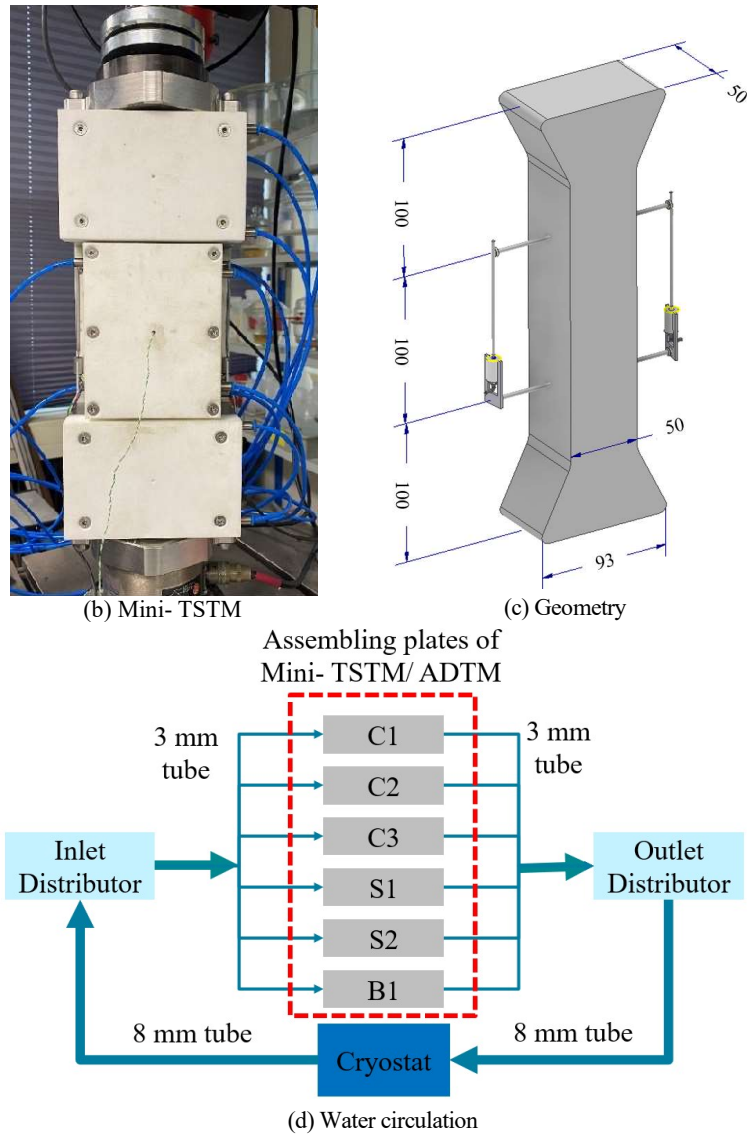


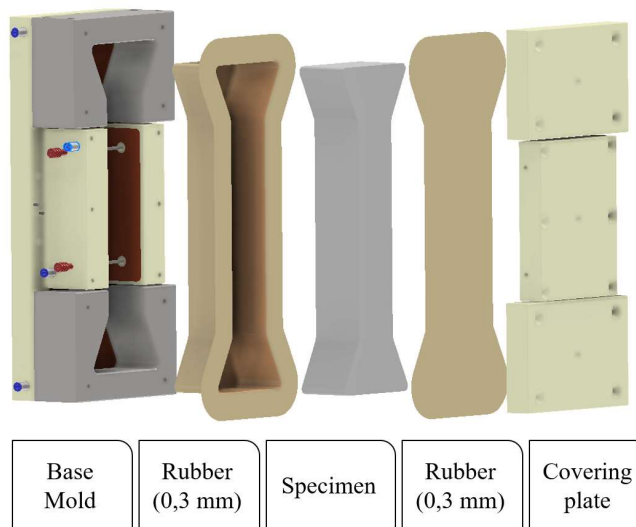
**Figure 5-1** The Mini-TSTM: (a) overall design; (b) the Mini-TSTM installed in the loading machine; (c) geometry of the dog-bone specimen (unit: mm); (d) parallel connection of water circulation system.

#### 5.2.1.4 Assembly procedure

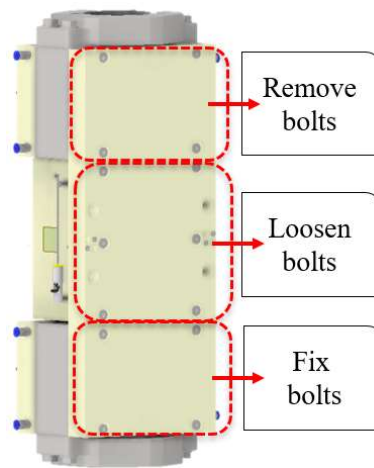
The assembly of the Mini-TSTM and Mini-ADTM is shown in [Figure 5-2](#). Before the test, the plates CH1, CH2, S1, S2, and B1 should be firstly assembled by bolting to form the base mold. A layer of thin rubber (or plastic sheet) is laid on the inner surface of the mold to prevent leaking of

the fresh material. Then, the two embedded bars should be fixed in position by the plugs. Afterwards, the specimen can be casted the base mold, and another layer of rubber/ plastic sheet is placed on top of the specimen. Then the plates C1, C2 and C3 are covered on top and fixed by bolts. Finally, the thermocouples are inserted into the fresh specimen and the water circulation systems are assembled by connecting all the water tubes and joints to control the temperature. Note that during the described procedure the specimen is still liquid and should be kept horizontally.

After a few hours (3-4 hours herein, corresponding to the initial setting time of adopted cements), the Mini-TSTM and Mini-ADTM can be put vertically. The Mini-ADTM is placed freely, while the Mini-TSTM is installed in the Instron loading machine. As shown in [Figure 5-2 \(b\)](#), the plugs are removed and the LVDTs should be set up for strain measurement as described in section 5.2.1.2. Moreover, during this step, the bolts connecting the plate CH1 to the plate B1 should be fully removed to ensure that the upper cross head of the specimen can move freely. The bolts connecting the plates S1, S2 to the plate B1 should be loosened to remove lateral restraint to the specimen brought by plates S1 and S2. Only the four bolts connecting the plate CH2 to B1 should be tightened to fully fix the bottom crosshead.



(a) assembly steps  
(Continue in the next page)



(b) Bolts removal

Figure 5-2 Assembly of Mini-TSTM and ADTM: (a) Assembly steps; (b) Bolts removal

### 5.2.2 Improvements

In view of the concerns of existing TSTMs discussed in Chapter 2, the Mini-TSTM results in the following improvements:

- 1) With the 3D printed plates, the mold of Mini-TSTM can be assembled and disassembled precisely and efficiently simply by bolting. The process of pre-test installation, casting, and post-test disassembling for the Mini-TSTM takes approximately 2 hours for a single operator. For each Mini-TSTM and ADTM test, the volume of fresh material needed is around 0.7 liters, which is significantly less than the existing TSTMs, which often needs over 60 liters for each test.
- 2) In the Mini-TSTM test, the full-restraint is achieved continuously by a PID controller. The PID controller takes the deformation measured by the LVDTs as input and continuously adjusts the applied force of the universal loading machine to fix the deformation at zero. Compared to the frequently used stepping control mode as introduced in chapter 2, the Mini-TSTM does not require an input of threshold value which could influence the test result.
- 3) The strain in the Mini-TSTM is measured by only two LVDTs, which is less than in most TSTMs. The LVDTs are positioned at the middle (i.e., straight) part of the specimen and therefore the influence of stress concentration near the two crossheads can be eliminated. Meanwhile, the LVDTs are arranged at the two sides of the specimen and therefore any eccentric deformation of the specimen can be detected. The connection of LVDTs by magnetic

- blocks makes the assembly of LVDTs easier and more efficient compared to existing TSTMs.
- 4) In the Mini-TSTM test, the specimen is loaded vertically. The specimen is detached from the covering plates by removing the upper bolts and loosening the middle bolts. Therefore, in principle, the influence of friction that may happen in most TSTMs is eliminated in the Mini-TSTM test.

### 5.3 Experimental methods and validation schemes

The validation of the Mini-TSTM and ADTM is conducted experimentally and theoretically. The experimental validation comprises the tests for EAS evolution, elastic modulus, aging creep, and AD, as shown in the left of **Figure 5-3**. Afterwards, the measured AD, elastic modulus, and aging creep compliance function will be used as input of a viscoelastic model to simulate the EAS evolution. Finally, the EAS evolution derived by the Mini-TSTM test, and the EAS evolution calculated by the viscoelastic model can be compared, as shown in the right of **Figure 5-3**.

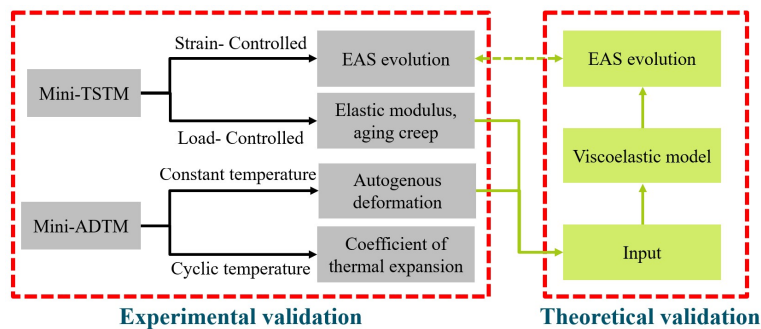


**Figure 5-3** Validation schemes for the Mini-TSTM and Mini-ADTM

#### 5.3.1 Experimental methods

##### 5.3.1.1 EAS test

To test the EAS evolution, the PID controller should be used to control the universal loading machine based on the input of LVDT, to fulfil the full-restraint condition as described in section 5.2.1.3. Besides, in this test, a constant temperature in the specimen is maintained (see section 5.2.1.3). Therefore, only the stress induced by AD is measured. The EAS evolution (measured by the Mini-TSTM) needs to be tested at the same time as the test of AD (measured by the Mini-ADTM).

### 5.3.1.2 Elastic modulus and aging creep test

The elastic modulus and aging creep are key parameters reflecting the viscoelastic properties of cementitious materials and directly determine how much stress can build up when the shrinkage is restrained. In this study, the elastic modulus and aging creep are key input parameters for the viscoelastic model to predict the EAS evolution, which can then be compared with the experimentally-measured EAS.

To test the elastic modulus and aging creep, an hourly-repeated load is applied to the sample. Assuming that the influence of aging within a time interval ranging from minutes to hours can be neglected, repeated load cycles were used to test the aging creep of cementitious materials at different ages [149,150]. In this study, the magnitude of the hourly-repeated load is determined by the TSTM test results, and the duration of each cycle is 1 hour. An example of the repeated load cycle for such a test is shown in **Figure 5-4**. The hourly-repeated loading cycles consist of a loading phase, sustained load phase, unloading phase, and phase of sustaining at a nearly zero load. The loading and unloading phases are short ( $t_0=30$  seconds in this study), allowing the elastic modulus at a certain age to be tested. Meanwhile, the loading speed ensures that the loading/unloading phase is shorter by two orders of magnitude compared to the creep test [149]. The duration of sustained load phase ( $t_c$ ) is 3600 seconds, allowing the creep compliance at a certain age to be tested. Aging creep needs to be tested at the same time as the test of AD test and using same batch of fresh material.

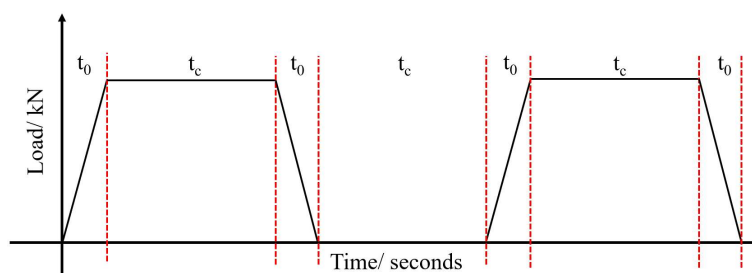


**Figure 5-4** Hourly repeated load for elastic modulus/ aging creep test ( $t_0$ : 30 seconds loading time for testing elastic modulus;  $t_c$ : 3600 seconds sustaining at a constant load for testing creep)

### 5.3.1.3 AD test

AD occurs due to cement hydration: self-desiccation induces internal capillary pressure and then the contraction of the microstructure [46,68,104,108,110]. The thermal deformation and drying deformation are the results of heat transport and moisture transport and therefore depend

on the material properties, the structural geometry and environmental conditions [70,298,299]. In comparison, AD is an intrinsic material behaviour and the EAC issues it may induce are the main focus in this study. In the theoretical validation part, the measured AD will be used as input, together with the elastic modulus and aging creep, to predict the EAS results and compare with the EAS tested by Mini-TSTM. To test the AD, the Mini-ADTM is used. In this test, the Mini-ADTM just stands vertically and the temperature in the specimen is controlled at a constant value based on the temperature regulation system (see section 5.2.1.3). Therefore, thermal and drying deformation are excluded, and only the AD is measured.

#### 5.3.1.4 Coefficient of thermal expansion (CTE)

The test of CTE is performed to validate the following two aspects: 1) the reasonability of the measured evolution process of CTE; 2) the heating/cooling efficiency of the designed Mini-TSTM and ADTM systems, which will be shown by a fast heating/cooling temperature profile with a rate of 5°C/hour.

To test the CTE, the Mini-ADTM test is conducted under a cyclic temperature profile. An example of such temperature cycle is shown in **Figure 5-5**. Under such temperature cycles, the total deformation measured by the ADTM is the sum of AD and thermal deformation. It is assumed that the effects of aging can be neglected and the AD is constant (i.e.,  $\varepsilon_{au,h} = \varepsilon_{au,c}$  in **Figure 5-5 (b)**, where  $\varepsilon_{au,h}$  and  $\varepsilon_{au,c}$  stands for the AD during subsequent heating and cooling phase) within each temperature cycle which lasts for  $2t_r$ ). Assuming that the coefficient of thermal contraction (CTC) is the same as the CTE [27], the total deformation within the heating phase of each temperature cycle can be calculated as:

$$\varepsilon_{toh} = CTE \times \Delta T_h + \varepsilon_{au} \quad (5-1)$$

In the subsequent cooling phase, the total deformation can be calculated as:

$$\varepsilon_{toc} = CTC \times \Delta T_c + \varepsilon_{au} \quad (5-2)$$

where  $\varepsilon_{au}$  is the autogenous shrinkage in the heating/cooling phase;  $\Delta T_h$  and  $\Delta T_c$  are the temperature change in the heating and cooling phase, respectively;  $\varepsilon_{toh}$  and  $\varepsilon_{toc}$  are the total strains that happen in the heating and cooling phases, respectively. By calculating Eq (5-1)–Eq (5-2), one can calculate the CTE as follows:

$$CTE = \frac{\varepsilon_{toh} - \varepsilon_{toc}}{\Delta T_h - \Delta T_c} \quad (5-3)$$

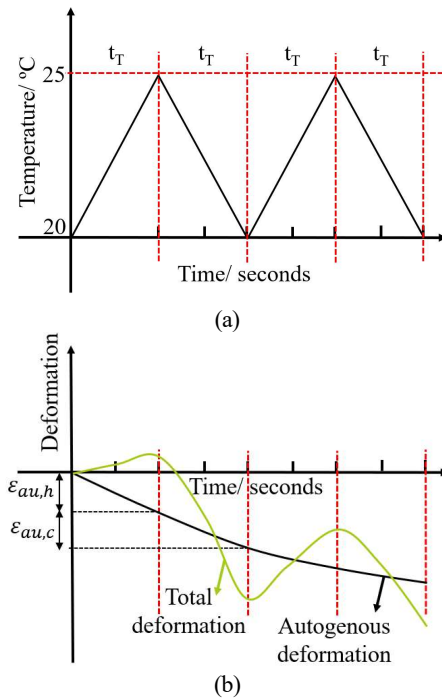


Figure 5-5 Examples of a CTE test: (a) Temperature cycles; (b) Deformation

### 5.3.2 Detailed validation schemes

The validation of the Mini-TSTM is conducted by the tests described in section 5.3.1 based on cement paste made of two types of cement, CEM I 42.5N and CEM III/B 42.5N. Both cements were manufactured by the ENCI, Netherlands and the compositions have been shown in chapter 3.0. A detailed experimental validation scheme of the Mini-TSTM is listed in [Table 5-1](#). The materials are labeled to show the difference in cement types and w/b ratios. For example, “C1-30” stands for the material that uses CEM I and a w/b ratio of 0.30. In this study, it was found that even for the same type of cement, some testing results (i.e., initial deformation and autogenous expansion) can vary significantly if different batches of cement are used (see section 5.4). For the tests using CEM I paste, different batches of cement were used in different tests. For the cement type CEM III/B, two batches of cement were used: the C3-30 and C3-35 were from the first batch of CEM III/B, while the C3-30A was from the second batch. It should be stressed that this study aims to validate the proposed Mini-TSTM and Mini-ADTM setup. Therefore, while the variability of material behavior of the same type of cement can be detected by the proposed setup, the

mechanisms behind this variability are outside of the scope of the current study.

In tests 1~6, both the Mini-ADTM and Mini-TSTM were performed at a constant temperature of 20 °C. In test 7, only the Mini-ADTM test was performed, and a cyclic temperature profile was used. In tests 1 and 2, the repeatability of the tests was examined. In test 1, both passive (C1-30-P1 and C1-30-P2) and active (C1-30-A1) temperature control methods were used. The active temperature control method has been described in the section 5.2.1, where a PID controller will be used to actively adjust the water temperature to fix the temperature measured in the center of the specimen at a constant value (i.e., 20 °C). In comparison, the passive temperature control method is also used, which directly set the water temperature as the desired value (i.e., 20 °C).

**Table 5-1 Details of the testing schemes for validation of Mini-TSTM**

Test	Material	Testing conditions	Objectives	Repetition
1	C1-30	LVDT- controlled full restraint Active/ passive temperature control	EAS	C1-30-P1 C1-30-P2 C1-30-A1
2	C3-30	LVDT-controlled full restraint Active temperature control	EAS	C3-30-1 C3-30-2 C3-30A
3	C3-35	LVDT-controlled full restraint Active temperature control	EAS W/b influence	No
4	C3-30A	LVDT-controlled full restraint Active temperature control	EAS	No
5	C1-30	Load-controlled Active temperature control	Elastic modulus Aging creep	No
6	C3-30A	Load-controlled Active temperature control	Elastic modulus Aging creep	No
7	C3-30A	Free deformation Active cyclic temperature control	CTE Heating/ cooling	No

### 5.3.3 Viscoelastic model

The stress buildup in a restrained cementitious material can be calculated by viscoelastic models, as shown in numerous studies [4,238,300,301]. In the Mini-TSTM test, the strain measurements are performed in the middle (i.e., straight) part of the dog-bone specimen, where stress should be evenly distributed because this part is far away from the cross-head (see section 5.2.1.2). Therefore, a 1-D model should be able to describe the stress buildup in the Mini-TSTM test. Considering cement paste as a viscoelastic material, the stress buildup in the Mini-TSTM test corresponds to a relaxation process, which can be calculated by the principle of Boltzmann superposition described as the convolution below:

$$\sigma(t) = \int_0^t R(t, t_0) \dot{\varepsilon}(t_0) dt_0 \quad (5-4)$$

where  $\sigma$  is the stress buildup calculated by the viscoelastic model;  $\varepsilon$  is the restrained strain;  $R$  is the relaxation modulus (GPa);  $t_0$  is the time when deformation is restrained;  $t$  is the current time. By using the mid-point rule, the integration of Eq (5-4) can be simplified as:

$$\sigma(t) = \sum_{t_0=0}^{t_0=t} R\left(t + \frac{1}{2} \Delta t, t_0\right) \times \Delta \varepsilon(t_0) \times \Delta t_0 \quad (5-5)$$

The relaxation modulus can be derived from the creep compliance, which is easier to test. The creep compliance can be described by the double power law [111,193] as:

$$J(t, t_0) = \frac{1}{E(t_0)} + a * \left(\frac{1}{t_0}\right)^b * (t - t_0)^c \quad (5-6)$$

where  $a$ ,  $b$  and  $c$  are fitting parameters that can be derived from tests, which reflect the impact of mix design, aging time and loading duration on creep evolution. Then, the relaxation modulus can be derived as follows [237,250,251]:

$$R(t, t_0) = e^{1-J(t,t_0)E(t)} E(t) \quad (5-7)$$

In comparison, a 1D elastic model is also used, which can be described as below:

$$\sigma_{el}(t) = \int_0^t E(t) \dot{\varepsilon}(t_0) dt_0 \quad (5-8)$$

where  $\sigma_{el}$  is the stress buildup if the relaxation effect is neglected. Similarly, by the midpoint rule, Eq (5-8) can be simplified as:

$$\sigma_{el}(t) = \sum_0^t E(t + \frac{1}{2}\Delta t) \times \Delta\varepsilon(t) \times \Delta t \quad (5-9)$$

Based on the simple viscoelastic model in Eq ((5-4)-(5-7)) or elastic model in Eq ((5-8)-(5-9)), using the AD measured in tests 1-4, and the elastic modulus and aging creep measured in tests 5-6, the EAS can be calculated and then compared with the EAS measured in tests 1-4.

## 5.4 Results and discussion

### 5.4.1 EAS test

The EAS induced by AD, which is the most direct and important index for assessing early-age cracking potential, can be tested by applying a full-restraint boundary condition. In this test, the temperature in the specimen is controlled at 20 °C to exclude the influence of thermal deformation.

#### 5.4.1.1 EAS results of CEM I paste

Two temperature control methods were used in the EAS test for CEM I: passive control (C1-30-P1 and C1-30-P2) and active control (C1-30-A1). C1-30-P1 and C1-30-P2 are two repetitive tests with the same w/b ratio. As shown in **Figure 5-6**, taking the C1-30-P1 as an example, passive control (see **Figure 5-6 (a)**) works by keeping the temperature of the water at the target value (20 °C); on the other hand, active control (see **Figure 5-6 (b)**) takes feedback from the measurement of thermocouples embedded in the specimens (see section 5.2.1.3) and actively adjusts the water temperature to maintain the temperature measured by thermocouples (embedded in the specimen) at a fixed value (20 °C). The temperature results show that active control method can perfectly keep the temperature of the specimen at 20 °C (blue line in **Figure 5-6 (b)**) by more cooling within the first day (orange line in **Figure 5-6 (b)**) to compensate for the hydration heat and room temperature. In comparison, the passive control shows only a limited effect: the temperature in the specimen increased to 21.5 °C due to hydration heat release, and then slowly decreased to 20.5 °C. Overall, to strictly exclude the influence of temperature and ensure that only the AD is considered, active control method is preferred.

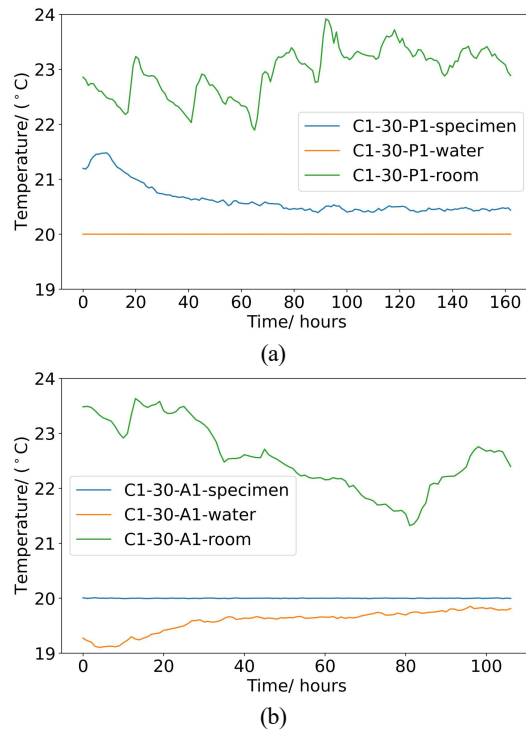


**Figure 5-6 Temperature measurement in EAS test for CEM I paste: (a) Passive control; (b) Active control**

The deformation in the specimen in the Mini-TSTM can be controlled within 1  $\mu\text{strain}$  (0.1  $\mu\text{m}$ ) with the PID controller which takes the strain measured by the LVDTs (see section 5.2.1.2) as feedback to continuously adjust the applied load. As shown in [Figure 5-7](#). In other words, the full-restraint condition in the Mini-TSTM is achieved with a precision of 1  $\mu\text{strain}$ .

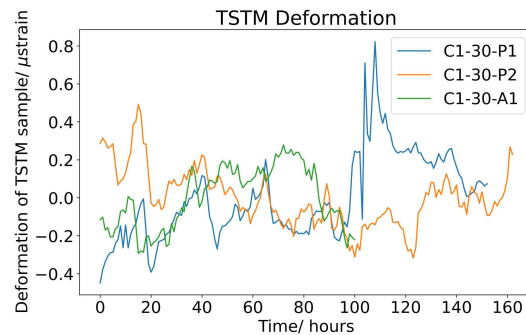


**Figure 5-7 Mini-TSTM deformation under full-restraint condition**

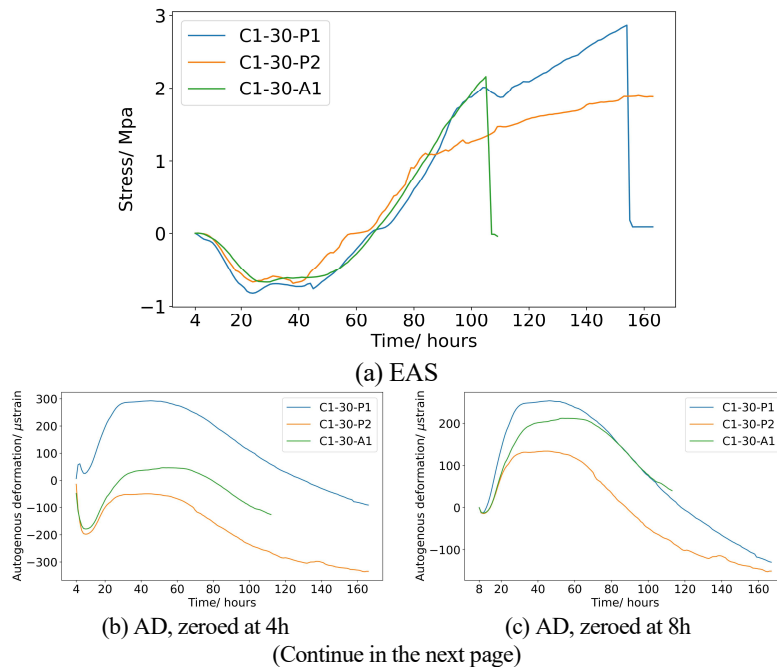
The testing results of Mini-TSTM and ADTM for the CEM I paste with the w/b ratio 0.30 are shown in **Figure 5-8**. In the three CEM I tests (C1-30-P1, C1-30-P2, and C1-30-A1), different batches of cement were used. The EAS (**Figure 5-8 (a)**) and the corresponding AD (**Figure 5-8 (b)**) were recorded 4 hours after the placement of fresh cement. AD is often characterized by a fast chemical shrinkage in the first few hours followed by autogenous expansion and autogenous shrinkage. For the three CEM I tests, the AD was zeroed at the onset of autogenous expansion (i.e., 8 hours as in **Figure 5-8 (c)**) and the onset of autogenous shrinkage (i.e., 30 hours as in **Figure 5-8 (d)**). Based on the measured EAS (**Figure 5-8 (a)**) and AD (**Figure 5-8 (b-g)**), the following results in different tests validates the reasonability of the measurement:

- 1) The expanding/ shrinking process measured in the Mini-ADTM (**Figure 5-8 (b-d)**) corresponds to the stress decreasing (compression)/ increasing (tension) measured in the Mini-TSTM (**Figure 5-8 (a)**).
- 2) The EAS of the three tests shows a similar trend (**Figure 5-8 (a)**), with compression in first 60 hours and tension afterwards. However, the exact timing of cracking is different: The C1-30-A1 cracked after around 100 hours, while the C1-30-P1 cracked later, after 150 hours. In the test for C1-30-P1, the loading machine of the Mini-TSTM stopped working for an hour at around 100 hours, and therefore at that period, a drop of the load was observed, which stopped the specimen from cracking. The C1-30-P2 did not crack after 160 hours.
- 3) The rate of AD of the three tests is similar (**Figure 5-8 (e-g)**). All tests for autogenous shrinkage after 30 hours (**Figure 5-8 (d)**) displayed good consistency and similar magnitude. Note that the rate of AD is more relevant than the absolute value since it directly determines the accumulation of stress (see Eq (5-4)).

Despite the consistency described above, significant variation in the absolute values of AD is found between the three tests, especially for the initial deformation in the first 4-8 hours (**Figure 5-8 (b)**) and autogenous expansion between 8-30 hours (**Figure 5-8 (c)**). This variation is caused by using different batches of cement and also slight difference of operation during the tests, which may induce high scatter in the measurement of the initial deformation, as pointed out by a systematic statistical study [16]. However, due to a very low elastic modulus and high creep/ relaxation, the very high initial deformation only induces a very low stress and therefore such variation does not influence the EAS measurement, as quantitatively proved by the viscoelastic model in section 5.3.3. Specifically, according to the EAS result (**Figure 5-8 (a)**), the measured stress at 4 hours was 0.02,

0.04, and 0.03 MPa for the three tests C1-30-P1, C1-30-P2, and C1-30-A1, respectively. Therefore, the initial deformation at 4-8 hours seems to be insignificant for the EAS buildup. Similarly, in the autogenous expansion phase at 8-30 hours, the differences in compressive EAS (**Figure 5-8 (a)**) are much less significant than that in the autogenous expansion (**Figure 5-8 (c)**). This can also be explained by the low elastic modulus and high creep/relaxation of the cement paste in the first day.

In Chapter 3, it was found that the autogenous expansion at 8-30 hours is caused by the ettringite formation, which applies pressure on pore walls and leads to macroscopic expansion. In this process, the amount of ettringite determines the internal pressure, and the micromechanical properties (i.e., elastic modulus and creep) determine how much expansion can be obtained given a certain pressure [68,108]. Although significant difference in initial deformation and autogenous expansion is measured, the EAS development in the different tests is similar (**Figure 5-8 (a)**). This will be further quantitatively explained in section 5.4.5, where EAS measurement will be presented by a verified viscoelastic model.



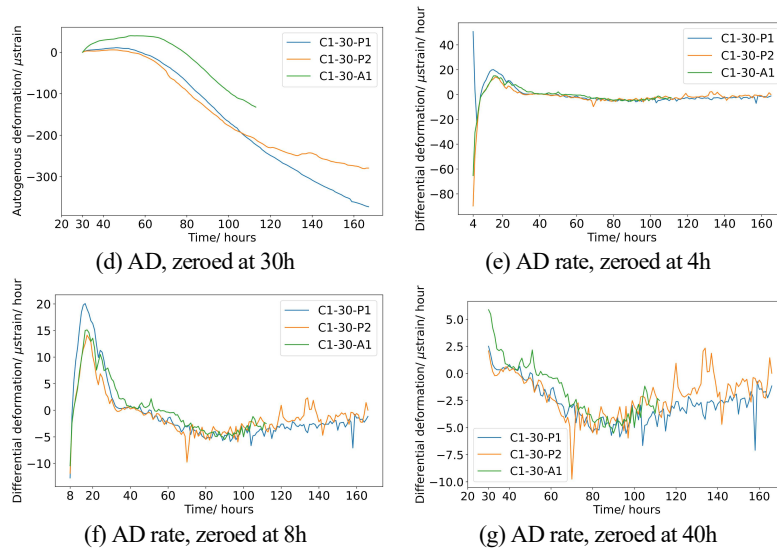


**Figure 5-8** Testing results of CEM I paste with  $w/b = 0.30$ : (a) EAS; (b-d) AD zeroed at 4, 8, and 30 hours; (e-g) AD rate zeroed at 4, 8 and 30 hours.

#### 5.4.1.2 EAS results of CEM III/B paste

Development of EAS was tested in paste specimens with two  $w/b$  ratios (0.3 and 0.35) with CEM III/B. Two batches of cement were used, with the first batch of cement in tests C3-30-1, C3-30-2, and C3-35, and the second batch of cement in the test C3-30A. The tests C3-30-1 and C3-30-2 were to check the repeatability of the Mini-ADTM and Mini-TSTM tests. The EAS results of the CEM III/B pastes are shown in [Figure 5-9](#). The EAS results on CEM III/B show the following results for validating the reasonability of the Mini-TSTM and Mini-ADTM setup:

- 1) In all four tests, the expanding/shrinking process as measured by the Mini-ADTM ([Figure 5-9 \(b\)](#)) corresponds well to the stress decreasing (compression)/ increasing (tension) as measured by the Mini-TSTM ([Figure 5-9 \(a\)](#)).
- 2) An excellent agreement in EAS results ([Figure 5-9 \(a\)](#)) and rate of AD ([Figure 5-9 \(e\)](#)) was found in the two repetitive tests C3-30-1 and C3-30-2.
- 3) In the expansion phase, C3-30-1 shows a slightly higher expansion than C3-30-2. This is also reflected in the EAS result - a slightly higher compressive stress develops in C3-30-1. As also observed in the EAS results of CEM I ([Figure 5-8 \(a\)](#)), the difference in autogenous expansion is much more significant than that in EAS, which is caused by the low elastic modulus and high relaxation/creep which limit the compressive stress induced by this

- restrained expansion.
- 4) The C3-35 shows higher expansion and lower shrinkage compared to C3-30 (see **Figure 5-9 (b, c)**). This difference is expected: with a higher w/b ratio, more ettringite will be produced, reducing higher expansion (see chapter 3). Furthermore, a slower drop of relative humidity and larger pore sizes will occur in specimens with higher w/b ratio [46,108], resulting in lower internal capillary pressure (according to Kelvin's equation) and therefore easing the contraction induced to the microstructure. As a result, the autogenous shrinkage for a higher w/b ratio should be lower (see **Figure 5-9 (d)**). However, it should also be noted that even with higher autogenous expansion, the compressive stress in C3-35 is lower than that in C3-30. This is attributed to the lower elastic modulus and higher relaxation/creep of a higher w/b ratio paste according to chapter 3 and 4.
  - 5) The consistent measurement of the AD and the EAS in the C3-30 and C3-30A tests shows that different batches of CEM III/B at the w/b ratio 0.30 can lead to different EAC potentials. Note that such difference in AD measurement was also observed in the creep test and CTE test shown later. The difference between different batches of CEM III/B paste are discussed as below:
    - i. The C3-30A shows higher initial shrinkage, almost no autogenous expansion, and much earlier and faster autogenous shrinkage afterwards, as measured by the Mini-ADTM (**Figure 5-9 (b, c)**). Accordingly, C3-30A obtained higher initial tensile stress in chemical shrinkage phase (first 10 hours in **Figure 5-9 (b)**), almost no compressive stress, and much earlier tensile stress accumulation in the autogenous shrinkage phase starting from around 24 hours (**Figure 5-9 (b)**).
    - ii. In comparison, the C3-30 tests showed very low initial tensile stress at first 20 hours (**Figure 5-9 (a)**) and remained in compression in 20-52 hours (**Figure 5-9 (a)**). Such significant difference clearly exposed the C3-30A to a higher risk of EAC and therefore the influence of batch difference of CEM III/B mix with a low w/b ratio on early-age AD should be an essential issue for cracking-sensitive structures.
  - 6) The cracking time of C3-30A, C3-30, C3-35, and C1-30 is around 45, 58, 68, and 100 hours, respectively. This is consistent with previous studies reporting that GGBFS concrete with a low w/b ratio shows higher risk of EAC due to autogenous shrinkage compared to OPC concrete [10,58,225].

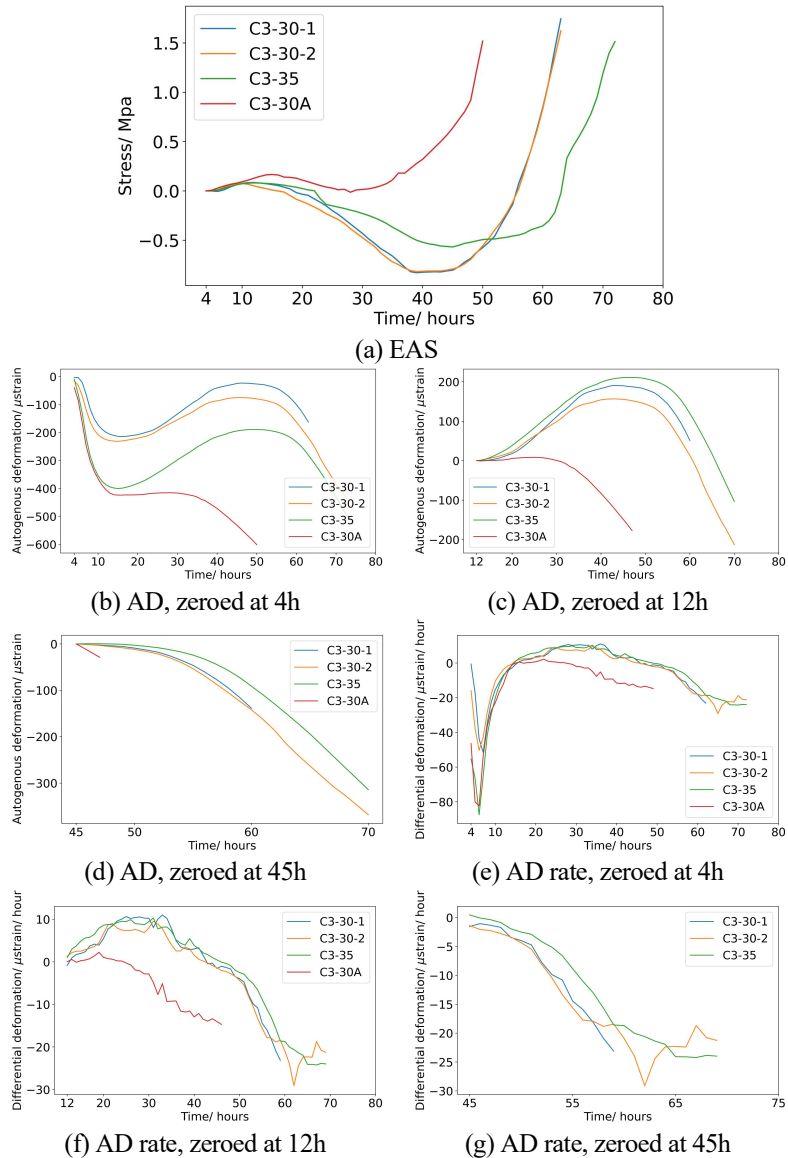
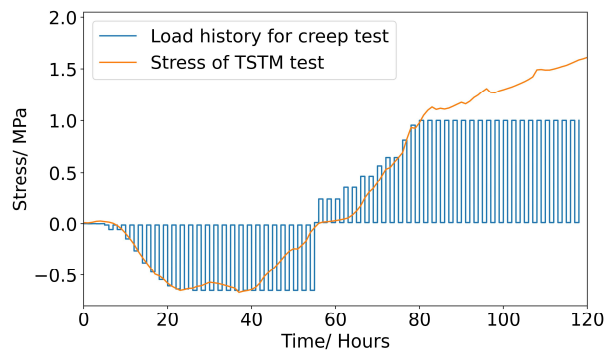


**Figure 5-9** Testing results of CEM III/B paste with  $w/b = 0.30$ : (a) EAS; (b-d) AD zeroed at 4, 12, and 45 hours; (e-g) First derivative of AD zeroed at 4, 12 and 45 hours.

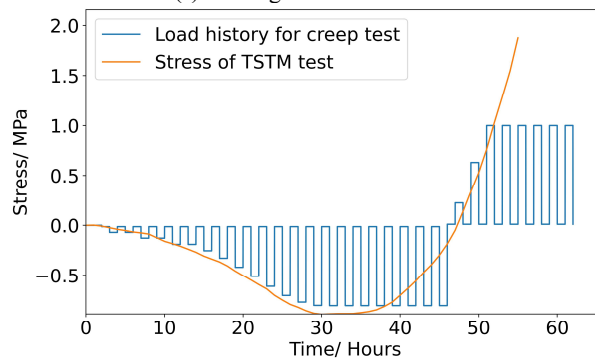
#### 5.4.2 Measurement of elastic modulus and aging creep

The time-dependent elastic modulus and creep of C1-30 and C3-30A paste were tested following the hourly-repeated loading method introduced in section 5.3.1.2. In this test, the Mini-ADTM and Mini-TSTM were both used:

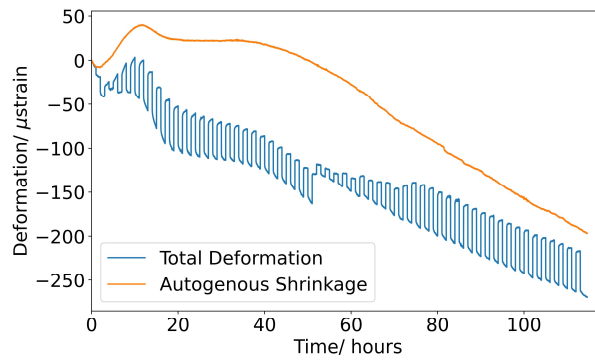
Mini-ADTM to measure AD, and the Mini-TSTM to measure the elastic modulus and creep at different ages. The hourly-repeated loading scheme for C1-30 and C3-30A paste with a w/b ratio of 0.30 is shown in **Figure 5-10**. To ensure that the applied load does not exceed the strength of the material and induce damage, the loading scheme was designed according to the EAS results of C1-30-P2 and C3-30-2 and the maximum tensile load was set to 2.5kN. Accordingly, the AD tested by Mini-ADTM and the total deformation tested by Mini-TSTM is shown in **Figure 5-10 (c-d)**. The test started at 10 and 14 hours and lasted for around 117 and 60 hours for C1-30 and C3-30A pastes, respectively. Note that the total deformation measured here includes AD induced by hydration and basic creep strain induced by the sustained load.



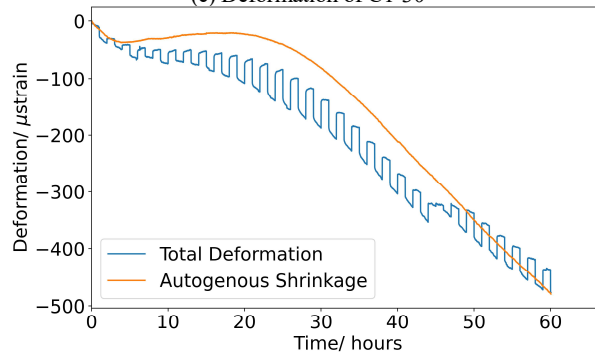
(a) Loading scheme of C1-30



(b) Loading scheme of C3-30A  
(Continue in the next page)



(c) Deformation of C1-30



(d) Deformation of C3-30A

**Figure 5-10** Testing results for elastic modulus and creep of CEM I w/b = 0.30: (a-b) Hourly-repeated loading scheme for C1-30 and C3-30A, respectively; (c-d) Deformation results of the test for C1-30 and C3-30A, respectively.

The total deformation and stress at every loading and unloading period were extracted to calculate the elastic modulus at different ages using linear regression [28]. Examples of testing results and the calculation are given in [Figure 5-11 \(a-h\)](#). Finally, the evolution of elastic modulus of C1-30 and C3-30A with time can be obtained, as shown in [Figure 5-11 \(i\)](#). At around 46 and 55 hours, the elastic modulus- time curve of C1-30 and C3-30A showed an upward jump and then decreased. The jump and the decreasing trend may be attributed to the transition from compression to tension and the sudden decrease in load level. Afterwards, the load gradually increased from 0.75 kN to 2.5 kN (i.e., 0.3 and 1 MPa, respectively). Note that the deformation may be small when very low tensile load is applied (i.e., 0.3 MPa) resulting in a measurement error. With higher tensile load, the deformation will be larger, resulting in higher measurement accuracy. However, the increasing tensile load may also induce internal damage to the specimen and therefore result in the decrease of elastic modulus. Note that to understand the influence of load

(including level, compression/ tension, loading/ unloading) on the testing results of elastic modulus, a more refined testing scheme should be devised to exclude the influence of age, which is beyond the scope of the current study.

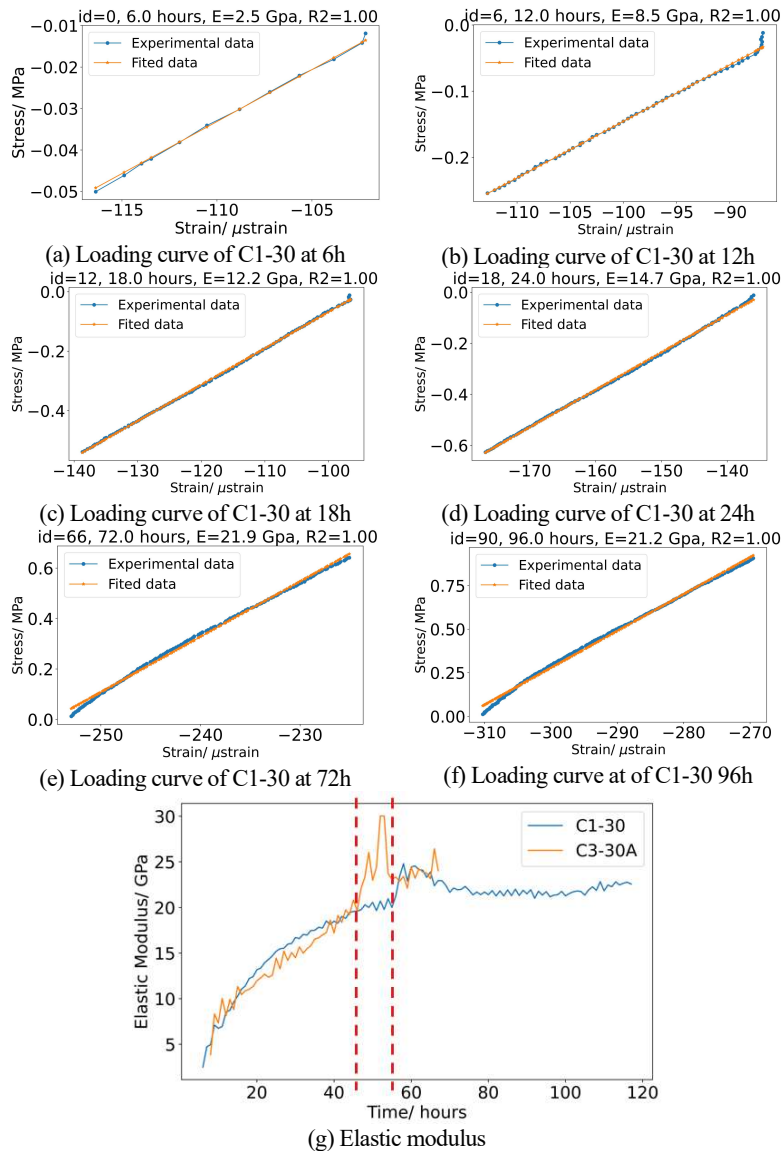
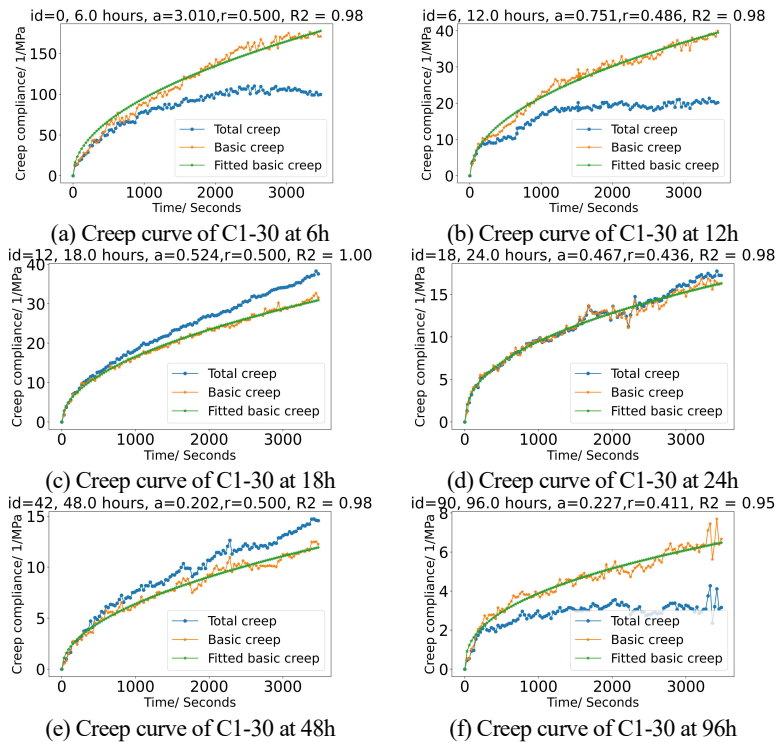
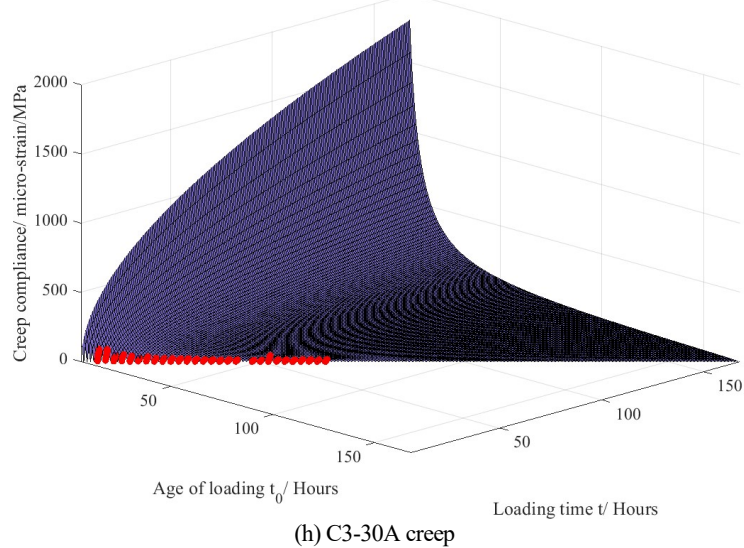
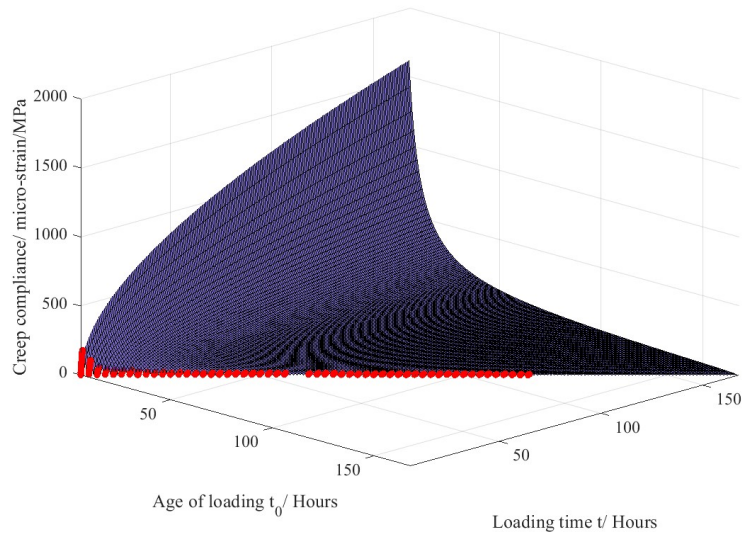


Figure 5-11 Testing results for evolution of elastic modulus: (a-g) elastic modulus of C1-30 paste tested and calculated at 6, 12, 18, 24, 48, and 96 hours; (i) summary of elastic modulus of C1-30 and C3-30A

The total deformation measured by Mini-TSTM and the AD measured by Mini-ADTM at every hour were extracted to calculate the creep at different ages. The basic creep compliance is calculated by deducting the AD from the total deformation and normalized by the corresponding sustained load level. As an example, the results of creep of C1-30 paste at different ages are shown in **Figure 5-12**. To check the reasonability of the basic creep compliance results, all the basic creep curves were fitted to a non-aging power function ( $J(t)=a \times t^r$ ) [111,277]. The quality of fitting was quantified by a coefficient of determination  $R^2$  between the fitted and experimental values of creep compliance. A  $R^2$  of 1 means a perfect fit is obtained and a  $R^2$  lower than 0.70 were considered as incorrect testing data and removed. Finally, the basic creep data collected every two hours were used to fit the aging creep function  $J(t, t_0)$  as expressed in Eq (5-6) and the creep surface was obtained **Figure 5-12**, which was used as input in the viscoelastic model. The fitting parameters for the creep compliance function  $J(t_0, t)$  and corresponding coefficients of determination are shown in **Table 5-2**. The final aging creep surfaces of the two tested materials are in **Figure 5-12 (i-j)**, where the red dots indicate the experimental values of fitted surface based on Eq (5-6).



(Continue in the next page)



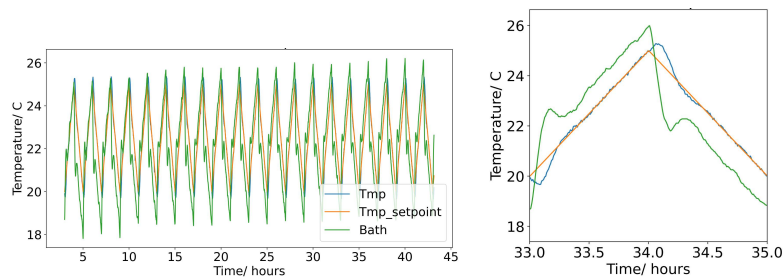
**Figure 5-12** Testing results for evolution of creep compliance: (a-f) creep compliance of C1-30 paste tested at 6, 12, 18, 24, 48, 72, 96 and 116 hours; (g-h) summary of creep compliance of C1-30 and C3-30A.

**Table 5-2** Fitting parameters obtained from creep test for creep function

Specimens	a	b	c	R <sup>2</sup>
C1-30	$1.000 \times 10^5$	1.079	0.500	0.8674
C3-30A	$3.622 \times 10^5$	1.197	0.500	0.8655

### 5.4.3 CTE test

Based on the methods introduced in section 5.3.1.4, the CTE of the C3-30A paste was measured with aims to: 1) provide a method for measuring CTE and 2) validate the temperature control ability of the proposed setup. The CTE test was performed on C3-30A using the Mini-ADTM, started 7.5 hours and lasted for around 44 hours. The results are shown in **Figure 5-13**. Temperature cycles varying between 20 and 25 °C in every two hours were adopted, as specified by the “Tmp\_setpoint” curve in **Figure 5-13 (a-b)**. The temperature results here also show the heating/ cooling efficiency of the setup: To follow the specified temperature curves (i.e., “Tmp\_setpoint” curve), at every turning point, the cryostat heated/ cooled the water bath (i.e., “Bath” curve) to regulate the temperature of the specimen (i.e., “Tmp” curve) based on the PID controller, as mentioned in section 5.2.1.3. As clearly shown in **Figure 5-13 (b)**, when reaching the turning point, it took about 10 minutes for the cryostat to adjust the temperature of the water bath to adapt to the new heating/ cooling curve, and therefore there was always an overshooting observed in the specimen temperature. Afterwards, the specimen temperature can be precisely regulated to follow the specified temperature curve. With the temperature cycles, the total deformation is a superposition of continuous AD and cyclic thermal deformation, as shown in **Figure 5-13 (c)**. Assuming that within every two hours the rate of AD stays the same, the influence of AD can be eliminated by taking the average of deformation measured in the heating and cooling phase, as shown in **Figure 5-13 (d)** and explained by Eq ((5-1)-(5-3)). The CTE of each temperature cycle was calculated using linear regression [277] and the evolution of CTE is shown in **Figure 5-13 (e)**. An increase in CET was observed from around 6.6 to 14.4  $\mu\text{strain}/^\circ\text{C}$  on the first and second day, which is in accordance with the literature [28,234].



(a) Temperature

(b) Temperature 33-35h

(Continue in the next page)

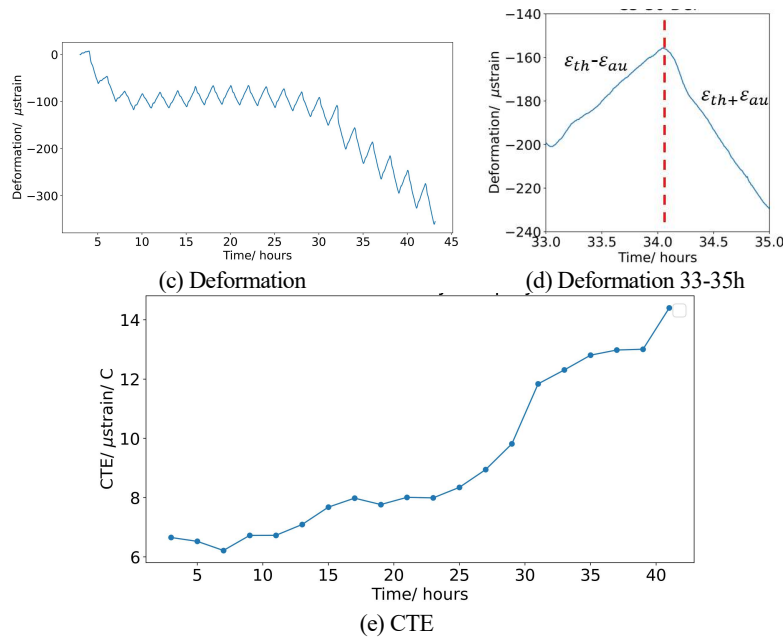


**Figure 5-13** Testing results for evolution of CTE of C3-30A paste: (a-b) temperature history; (c-d) total deformation; (e) CTE

#### 5.4.4 Modelling results

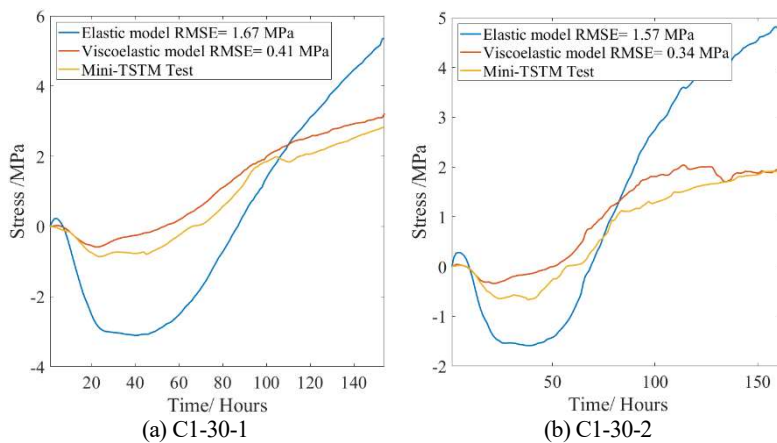
Based on the AD measured from 4 hours after casting (section 5.4.1), the elastic modulus, and the aging creep (section 5.4.2), the EAS can be predicted using the viscoelastic models proposed in section 5.3.3. Specifically, the AD s measured from 4 hours after casting in tests C1-30-P1, C1-30-P2, C1-30-A1, C3-30-1, C3-30-2, and C3-30A were used as input to calculate the EAS in the corresponding tests. For the input of elastic modulus and aging creep, the test performed on C1-30 and C3-30A were used for CEM I (i.e., C1-30-P1, C1-30-P2, C1-30-A1) and CEM III/B (i.e., C3-30-1, C3-30-2, and C3-30A) paste, respectively. The modeling results of EAS and comparison to the experimental results are shown in [Figure 5-14](#). The root mean square error (RMSE) between the modeling and experimental results of EAS were calculated to show the precision obtained by the models:

$$RMSE = \sqrt{\frac{\sum_t (\sigma_M(t) - \sigma_T(t))^2}{t_{total}}} \quad (5-10)$$

where  $\sigma_M(t)$  and  $\sigma_T(t)$  are modelling and testing results of EAS at time step  $t$ , respectively. The results in [Figure 5-14](#) show a good match between the

EAS calculated by the viscoelastic model and the results obtained directly from the EAS test. As expected, the influence of creep/relaxation must be considered in the EAS calculation and therefore an elastic model is not acceptable for the prediction of EAS.

Despite the significant differences in the measured initial shrinkage and autogenous expansion of C1-30-1, C1-30-2, and C1-30-3 (presumably caused by using different batches of cement), the calculated EAS results for all three tests are similar to the testing results. In the CEM III/B tests, although with a completely different AD and EAS between the batch 1 (i.e., C3-30-1 and C3-30-2) and batch 2 (i.e., C3-30A), their EAS can still be predicted with good accuracy given the corresponding AD as input. What is more interesting is that only using the elastic modulus and creep tested on C3-30A as input, the EAS results of C3-30-1 and C3-30-2, which are of different batches of cement and show different AD, can still be predicted with good accuracy. This means that the batch difference of CEM III/B does not result in a significant difference in mechanical properties (i.e., elastic modulus and creep in this case). In conclusion, the good match between the modeling and the experimental results directly validates that the devised Mini-TSTM and ADTM setup can detect the true material behavior and properties with good accuracy.



(Continue in the next page)

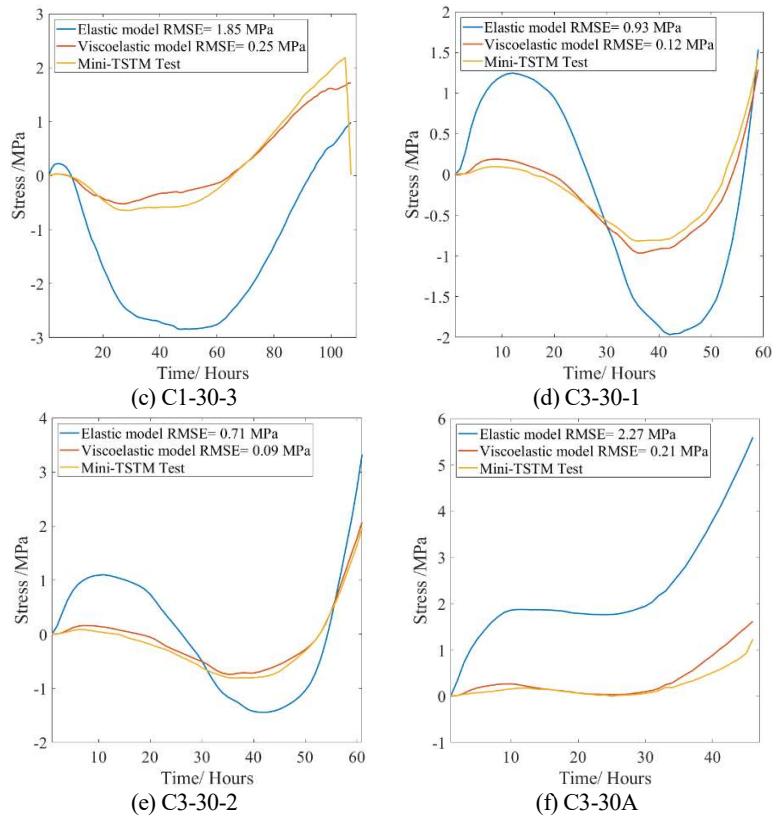


**Figure 5-14 Modelling results and comparison to EAS test: (a-c) results of CEM I paste C1-30-1, C1-30-2 and C1-30-3, respectively; (d-f) results of CEM III/B paste C3-30-1, C3-30-2, and C3-30A, respectively;**

#### 5.4.5 Variation analysis

To explain why such a significant variation in early chemical shrinkage and autogenous expansion causes only a small difference in EAS, as shown in section 5.4.1, more detailed quantitative explanations are given from two aspects: 1) a sensitivity study and 2) the principle of stress superposition.

##### 5.4.5.1 Sensitivity study

Taking the EAS and AD of C1-30 (see Figure 5-8) as an example, one can see that the AD can be divided in 4 stages:

- 1) S1: fast shrinkage in 1~10 hours;
- 2) S2: fast expansion in 10~20 hours;
- 3) S3: small deformation in 20~50 hours;

## 4) S4: fast shrinkage after 50 hours.

To show the influence of variation of AD on the EAS, a sensitivity study is conducted based on the viscoelastic model. The sensitivity study assumes that a fictitious AD of  $100 \mu\text{strain}$  happens linearly from  $t_0$  and lasts for 10 hours. Accordingly, using the measured creep function of C1-30 (Table 5-2) as input, the EAS of the period corresponding to the fictitious AD can be calculated. Four different scaling factors (i.e., 0.5, 1.0, 1.5, 2.0) are used to scale the magnitude of AD and compare the variance of calculated EAS. The example of the fictitious AD and corresponding EAS happening from 1 and 41 hours ( $t_0=1, 41$ ) are shown in Figure 5-15. By calculating the variance of the EAS induced by AD of different magnitudes at different  $t_0$ , the influence of AD on the EAS evolution can be quantified. From 1~100 hours, the variance of EAS in each 10-hour interval can be calculated, as shown in Figure 5-16. The results show that the variant AD happening in Stages 1 and 2 (i.e., S1 and S2 in Figure 5-16) can only result in negligible variance of EAS, which explains why the variation of initial shrinkage and expansion does not make an apparent difference in the EAS (see Figure 5-8).

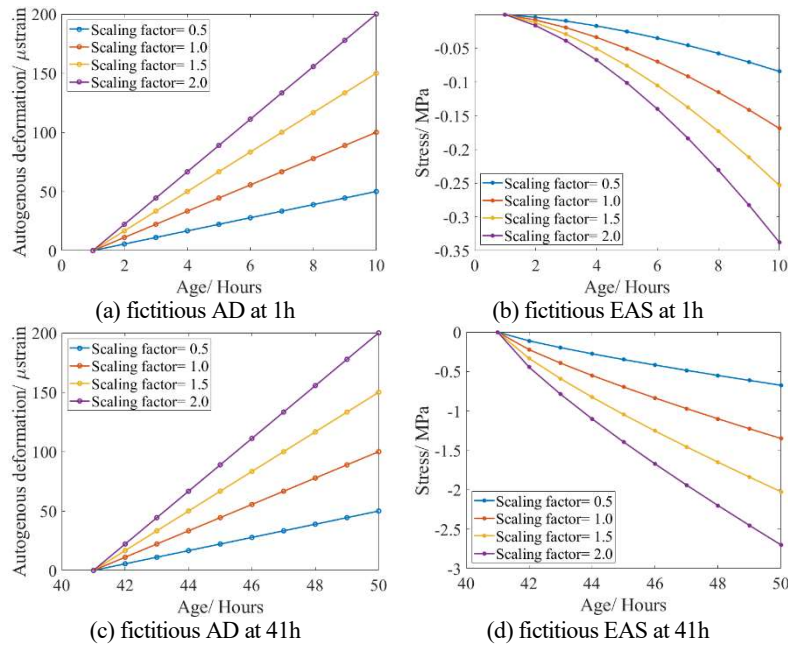
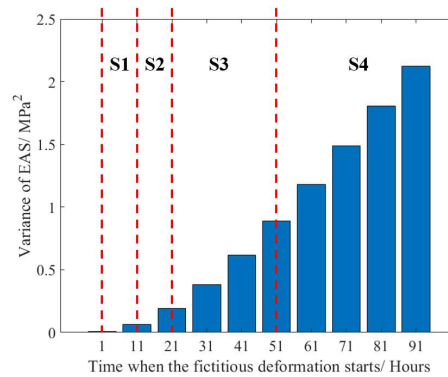


Figure 5-15 Examples of sensitivity study: (a, c) fictitious AD happening at  $t_0=1$  and 41 hours; (b, d) Fictitious EAS caused by the fictitious AD.



**Figure 5-16** Variance of EAS induced by fictitious AD (S1: fast shrinkage in 1~10 hours; S2: fast expansion in 10~20 hours; S3: small deformation in 20~50 hours; S4: fast shrinkage after 50 hours.)

#### 5.4.5.2 Stress superposition

The viscoelastic model in section 5.3.3 is built based on the Boltzmann superposition principle, which assumes that the stress at a certain time is a superposition of all the stress increments of all previous time intervals. Using the modelling case of C3-30-1 as an example, the stress increment at every time interval is shown in **Figure 5-17**. **Figure 5-17 (a)** shows that in every time interval, the stress instantly increases, which is an elastic response to the restrained shrinkage in the corresponding time interval (i.e., autogenous shrinkage rate as in Eq (5-9)). The magnitude of the instant stress increase depends on both the autogenous shrinkage rate and the elastic modulus of the material, as explained by Eq (5-9). Furthermore, the stress starts to decrease with time due to the viscous nature (i.e., creep/relaxation) of the material and is quantified by the relaxation modulus  $R(t_0, t)$  in Eq (5-5), which is calculated based on the creep compliance surface function  $J(t_0, t)$  as measured by the Mini-ADTM and Mini-TSTM. **Figure 5-17 (b)** shows the stress at incremental time steps 4, 30, and 55 hours, which corresponds to the initial shrinkage, autogenous expansion, and autogenous shrinkage phase. Due to relaxation and creep, the stress increment starting from 4 hours (within the initial chemical shrinkage phase) almost disappears after one day and that starting from 30 hours (within the autogenous expansion phase) significantly decreases (by 70%) at 60 hours. The stress increment starting from 55 hours only decreases by 20% at 60 hours. Note that the EAS test of C3-30-1 only lasts for 60 hours. If considering later times, such as 168 hours, one can find in **Figure 5-17 (a)** that the stress increment starting from phases of chemical shrinkage and

autogenous expansion both almost disappear, and only that starting from the phase of autogenous shrinkage remains at a certain level.

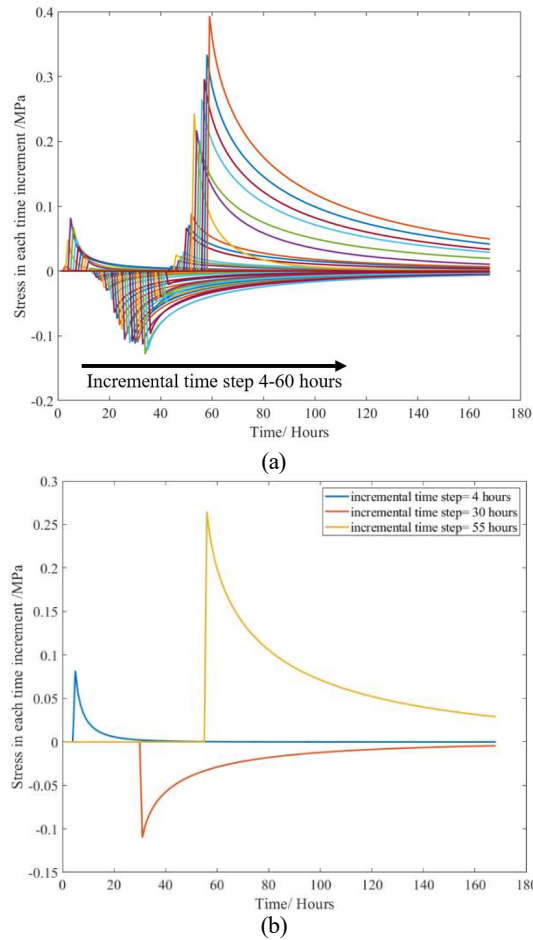


**Figure 5-17 Stress increment of C3-30-1 modelling result: (a) stress increment at every hour; (b) stress increment at 4, 30, and 55 hours.**

## 5.5 Conclusions

This chapter describes the development of a light version of Mini-TSTM and Mini-ADTM. The developed setups allow efficient measurement of time-dependent behaviors and properties of cementitious materials related to EAC issues, including the EAS, autogenous/ thermal deformation, elastic modulus, creep and CTE. The design, implementation and methods of the new setup and experiments are introduced in detail. Systematic validation was conducted to examine the reasonability of the proposed

setup, from the perspective of experiments and theories, The study resulted in the following conclusions:

- 1) The Mini-ADTM and Mini-TSTM improved the testing efficiency and addressed several issues in “standard” TSTM and ADTM tests, including the difficulty in pre-test installation and post-test disassembling, continuous control for full-restraint condition, LVDT installation, and friction between the specimen and the supporting table.
- 2) The Mini-ADTM and Mini-TSTM showed good consistency in EAS test. The expanding/ shrinking process detected by the Mini-ADTM matched well with the stress decreasing (compression)/ increasing (tension) detected by the Mini-TSTM. The influence of cement type and w/b ratios on EAC potentials were correctly reflected. The heating/ cooling efficiency of the proposed setup was examined in a CTE test, which obtained reasonable results compared with existing studies.
- 3) The Mini-ADTM and Mini-TSTM showed good repeatability. In EAS tests of CEM I, all mixes showed a similar EAS despite differences found in measurements of early chemical shrinkage and autogenous expansion. In EAS tests of CEM III/B, the results from the same batch C3-30-1 and C3-30-2 also showed good repeatability in measurement of both AD and EAS.
- 4) The Mini-ADTM and Mini-TSTM found that batch difference of CEM III/B mix with a low w/b ratio (0.30 in this study) can result in a different EAC potential. The C3-30A batch showed faster chemical shrinkage, almost no autogenous expansion and earlier autogenous shrinkage, which led to higher EAC risk.
- 5) The measured AD, elastic modulus, and creep can be used as input for a viscoelastic model to predict the EAS with good accuracy, which validated that the proposed setup correctly simulated and measured the process of EAS evolution. Simulating the EAS evolution of one batch of CEM III/B (i.e., C3-30-1 and C3-30-2) based on the elastic modulus and creep data measured on another batch of CEM III/B (i.e., C3-30A) shows good accuracy. The same holds for CEMI-mixes.
- 6) It was shown quantitatively (i.e., using the viscoelastic model) that the lower elastic modulus and relaxation are the reasons that the initial chemical shrinkage and autogenous expansion at an early age played a much less significant role on stress development than autogenous shrinkage afterward.



# 6. EFFECTS OF CURING TEMPERATURE ON AD AND EARLY-AGE STRESS EVOLUTION

*This chapter investigates the influence of temperature on AD and early-age stress (EAS) evolution in ordinary Portland cement paste using the Mini Temperature Stress Testing Machine (Mini-TSTM) and Mini AD Testing Machine (Mini-ADTM) developed in chapter 5. In the Mini-TSTM/ADTM, CEM I 42.5 N paste with a water-cement ratio of 0.30 is tested under different curing temperature of 10, 15, 20, 25, 30, and 40 °C. X-Ray diffraction (XRD) tests are conducted to measure the amount of ettringite and calcium hydroxide, which reveals the micro-scale mechanisms of autogenous expansion. The applicability of the Maturity Concept (MC) for prediction of AD and relaxation modulus under different temperatures is also examined by the experimental data and the viscoelastic model. This chapter leads to the following findings: 1) the AD of ordinary Portland cement paste is a four-stage process including the initial deformation, autogenous expansion, plateau, and autogenous shrinkage; 2) A higher temperature leads to higher EAC risk because it accelerates the transitions through the first three stages and causes autogenous shrinkage stage to occur earlier. Moreover, higher temperatures also result in higher rates of autogenous shrinkage and EAS in the autogenous shrinkage stage; 3) The autogenous expansion and plateau are attributed to the crystallization pressure induced by CH. Temperature-dependent CH production rates determine the duration of the plateau stage; 4) Low-temperature curing can delay but not completely prevent the EAC induced by AD ; 5) The maturity concept (MC) cannot be used to predict the AD at different temperatures but can be used to calculate the relaxation modulus, which in turn aids in EAS prediction based on AD data.*

*Parts of this chapter have been published in Liang, M., Liu, C., Liang, X., Chang, Z., Schlangen, E., & Šavija, B. (2024). Effects of temperature on autogenous deformation and early-age stress evolution in cement pastes with low water to cement ratio. Construction and Building Materials, 411, 134752.*

## 6.1 Introduction

Temperature significantly influences the hydration kinetics and therefore the AD and early-age stress (EAS) evolution. In chapter 5, all the AD, viscoelastic properties, and EAS were tested at a constant temperature (i.e., 20 °C) to exclude the influence of thermal deformation and different hydration kinetics. However, such tests provide limited guidance on the real-world applications where the temperature always varies. The maturity concept (MC) [49] has been widely adopted to predict the properties/ behaviors under variable temperature based on the tested properties/ behaviors under a constant isothermal condition (often 20 °C), in which a temperature-dependent equivalent age can be calculated by the Arrhenius equation.

However, numerous studies [39,50,51] observed that MC was not suitable for prediction of AD under variable temperatures, because temperatures not only change the hydration kinetics but also RH and surface tension stress, which are key parameters in the process of self-desiccation. Due to the complexity, findings on effects of temperature on AD are often vague [42] or even contradictory: with increasing temperature, the studies [33,53,54] observed decreased autogenous shrinkage while others [41,51,55] saw an increased one.

In this chapter, AD and EAS of ordinary Portland cement paste will be tested under different curing temperatures using the Mini-TSTM and Mini-ADTM developed in chapter 5. The applicability of MC for prediction of AD, EAS, elastic modulus and creep in early-age cracking (EAC) analysis will be examined. Detailed analysis about the influence of curing temperatures on AD will be conducted.

## 6.2 Methods

### 6.2.1 Mini-TSTM and Mini-ADTM tests

The EAS and AD of CEM I 42.5 paste with a w/c ratio of 0.30 were tested by Mini-TSTM and Mini-ADTM, respectively. In total, the AD and corresponding stress evolution of cement paste under six different temperatures (i.e., 10 °C, 15 °C, 20 °C, 25 °C, 30 °C, 40 °C) were tested. For details regarding testing methods and materials, the readers are referred to chapter 5. The tests for the temperatures 10 °C and 15 °C started 6 hours after the casting, while for 20 °C, 25 °C, 30 °C and 40 °C, the tests started 4

hours after casting. The tests lasted until the specimens cracked, which occurred before 168 hours in all the studied specimens.

### 6.2.2 X-Ray diffraction (XRD) test

The XRD test was carried out on a Philips PW 1830/40 powder diffractometer using the Cu K-alpha radiation. The adopted acceleration voltage was 40 kV and the X-ray beam current was 40 mA. The XRD data were collected with a step size of 0.03° for a 2θ range from 5° to 60°.

### 6.2.3 Maturity concept (MC)

The MC assumes that the influence of temperature on the hydration rate is independent of the hydration degree and can be described by the following equation [49]:

$$\frac{d\alpha}{dt} = g(\alpha)f(T) \quad (6-1)$$

where  $\alpha$  is the hydration degree; functions  $g(\alpha)$  and  $f(T)$  quantify the effects of hydration degree and temperature on the hydration rate, respectively. The function  $f(T)$  is the so-called time-temperature function (TTF). The degree of hydration can then be quantified by integrating Eq(5-1) as follows:

$$\int_0^\alpha \frac{d\alpha}{g(\alpha)} = \int_0^t f(T(\tau)) d\tau \quad (6-2)$$

Eq(6-2) further leads to the definition of maturity function  $M(t)$  as the integration of TTF over time, normalized by a constant obtained at a reference temperature:

$$M(t) = \int_0^t \frac{f(T(\tau))}{f(T_{ref})} d\tau \quad (6-3)$$

Based on different TTF, Eq(6-3) gives different expressions of maturity index. Using the Arrhenius equation, the expression of the so-called equivalent age can be derived [49]:

$$M(t) = \int_0^t \exp\left(\frac{E_a}{R}\left(\frac{1}{273 + T_{ref}} - \frac{1}{273 + T(\tau)}\right)\right) d\tau \quad (6-4)$$

where  $E_a$  is the activation energy of ordinary Portland cement;  $R$  is the universal gas constant (i.e., 8.314 J/ (K· mol)). The value for apparent activation energy  $E_a$  is dependent on the cement type and temperature. The activation energy increases with temperature when the temperature is lower than 20°C, but remains constant when temperature is equal to or

higher than 20°C [302]. Based on tests, the following bilinear relationship for apparent activation energy has been proposed [49]:

$$E_a = \begin{cases} E_{a0}, & \text{if } T \geq 20^\circ\text{C} \\ E_{a0} + 1470(20 - T), & \text{if } T < 20^\circ\text{C} \end{cases} \quad (6-5)$$

where  $E_{a0}$  is the apparent activation energy of a certain cement type at 20 °C. In this study, the value of 40500 J/mol for the activation energy  $E_{a0}$  of ordinary Portland cement [303] is used.

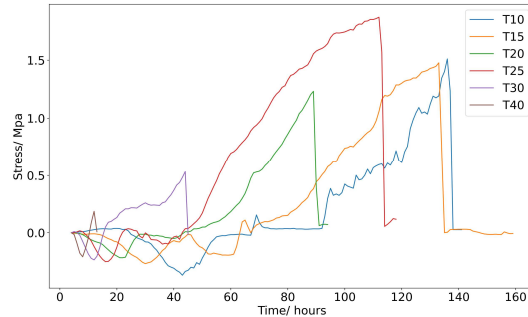
## 6.3 Results and discussion

### 6.3.1 AD and EAS

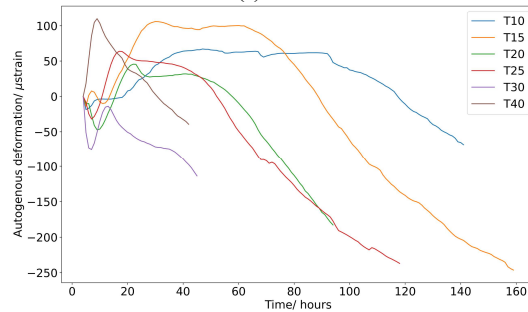
The results of EAS and AD of cement paste under six different temperatures are shown in **Figure 6-1**. The stress results (**Figure 6-1(a)**) show clearly that the EAS evolution all begins with compression, goes into tension, and then the specimen cracks when the EAS exceeds the tensile strength. When the temperature increases, the EAC happens much faster: under 10 °C, the EAC happens at around 140 hours, while the EAC timing under 40 °C is around 11 hours. However, an exception is the result under 25 °C, in which the strength development seems to be fast and therefore the timing of EAC is later than that of 20 °C. In addition, the scatter of the Mini-TSTM/ ADTM tests may also be a reason of such inconsistency. On the other hand, it is also worth noting that for lower temperatures, a plateau can often be found at the transition from compression to tension, which seems to delay the EAC.

The results of AD (**Figure 6-1(b)**) indicate that the AD mostly begins with initial shrinkage, then expansion, and finally shrinkage. An exception is the result at 40 °C, where only the expansion and shrinkage are observed because the starting time of the test at 40 °C is 4 hours, when the initial shrinkage has probably already finished and the expansion has begun. Considering the following two reasons that 1) the measurement of the exact magnitude of initial shrinkage and expansion is very scattered [16,28,304] and 2) the low elastic modulus and high creep greatly limit the influence of the AD on EAS evolution (as discussed in chapter 5), the exact magnitude of the initial shrinkage and expansion will not be used as evidence to show the influence of temperature. Therefore, to exclude the influence of initial shrinkage on the clarity of the results, the time-zero of AD is set at the onset of expansion, which is around 15, 12, 10, 8, 7 and 5 hours after casting for the temperatures of 10 °C, 15 °C, 20 °C, 25 °C, 30 °C, and 40°C, respectively, as shown in **Figure 6-1(c)**. The results clearly show

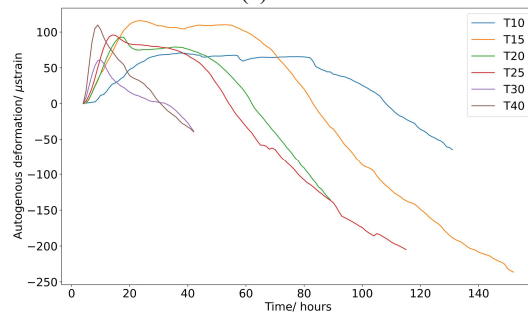
the influence of temperature on AD: higher temperatures result in faster expansion within shorter duration. Besides, higher temperatures also induce faster transition from expansion to shrinkage. A much longer plateau can be found for a lower temperature at the transition from expansion to shrinkage. Such plateau disappears when the temperature reaches 40°C.



(a) EAS



(b) AD



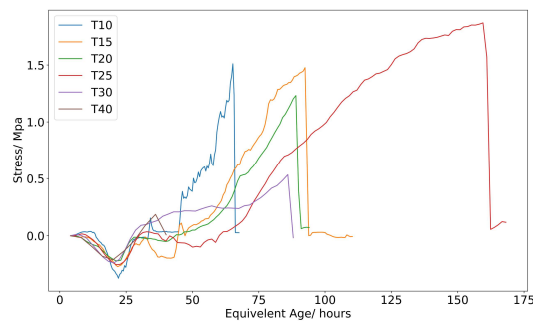
(c) AD zeroed at the onset of expansion

**Figure 6-1 The AD and EAS of cement paste under 6 different temperatures: (a) EAS; (b) AD; (c) AD with the time-zero being the onset of autogenous expansion**

The results in **Figure 6-1** show that, in accordance with the MC, the increased temperature accelerates the development of AD and EAS. This is

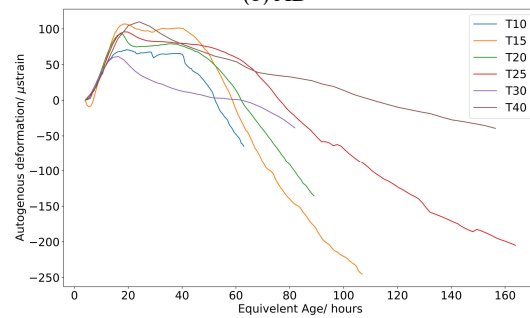
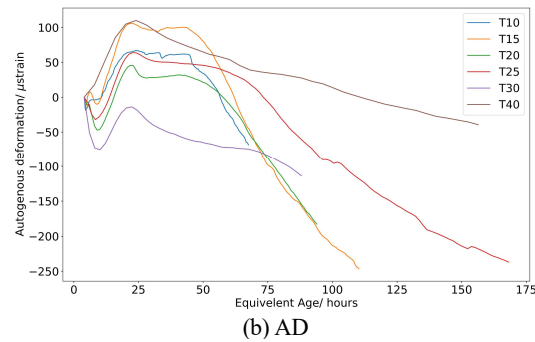
especially clear if one looks at the EAS results (**Figure 6-1 (a)**): the EAS at lower temperatures seems to be a stretched version along the time axis of that at higher temperatures. On the other hand, the AD (**Figure 6-1 (b, c)**) does not show such effect clearly because the scatter in measurement of initial shrinkage and expansion may not convey meaningful indication about the influence of temperature on the magnitude of AD.

However, the existence of a plateau at the expansion-shrinkage transition significantly changes the shape of curves, which indicates that a strict time-scaling effect like MC may not be valid. This can be directly examined by applying the Eq (6-4) to calculate the equivalent ages under the six different temperatures and replot the results of AD and EAS in **Figure 6-1** with respect to the calculated equivalent ages as shown in **Figure 6-2**. If a strict time-scaling effect such as MC stands, the AD and EAS with respect to the equivalent age under different temperatures should show the same pattern. To some extent, **Figure 6-2** shows that the MC can predict the peak of compressive stress (**Figure 6-2(a)**) and expansion (**Figure 6-2(b)**) in a seemingly consistent way. However, **Figure 6-2** also shows that different plateaus are obtained under different temperatures. In 30 °C and 40°C, the plateaus almost disappear. Moreover, after the plateau, the shrinkage rate is also different: the shrinkage rates evaluated by the equivalent age in 30 °C and 40°C are slower than those below 30 °C. Therefore, the MC does not fully quantify the changes of AD under different temperatures.



(a) EAS

(Continue in the next page)



(c) AD zeroed at the onset of expansion

**Figure 6-2** The AD and EAS of cement paste with respect to the equivalent age calculated by the MC: (a) EAS; (b) AD ; (c) AD with the time-zero being the onset of autogenous expansion

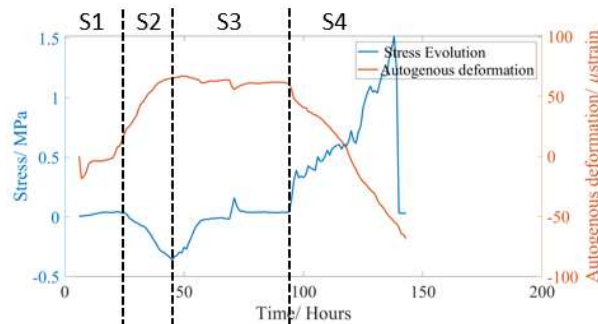
### 6.3.2 Four-stage Process

The AD and EAS in **Figure 6-1** demonstrate a clear four-stage process, as shown in **Figure 6-3**. The consistency between the EAS and AD in **Figure 6-3**, that the compressive/ tensile stress corresponds to the autogenous expansion/ shrinkage, also validates the reasonability of the Mini-TSTM/ADTM tests as discussed in the chapter 5. More importantly, the process of the four stages is given as below:

- 1) Stage 1 (S1): the initial deformation before the onset of autogenous expansion and compressive stress, which is mostly induced by chemical shrinkage and settling of the fresh material after casting [304]. In S1, the material is still very soft and has very low elastic modulus and high creep, so the stress is very low and can be neglected. Although the magnitude of the deformation in this stage is very scattered among different batches of tests for the same type of cement paste, as shown by the chapter 5 and also observed by other studies [16], its influence can be neglected since the stress is almost 0. Note that, although various studies have given indirect definitions for time-zero such as the rate of relative

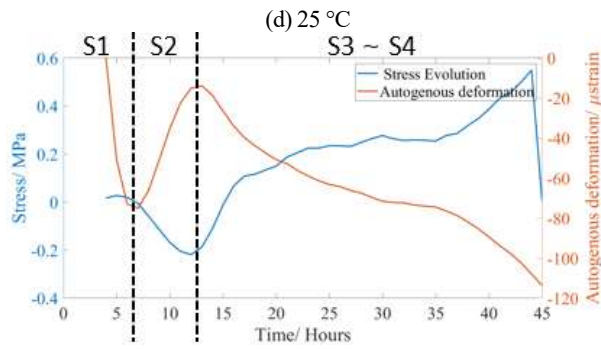
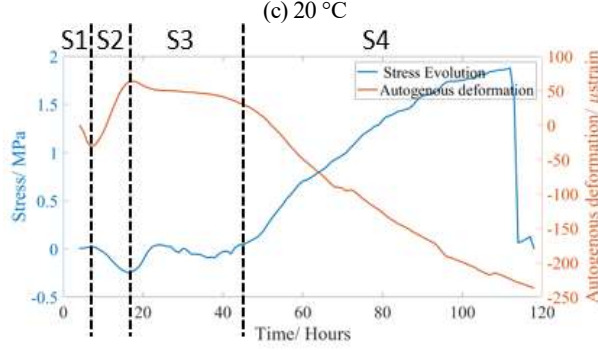
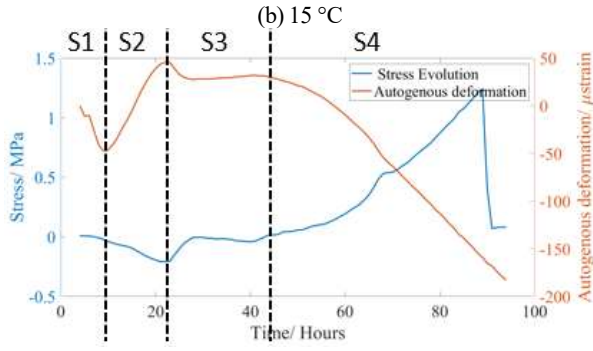
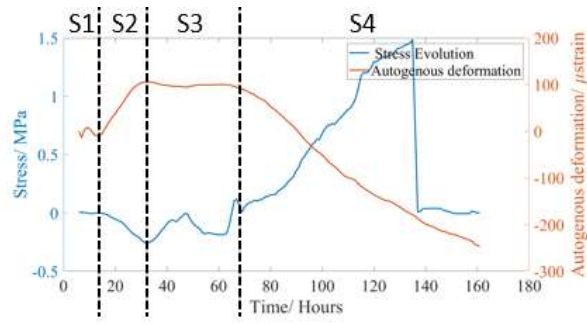
humidity and setting time [14,15,43], the onset of EAS evolution is the most straightforward definition of time-zero because the EAS is the direct index for EAC risk assessment. Therefore, the end of the S1 is exactly the time-zero after which the AD should be taken into account in stress calculation.

- 2) Stage 2 (S2): the autogenous expansion, which is induced by crystal growth such as formation of ettringite [305,306] (as also shown in the chapter 3) and calcium hydroxide (CH, as also observed by [307]). Note that the Mini-TSTM/ADTM tests are all conducted under constant temperatures, so the significant autogenous expansion in S2 is not the result of thermal deformation. In S2, an apparent expansion happens and induces compressive stress in the restrained specimens. The magnitude of such compressive stress is low, but it counteracts the tensile stress happening afterward. To quantify this compressive stress, accurate data of the viscoelastic properties is essential because creep at this stage is very high.
- 3) Stage 3 (S3): the transition from autogenous expansion to self-desiccation shrinkage, which shows as a plateau at low and medium temperatures (**Figure 6-3 (a-d)**), indicating a slow transition process. But as temperature increases, such plateau disappears, and the autogenous shrinkage takes over much sooner. A slow transition from autogenous expansion to autogenous shrinkage (resulted from a lower or medium temperature) can delay the occurrence of tensile stress and therefore lower the EAC risk.
- 4) Stage 4 (S4): the autogenous shrinkage, which induces fast development of tensile stress and causes EAC [225].



(a) 10 °C

(Continue in the next page)



(e) 30 °C  
(Continue in the next page)

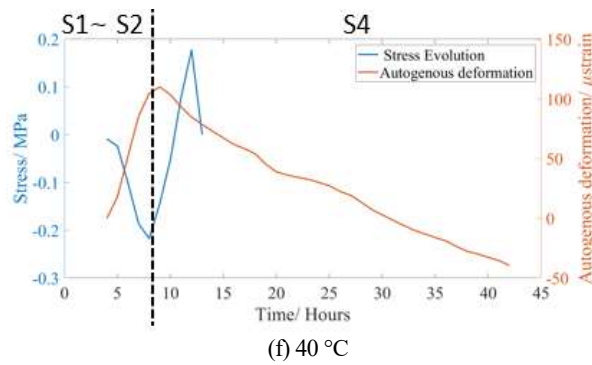


**Figure 6-3** The four-stage process of the AD and EAS evolution under six different temperatures: (a~ f) corresponds to the temperatures of 10 °C, 15 °C, 20 °C, 25 °C, 30 °C, and 40°C respectively.

Overall, in S1~S3, the EAS magnitude is limited because of very low elastic modulus and high creep in S1 and S2 (see variation analysis in chapter 5) and slow deformation rate in S3. In fact, S4 is the stage that really induces the EAC risk. Therefore, regarding the influence of AD on EAS evolution and EAC risk, the duration of the S1~S3 matter much more than the magnitude of the AD, because the duration of the three stages determines when the S4 will begin. **Figure 6-4** clearly shows the influence of the temperature on the duration of each stage:

- 1) As temperature increases, the duration of S1 is shortened, which is similar to the decrease of setting time in higher temperatures as observed in [307–309].
- 2) As temperature increases, the S2 begins earlier and its duration is shorter.
- 3) The duration of S3 follows a decreasing trend as the temperature increases. At 30 °C, the plateau of S3 is not very apparent but the shrinkage and tensile EAS increases gradually from a lower rate. At 40 °C, the S3 disappears, which indicates a direct transition from autogenous expansion (S2) to autogenous shrinkage(S4) and therefore higher EAC risk.
- 4) The end of the S4 is the timing of EAC. The results show that, as temperature increases, the EAC happens earlier, except for the results in 25 °C. Reasons for such inconsistency may be the faster strength development under 25 °C or the scatter of the Mini-ADTM/ TSTM tests.

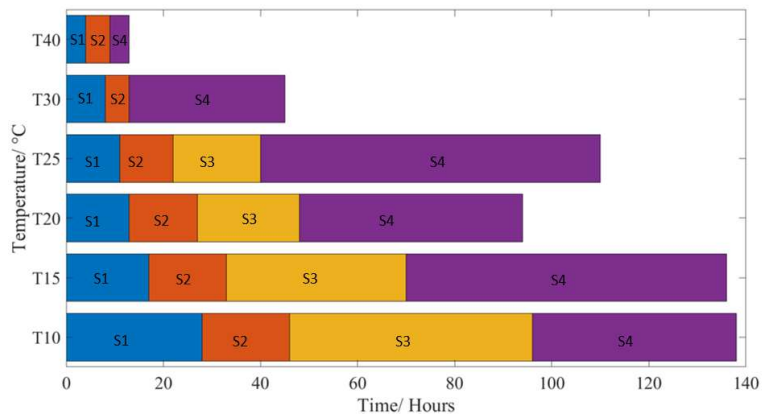


**Figure 6-4 Durations of the four stages of AD and EAS evolution under different temperatures**

In summary, this section describes the four-stage process. In S1, there is no stress in the specimen (i.e., time-zero) and therefore the analysis can start from the S2. Two essential aspects that influence the EAC risk are 1) the duration of S2~S3 which determine the onset of S4 and 2) the rate of autogenous shrinkage and EAS evolution in S4. These two aspects will be investigated in detail in the following sections.

### 6.3.3 Autogenous expansion in S2~S3 due to CH formation

The autogenous expansion in S2 is induced by crystal formation of either ettringite [305,306] or calcium hydroxide [307], which can both be detected and quantified by XRD tests. To investigate the influence of temperature on the AD and EAS in S2~S3, samples cured at 20 and 40 °C are selected for the XRD tests, at three specific ages: 1) the age at the onset of expansion (i.e., beginning of the S2); 2) the age at the end of expansion (i.e., end of the S2); and 3) an age in S4. As a result, the selected ages are 9h, 23h, and 54h for the samples cured at 20°C and 4h, 9h and 24h for the samples cured at 40°C. The curing temperatures are ensured by a cryostat. Before the XRD test, 10% silicon was added to the sample powder as an internal standard, and then Rietveld refinement [280] was conducted to decompose the raw XRD curve. By predefining the mineral types of different hydration products and clinkers, the decomposition is conducted based on the program BGMN [281] and the ICDD database. As shown in [Figure 6-5](#), a good fit was obtained for XRD patterns of all samples, whose weighted profile R-factors ( $R_{wp}$ ) were all lower than 3.4%.

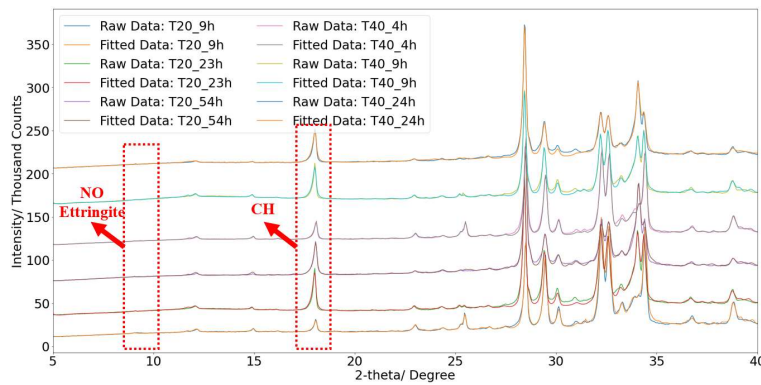


**Figure 6-5 XRD and Rietveld refinement of the six selected samples at different ages**

The main peak at around  $18^\circ$  in XRD results in **Figure 6-5** clearly shows that CH is the major crystal products across the S2 and S3 in both temperatures of  $20^\circ\text{C}$  and  $40^\circ\text{C}$ . On the other hand, the amount of ettringite is almost negligible since there are no peaks at  $9\sim 9.5^\circ$  in the XRD results. Thereby, the general XRD results confirm that CH is the main crystal phase that induces crystallization pressure on the pore walls and then causes autogenous expansion. By comparing the CH content (calculated by the Rietveld refinement) at different ages with the AD, as shown in **Figure 6-6**, patterns regarding the mechanisms of AD in S2~S4 and the influence of temperature can be described as follows: 1) In S2, the fast increase of CH corresponds to the fast autogenous expansion. The CH production rates in S2 for  $20^\circ\text{C}$  and  $40^\circ\text{C}$  are 0.179% wt./hour and 0.822% wt./hour, respectively; 2) After S2, the CH production rates for  $20^\circ\text{C}$  and  $40^\circ\text{C}$  are 0.064% wt./hour and 0.033% wt./hour respectively. In other words, after S2, the CH production rate in  $20^\circ\text{C}$  decreases to 35.7% of the previous rate, while in  $40^\circ\text{C}$ , the CH production rate accounts for only 4.01% of the previous rate. The patterns described above explain the mechanisms of autogenous expansion in S2 and the plateau in S3. In S2, the fast increase of CH induces the autogenous expansion in both temperatures. After S2, in lower temperature, the CH production rate decreases gradually, but the continuous production of CH is still able to generate the crystallization pressure (that induces expansion) to counteract the effect of capillary pressure caused by self-desiccation (that induces shrinkage) [17], and therefore causes the plateau of AD and EAS in S3. On the other hand, at higher temperature, the CH production rate drastically decreases after S2 and the CH content increase does not result in enough crystallization pressure that can balance the capillary pressure caused by self-desiccation. As a result, at higher temperature, self-desiccation effects take over much

sooner and there is no plateau at the transition of autogenous expansion and shrinkage.

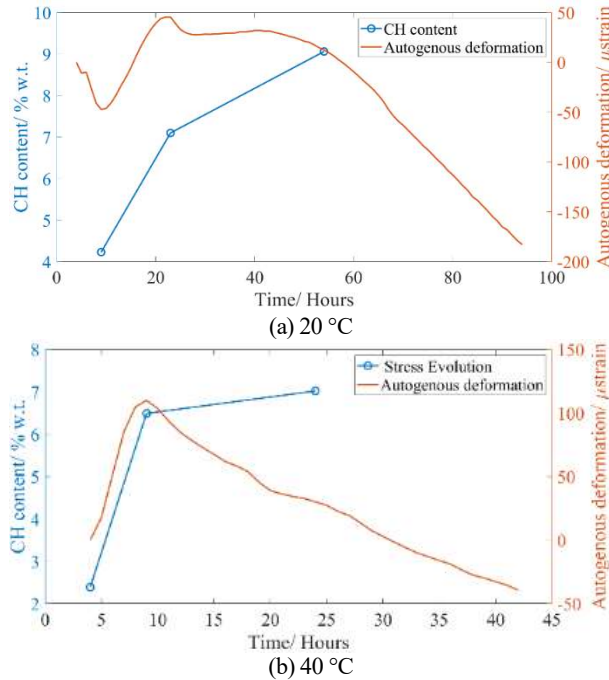


Figure 6-6 CH content and the AD of the six selected samples: (a) 20°C; (b) 40°C.

### 6.3.4 Autogenous shrinkage in S4 due to self-desiccation

In S4, rapid autogenous shrinkage and EAS evolution happen, which indicates significant risks of EAC. The mechanism of the autogenous shrinkage in S4 is self-desiccation [108]. The rates of autogenous shrinkage and EAS in S4 at different temperatures are the main factors concerning the EAC risk and have been calculated and shown in Figure 6-7. The results indicate that increasing temperature causes faster development of autogenous shrinkage and EAS, as also observed by [53,55,308]. However, for temperatures in 10-30 °C, the rates of EAS and autogenous shrinkage are similar, which means that even in low-temperature environment, autogenous shrinkage-induced EAC risk cannot be neglected. At 40°C, a drastic increase of autogenous shrinkage and EAS rate is observed, which indicates very high EAC risk.

The influence of temperature on the autogenous shrinkage is a complex result of several counteracting factors [42]. Specifically, increasing temperature results in the following changes: 1) faster hydration [49,122]

and therefore faster drop of RH [33,50]; 2) higher ultimate RH due to the free water equilibrium inside the capillary pores [50,310,311]; 3) a more heterogenous microstructure with coarser porosity and increased mean pore radii [312–315]. According to the Kelvin equation, faster drop of RH increases capillary pressure and therefore causes faster autogenous shrinkage, while coarser porosity reduces the capillary pressure and therefore results in slower autogenous shrinkage [17]. In general, it seems that the faster hydration and decrease of RH is the main mechanism of the influence of temperature on autogenous shrinkage in the studied ages, since the overall trend of the test shows a positive correlation between temperature and autogenous shrinkage rate. However, it should be noted that such influence is not significant in 10-30 °C, as also observed by many other studies [42,304,308] that the rate of autogenous shrinkage under different temperatures (in the range of 10-30 °C) remains similar. Therefore, a comparable trade-off between the aforementioned three factors may be achieved in the temperature range of 10-30 °C, and results in a similar rate of autogenous shrinkage. When the temperature increases to 40 °C, a significant increase of the AD rate (and therefore the EAS rate) is observed, indicating that the fast hydration and RH drop is the governing mechanism among the aforementioned three factors. A drastic increase of autogenous shrinkage at 40 °C was also observed by others [307,309,316].

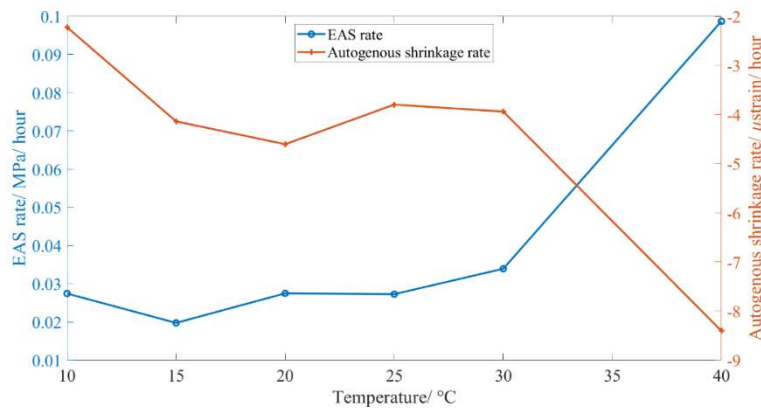


Figure 6-7 Rate of EAS and AD in S4

### 6.3.5 Predicting the EAS under different temperatures

The prediction of EAS under different temperatures is conducted based on the viscoelastic model introduced in Eq ((5-4)- (5-7)) in chapter 5. The required inputs are AD and relaxation modulus, as shown by the Eq (5-5) in chapter 5. Based on the section 6.3.1, the MC is not applicable for AD. Therefore, the tested ADs under different temperatures are directly used

as input for the model. On the other hand, the relaxation modulus is obtained based on the conversion method of Eq (5-7), which uses the elastic modulus and creep compliance function as input. As a property that is positively correlated to the compressive strength, as revealed by macroscale loading-unloading tests [118], the evolution of elastic modulus under different temperatures can be successfully predicted by the MC [121,122]. The influence of temperature on creep was mainly influenced by two different mechanisms [173]: 1) A temperature increase accelerates the bond breakages and restorations causing creep, and thus increases the creep rate [166,174]; 2) A temperature increase accelerates the hydration and therefore reduces the creep. For early-age concrete, the effect of hydration dominates and therefore the maturity concept can still be used for predicting the basic creep at the early age [173,175]. The increase of RH can increase the long-term creep rate [174,176], and can be quantified by the microstress-solidification theory [173,177].

Therefore, in this section, the MC is applied to first calculate the elastic modulus and creep compliance at different temperatures based on the testing results in chapter 5 (as given in [Figure 5-12](#) and [Table 5-3](#)). Then, the relaxation modulus can be further calculated by the Eq (5-7) using the elastic modulus and creep compliance at different temperatures as the input. Part of the relaxation modulus at four different time of loading (i.e., 12, 24, 48, 72 hours) at different temperatures are given in [Figure 6-8](#). The results show that, as the time of loading and temperature increase, the relaxation modulus increases, which is reasonable because a later timing of loading indicates longer hydration and higher temperatures accelerate the hydration. Using the calculated relaxation modulus and the tested AD as the input for Eq (5-5), the EAS at different temperatures can be predicted, as shown in [Figure 6-9](#). Root Mean Square Error (RMSE) is calculated to show the difference between the predicted and tested EAS, based on Eq (5-10). The results show that, using the relaxation modulus converted by the MC as the input, the viscoelastic model (Eq ((5-4)- (5-7))) can still predict the EAS at different temperatures with only limited errors in some cases. Such error may be attributed to the variation in the different batches of the cement, as discussed in detail in chapter 5. The prediction of the EAS under different temperatures shows that the MC is applicable to the early-age viscoelastic properties (i.e., elastic modulus and creep/ relaxation).

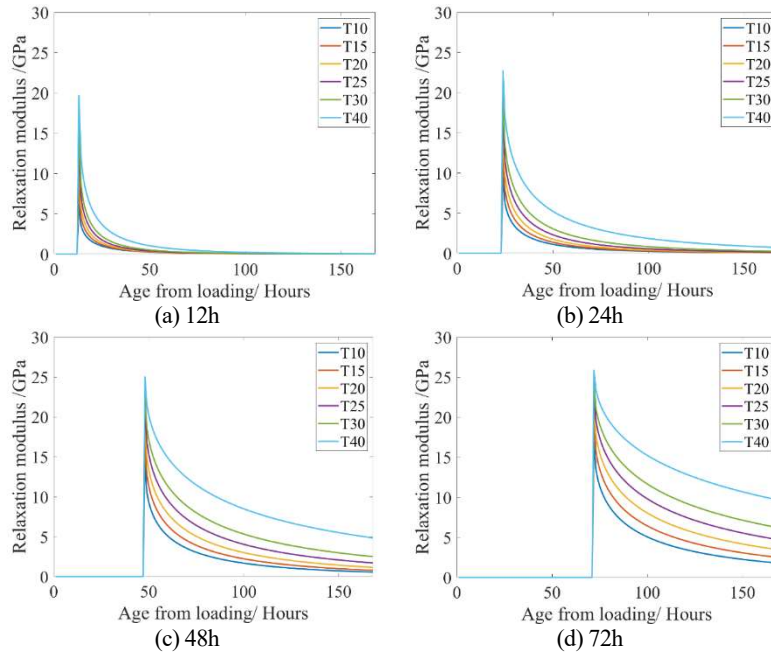
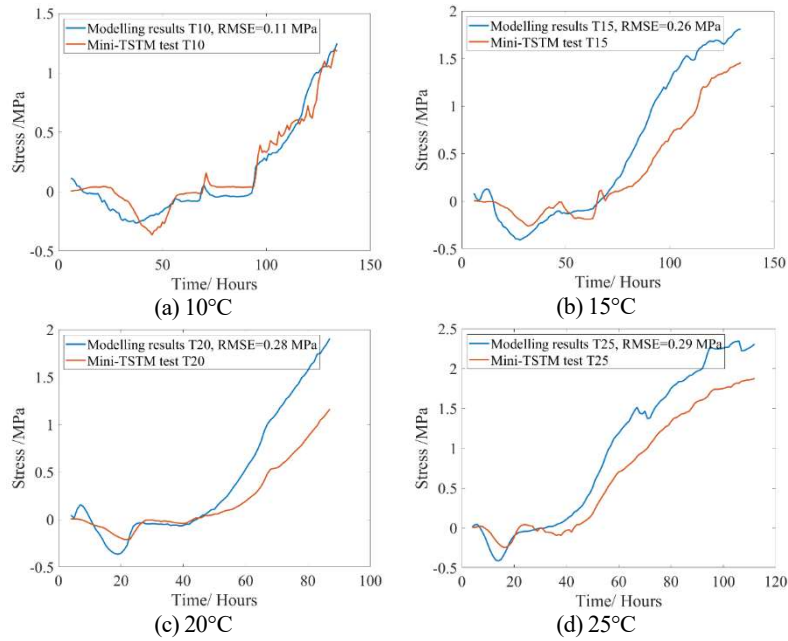


**Figure 6-8** Relaxation modulus at different temperatures (a-d) are for time of loading ( $t_0$ ) since 12, 24, 48, and 72 hours, respectively.



(Continue in the next page)

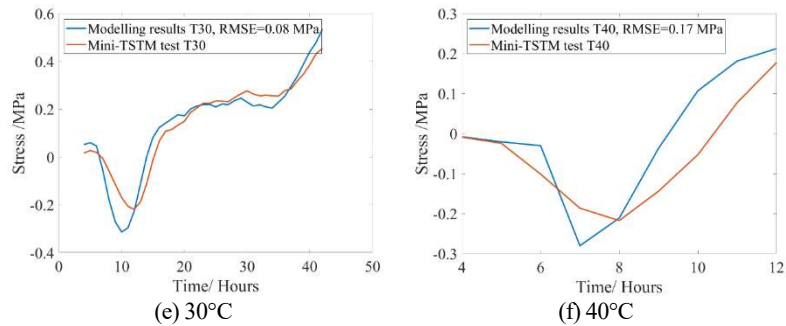


**Figure 6-9 Predicted EAS evolution at different temperatures (a-f) are for different temperatures of 10°C, 15°C, 20°C, 25°C, 30°C, and 40°C respectively.**

## 6.4 Conclusions

Based on the Mini-TSTM/ ADTM tests under different temperatures, this chapter revealed the influence of temperature on the four-stage process of the AD and EAS in restrained cementitious materials. XRD tests were performed to investigate in-depth the micro-scale mechanisms of autogenous expansion. The applicability of MC on the prediction of AD and relaxation modulus was also examined by experimental data and the viscoelastic model. The following can therefore be concluded:

- 1) The AD of ordinary Portland cement paste can be described as a four-stage process: the initial deformation (i.e., time-zero), autogenous expansion, plateau, and autogenous shrinkage. Due to the low elastic modulus and high creep in the first two stages, the magnitude of EAS is low. The plateau in the third stage delays the occurrence of tensile stress which will accumulate drastically in the fourth stage when autogenous shrinkage is induced by self-desiccation.
- 2) Higher temperatures can increase the risk of EAC. Higher temperatures accelerate the transition through the initial stages, causing the autogenous shrinkage stage to occur earlier. Beyond 30°C, the plateau stage disappears, which directly leads to autogenous shrinkage. Moreover, higher temperatures lead to increased rates of autogenous shrinkage and EAS.
- 3) The autogenous expansion and plateau of slow deformation are attributed to the CH content, as quantified by the XRD analysis. At the beginning of the second stage, the fast CH production induces the autogenous expansion. As the temperature increases, the CH production rate decreases. At temperatures below 30°C, the produced CH after the second stage can still generate crystallization pressure to balance the effect of self-desiccation

capillary pressure and result in the plateau of slow AD. However, when temperature is above 30°C, the CH production rate decreases drastically and the self-desiccation effect dominates, resulting in a direct autogenous shrinkage after the second stage.

- 4) Low-temperature curing delays but does not entirely prevent AD-induced EAC. In moderate temperatures (10~30°C), the rates of autogenous shrinkage and EAS in the fourth stage are approximately at the same level, leading to the EAC issues at the end.
- 5) While the MC cannot accurately predict AD across temperatures, it successfully calculates relaxation modulus. This, in turn, aids in EAS estimation based on AD data.

# 7. MODELLING OF STRESS RELAXATION IN EARLY-AGE CEMENTITIOUS MATERIALS

*This chapter investigates numerical methods for simulating very early-age stress relaxation in restrained cementitious materials. The AD, elastic modulus, aging creep, and early-age stress evolution of two types of cement paste tested in chapter 5, CEM I 42.5N and CEM III/B 42.5 N, were used as input and validation for the numerical models. Two methods for converting creep compliance to relaxation modulus were discussed in detail and used for the one-dimensional simulation of stress evolution in the Mini-TSTM test. Furthermore, virtual creep and relaxation tests were conducted using an exponential algorithm with either the Kelvin or Maxwell chains to show their applicability in simulating the viscoelastic behavior of early-age cementitious materials. The results showed that the exponential algorithm with the Maxwell chain can obtain good prediction accuracy of EAS in 3D analysis. The current numerical solutions of the Volterra integral of creep compliance can lead to a negative relaxation modulus, thus introducing calculation errors in terms of stress for both 1D and 3D analysis.*

*Parts of this chapter have been published in Liang, M., Luzio, G. Di, Schlangen, E., & Šavija, B. (2024). Experimentally informed modeling of the early -age stress evolution in cementitious materials using exponential conversion from creep to relaxation. Computer-Aided Civil and Infrastructure Engineering.*

## 7.1 Introduction

Based on the TSTM test in either chapter 3 or chapter 5, the early-age stress (EAS) can be obtained and used to evaluate the risk of early-age cracking (EAC). It was found in chapter 4 and other different studies [72,110,237] that relaxation significantly influences the EAS evolution. Therefore, to model the EAS evolution, early-age viscoelastic properties are necessary inputs that must be addressed under any conditions [238,317]. Comparing the measurements of creep and relaxation, creep tests are much more straightforward than relaxation tests to perform because they only require recording the deformation under a load-controlled condition. Thereby, to simulate the stress relaxation in the EAS modeling, many studies need to convert the measured creep compliance to relaxation modulus [112]. Wei et al. [252] converted the creep compliance given by the MicroPrestress-Solidification (MPS) theory and successfully predicted the EAS under varying temperatures in restrained concrete with good precision. Li et al. [110,237,253] also converted the creep compliance to relaxation modulus. In multiple testing cases, they successfully predicted the EAS induced by restrained AD of alkali-activated material. Note that the conversion methods adopted by Wei et al. [252] and Li et al. [110,237,253] are different: Wei et al. [252] used the numerical solution of a linear viscoelastic constitutive equation with the form of a Volterra integral; the conversion method adopted by Li et al. [110,237,253] is significantly more straightforward, based on a specific solution derived from the definition of relaxation. In addition, it is also worth noting that some methods do not require obtaining the relaxation modulus. Instead, it is also possible to simulate the EAS from the perspective of creep. For example, Klausen et al. [28] first calculated the incremental creep strain, and then, assuming that both the AD and the creep deformation were restrained, they calculated the incremental EAS with an elastic relation, which matched well with the experiments.

The modeling studies mentioned above were all based on a 1D case since the validation data is from the TSTM test, which is indeed a 1D restraint test. Generalizing the obtained creep and shrinkage data to 3D structures and getting the corresponding EAS distribution requires the use of a Finite Element (FE) model. Simulating the viscoelastic behavior still requires solving the Volterra integral. However, solving the Volterra integral is difficult in FEM because, at every time step, the strain/ stress history of every previous time step at every Gaussian point needs to be restored, which is computationally heavy and the model may be significantly

hindered if a large structure with fine meshes is constructed [212,213]. Instead, the exponential algorithm, based on either a Kelvin chain [111,212,213] or a Maxwell chain [112], can be used to solve the Volterra integral with a rate-type form, which then only requires storing a few internal variables of the rheological chains during the modeling process. It should be noted that the Kelvin chain can be calibrated directly by the measured creep data by a continuous retardation chain [209,210]. In contrast, the Maxwell chain needs the relaxation data, so the conversion from creep to relaxation is required. Due to the better availability of creep data, Kelvin Chain has often been used for EAS modeling. Liu et al. [29] fitted the creep data of the B3 model [318] to a Kelvin chain and successfully predicted the EAS evolution in a TSTM test by the exponential algorithm. Similarly, in Chapter 4, the Kelvin chain-based exponential algorithm is combined with Bayesian Optimization in simulating the EAS in TSTM tests of GGBFS concrete.

The studies mentioned above form a solid basis for modeling the EAS evolution in restrained concrete. However, most studies only did the EAS test and used other (empirical) material models as the input for creep and elastic modulus, which compromises their validation reliability. To some extent, the complexity and high cost of TSTM tests hindered a comprehensive experimental campaign to provide first-hand data for validating the modeling results. Moreover, most studies directly implemented the models for EAS prediction, while these models and their applicability are rarely compared and discussed. In this chapter, based on comprehensive experimental results in chapter 5, four representative numerical models (two for 1D simulation and two more for 3D simulation) will be used to predict the EAS, and their applicability will be discussed. Notably, the prediction results of EAS will be analyzed and compared in detail.

## 7.2 Theory

EAS evolution in restrained concrete is the result of a non-stop relaxation test: During the hardening of cementitious materials, within every time interval, an imposed deformation is applied to the hardening concrete to compensate for the AD and keep the specimen fully restrained, which then induces EAS. If the concrete material is linearly elastic, then the EAS in each time interval can be expressed as:

$$\Delta\sigma(t_0) = E(t_0)\Delta\varepsilon(t_0) \quad (7-1)$$

where  $t_0$  is the time when the imposed deformation  $\Delta\varepsilon$  is applied. Then under the assumption of Boltzmann superposition, the total EAS at time  $t$  should be the integration of the elastic modulus  $E$  over the imposed deformation, expressed as:

$$\sigma(t) = \int_0^t E(t_0) d\varepsilon(t_0) \quad (7-2)$$

However, cementitious materials are viscoelastic, and stress relaxation must be considered [238]. Therefore, in Eq (7-2), instead of the elastic modulus, the relaxation modulus  $R(t_0, t)$  should be used, expressed as:

$$\sigma(t) = \int_0^t R(t_0, t) d\varepsilon(t_0) \quad (7-3)$$

Eq (7-3) is the exact solution of EAS, a Volterra integral obtained by the Boltzmann superposition. Using the mid-point rule, EAS can be expressed as:

$$\sigma(t) = \sum_{t_0=0}^{t_0=t} R(t_0 + \frac{1}{2}\Delta t_0, t) \times \Delta\varepsilon(t_0) \quad (7-4)$$

Eq (7-4) gives the numerical solution of EAS. There are only two inputs required: 1) relaxation modulus for viscoelasticity  $R(t_0, t)$ , and 2) rate of AD  $\Delta\varepsilon$ . The  $\Delta\varepsilon$  can be directly obtained from the test. However, the  $R(t_0, t)$  requires a conversion from creep compliance to relaxation modulus since most tests for viscoelasticity are creep tests. Creep compliance function  $J(t_0, t)$  and relaxation modulus function  $R(t_0, t)$  are fully coupled if linear viscoelasticity is applied. Given a stress history  $\sigma(t)$  applied at  $t_0$  and continuously last until  $t_f$ , the strain at  $t_f$  can be expressed as:

$$\varepsilon(t_f) = J(t_0, t_f)\sigma(t_0) + \int_{t_0+}^{t_f} J(t', t_f)\sigma'(t') dt' \quad (7-5)$$

Then, considering a relaxation test and the definition of relaxation modulus, Eq (7-5) can be rewritten as:

$$J(t_0, t_f)R(t_0, t_0) + \int_{t_0+}^{t_f} J(t', t_f)R(t_0, t') dt' = 1 \quad (7-6)$$

Eq (7-6) gives the exact relationship between creep and relaxation. Substituting the creep compliance  $J(t_0, t)$  in Eq (7-6) allows the derivation of relaxation modulus  $R(t_0, t)$ , which will form the basis of the first model in this study. Moreover, substituting the obtained creep compliance function  $J(t_0, t)$  and relaxation modulus function  $R(t_0, t)$  in the left of Eq (7-6), the results should be equal to 1.0. This can be used to check the conversion process from creep to relaxation and will be termed "integral check" in the

remainder of this chapter. Given the creep compliance function  $J(t_0, t)$  and relaxation modulus function  $R(t_0, t)$ , Eq (7-6) can be solved as:

$$J(t_0, t_f)R(t_0, t_0) + \sum_{i=t_0+1}^{t_f} J(t_{i+1/2}, t_f)[R(t_0, t_i) - R(t_0, t_{i-1})] = 1 \quad (7-7)$$

### 7.3 EAS models

Modeling the EAS requires three time-dependent inputs: the AD, the elastic modulus, and the relaxation modulus. In this chapter, AD was measured by the Mini-ADTM by specifying a free mechanical boundary and constant temperature. The elastic modulus and creep were measured by the Mini-TSTM by an hourly-repeated loading scheme. The Mini-TSTM also measured the EAS with a fully restrained boundary condition and then was used to validate the four proposed models. Conversion from creep to relaxation is a crucial step in the simulation of EAS evolution and will be the key focus of this study.

#### 7.3.1 Models for 1D analysis

The 1D analysis model only considers the case of a shrinking bar that is fully restrained at the two ends. Because TSTM tests are also uniaxial loading tests, the 1D analysis applies to EAS calculation in TSTM tests. In 1D analysis, Eq ((7-3)~(7-4)) can directly calculate the corresponding EAS. A significant problem with 1D analysis lies in converting a creep compliance function to a relaxation modulus function. For 1D analysis, two methods will be used to conduct this conversion. The obtained relaxation modulus function will be analyzed by the integral check using Eq ((7-6)~(7-7)). The final validation will be done by comparing the tested and the predicted EAS. The working procedures for the 1D analysis are shown in **Figure 7-1**.

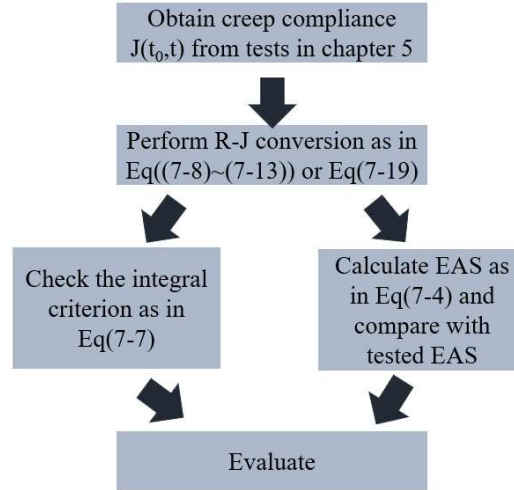


Figure 7-1 Procedures of 1D analysis

### 7.3.1.1 Model 1 (M1): Numerical solution from the integral form

The conversion from creep to relaxation in Model 1 (M1) is done by substituting the creep compliance into Eq (7-6) and solving the corresponding relaxation modulus numerically. Therefore, M1 is intrinsically based on the numerical solution of the integral form. Wei et al. [252] applied M1 to transfer the creep compliance function adjusted by MPS theory and successfully predicted the EAS under varying temperatures. Given the creep compliance function  $J(t_0, t)$ , the relaxation function  $R(t_0, t)$  can be obtained numerically as [111]:

$$R(t_0, 1) = 0 \quad (7-8)$$

$$R(t_0, 2) = \frac{1}{J(t_0, t_0)} \quad (7-9)$$

$$R(t_0, k+1) = R(t_0, k) - \frac{1}{J_{k,k+1}} \sum_{i=1}^{k-1} \Delta J_{i,k} (R(t_0, i+1) - R(t_0, i)) \quad (7-10)$$

$$J_{k,k+1} = \frac{J(k+1, k+1) + J(k, k+1)}{2} \quad (7-11)$$

$$\Delta J_{i,k} = J(k, k+1) - J(k, k) \quad (7-12)$$

It should be noted that the first term as in Eq (7-8) is merely an auxiliary term that enables to start the iteration in Eq (7-10). However, due to the highly non-linearity of the relaxation modulus at the beginning, directly implementing the numerical solution, as in Eq ((7-8)~(7-12)), can lead to an underestimation of the relaxation modulus. Therefore, instead of following the initial conditions as in Eq (7-9), it was also suggested to keep the second and third term of the relaxation modulus constant [111], expressed as:

$$R(t_0, 2) = R(t_0, 3) = \frac{1}{J(t_0, t_2)} \quad (7-13)$$

It should be noted that the initial conditions as in Eq (7-13) are merely used for calculating the other relaxation modulus after  $t=3$ , while the real relaxation modulus of the first two terms stays the same as in Eq ((7-8)~(7-9)).

### 7.3.1.2 Model 2 (M2): A simple explicit solution from the definition of relaxation test

Model 2 (M2) was initially proposed by Wittmann and van Breugel [250,251] to calculate the EAS in young concrete and obtain good prediction accuracy with concrete. M2 has already been used in the chapter 5 to predict the EAS of ordinary Portland cement paste tested by the Mini-TSTM. In the past, M2 was also successfully applied to alkali-activated materials [110,237,253]. In this section, the M2 is introduced in detail to compare with other models. It is assumed that the total strain is composed of two parts, the elastic and the creep part, as:

$$\varepsilon = \varepsilon_{el} + \varepsilon_c \quad (7-14)$$

where  $\varepsilon_{el}$  and  $\varepsilon_c$  are the elastic and the creep strain, respectively. Note that with the definition of relaxation tests, the total strain is a constant independent of time. Then, by taking the derivative at the two sides and expressing the elastic strain with Hook's law, one gets:

$$\frac{1}{E(t_0)} \frac{d\sigma}{dt} = -\frac{d\varepsilon_c}{dt} \quad (7-15)$$

Assuming that the creep strain at a certain  $t_0$  can be expressed by power functions [111,193] (i.e.,  $J(t_0, t) = a(t-t_0)^n$ ), the Eq (7-15) can be rewritten as:

$$\frac{1}{E(t_0)} \frac{d\sigma}{dt} = -\sigma a n (t - t_0)^{n-1} \quad (7-16)$$

Note that  $a$  and  $n$  are fitting parameters of the power function of creep. Integrating the Eq (7-16) leads to:

$$\ln \sigma = -E(t_0)a(t-t_0)^n + C \quad (7-17)$$

Where  $C$  is a constant depending on the initial condition. Assuming the initial stress is  $\sigma_0$ , the ratio of stress  $\sigma$  and  $\sigma_0$  can be obtained as:

$$\frac{\sigma}{\sigma_0} = e^{-E(t_0)a(t-t_0)^n} \quad (7-7-18)$$

Therefore, the relaxation modulus can be written as:

$$R(t_0, t) = e^{1-J(t_0,t)E(t_0)}E(t_0) \quad (7-19)$$

Note that the exponent in Eq (7-19) is the creep coefficient. It should also be noted that M2 is significantly more straightforward to handle than M1 because Eq (7-19) can be directly solved. On the contrary, M1 needs a more complex numerical scheme, as in Eq ((7-8)~(7-13)), to obtain the relaxation modulus. By substituting the tested elastic modulus and creep compliance into Eq (7-19), one obtains the relaxation modulus explicitly, and then the EAS can be calculated directly by Eq (7-4).

### 7.3.2 Models for 3D analysis

For the final aim to assess the EAS in real concrete structures, the FEM method should be used for 3D analysis. Because solving the Volterra integral Eq ((7-3)~ (7-4)) in FEM is computationally expensive, this study employed the exponential algorithm [111,112,212,213] based on the Kelvin chain model and Maxwell chain model, which turns the Volterra integral into a rate-type form and allows to solve it with a quasi-elastic constitutive relationship. The exponential algorithm is also based on the integral formation of Eq (7-3) and Eq (7-5). The first step of the exponential algorithm is to reformulate Eq (7-3) and Eq (7-5) in the following incremental form:

$$\Delta \sigma = E^*(\Delta \varepsilon - \Delta \varepsilon_{ad}) - \sigma^* \quad (7-20)$$

where  $E^*$  is the incremental modulus;  $\sigma^*$  is an internal variable in the rheological chain that should be updated in each computation cycle;  $\Delta \varepsilon_{ad}$  is the incremental AD. The adopted Kelvin chain or Maxwell chain gives the exact solution of the  $E^*$  and  $\sigma^*$  that will be introduced in detail in the following sections. Firstly, using Eq (7-20) as the constitutive equation and setting  $\Delta \varepsilon_{ad}$  to 0, virtual uniaxial creep/relaxation tests will be conducted on a 150×150×750 prism (**Figure 7-2 (a)**). The boundary condition of creep/relaxation tests is formulated by fixing the bottom of the prism and applying unit load/displacement on the top. Creep/relaxation tests aim to check the applicability of the exponential algorithm in simulating the viscoelastic behavior in FEM. Then, a virtual Mini-TSTM test will be conducted based on a dog-bone specimen restrained at the two ends and

with the same geometry as the Mini-TSTM specimen (Figure 7-2 (b)). The measured AD in the Mini-ADTM is then used as input of  $\Delta\varepsilon_{ad}$ .

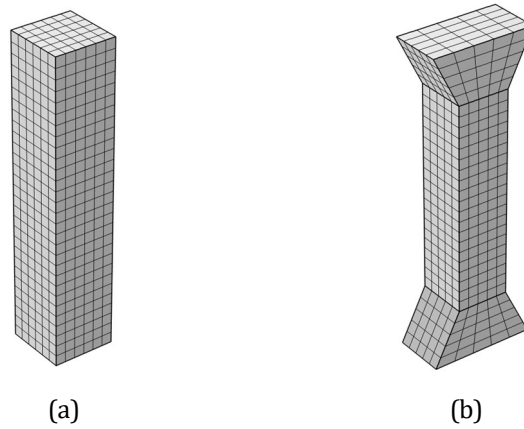


**Figure 7-2 Virtual specimens in FEM simulation of viscoelastic behavior: (a) prism for basic creep/ relaxation tests; (b) Dog-bone specimen for Mini-TSTM tests**

Because the integral check requires solving Eq ((7-6)~(7-7)) at every  $t_0$  and  $t$ , which is very computationally expensive for FEM, this study only checks the coupling between creep and relaxation in FEM with virtual creep/ relaxation tests at four different ages, including 7, 24, 48, and 72 hours. The final validation of the FEM will still be using the tested AD, elastic modulus, and creep to calculate the EAS, and then the calculated EAS can be compared to the tested EAS.

### 7.3.2.1 Model 3 (M3): Exponential Algorithm Based on Kelvin-chain

A typical Kelvin chain with  $n$  units is shown in Figure 7-3. Solving the system of the differential equations of rheological units, the creep compliance function can be obtained by adding the strain in each rheological unit under a constant unit load, which then can be expressed as:

$$J(t_0, t) = \frac{1}{E_0(t_0)} + \sum_{j=1}^n \frac{1}{E_j(t_0)} \left(1 - e^{-\frac{t-t_0}{\mu_j}}\right) \quad (7-21)$$

where  $E_j$  and  $\eta_j$  are the elastic modulus of the spring and viscosity coefficient in  $j$ -th rheological unit, respectively, and  $\mu_j$  is the retardation time of  $j$ -th unit and  $\mu_j = \eta_j / E_j$ .

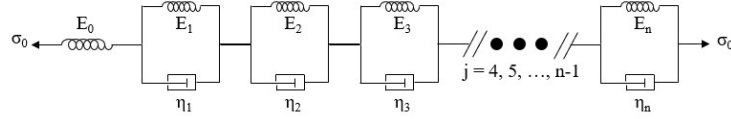


Figure 7-3 A Kelvin chain with  $n$  units

Rewriting Eq (7-5) into the incremental form as Eq (7-20) and substituting the creep compliance function Eq (7-21) into the incremental form derived from Eq (7-5), one obtains the numerical solution of incremental modulus  $E^*$  and internal variable  $\sigma^*$  as below [111,212,213] :

$$E^*(t^*) = \frac{1}{\frac{1}{E_0(t^*)} + \sum_{j=1}^n \frac{1}{E_j(t^*)} (1 - (1 - e^{-\frac{\Delta t}{\mu_j}}) \frac{\mu_j}{\Delta t})} \quad (7-22)$$

$$\sigma^*(t_i) = E^*(t^*) \sum_{j=1}^n (1 - e^{-\frac{\Delta t}{\mu_j}}) \varepsilon_j^*(t_i) \quad (7-23)$$

$$\varepsilon_j^*(t_{i+1}) = e^{-\frac{\Delta t}{\mu_j}} \varepsilon_j^*(t_i) + \frac{1}{E^*(t_i)} (1 - e^{-\frac{\Delta t}{\mu_j}}) \frac{\mu_j}{\Delta t} \Delta \sigma \quad (7-24)$$

where  $t^*$  is the average of two consecutive time steps  $t_i$  and  $t_{i+1}$ . Eq (7-20) and Eq ((7-22)~(7-24)) encompass the incremental viscoelastic constitutive relationship for simulating the development of stress induced by AD. Note that the  $\varepsilon^*$  of each Kelvin chain unit is the internal state variable, a second-order strain tensor that must be updated on each integration point according to Eq (7-24) at every time step.

It is important to note that the input of the Kelvin chain is creep compliance, as in Eq (7-21). Therefore, implementation of Model 3 (M3) requires determining the parameters of the adopted Kelvin chain (i.e.,  $E_j$  and  $\mu_j$  in Eq (7-21)) by fitting Eq (7-21) with the tested creep compliance function (i.e., Eq (5-6) with parameters obtained from the tested creep data as in [Table 5-3](#)). Herein, the continuous retardation spectrum method [209,211,213] is used. First, based on a 13-unit Kelvin chain, the retardation time  $\mu_j$  is chosen a priori to prevent an ill-conditioned equation system as:

$$\mu_j = 10^{-7+j}, j = 1:13 \quad (7-25)$$

Then the continuous fitting form for the non-aging term in Eq (5-6) (i.e.,  $C(t-t_0) = (t-t_0)^c$ ) is as follows:

$$C(t-t_0) = \int_0^\infty \frac{1}{E_j} (1 - e^{-\frac{t-t_0}{\mu_j}}) d(\ln \mu_j) \quad (7-26)$$

Using the Laplace transform and Widder's formula, the solutions of  $E_j$  can be derived [209]:

$$\frac{1}{E_j} = -\ln 10 * \lim_{k \rightarrow \infty} \frac{(-k\mu)^k}{(k-1)!} C^k(k\mu) \quad (7-27)$$

In this study, the spectrum of third order ( $k=3$ ) is used, which shows high accuracy in fitting Kelvin chain parameters [209,211,213]. The working procedures for the M3 are shown in **Figure 7-4**. Three checkpoints are proposed to examine the feasibility of the M3: 1) by doing a virtual creep test, the obtained creep compliance function should be the same as the input creep compliance function; 2) by doing a virtual relaxation test, the obtained relaxation modulus should show a similar coupling as obtained by M1; 3) by simulating a Mini-TSTM test, which uses the AD tested by the Mini-ADTM as the input, the obtained EAS should match the tested EAS.

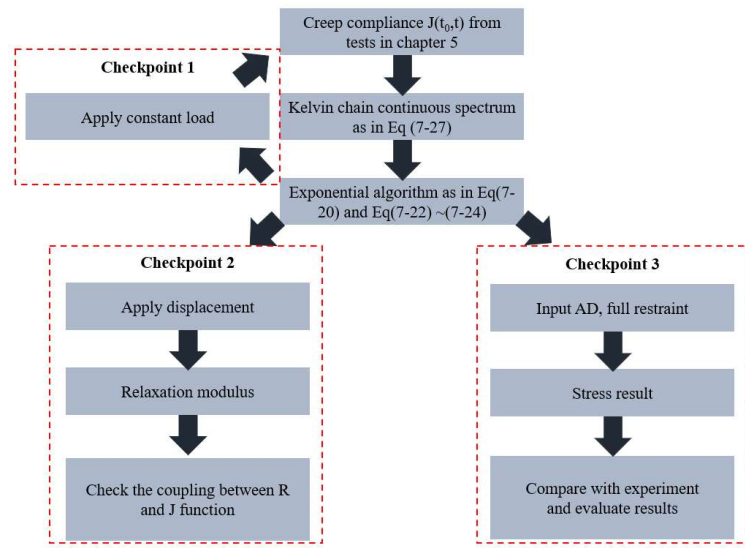


**Figure 7-4 Procedures for exponential algorithm based on Kelvin chain.**

### 7.3.2.2 Model 4 (M4): Exponential Algorithm Based on Maxwell-chain

Model 4 (M4) is based on the Maxwell chain, as shown in **Figure 7-5**. By solving the system of differential equation of the Maxwell chain with  $n$  units, the relaxation modulus can be explicitly expressed as:

$$R(t_0, t) = E_0(t_0) + \sum_{j=1}^n E_j(t_0) e^{-\frac{t-t'}{\mu_j}} \quad (7-28)$$

Similarly, by substituting Eq (7-28) into the incremental form as in Eq (7-20) derived by Eq (7-3), one obtains the numerical solution of modulus  $E^*$  and internal variable  $\sigma^*$ , as [112]:

$$E^*(t^*) = \sum_{j=1}^N E_j(t^*) \left( 1 - e^{-\frac{\Delta t}{\mu_j}} \right) \frac{\mu_j}{\Delta t} + E_0(t^*) \quad (7-29)$$

$$\sigma^*(t_{i+1}) = \sum_{j=1}^n \left( 1 - e^{-\frac{\Delta t}{\mu_j}} \right) \sigma_j^*(t_i) + E^*(t_{i+1}) \Delta \varepsilon_{ad}(t_{i+1}) \quad (7-30)$$

$$\sigma_j^*(t_i) = e^{-\frac{\Delta t}{\mu_j}} \sigma_j^*(t_{i-1}) + E^*(t^*) \left( 1 - e^{-\frac{\Delta t}{\mu_j}} \right) \frac{\mu_j}{\Delta t} (\Delta \varepsilon(t_i) - \Delta \varepsilon_{ad}(t_i)) \quad (7-31)$$

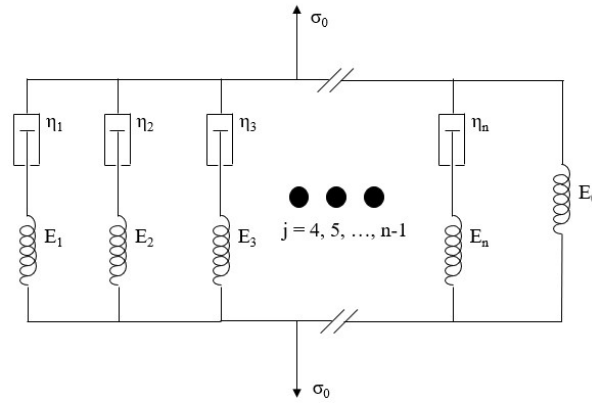


Figure 7-5 A Maxwell chain with n units

Eq (7-20) and Eq ((7-29)~(7-31)) form the exponential algorithm based on the Maxwell chain and can be implemented in FEM to simulate the viscoelastic behavior. However, it should be noted that the Maxwell chain-based model requires an input of relaxation modulus, as shown in Eq (7-28). Therefore, the tested creep compliance function (i.e., Eq (5-6) with parameters obtained from the tested creep data as in [Table 5-3](#)) should be converted to a relaxation modulus function before it can be used as input for the Maxwell model. In this study, the conversion method as given by M2 (i.e., Eq (7-19)) was used for conversion. After the relaxation modulus is available, the nonlinear optimization tool [319–327] developed by

MATLAB is adopted to complete the fitting process of the Maxwell chain spectrum. Note that the studied time range is from 0~168 hours after the placement of fresh material, with 1 hour as the time step. Assuming the adopted Maxwell chain has 13 units and the retardation time is selected as Eq (7-25), the objective of the optimization process is to find the  $E_j$  ( $j=1, 2, \dots, 13$ ) that can make the relaxation modulus derived by the Maxwell chain (i.e., Eq (7-28)) as similar as the relaxation modulus converted from the tested creep compliance. Therefore, this study's retardation spectrum of the Maxwell chain would be a  $168 \times 13$  array, with the first axis corresponding to the loading time and the second axis corresponding to the  $j$ -th unit in the Maxwell chain.

The working procedure for the exponential algorithm based on the Maxwell chain is formulated in Figure 7-6. Three checkpoints are proposed to examine the feasibility of the M3: 1) by doing a virtual relaxation test, the obtained relaxation modulus function should be the same with the input relaxation modulus function; 2) by doing a virtual creep test, the obtained creep compliance should show a similar coupling as obtained by M2; 3) by simulating a Mini-TSTM test, which uses the AD tested by the Mini-ADTM as the input, the obtained EAS should match the tested EAS.

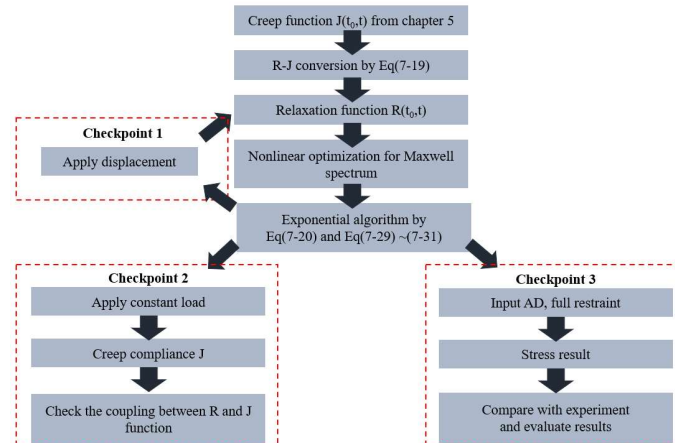


Figure 7-6 Procedures for exponential algorithm based on Maxwell chain.

## 7.4 Results and discussion

### 7.4.1 The 1D analysis for conversion from creep to relaxation

The 1D study was conducted by M1 and M2, as introduced in section 7.3.1. In this section, the conversion results of M1 and M2 will be analyzed, and the integral check will be performed.

#### 7.4.1.1 Conversion results

After obtaining the viscoelastic properties from the chapter 5 (i.e., Eq (5-6) with parameters obtained from the tested creep data as in **Table 5-3**), the conversion from creep to relaxation can be done by M1 (i.e., Eq ((7-8)~(7-13))) or M2 (i.e., Eq (7-19)). The conversion results of the two types of cement paste are shown in **Figure 7-7**. Note that in this study, the time range of interest is 1~168 hours, with a time step of 1 hour. Therefore, the relaxation modulus  $R(t_0, t)$  is a  $168 \times 168$  array. To clearly display the relaxation modulus  $R(t_0, t)$ , only 16 sets of  $R(t_0, t)$  are shown below, with  $t_0$  equal 10, 20, 30, ..., and 160 hours. As expected, the relaxation modulus obtained by both M1 and M2 follows a clear decreasing trend. However, the results of M1 (**Figure 7-7 (a, c)**) do not converge to 0 but to negative values. In comparison, the results obtained by M2 (**Figure 7-7 (b, d)**) always converge to 0. It is clear that the negative values in M1 already suggest that it is not applicable for EAS simulation because the negative relaxation modulus indicates that in the relaxation process, the stress not only decreases but also changes the direction afterwards. For example, considering a relaxation test with initial compression, a negative relaxation modulus means that the compressive stress will not only decrease but also become tensile stress afterwards. It should be noted that such a problem with M1 has already been reported in [111], suggesting that the high nonlinearity of the relaxation modulus results in the underestimation of the relaxation modulus by numerical solutions. And therefore, instead of the initial conditions as in Eq (7-9), Bažant and Jirasek [111] proposed an empirical solution by using the initial conditions as in Eq (7-13) to ease problems in the conversion of relaxation modulus of later ages (several days to weeks). However, despite the improvement brought by Eq (7-13), it is shown here that the negative relaxation modulus still exists (**Figure 7-7 (a, c)**), which indicates that M1 needs further improvement (probably in numerical schemes) before it can be used to simulate stress relaxation in very early age cementitious materials (from several hours to a week in this study).

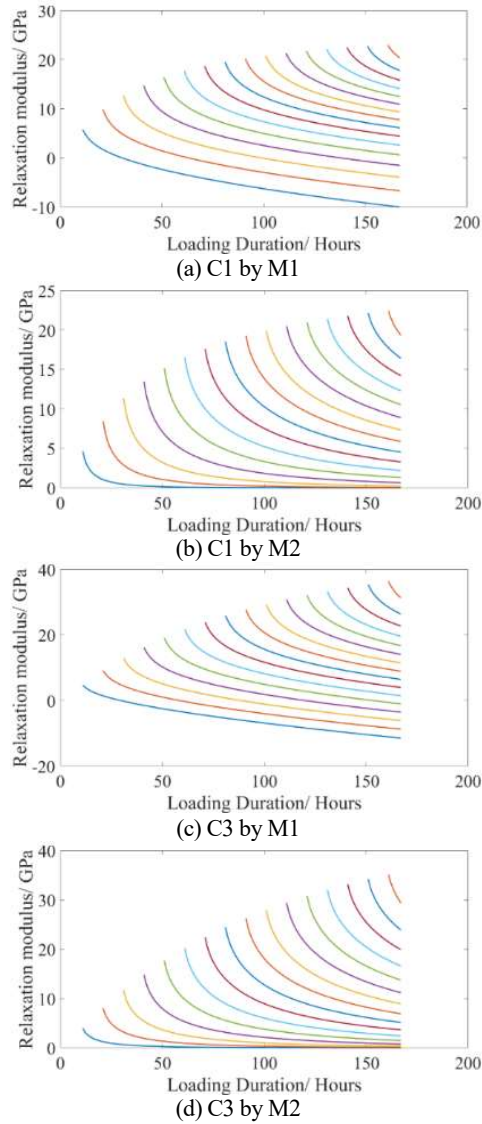


**Figure 7-7 Relaxation modulus  $R(t_0, t)$  converted from measured creep compliance function by M1 and M2 for two types of cement paste: (a) C1 results converted by M1; (b) C1 results converted by M2; (c) C3 results converted by M1; (d) C3 results converted by M2. (Note that the results displayed here are  $R(t_0, t)$  with  $t_0$  equal to 10, 20, 30, ..., and 160 hours.)**

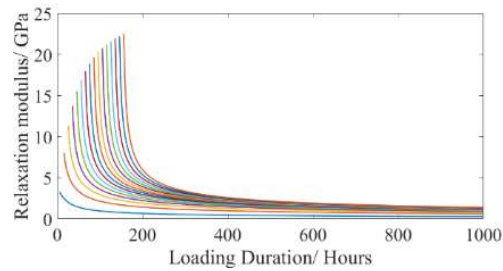
In fact, the negative relaxation modulus (caused by M1) is mainly resulted from the rapid decrease of the creep compliance function due to the aging term (specifically, term  $(1/t_0)$  in Eq (5-6)). This becomes evident when assuming that concrete creep is not subject to aging (by omitting the aging

term) and then recalculating the relaxation modulus using M1, as depicted in **Figure 7-8 (a)**. When the load is applied at intervals of 10, 20, ..., up to 160 hours, within a total timeframe of 1000 hours, the issue of the negative relaxation modulus is completely addressed. Additionally, employing a creep compliance function for normal concrete, which is typically recommended for long-term creep analysis by many design codes, also resolves this negative issue. For instance, by applying the creep compliance function from the ACI code [30], with parameters equivalent to those for normal concrete as described in Eq ((7-32)~(7-34)) [212], the relaxation modulus following M1 can be calculated, as shown in **Figure 7-8 (b)**. The negative relaxation modulus is only observed at the very beginning. Consequently, the negative relaxation modulus problem induced by M1 primarily occurs in very early-age materials with high creep. For long-term creep analysis, such concerns regarding M1 are likely negligible.

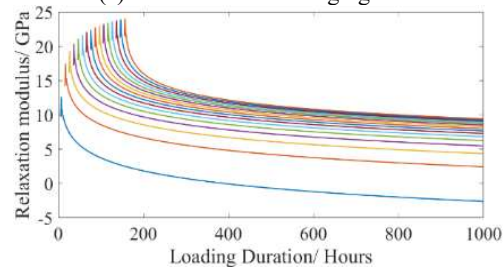
$$E(t_0) = 38000 * (e^{0.2 * (1 - \sqrt{\frac{28}{t_0}})})^{0.3} \quad (7-32)$$

$$\varphi(t_0, t) = 2 * (1.25 * t_0)^{-0.118} * (t - t_0)^{0.2} \quad (7-33)$$

$$J(t_0, t) = \frac{1 + \varphi(t_0, t)}{E(t_0)} \quad (7-34)$$



(a) C1 with a constant aging term



(b) Normal concrete with ACI

**Figure 7-8 Relaxation modulus  $R(t_0, t)$  converted from creep compliance function by M1 for: (a) C1 creep compliance function with a constant aging term; (b) ACI-based creep compliance function for normal concrete as used in [212].**

### 7.4.1.2 The integral check

The integral check is performed here by substituting the converted relaxation modulus (obtained by M1 and M2) and creep compliance function (i.e., Eq (5-6)) into Eq (7-7) and checking if the integral is equal to 1. To evaluate the difference between the obtained integral value and 1, the index root mean square error (RMSE) is used here, which can be expressed as:

$$RMSE = \sqrt{\frac{\sum_t (y_c(t) - y_r(t))^2}{t}} \quad (7-35)$$

where  $y_c$  is the calculated value, and in this case, it is the integral value;  $y_r$  is the real value that the integral in Eq (7-7) should be equal to, which in this case is 1. The integral check results for the converted relaxation modulus of both pastes obtained by M1 and M2 are shown in **Figure 7-9**. The results of the integral check for  $t=20:168$  and  $t_0=1:168$  are shown. To present the overall shape of the relaxation function, the results in the very beginning (i.e.,  $t=1:20$ ) are not shown. However, it should be noted that the RMSEs in each result were calculated based on all the results. The integral check results clearly show that the relaxation modulus converted by the M1 (**Figure 7-9 (a, c)**) has a much lower RMSE (around 0.10) than the relaxation modulus converted by the M2 (**Figure 7-9 (b, d)**), which obtained a higher RMSE around 0.43.

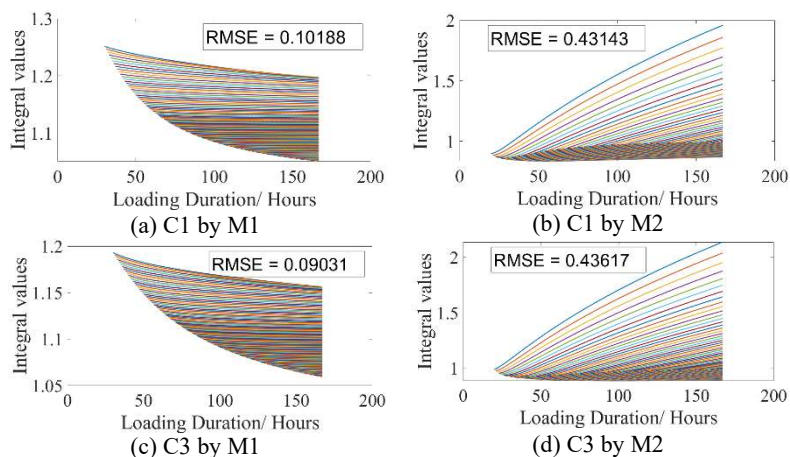


**Figure 7-9** Integral values given by Eq (8) using converted relaxation modulus and tested creep compliance function as input: (a) C1 results converted by M1; (b) C1 results converted by M2; (c) C3 results converted by M1; (d) C3 results converted by M2.

Such results are understandable if one checks the detail of the M1 and M2: M1 is basically another form of numerical solution of the integral check (Eq (7-6)), and therefore M1 naturally satisfies the criterion that the integral value calculated by Eq (7-7) should be equal to 1. The RMSE of near 0.1 is just the accuracy loss of the adopted numerical scheme (i.e., mid-point rule). However, on the other hand, it should be noted that the derivation of M2 does not have any prior information regarding the integral, and thus it results in a higher RMSE of about 0.43. Specifically, looking at **Figure 7-9 (b, d)**, it is found that the error of M2 in the integral check tends to be higher, especially at a very early age (i.e., at small  $t_0$ ). Note that the problem of negative values of relaxation modulus obtained by M1 (**Figure 7-7 (a, c)**) also tends to be more significant at a very early age (i.e., at small  $t_0$ ). Considering all the negative values in **Figure 7-7 (a, c)** as mere errors of adopted numerical schemes, one can correct all negative values to zero and do the integral check again with the adjusted relaxation modulus. The results of the relaxation modulus obtained by such adjusted M2 are shown in **Figure 7-10**. It is interesting to see that, after correcting all the negative values to 0, the adjusted M1 obtains a similar RMSE with M2. Moreover, the error distribution of the adjusted M1 is also similar to that of M2: earlier ages tend to have higher RMSE and, therefore, more deviation from the criterion of integral check.

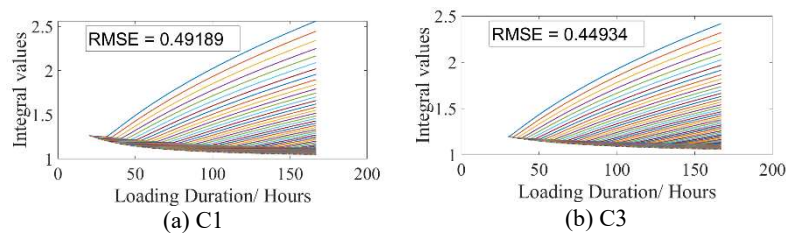


**Figure 7-10 Integral values given by Eq (8) using adjusted M1 by setting all negative values to 0: (a) C1 results; (b) C3 results.**

From the result analysis of this section, it is found that despite M1 satisfying the integral check with better accuracy with a low RMSE of around 0.10, it obtains negative values of the relaxation modulus, especially in early age, which is due to the high nonlinearity of relaxation modulus function at the beginning according to Bažant and Jirasek [111]. In comparison, M2 does not lead to negative values but only a smooth convergence to 0. Negative values of the relaxation modulus represent problematic stress relaxation process with a change of stress direction, and may not be acceptable for simulating stress relaxation in early-age cementitious materials. Considering the negative values in M1 as numerical loss and correcting

them to zero, the obtained RMSE in the integral check is similar to M2, which is around 0.40.

### 7.4.2 The 3D analysis based on exponential algorithms (Checkpoints 1 and 2)

The 3D analysis implements M3 and M4 in FEM, extensions of the 1D method M1 and M2. The exponential algorithm solves the Volterra integral with a quasi-elastic constitutive relationship, which is more efficient than directly solving the integral with classical numerical schemes and therefore is more suitable in simulating viscoelastic behavior in massive structures, including the EAS prediction. In this section, virtual creep and relaxation tests will be done using the M3 and M4, respectively, to illustrate the applicability of the exponential algorithm based on either Kelvin or Maxwell chain in simulating the viscoelastic behavior of very early-age cementitious materials. Specifically, checkpoints 1 and 2 in [Figure 7-4](#) and [Figure 7-6](#) will be examined in this section for both M3 and M4. All the virtual tests will be conducted at four different ages, including 7, 24, 48, and 72 hours.

#### 7.4.2.1 Kelvin-chain

The M3 is the exponential algorithm based on the Kelvin chain model. The spectrum of the Kelvin chain was fitted using the continuous retardation chain method based on the experimental results of the creep compliance function. Checkpoint 1 of M3 aims to conduct a virtual uniaxial creep test on a prism and compare the obtained creep compliance function from such tests with the experimental results (i.e., the input for the Kelvin chain.). The results of checkpoint 1 of M3 are shown in [Figure 7-11](#). The results of checkpoint 1 indicate that the M3 can almost perfectly simulate the creep test given a specific input, meaning that high precision is achieved by the exponential algorithm based on the Kelvin chain to calculate the Volterra integral. However, this suggests that similar problems of negative relaxation modulus happening to M1 will also occur in M3 if it comes to the conversion from creep to relaxation. The relaxation modulus can be obtained by applying a constant displacement on top of the prism, as shown in [Figure 7-12](#). The relaxation modulus converted by M1 and M2 are also compared. The results of virtual relaxation tests by M3 show a similar non-converging trend as the results of M1, which leads to a negative relaxation modulus, which indicates a problematic change of stress direction in the relaxation process, and may not be acceptable for EAS simulation.

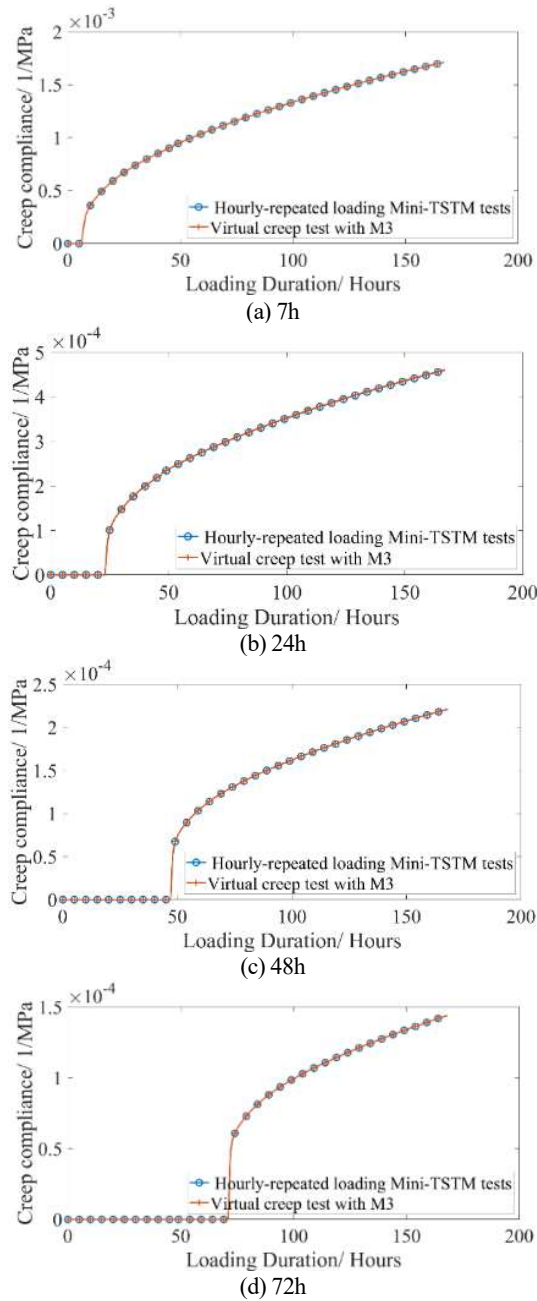


**Figure 7-11** Creep compliance obtained from virtual creep test of M3 (checkpoint 1), with loading time  $t_0=7, 24, 48,$  and  $72$  hours for Fig (a~ d), respectively.

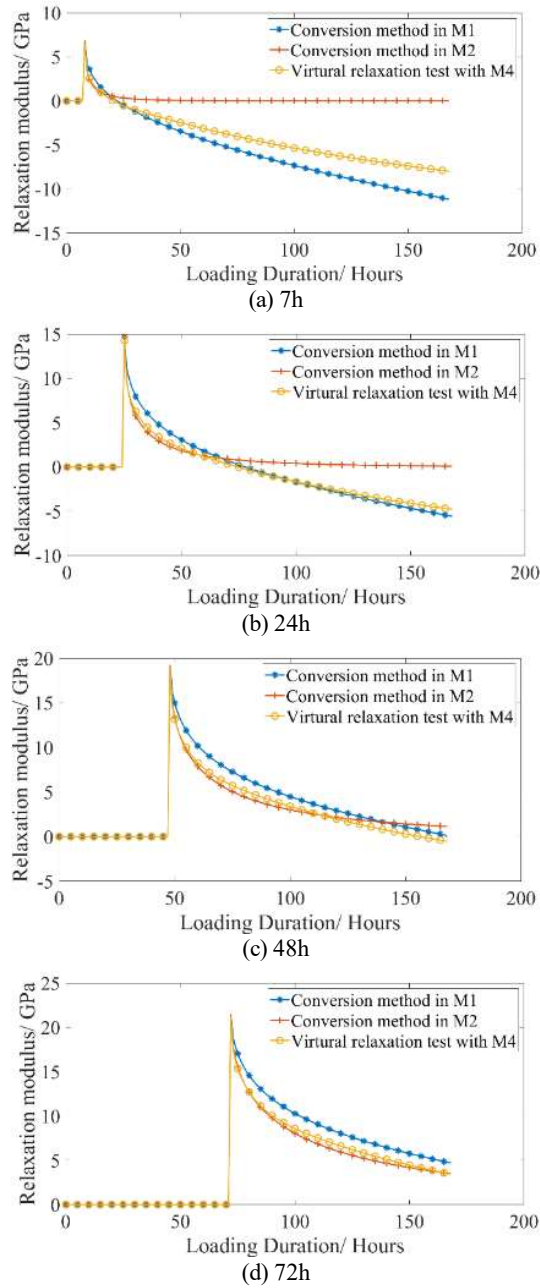


**Figure 7-12** Relaxation modulus obtained from virtual relaxation test of M3 (checkpoint 2), with loading time  $t_0=7, 24, 48,$  and  $72$  hours for Fig (a~ d), respectively.

### 7.4.2.2 Maxwell-chain

Compared to the Kelvin chain, the Maxwell chain is less used because it is difficult to obtain the relaxation modulus which the Maxwell chain requires as the input. In this study, we first used the M2 to convert the creep compliance function obtained from the hourly-repeated loading test to the relaxation modulus. Then, a nonlinear optimizer was employed to fit a 13-unit Maxwell chain using the relaxation modulus obtained by M2. The obtained spectrum of the Maxwell chain for the two cementitious materials CEM I/ 42.5N and CEM III/B 42.5N with a w/c ratio of 0.30 are shown in **Figure 7-13**. Note that the Maxwell spectrum is a  $168 \times 13$  array, with the horizontal axis being the investigated time ranging from 1 to 168 hours and the vertical axis being the 13 different Maxwell units with relaxation time logarithmically distributed from  $10^{-6}$  to  $10^6$  hours. The values in the array are the ratio between the elastic modulus of the spring in the unit and the elastic modulus of the cement paste material.

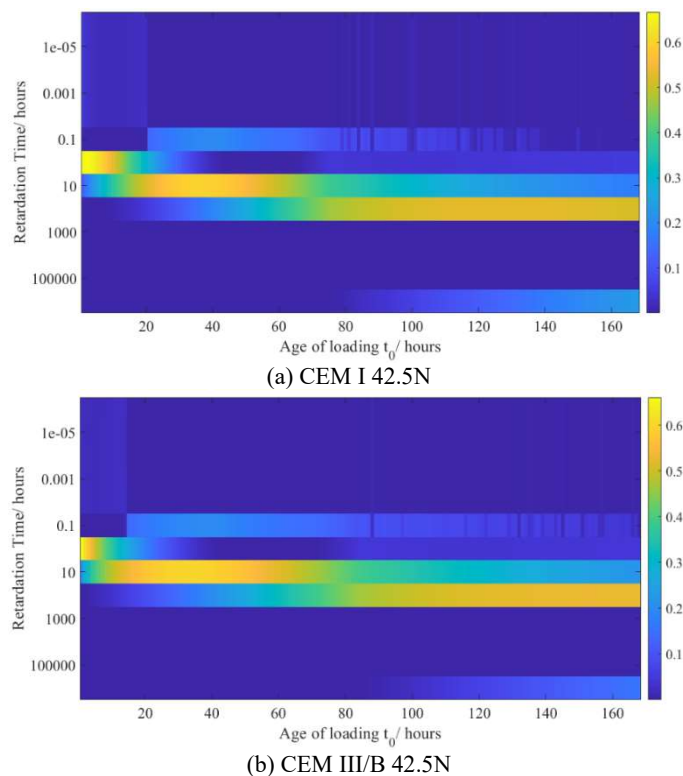
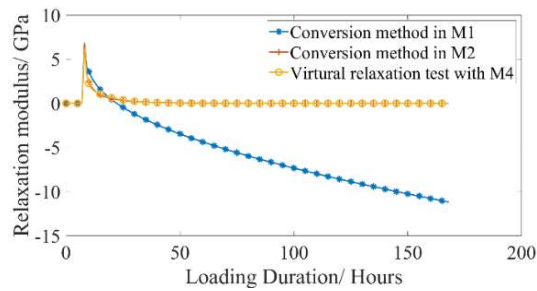
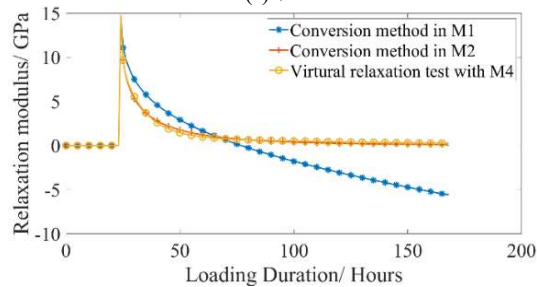


**Figure 7-13** Spectrum of the Maxwell chain model of two types of adopted cementitious materials: (a) CEM I 42.5N; (b) CEM III/B 42.5N

The relaxation modulus can be obtained by applying a constant unit displacement on the top of the prism, which can then be compared to the input of the adopted Maxwell chain model (i.e., checkpoint 1). The relaxation modulus in the virtual relaxation test is shown in **Figure 7-14**. The relaxation moduli obtained by M1 and M2 are also compared. From the perfect match between the relaxation modulus obtained by M4 and M2, it is clear that the exponential algorithm based on the Maxwell chain can simulate the relaxation behavior with good precision, indicating the applicability of M4 in EAS simulation. By applying a constant unit load on top of the prism, virtual creep tests can be done, and checkpoint 2 can be examined, as shown in **Figure 7-15**. If M2 can perfectly reflect the coupling between creep and relaxation, then the obtained creep compliance in virtual creep test should match the experimental results. However, the results of checkpoint 2 in **Figure 7-15** clearly show that at an early age, the creep compliance function obtained by M4 (which is calibrated based on the input of M2) does not match the experimental creep results. However, at a later age, the difference decreases. At 72 hours, the two creep compliance curves become very similar. Such a pattern has been shown in the integral check of M2, in which the integral values are far from 1 if at an earlier age, and vice versa. Since M4 is calibrated by the relaxation modulus of M2, a similar weak coupling between creep and relaxation like M2 at a very early age is understandable.

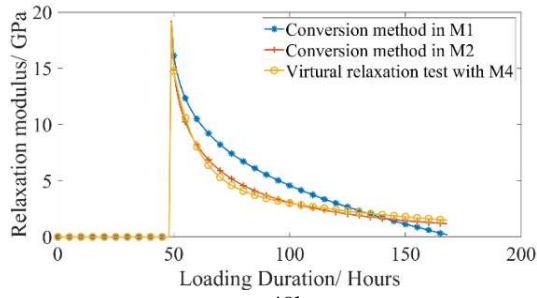


(a) 7h

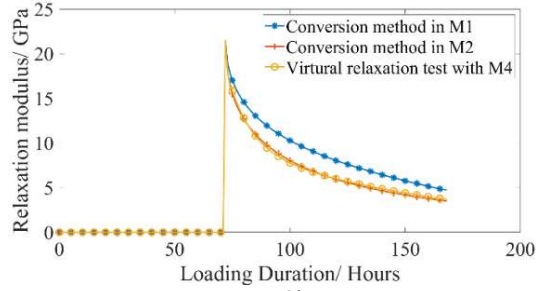


(b) 24h

(Continue in the next page)

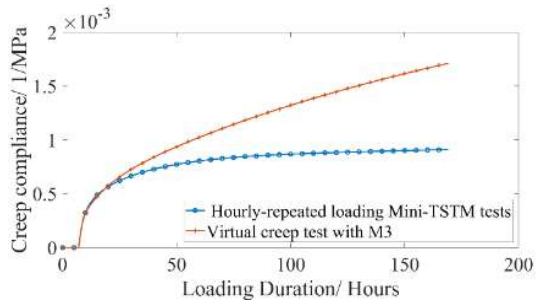


(c) 48h

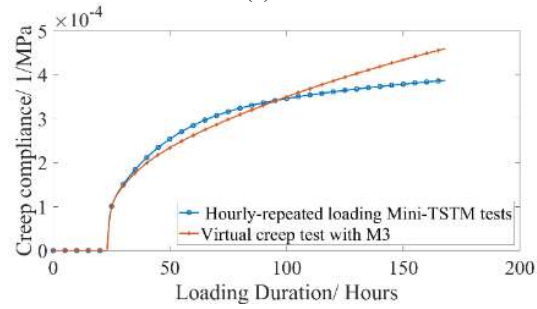


(d) 72h

**Figure 7-14 Relaxation modulus obtained from virtual relaxation test of M4 (checkpoint 1), with time of loading  $t_0=7, 24, 48,$  and  $72$  hours for Fig (a~ d), respectively.**



(a) 7h



(b) 24h

(Continue in the next page)

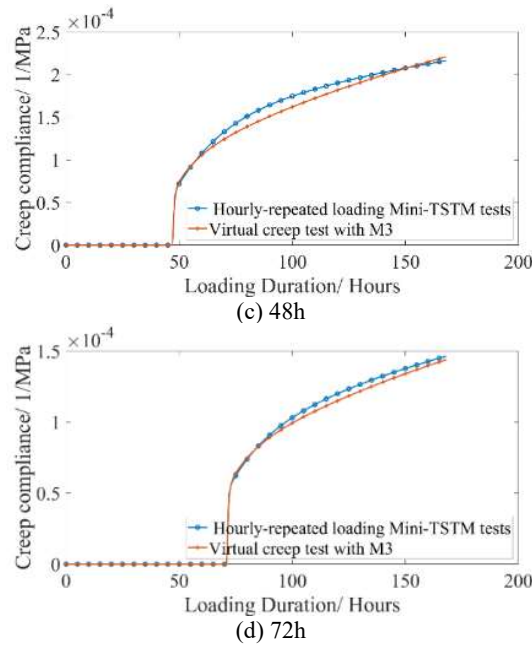


**Figure 7-15 Creep compliance obtained from virtual creep test of M4 (checkpoint 2), with time of loading  $t_0=7, 24, 48,$  and  $72$  hours for Fig (a~ d), respectively.**

Overall, given the input of the creep compliance function or relaxation modulus function, M3 and M4 can perfectly simulate the creep and relaxation behavior with high precision, respectively. However, M3 and M4 cannot well reflect the coupling between creep and relaxation. In M3, given the creep compliance function as input, the relaxation modulus obtained from a virtual relaxation test can be negative, especially when the loading time  $t_0$  is small. Such a problem is similar to M1 which is understandable since M1 and M3 are based on the same original Volterra integral (Eq (7-5)). To simulate EAS in this chapter, a negative relaxation modulus may not be favorable because it conveys a problematic relaxation process with a change of stress direction. On the other hand, using the relaxation modulus obtained by M2 as input for the M4, a more reasonable relaxation modulus can be obtained in the virtual relaxation test, which always converges to 0. However, a weaker coupling between creep and relaxation still exists at a very early age (as observed in the integral check of M2).

### 7.4.3 Prediction of early-age stress (Checkpoint 3)

In this section, the M1~M4 will be used to predict the EAS using the AD (Figure 5-8 (b) and Figure 5-9(b)) and measured viscoelastic properties (Eq (5-6) with parameters in Table 5-3) as input. The predicted EAS can

then be compared to the experimental results of EAS (in **Figure 5-8 (a)** and **Figure 5-9(a)**). For 1D analysis methods M1 and M2, the prediction of EAS was calculated based on Eq (7-4), using the relaxation modulus given by Eq ((7-8)~(7-13)) and Eq (7-19), respectively. For 3D analysis methods M3 and M4, the prediction of EAS was simulated based on the dog-bone specimen with two ends fixed, similar to the Mini-TSTM test (**Figure 5-1 (c)**). The exponential algorithm based on Kelvin and Maxwell chains was implemented based on Eq ((7-20), (7-22)~(7-24)) and Eq ((7-20), (7-29)~(7-31)), respectively. The experimental and numerical results of EAS are shown in **Figure 7-16** below. To display the difference between the experimental and numerical results, the RMSE was calculated based on Eq (7-35). Note that for M1, there are four different variants:

- 1) M1: Original M1, based only on Eq ((7-8)~(7-12)).
- 2) M1-zeroed: Adjusted M1, which sets all negative relaxation modulus obtained by M1 as 0.
- 3) M1-2: Improved M1, based on Eq ((7-8)) and Eq ((7-10)~(7-13)). The initial condition changes in Eq (7-13) mainly aim to reduce the error of high nonlinearity of the relaxation modulus function [111].
- 4) M1-2-zeroed: Adjusted M1-2 sets negative relaxation modulus obtained by M1-2 as 0.

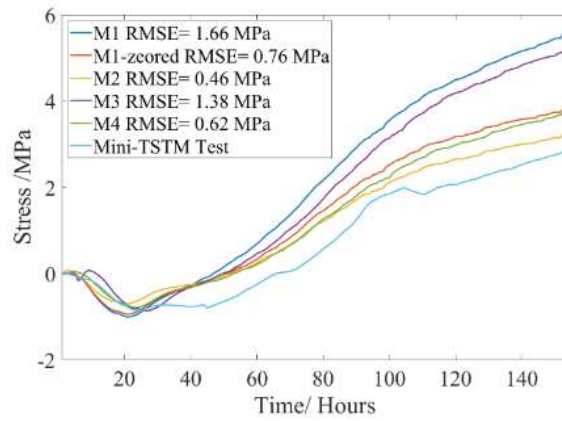
**Figure 7-16** shows only the original and adjusted M1 for clarity. But RMSEs of all studied methods are shown in **Table 7-1**. Comparing the averaged RMSEs of all models, the rank of prediction accuracy is as follows: M2 (0.265) < M4 (0.297) < M1-2-Zeroed (0.302) < M1-Zeroed (0.393) < M1-2 (0.52) < M1 (0.743) < M3 (0.775). The following analysis can be obtained:

- 1) Models M2 and M4 both show good accuracy with a low averaged RMSE below 0.300 MPa. Note that M4 is the FEM model that can be generalized to 3D analysis of a more realistic structure. At the same time, M2 is a simple model for 1D analysis, such as the uniaxial restraint test in this study. A similar accuracy of M2 and M4 is expected because M4 uses the relaxation modulus derived from M2 to calibrate the spectrum of the Maxwell chain. The good prediction accuracy of M2 and M4 also shows that, in the results of Mini-TSTM and Mini-ADTM tests, each AD is an exclusive description of the corresponding EAS results, which verifies the variation of AD between different batches of cement.
- 2) Models M1 and M3 obtain the highest RMSE and, therefore, the lowest accuracy of EAS prediction. This result is expected if considering the influence of high nonlinearity of the relaxation modulus function [111], which causes underestimation of relaxation modulus calculation if strictly following Eq ((7-8)~(7-12)) for the conversion. The similar performance of M1 and M3 is expected

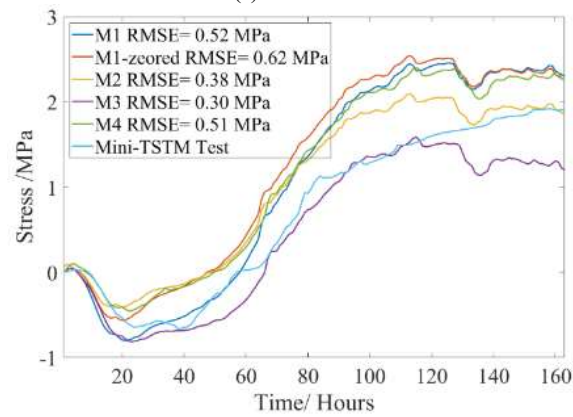
- because both are based on the same governing equation: M3 employs the exponential algorithm using the Kelvin chain by Eq ((7-20), (7-22)~(7-24)), which is initially derived by the incremental form of Eq (7-5), and Eq (7-5) is also the basis of M1.
- 3) The negative values of relaxation modulus and error brought by the high nonlinearity of the relaxation function in the conversion process are mainly responsible for the poor prediction: By correcting all the negative relaxation modulus to 0, the prediction accuracy is significantly improved, which can be seen by comparing the RMSE of M1 to M1-zeroed and M1-2 to M1-2-zeroed. By reducing the error brought by the high nonlinearity of the relaxation function using Eq (7-13), the prediction accuracy is also improved, which can be seen by comparing the RMSE of M1 to M1-2 and M1-zeroed to M1-2-zeroed. If correcting both, the adjusted M1-2-Zeroed can obtain comparable accuracy to M2 and M4, which brings a low averaged RMSE of around 0.302 MPa.
  - 4) It should be noted that simply correcting all negative values to zero or applying a different initial condition (as in Eq (7-13)) may not intrinsically solve the numerical issue induced by the high nonlinearity of the relaxation function. Therefore, such improvement cannot be extended to 3D models (i.e., M3). For better application of M3 in EAS analysis, improvements are needed, given the high nonlinearity of relaxation functions. Alternatively, this study proves that the M4 model, which uses the relaxation modulus from M2 as input, is well applicable in EAS simulation.

Overall, the analysis above proves that the M4, based on aging Maxwell Chain, exponential algorithm, and the exponential conversion from creep to relaxation, can well address the problem of negative relaxation modulus and high non-linearity as brought by M1 and M3, and therefore significantly improves the EAS prediction accuracy. Despite the EAS can be well quantified through M3, it is worth mentioning that the EAC criterion is equally important to achieve a full assessment of EAC risk. A straightforward assessment criterion is the stress-nominal strength ratio. Many studies [278] on TSTM tests showed that EAC always happens before the stress- nominal strength ratio reaches 1.0 and mostly between 0.60 and 0.80. Therefore, for engineering applications, a stress- nominal strength ratio of 0.5 is often used. To precisely assess the EAC risk, a more sophisticated damage criterion is needed, which often combines the EAS and strain [24]. Moreover, it should be noted that, the models M1~M4 are built based on the Boltzmann superposition, which assumes that the EAS induced at every time point is additive. However, this assumption is less valid and can compromise the EAS prediction accuracy when the stress is close to the strength. Finally, it should be mentioned that this chapter uses the EAS caused by AD as an example. The calculation methods hold also for

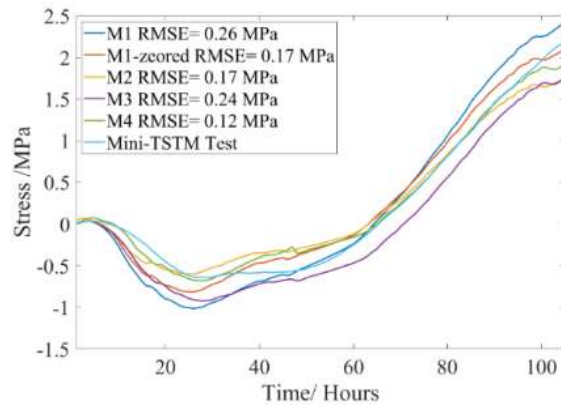
the EAS caused by thermal and drying deformation, since the imposed deformation does not refer to a specific type of deformation.



(a) C1-30-1

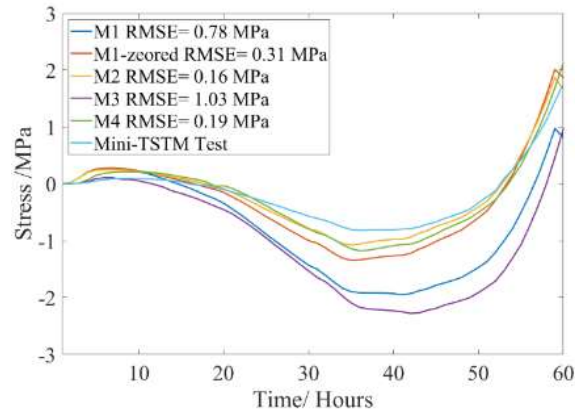


(b) C1-30-2

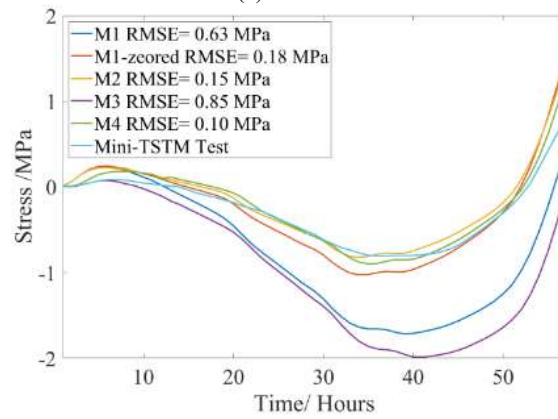


(c) C1-30-3

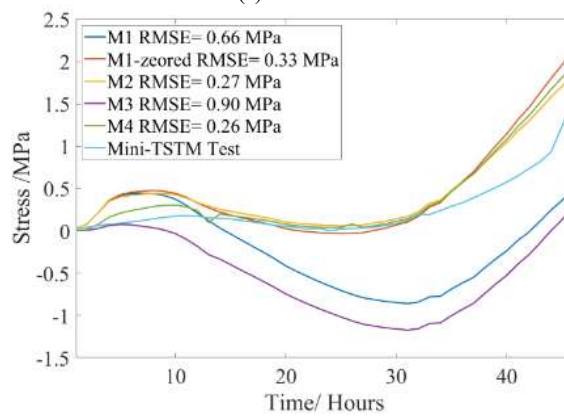
(Continue in the next page)



(d) C3-30-1



(e) C3-30-2



(f) C3-30A

Figure 7-16 Experimental and numerical results of EAS, Fig (a~f) corresponds to results of C1-30-1, C1-30-2, C1-30-3, C3-30-1, C3-30-2, C3-30-3, respectively.

**Table 7-1 RMSE between predicted EAS made by M1~M4 with 6 tested EAS.**

	M1	M1-zeroed	M1-2	M1-2-zeroed	M2	M3	M4
C1-30-1	1.62	0.75	1.20	0.59	<b>0.47</b>	1.35	0.61
C1-30-2	0.52	0.63	0.49	0.49	0.38	<b>0.28</b>	0.51
C1-30-3	0.26	0.17	0.17	0.15	0.17	0.24	<b>0.12</b>
C3-30-1	0.79	0.30	0.50	0.18	<b>0.15</b>	1.03	0.18
C3-30-2	0.63	0.18	0.35	0.14	0.15	0.85	<b>0.10</b>
C3-30-3	0.64	0.33	0.41	<b>0.26</b>	0.27	0.90	<b>0.26</b>
Average	0.74	0.39	0.52	0.30	<b>0.27</b>	0.78	0.29

## 7.5 Conclusions

This chapter investigated four different numerical approaches (two for 1D analysis and another two for 3D analysis) for simulating the EAS evolution in cementitious materials. Based on the experimental results of AD, viscoelastic properties (i.e., elastic modulus and aging creep), and EAS of two different cement pastes (i.e., CEM I 42.5N and CEM III/B 42.5N) in chapter 5, the theories, applicability, and reasonability of the four different numerical models M1~M4 were introduced and analyzed in detail. The following conclusions can be drawn:

- 1) As the numerical solution of the Volterra integral, the 1D model M1 and 3D model M3 both lead to negative relaxation modulus in a similar manner, which is physically impossible and suggests that the M1 and M3 can induce more error when simulating EAS. As expected, in the EAS comparison, M1 and M3 show the highest error. However, it should be noted that the negative issue of M1 is mainly induced by the fast aging in very early age. For mature material or long-term creep/relaxation analysis, such negative issue can be neglected.
- 2) Derived by the definition of a relaxation test, the M2 can provide reasonable relaxation modulus using the measured viscoelastic properties as input. The 1D model M2 obtained the highest accuracy in EAS prediction among the investigated models. To generalize into 3D, a FEM model with the exponential algorithm based on the Maxwell chain (i.e., M3) was developed, which takes the relaxation modulus of M2 as input and obtains good prediction accuracy of EAS in 3D analysis that is comparable to M2.

- 3) The relaxation modulus function's high nonlinearity is the main reason for the negative relaxation modulus. By correcting the negative relaxation modulus to zero and using a different initial condition, the error brought by such non-linearity can be reduced, and good prediction accuracy of EAS can be obtained (see the prediction performance of M1-2-Zeroed).
- 4) The prediction of EAS made by the models M1-2-Zeroed, M2, and M4 all predicts the EAS based on the AD with a high accuracy, indicating that each of the AD s is an exclusive description of the corresponding EAS evolution, despite variations in AD in different batches of the same type of cement.



# 8. A SURROGATE MODEL OF EARLY AGE STRESS EVOLUTION IN RESTRAINED CONCRETE BASED ON THERMO- CHEMO- MECHANICAL SIMULATION AND ACTIVE LEARNING

*This chapter encompasses a thermo-chemo-mechanical (TCM) model and Active Ensemble Learning (AEL) for predicting the EAS evolution. First, a TCM model is built to simulate the heat transfer, cement hydration, viscoelasticity and the early-age stress (EAS) evolution. Then, a material model composed by an XGboost model and adjusted Model Code 2010 is built to allow for parametric study and database construction. Finally, an AEL framework is built for EAS prediction. This study resulted in the following findings: 1) The dimensionality of the 672-by-1 EAS vector can be effectively reduced by PCA, and the 1st principal component (PC) is a global index representing the magnitude of the EAS; 2) Correlation analysis on the 1<sup>st</sup> principal component (PC) quantifies the influence of various input parameters of the TCM model, which complies with common understandings of the EAS evolution process. 3) The AEL and One-Shot Ensemble Learning (OSEL) both achieve high prediction performance in the testing set, whose  $R^2$  reaches 0.961 and 0.948, respectively. 4) AEL can significantly reduce the number of samples required for training, which is a major improvement in efficiency considering the computational cost of the TCM model.*

*Parts of this chapter have been published in Liang, M., Chang, Z., He, S., Chen, Y., Gan, Y., Schlangen, E., & Šavija, B. (2022). Predicting early-age stress evolution in restrained concrete by thermo-chemo-mechanical model and active ensemble learning. *Computer-Aided Civil and Infrastructure Engineering*, 37(14), 1809–1833.*

## 8.1 Introduction

Early-age stress (EAS) is an important indicator of the early-age cracking (EAC) risk. Based on various restraint tests [28,224,226,227], the EAS under different temperature histories can be quantified. However, these tests are often time-consuming, laborious, and resource intensive. As a result, to quantify the EAS evolution over a wide range of parameters, computer-aided modeling techniques could be an alternative approach to overcome these practical difficulties, allowing wide-range parametric studies.

EAS evolution is a result of multiple physical and chemical process occurring during the early age of concrete structures, including the hydration reaction of cement, heat transfer, autogenous shrinkage, drying shrinkage, and creep/relaxation [238,283]. Therefore, a multifield model that capable of coupling the aforementioned effects is needed to simulate the EAS [96,97,298,317,328–332]. However, the complexity of such models results in a huge demand of computational resources. An effective way to cope with this is through data-driven approaches (or so-called surrogate models, Machine Learning models, metamodels, etc.) [333–337]. These data-driven models adopt advanced training/fitting algorithms to build statistical model with fixed weights to directly map the input parameters to the objective, which can replace the original complex model. Such data-driven approaches have been used for prediction of autogenous shrinkage [91], drying shrinkage [92], creep [174,201], crack propagation [338], compressive strength [339], elastic modulus [340], breakout capacity [341], shear capacity [342], slump flow [343], flexural strength [344], interfacial bond strength [345], etc.

The performance of surrogate models lies in the adequacy of the data. An efficient way for building up database and training machine learning models is the active learning approach [346,347], by which the surrogate model is adaptively trained based on a selective set of data samples. An active ensemble learning model is developed in this chapter, which is trained using the data generated by a Thermo-Chemo-Mechanical (TCM) model for efficiently predicting the EAS evolution. The workflow of this chapter is shown in [Figure 8-1](#). The sampling space is first generated by the Latin Hypercube Sampling (LHS) method and processed by a material model, which is built by an eXtreme Gradient Boosting (XGBoost) Machine Learning model and Model Code 2010 (MC 2010) [113]. Based on the Fourier's law, Arrhenius' equation, the maturity concept, and the rate-type creep law [111], the TCM model is built to simulate the hydration effects,

thermal deformation, creep/ relaxation of concrete, and run incremental viscoelastic analyses of EAS evolution. In the Active Ensemble Learning (AEL) process, Principal Component Analysis (PCA) is conducted first to reduce the dimensionality of the EAS vector and perform correlation analysis. The AEL process uses a Gaussian Process (GP) model to measure the uncertainty for active sampling and train a Light Gradient Boosting Machine (LGBM) on the selective sample. In each learning step, the most uncertain sample (measured by the variance distribution) is selected by the GP model and imported to the TCM model as input. The EAS output by the TCM model is then used to update the GP model and the LGBM model. The generalization capabilities of AEL are quantified by cross validation and compared with One-Shot Ensemble Learning (OSEL).

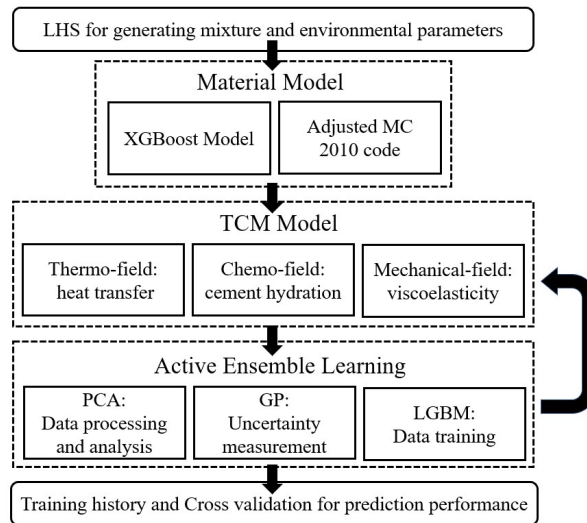


**Figure 8-1 Work flow of this chapter**

## 8.2 Thermo-Chemo-Mechanical (TCM) Model

The formulation of the multifield TCM model is shown in [Figure 8-2](#). In previous studies on multifield modelling of early-age concrete [96,97,331,332], the applicability of Fourier's law for heat transfer and Arrhenius's equation for hydration reaction have been validated. These two constitutive equations are also adopted in this work to simulate the thermo- and chemo- field of the TCM model. The thermo- and chemo- fields are fully coupled by the temperature and hydration degree: the temperature distribution output by the thermo- field is in the exponential term of the hydration degree kinetics in the chemo-field, while the

hydration degree output by the chemo-field is in the heat source term of the thermo-field. In the TCM model, the temperature distribution/ evolution influences the hydration kinetics and results in different developing speed of the concrete properties and behaviors. This impact is quantified by the equivalent age of the maturity concept, as shown in the upper arrow connecting the TC-field and material model in the [Figure 8-2](#). On the other hand, the temperature distribution/ evolution induces thermal deformation, which is restrained by the boundary and is one of the major deformations that causes EAS. This impact is quantified linearly by a coefficient of thermal expansion, as shown in the lower arrow connecting the TC-field and material model in the [Figure 8-2](#).

Note that the hygro-field, which is important for shrinkage and creep, is not considered in this chapter due to the following reasons: 1) general formulas of material parameters involved in hygro-field are scarce; 2) the mechanisms of autogenous shrinkage, drying shrinkage, and creep induced by moisture transport are still under debate; 3) the heterogeneity of concrete plays an important role in the hygro-field, and the mechanisms for building a micro- or meso- scale model for a wide range of practical cases are not clear. In view of these complexities, this chapter refers to the MC 2010 to retrieve the input of shrinkage and creep from empirical formulas. The material model is constructed by an XGBoost model and an adjusted MC 2010. The XGBoost is used to predict the compressive strength based on given mixture parameters. Subsequently, the compressive strength is used as one of the input parameters for the MC 2010. Thereby, the material model can output the evolution of shrinkage, creep compliance, and elastic modulus, which provide input for the TCM model.

The mechanical-field is formulated by a 13-unit Kelvin chain rheological model, and solved incrementally by the exponential algorithm [348]. Taking the output of the material model and the TC field, the mechanical field can output the EAS evolution (i.e., a 672 by 1 vector), which is prepared for the further AEL process.

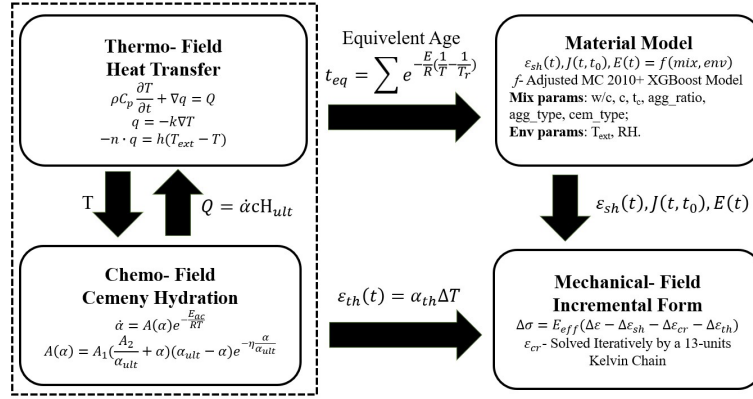


Figure 8-2 Formulation of the TCM model

### 8.2.1 Chemo-field

In this chapter, the hydration reaction is simulated as an overall hydration process, similar to many other multifield models [96,97,299,328,329,349]. Assuming that the hydration kinetics can be described by postulating the existence of a Gibb's free energy dependent on temperature and hydration extent, the hydration reaction can be described by the following Arrhenius-type equation [97,329,350]:

$$\dot{\alpha} = A(\alpha)e^{-\frac{E_{ac}}{RT}} \quad (8-1)$$

$$A(\alpha) = A_1 \left( \frac{A_2}{\alpha_{ult} + \alpha} + \alpha \right) (\alpha_{ult} - \alpha) e^{-\eta \frac{\alpha}{\alpha_{ult}}} \quad (8-2)$$

where  $\alpha$  is the hydration degree; the  $(\cdot)$  in Eq (8-1) represents the first-order derivative with respect to time;  $E_{ac}$  is the apparent activation energy;  $R$  is the universal gas constant;  $T$  is the temperature;  $\eta$ ,  $A_1$ , and  $A_2$  are fitting parameters corresponding to a certain type of cement, which can be calibrated according to adiabatic test results [97];  $\alpha_{ult}$  is the ultimate hydration degree dependent on the water cement ratio, which can be expressed as [351]:

$$\alpha_{ult} = \frac{1.031w/c}{0.194 + w/c} \quad (8-3)$$

In this chapter, three sets of fitting parameters  $\eta$ ,  $A_1$ , and  $A$  are used to represent three cement types (i.e., SL, N, R corresponding to slow, normal, and rapid set cement respectively), as classified by the MC 2010 [113]. The value for apparent activation energy  $E_{ac}$  is dependent on the cement type and temperature. The activation energy decreases with temperature when the temperature is lower than 20°C, but remains constant when

temperature is equal to or higher than 20°C [302]. Based on tests, the following bilinear relationship for apparent activation energy has been proposed [49]:

$$E_{ac} = \begin{cases} E_{ac,0}, & \text{if } T \geq 20^\circ\text{C} \\ E_{ac,0} + 1470(20 - T), & \text{if } T < 20^\circ\text{C} \end{cases} \quad (8-4)$$

where  $E_{ac,0}$  is the apparent activation energy of a certain cement type at 20 °C. The specific parameters can be found in the Section 8.3.3. At every time step, the output of the hydration degree  $\alpha$  of the chemo-field is used to compute the hydration heat of cement, which is the heat source term of the thermo-field, as will be shown in Section 8.2.2.

### 8.2.2 Thermo-field

When temperature is below 100 °C, the heat conduction in concrete can be described by Fourier's Law [49]:

$$\rho C_p \frac{\partial T}{\partial t} + \nabla q = \dot{Q} \quad (8-5)$$

$$q = -k\nabla T \quad (8-6)$$

$$-n \cdot q = h(T_{ext} - T) \quad (8-7)$$

where  $\rho$  is the density of concrete;  $\nabla$  is the Nabla operator which calculates the spatial gradient,  $\nabla = (\frac{\partial}{\partial x}, \frac{\partial}{\partial y}, \frac{\partial}{\partial z})$ ;  $C_p$  is the heat capacity;  $q$  is the heat flux;  $k$  is the thermal conductivity. Note that Eq (8-7) is the convective boundary attached to the surface of the concrete specimen, where  $n$  is the normal vector of the specimen surface;  $h$  is the heat transfer coefficient, and  $T_{ext}$  is the environmental temperature. The internal heat source term  $\dot{Q}$  in Eq (8-5) represents the heat release rate of cement hydration, which can be calculated by the hydration degree from the chemo-field, expressed as follows [329]:

$$\dot{Q} = \dot{\alpha} c Q_{ult} \quad (8-8)$$

where  $c$  is the cement mass,  $Q_{ult}$  is the ultimate heat release of the hydration reaction per unit weight of cement, which is determined by the cement composition and can be measured by calorimetric tests. Typical values of  $Q_{ult}$  range from 400 kJ/kg to 550 kJ/kg [352]. In this chapter, three sets of values of  $Q_{ult}$  will be used to represent the three types of cement (see Section 8.3.3). The temperature distribution output by the thermo-field influences the hydration process (see Eq(8-1)), which ensures the full two-way coupling between the thermo- and the chemo-field.

In addition, the temperature distribution output by the thermo-field induces thermal deformation, expressed as:

$$\varepsilon_{th}(t) = \alpha_{th}\Delta T \quad (8-9)$$

where  $\alpha_{th}$  is the linear coefficient of thermal expansion (a constant value of  $1.0 \times 10^{-5}$  [1/K] is adopted herein [353]). On the other hand, the temperature distribution output by the thermo-field also determines the equivalent age of concrete, calculated by the maturity concept [49]:

$$t_{eq} = \sum e^{-\frac{E_{ac}}{R}(\frac{1}{T} - \frac{1}{T_r})} \quad (8-10)$$

where  $t_{eq}$  is the equivalent age;  $T_r$  is the reference temperature, which is 20 °C. The equivalent age  $t_{eq}$  calculated in Eq (8-10) will be used as the index of time to query the concrete properties and behavior from MC 2010, see the section 8.3.3.

### 8.2.3 Mechanical field

With the temperature output from the thermo- and chemo- field, the thermal deformation of the concrete can be determined. Meanwhile, the evolving properties and behaviors (i.e., shrinkage, creep) can be queried from MC 2010 based on the maturity concept, and used as input for the mechanical-field to carry out the EAS computations. The EAS is a direct index for evaluating the EAC risk by analysing the stress levels or cracking indexes (i.e., the ratio between the stress level and the tensile strength). In this section, the mechanical-field focuses on the EAS evolution in the pre-cracking stage; therefore, local cracks and damages in stress singular points are disregarded, as recommended by the RILEM TC 287-CCS on TCM modelling of EAC risk of concrete [238]. Besides, most the creep models assume that no damage occurs, and general formulas allowing for parameterization over a wide range of concrete properties and damage status are scarce. Thereby, the mechanical-field takes the viscoelasticity of concrete as the main mechanical constitutive model to compute the EAS evolution. In this section, the Kelvin-chain based model from chapter 2 is used to simulate the EAS evolution, with the incremental viscoelastic constitutive model as below:

$$\Delta\sigma = E^* \Delta\varepsilon - \sigma^* \quad (8-11)$$

$$E^*(t^*) = \frac{1}{\frac{1}{E_0(t^*)} + \sum_{j=1}^N \frac{1}{E_j(t^*)} (1 - (1 - e^{-\frac{\Delta t}{\mu_j}}) \frac{\mu_j}{\Delta t})} \quad (8-12)$$

$$\sigma^*(t_i) = E^*(t^*) \sum_{j=1}^N (1 - e^{-\frac{\Delta t}{\mu_j}}) \varepsilon_j^*(t_i) \quad (8-13)$$

$$\varepsilon_j^*(t_{i+1}) = e^{-\frac{\Delta t}{\mu_j}} \varepsilon_j^*(t_i) + \frac{1}{E^*(t_i)} (1 - e^{-\frac{\Delta t}{\mu_j}}) \frac{\mu_j}{\Delta t} \quad (8-14)$$

where  $\Delta\sigma$  and  $\Delta\varepsilon$  are the incremental stress and strain between two consecutive time steps  $t_i$  and  $t_{i+1}$ ;  $t^*$  is the average of two consecutive time steps  $t_i$  and  $t_{i+1}$ ;  $E_j$  and  $\mu_j$  are the elastic modulus and retardation time of  $j$ -th Kelvin chain units.

#### 8.2.4 Multifield model configuration

The geometry of the dog-bone specimen in the TSTM test in chapter 2 is used in the TCM model, which has a  $100 \times 150 \times 850$  mm<sup>3</sup> prism in the middle, and two clamping heads at the two ends. The dog-bone specimen simplifies structural factors (geometry, boundary conditions) which can significantly vary from case to case and are difficult to parametrize in a single model. Moreover, considering that the EAC is intrinsically caused by the material behavior (e.g., shrinkage and creep), the TSTM test configuration (and therefore the TCM-based AEL model) is used as a general and standard scenario for EAC risk evaluation. Hexahedral elements are used to mesh the whole specimen. Finer mesh is applied at the two ends of the middle prismatic part, as shown in **Figure 8-3**. A study on the influence of mesh size on the modelling results was performed in chapter 2, by changing the number of elements from 270 to 6318. It was found that the EAS results remain constant after increasing the number of elements from 1150 to 6318. Therefore, the number of elements in the current meshing scheme is taken as 1150 and the mesh size varies from 25mm to 145mm.

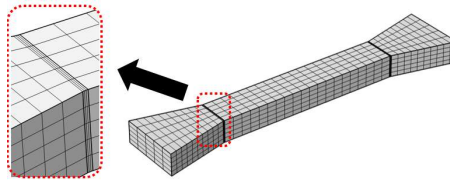


**Figure 8-3** Meshing scheme of the TSTM specimen

The boundary conditions for the thermo- and mechanical- field are shown in **Figure 8-4**. Convective boundary is applied to all surfaces of the specimen to determine the heat transfer between the specimen and the environment (see Eq (6-5)). Roller boundary, which restricts the normal deformation of the surface to 0, is attached to the lateral surface of the two ends of the dog-bone specimen.

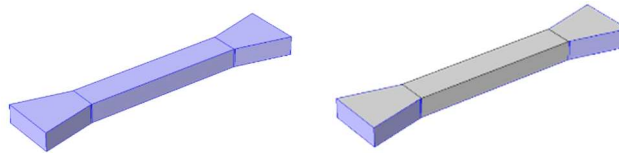


**Figure 8-4 Boundary conditions (Highlighted area): (a) Convective boundary; (b) Roller boundary**

To solve the system of ordinary and partial differential equations formed by the thermo-field (Eq (8-5)~(8-8)), chemo-field (Eq (8-1)~(8-2)) and mechanical-field (Equilibrium equation  $\nabla\sigma + F_v = 0$ , strain equation  $\varepsilon = \frac{1}{2}(\nabla u + (\nabla u)^T)$ ), and viscoelastic constitutive equation (Eq(8-11)~(8-14)), the backward difference method and damped Newton method are adopted to obtain convergent numerical solutions. Detailed procedure regarding the numerical solver can be found in [354,355]. A fixed time step (i.e.,  $\Delta t$ ) when conducting the backward difference method is needed due to the mid-point integration approximation in (Eq(8-11)~(8-14)). In this chapter, a time step of 1 hour is used, and the time range of interest is from 0 to 672 hours.

### 8.3 Material model

The formulation of the material model is shown in **Figure 8-5**. First, the mixture parameters are imported to an XGBoost model [356] for compressive strength prediction. Then, based on the predicted compressive strength and other parameters such as the ambient temperature and relative humidity, the MC 2010 model provides elastic modulus, creep, and shrinkage, which can be finally imported to the TCM model and used to calculate the EAS development. To consider a practical case of EAC, this study uses the following eight input parameters for the TCM model and AEL model: 1)  $c$ : cement mass; 2)  $w/c$ : water-to-cement ratio; 3)  $a/c$ : aggregate-to-cement ratio; 4)  $c\_type$ : cement type; 5)  $T$ : environmental temperature; 6)  $RH$ : environmental relative humidity; 7)  $t_c$ : time of curing, indicating the start of drying shrinkage; 8)  $a\_type$ : aggregate type. Note that parameters  $c\_type$  and  $a\_type$  are sparse categorical parameters that will be specified in Section 8.3.3. The parameter  $VS$  is the notational size of the specimen. Based on the formula of MC 2010 [113], the notational size of the dog-bone specimen used in the TCM model is calculated as 85.7 mm, according to the geometry of the TSTM test specimen [235].

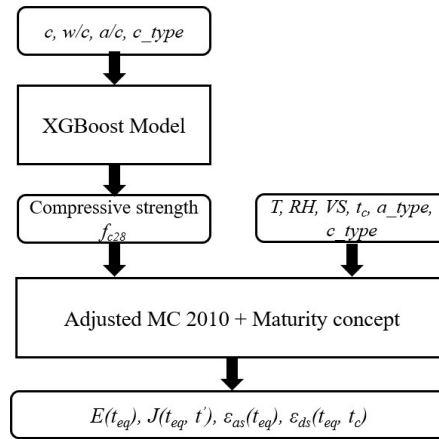


Figure 8-5 Formulation of the material model

### 8.3.1 Adjusted MC 2010

This chapter uses most of the formulas of MC 2010 [113], except for an adjustment in the drying shrinkage calculation. In the MC 2010, drying shrinkage is calculated as:

$$\varepsilon_{ds}(t, t_c) = \varepsilon_{ds0}(f_{c28})\beta_{RH}(RH)\beta_{ds}(t - t_c) \quad (8-15)$$

where  $\varepsilon_{ds0}$  is the asymptotic value of drying shrinkage, depending on the 28-day compressive strength  $f_{c28}$ ;  $\beta_{RH}$  is the coefficient for the effects of relative humidity;  $\beta_{ds}$  is the coefficient for the effects of drying time. However, Eq (8-15) neglects the evolving effects of drying shrinkage, by assuming the same drying shrinkage evolution even though the time of curing  $t_c$  may be different. It is clear that drying shrinkage starting from different age is different: with longer curing time, drying shrinkage starts at a more mature age and can be much lower [8,92]. In the TCM model, this would result in a jump in the EAS curve at the end of curing time. Thereby, in this study, an aging coefficient term is added to Eq (8-15) to complement this effect:

$$\varepsilon_{ds}(t, t_c) = \varepsilon_{ds0}(f_{c28})\beta_{tc}(t_c)\beta_{RH}(RH)\beta_{ds}(t - t_c) \quad (8-16)$$

$$\beta_{tc}(t_c) = \exp\left(1 - \left(\frac{t_c}{3}\right)^{0.21}\right) \quad (8-17)$$

where  $\beta_{tc}$  is the aging term, depending on the curing of time. The aging term of Eq (8-17) results in an exponential decay of drying shrinkage as the curing time increases. Note that the coefficients of Eq (8-17) are fitted by the results of [92], and are only used tentatively in this study to account for

the aging effects of drying shrinkage. For a solid conclusion about the aging pattern of drying shrinkage, additional experiments should be performed.

### 8.3.2 XGBoost model for compressive strength

Another important module of this material model is the XGBoost model for predicting the compressive strength, which is a significant input for the MC 2010. A number of studies on compressive strength prediction based on mix parameters have validated the advantages of XGBoost model over many other Machine Learning models and standard codes [357]. Based on the database of Northwestern University [203], an XGBoost model was created herein to predict the 28-day compressive strength of concrete, based on mixture proportions, including cement amount, water-cement ratio, aggregate-cement ratio, and cement type [356]. The database contains 2606 data of compressive strength and is open-source. Based on a total number of 490 decision trees, the XGBoost model is trained based on 1825 samples with a learning rate of 0.1712. As shown in **Figure 8-6**, with 1825 samples in the training set, the coefficient of determination ( $R^2$ ) over 781 unseen samples is 0.94. High accuracy in the testing set indicates the effectiveness of the XGBoost and the hyperparameter settings. Before XGBoost is incorporated in the material model, it is trained with the whole dataset to ensure the best prediction accuracy. It should be noted that typically 8-12 features are used in a compressive strength predictor. However, only the four most influential parameters are used as features of XGBoost model. This is done to remain consistent with the MC 2010 model, and can to some extent sacrifice the applicability of the XGBoost model.

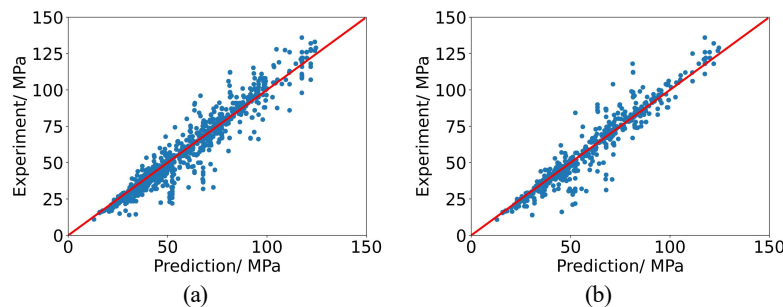


**Figure 8-6** Cross-validation results of the XGBoost Model of compressive strength: (a) Training set, 1825 samples,  $R^2=0.9837$ ; (b) Testing set, 781 samples,  $R^2=0.9443$

### 8.3.3 Parameter settings

The parameters used in the TCM model are given in **Table 8-1**. In the thermo-field, constant values are assumed for thermal conductivity and heat capacity of concrete, according to [358]. The heat transfer coefficient

is also taken as constant, assuming a curing measure of “Curing blanket and plastic sheet” according to [359]. Parameters  $A_1$ ,  $A_2$ , and  $\eta$  are material parameters controlling the chemical affinity and hydration degree in Eq (8-1)~(8-2).  $A_1$ ,  $A_2$ , and  $\eta$  can be obtained by fitting the temperature rise in an adiabatic test [329]. For the parameter *Ultimate hydration heat* and fitting parameters  $A_1$ ,  $A_2$ , and  $\eta$ , 3 different values are assumed for each parameter to characterize different cement types  $c\_type$  according to [96,97]. Furthermore, four aggregate types are contained in the parameter  $a\_type$ . The categorical parameter settings for cement type and aggregate type are shown in Table 8-2. The specific values for these parameters are determined by referring to published multifield models and thermal properties of concrete [96,97,360]. Note that the parameters settings are only used to set up the framework for parametric analysis of the TCM model and serve as the database for building the AEL model. For practical use, the parameter settings should be first validated through a rigorous experimental procedure.

**Table 8-1 Parameter settings of the TCM model**

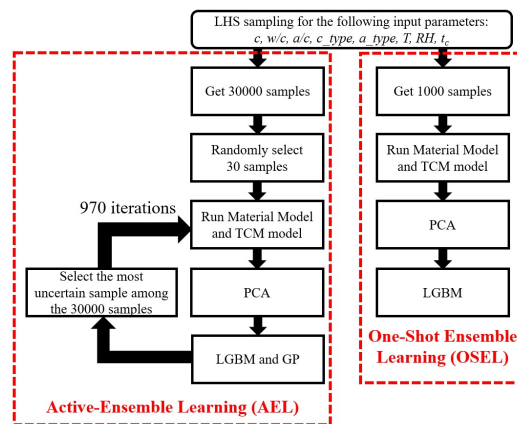
<b>Thermo-field</b>	
Thermal conductivity (W/(m*K))	2.3
Heat capacity (J/(kg*K))	1100
Heat transfer coefficient (W/(m <sup>2</sup> *K))	2.5
Ultimate hydration heat (J/g)	400, 439, 520
<b>Chemo-field</b>	
Fitting parameter $A_1$	$1.41 \times 10^7, 4 \times 10^7, 8 \times 10^7$
Fitting parameter $A_2$	$1 \times 10^{-2}, 5 \times 10^{-2}, 8 \times 10^{-2}$
Fitting parameter $\eta$	8, 8.5, 8
Ultimate hydration degree	$1.031 \times wc / (0.194 + wc)$
Activation energy/ $R$ (K)	$5000, 5292, 5490 + 1470 \times (20 - T)$
<b>Mechanical-field</b>	
Compressive strength $f_c$ (MPa)	XGBoost ( $w/c, a/c, c, c\_type, T$ )
Shrinkage $\varepsilon_{sh}$	MC2010 ( $f_c, t_c, RH, T$ )
Elastic Modulus $E$ (GPa)	MC2010 ( $f_c, a\_type, T$ )
Creep Compliance $J$ (Mpa <sup>-1</sup> )	MC2010 ( $f_c, E, RH, T$ )

**Table 8-2 Categorical parameter settings**

Cement type	
<i>c_type=1</i>	32.5N
<i>c_type=2</i>	32.5R and 42.5 N
<i>c_type=3</i>	42.5R, 52.5N, 52.5R
Aggregate type	
<i>a_type=1</i>	Basalt or limestone aggregates
<i>a_type=2</i>	Quartzite aggregates
<i>a_type=3</i>	Limestone aggregates
<i>a_type=4</i>	Sandstone aggregates

## 8.4 Active ensemble learning (AEL)

The Machine Learning workflow is shown in **Figure 8-7**, with the left branch being the Active Ensemble Learning (AEL) and the right being the One-Shot Ensemble Learning (OSEL). Both learning frameworks follow a similar technical route: 1) Latin Hypercube Sampling (LHS) is first conducted to obtain the sample space; 2) The material model (see Section 8.3) and the TCM model (see section 8.2) are run based on the selected samples; 3) Principal Component Analysis (PCA) is conducted to process the EAS vector; 4) A multi-output Light Gradient Boosting Machine (LGBM) is trained to be the predictor.

**Figure 8-7 Machine Learning workflow**

A major difference between AEL and OSEL lies in the sampling method during the training stage. For OSEL, there is only one-shot sampling by the LHS method, which will be iteratively solved by the TCM model and used to train the LGBM model. For AEL, a two-stage sampling strategy is used: 1) the first 30 samples are initially used to build a Gaussian Process (GP) model and the LGBM model; 2) the GP model is updated iteratively using all observed samples, and then, based on Bayesian inference, the variance distribution of the GP over the whole 30000-sample pool is calculated; the sample point with the highest variance is considered as the most uncertain sample in this study. This new sample is imported to the TCM model and the result is then used to update the GP model and the LGBM model. Such active learning method intentionally pays more attention on exploring uncertain samples, and uses these samples to update the predictor. The AEL model runs 970 iterations to gain another 970 samples, which ensures the same number of total samples for training the LGBM predictor with the OSEL method. This allows the effectiveness of AEL and OSEL to be compared.

### 8.4.1 Data sampling and preprocessing

#### 8.4.1.1 Latin Hypercube Sampling

To construct the database for Machine Learning, a sample pool is needed at first. Monte Carlo Sampling (MCS) is a frequently-used approach, which is often based on a pseudorandom number generator and a known transformation to randomly generate samples for each variable. However, an unavoidable drawback is that many samples are required for good accuracy and repeatability of a certain probabilistic distribution. In comparison, Latin Hypercube Sampling (LHS) achieves better representation of the interested probabilistic distribution using a smaller number of samples [361]. The LHS is conducted in the following 2 steps: 1) Samples for each variable are strategically chosen to represent the variable's probability density function; 2) Samples for the variables are ordered to match a certain target (e.g., correlations) between variables.

In this chapter, each sample is represented by 8 variables, given in [Table 8-3](#). The range of each variable is specified to 1) represent most general cases of concrete structures and 2) conform to the applicability range of the MC 2010. At first, all the variables are assumed as independent and uniformly-distributed to generate an initial database. Afterwards, two measures are taken to process the database: 1) the values of aggregate type and cement type are rounded down to obtain integers which represent categorical parameters as shown in the [Table 8-2](#); 2) According to practical

engineering experience, the  $w/c$  of lower strength cement (i.e.,  $c\_type=1$ ) should not be lower than 0.4. Therefore, the samples with a  $c\_type$  equal to 1 and  $w/c$  smaller than 0.4 are deleted from the initial database.

**Table 8-3 Variables range of the samples**

Variable Name	Variable Range
Temperature $T$ (°C)	0~40
Relative humidity $RH$ (%)	40~100
Time of curing $t_c$ (hours)	12~672
Aggregate-cement ratio $a/c$ (1)	2~8
Water-cement ratio $w/c$ (1)	0.2~0.6
Cement amount $c$ (kg/m <sup>3</sup> )	250~650
Aggregate type $a\_type$ (1)	Four kinds: 1,2,3,4
Cement type $c\_type$ (1)	Three kinds: 1,2,3

In the LHS process, based on the criterion of maximizing the minimum distance between sample points, five iterations are used to generate the sample pool. As a result, the one-shot training set for the OSEL learning is shown in [Figure 8-8](#).

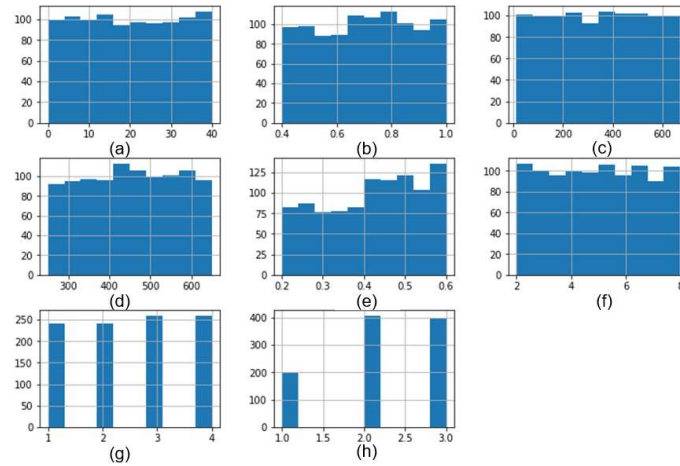


**Figure 8-8 LHS sampling for One-shot Ensemble Learning: (a) Temperature (°C); (b) Relative Humidity (%); (c) Time of curing (hours); (d) Cement amount (kg/m<sup>3</sup>); (e) w/c ratio; (f) a/c ratio; (g) Aggregate type; (h) Cement type. The Y axes presents the number of samples.**

#### 8.4.1.2 Principal Component Analysis

After the sample pools are prepared, the samples can be imported to the TCM model and run the EAS simulation. The EAS result of each sample is a 672-by-1 vector, which represents the restraint stress from the 1<sup>st</sup> hour to 672<sup>th</sup> hour. Such a long vector can be an issue for ML models. To address this problem, Principal Component Analysis (PCA) is used to reduce the dimensionality of the EAS vector, before it is used for training. By Singular Value Decomposition [362], PCA conducts linear dimensionality reduction of the data by projecting it to a lower dimensional space. In this chapter, the general process of PCA can be described as follows:

$$\sigma_{PCA} = U\sigma_{original} \quad (8-18)$$

where  $\sigma_{original}$  is the 672-by-1 EAS vector output by the TCM model;  $\sigma_{PCA}$  is the 5-by-1 principal component vector produced by PCA to represent the 672-by-1 EAS vector;  $U$  is a 5-by-672 matrix, which represents the new basis to project  $\sigma_{original}$  to  $\sigma_{PCA}$ .  $U$  is composed of the first 5 eigenvectors of the covariance matrix of  $[\sigma_{original}]_N$  (i.e.,  $(1/N) [\sigma_{original}]_N [\sigma_{original}]_N^T$ ,  $N$  is the number of samples that are used in PCA), ordered by their variance (i.e., eigenvalues). For OSEL, PCA can be conducted at once based on the 1000 randomly selected samples. For AEL, which conducts a progressive sampling procedure, PCA is first applied to the 30 initial samples and then restarted in every learning step to take new samples into account. Note that the reason why 5 eigenvectors are chosen is due to the variance ratio

distribution of Principal Components (PCs), as shown in [Table 8-4](#). It is found that the first 5 PCs already occupy almost 100% variance, and the 1<sup>st</sup> PC has already explained over 98% variance of the original EAS, which indicates a strong linearity of the original EAS vector in the projected space of PCA.

**Table 8-4 Variance ratios of the Principal Components**

PC rank	Variance ratio
1 <sup>st</sup> PC	$9.8637 \times 10^{-1}$
2 <sup>nd</sup> PC	$1.1917 \times 10^{-2}$
3 <sup>rd</sup> PC	$8.9869 \times 10^{-4}$
4 <sup>th</sup> PC	$3.6584 \times 10^{-4}$
5 <sup>th</sup> PC	$1.6026 \times 10^{-4}$

Nine cases are randomly selected to compare the original EAS vector and the corresponding PCA processed vector, as shown in [Figure 8-9](#). The mean squared error (MSE) between these two kinds of vectors are computed over the whole sample pool, and a value of 0.0005618 MPa is obtained. Such a low MSE validates that the PCA can effectively reduce the dimensionality of the EAS vector from 672-by-1 to 5-by-1 while maintaining the majority of the information.

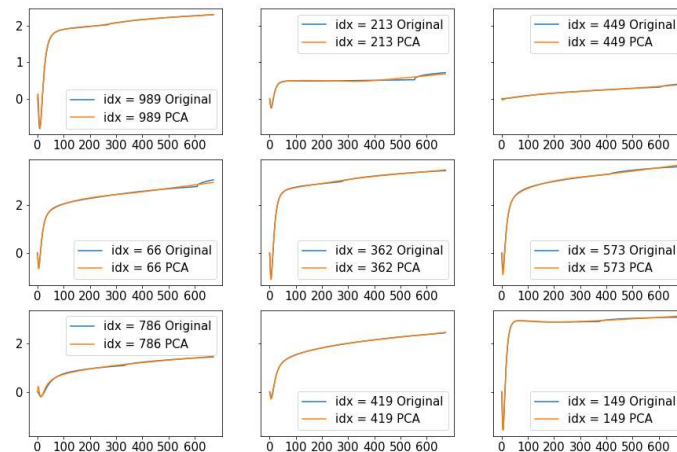


**Figure 8-9. Random cases for comparing PCA and original EAS vector. X axes represent the time (hours). Y axes represent stress (MPa).**

With the samples obtained by LHS and corresponding EAS results processed by PCA, the training data for Machine Learning approach are prepared. After a normalization procedure by the mean and variance of the

data, the dataset can be imported to Machine Learning models to start training process.

### 8.4.2 Uncertainty-based query

The number of labeled samples is essential for the generalization capabilities of ML models. However, obtaining a large amount of labeled data from the TCM model is computationally expensive. In this regard, this chapter adopts the uncertainty-based query to actively select samples and run the corresponding TCM model to obtain labeled data, which has higher potential of improving the performance of the ML model. The Gaussian Process (GP), which defines a stochastic process that any finite collection of random variables follows a multivariate Gaussian distribution, is adopted to quantify the uncertainty. Inheriting the properties of Gaussian distribution, GP can explicitly describe the marginalized distribution of any unobserved sample, which provides a direct measure of the uncertainty. Assuming having observed samples  $(X, Y)$ , a GP (denoted by  $f(x)$ ) is described by a mean and a covariance matrix of observed samples, i.e.,  $f(x) \sim GP(\mu(X), k(X, X))$ . By normalizing all the samples with their mean and variance, the  $\mu(X)$  can be set as 0. Therefore, the only key component defining the GP turns is the covariance matrix  $k(X, X)$ , which is assembled by the covariance of any two observed samples, and is also known as the kernel of GP. The selection criterion of the GP kernel is based on the requirement of smoothness and anticipated patterns of the data [293]. Herein, the radial basis function (RBF) is chosen as the kernel function, which is infinitely differentiable and therefore can result in good smoothness, expressed as:

$$k(x_s, x_t) = \sigma^2 \exp\left(-\frac{\|x_s - x_t\|^2}{2l^2}\right) \quad (8-19)$$

where  $\sigma$  and  $l$  are hyperparameters to be tuned;  $\mathbf{x}_s$  and  $\mathbf{x}_t$  are two observed samples. Eq (8-19) shows that the GP considers the dependence of any two samples according to their Euclidean distance. Based on the observed samples, GP makes prediction on other unobserved samples using Bayesian Inference. Assuming unobserved samples at  $\mathbf{X}^*$ , the joint distribution can be expressed as:

$$\begin{bmatrix} Y \\ f(X^*) \end{bmatrix} \sim GP \left( \begin{bmatrix} \mu(X) \\ \mu(X^*) \end{bmatrix}, \begin{bmatrix} k(X, X) & k(X, X^*) \\ k(X^*, X) & k(X^*, X^*) \end{bmatrix} \right) \quad (8-20)$$

$$k(X, X) = \begin{bmatrix} k(x_1, x_1) & \cdots & k(x_1, x_n) \\ \vdots & \ddots & \vdots \\ k(x_n, x_1) & \cdots & k(x_n, x_n) \end{bmatrix} \quad (8-21)$$

$$k(X^*, X) = [k(x^*, x_1) \quad k(x^*, x_1) \quad \cdots \quad k(x^*, x_n)] \quad (8-22)$$

By Bayesian Inference, the marginalized distribution of the unknown sample at  $X^*$  can be expressed as [293]:

$$f(X^*)|Y \sim GP(\mu^*, k^*) \quad (8-23)$$

$$\mu^* = k(X^*, X)k(X, X)^{-1}(Y - \mu(X)) + \mu(X^*) \quad (8-24)$$

$$k^* = k(X^*, X^*) - k(X^*, X)k(X, X)^{-1}k(X, X^*) \quad (8-25)$$

where  $k^*$  denotes the variance of prediction of GP for the unobserved sample  $X^*$ . Based on the marginalized distribution described by Eq (8-23)~(8-25), a series of learning functions can be defined for sample query. For example, in the studies of structural reliability, learning functions like the EFF function [363] and the U function [364] are often defined to evaluate which samples should be selected in the next learning iteration. These learning functions are built to achieve the exploitation-exploration tradeoff: 1) “exploitation” means that samples located near the limit state will be preferred; 2) “exploration” means that samples with high uncertainty will be preferred. The exploitation-exploration tradeoff guarantees that a surrogate model for reliability analysis can be obtained to achieve high accuracy within only dozens of learning iterations [346,347]. However, as this chapter aims to predict the EAS evolution over a certain time range (0~672 hours), the main problem is a global prediction, rather than a local prediction which only focuses on a certain boundary (i.e., a limit state). Therefore, in this chapter, there is no tradeoff between exploitation and exploration, but only greedy exploration for samples with highest uncertainty. Specifically, in every learning step, Equation (8-23)~(8-25) is performed over the whole sample pool of the AEL (i.e., 30000 samples) to obtain the variance distribution. The sample with the highest variance calculated by the Eq (8-25) will be selected for the next learning process. The variance distribution at some learning steps will be given in the Section 8.5.3.

### 8.4.3 Light Gradient Boosting Machine (LGBM)

The Light Gradient Boosting Machine (LGBM) is used as predictor due to its robustness, excellent generalizing capability, and efficiency. The base model used for LGBM is decision tree, the so-called weak learner. For regression aims, the decision tree consistently makes binary partitions of each variable of the sample at each level of the tree, until the maximum depth is reached [365]. Therefore, the whole dataset will be divided into multiple regions, with each region corresponding to a certain prediction value. However, a significant drawback of the decision tree is the high risk

of overfitting. Due to the hierarchical training process, the error induced at the top levels of a decision tree can easily propagate down. This makes the decision tree a high-variance predictor, and a slight change of input data can greatly change the output [365].

The ensemble learning methods like “bagging” or “gradient boosting” aim to combine a number of decision trees into a strong predictor. In this chapter, the gradient boosting framework is adopted, shown as **Figure 8-10**. Starting from a weak learner, the LGBM sequentially builds weak learners to compensate for the residual error of previous models, and finally assemble all these models to form a final model. Such residual error is the so-called gradient, making this method analog to gradient descent. During this process, the hyperparameter “learning rate” is set as 0.1 to control the step size. To account for the risk of overfitting, a regularization term will be used in the loss function to put preference on a model with lower complexity while preserving high accuracy. Furthermore, a random selection of features and bagging will also be adopted.

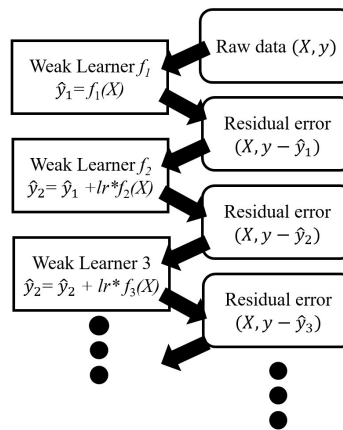


**Figure 8-10. Gradient Boosting workflow**

Compared to another well-known Gradient Boosting Model - XGBoost, the LGBM shows higher efficiency, which makes it a better choice for the AEL process. The advantage of LGBM is due to the following three aspects [366]:

- 1) Rather than splitting the leaf node of the base model level-wise, LGBM grows the tree leaf-wise using a histogram-based algorithm, which yields high efficiency and saves memory.
- 2) LGBM adopts Gradient-Based One-Side Sampling (GOSS) to select samples with high gradient and discards the ones with low gradient, to reduce the number of sample and increase efficiency.

3) LGBM adopts exclusive feature bundling (EFB) to identify exclusive features and then merge them into feature bundles to reduce the dimensionality of sample features and thus promote training efficiency.

As an iterative learning process, the high efficiency and accuracy of LGBM is essential for the AEL framework proposed herein. To efficiently tune the hyperparameters of the LGBM model, Bayesian Optimization is conducted based on an acquisition function of Expected-Improvement, which guarantees fast convergence within 30 iterations. A detailed description of the tuning process can be found in [174]. The results of hyperparameter tuning are given in **Table 8-5**. The hyperparameter “*Max\_bin*” controls the number of bins when conducting the histogram-based algorithm to find optimal split in each decision tree; the parameters “*Min\_data\_in\_leaf*”, “*Max\_depth*”, “*Num\_leaves*” specify the size of each decision tree to prevent overfitting; the parameters “*Feature\_fraction*”, “*Bagging\_fraction*” and “*Num\_estimators*” control the bagging and boosting process by specifying the fraction of features, the number of samples, and the number of decision trees to be used in the training process. For more details regarding how these parameters influence the performance of LGBM, the reader is referred to [366].

**Table 8-5 Hyperparameter settings for the LGBM model**

Hyperparameter	Value
<i>Max_bin</i>	76
<i>Min_data_in_leaf</i>	12
<i>Max_depth</i>	62
<i>Num_leaves</i>	38
<i>Feature_fraction</i>	0.883
<i>Bagging_fraction</i>	0.773
<i>Num_estimators</i>	100

## 8.5 Results and discussion

### 8.5.1 Applicability of the TCM model

Five representative cases are selected as input to run the proposed TCM model. The input for the case study is given in **Table 8-6**. In these 5 cases, the EAS evolution under different temperatures, ranging from 0 to 40 °C, is investigated. By setting the time of curing  $t_c$  as 672 hours, the autogenous shrinkage-induced EAS is calculated.

**Table 8-6 Details of the input for case study**

<b>Input variable</b>	<b>Value</b>
Cement amount $c$ ( $kg/m^3$ )	320
Relative humidity $RH(\%)$	100
Water-cement ratio $w/c$ (1)	0.42
Aggregate-cement ratio $a/c$ (1)	5.76
Temperature $T$ ( $^{\circ}C$ )	0~40
Time of curing $t_c$ (hours)	672
Aggregate type $a\_type$ (1)	3
Cement type $c\_type$ (1)	2

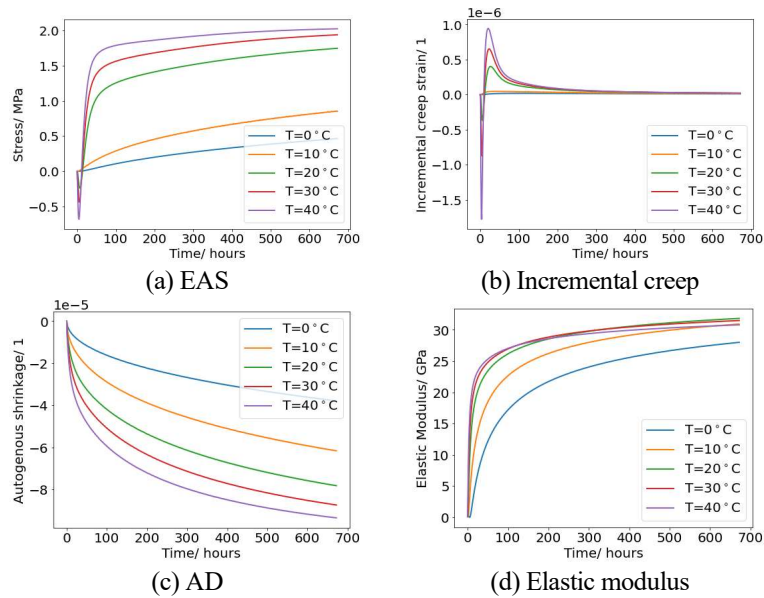
The results of EAS evolution of the 5-case study are shown in **Figure 8-11 (a)**. Note that the stress value is the surface average at the middle section of the dogbone specimen. The evolving concrete properties and behaviors, which together determine the EAS development, are also shown in **Figure 8-11 (b~g)**, including incremental creep strain (Eq (8-14)), autogenous shrinkage, effective elastic modulus (Eq (8-12)), specimen temperature, equivalent age (Eq (8-10)), and tensile strength. Note that, here, “incremental creep strain” is the internal state variable that stores the incremental strain history of the mechanical-field model, computed by Equation. The equivalent age is calculated based on the “maturity concept”, which takes the influence of temperature history on hydration speed into account. These results show that the TCM model can correctly simulate multiple effects related to EAS evolution:

1) **Figure 8-11 (f)** shows the influence of temperature on the rate of hydration, which then influences the development of elastic modulus, tensile strength, creep compliance, and autogenous shrinkage (see **Figure 8-11 (b, c, d, and g)**). High temperature accelerates the hydration and therefore accelerates the development of all these properties, which finally causes much higher EAS [42,367].

2) **Figure 8-11 (b)** shows that the magnitude of incremental creep strain decreases monotonically because of hydration. Negative and positive creep strain correspond to the occurrence of compressive and tensile EAS, respectively.

3) **Figure 8-11 (e)** shows that higher environmental temperature results in higher temperature increase in the specimen, and therefore causes higher compressive EAS in the first hours. On the other hand, low temperature can increase the activation energy (Eq (6-5)), slow down the hydration reaction, and cause rapid loss of heat (Eq (8-7)). As a result, the temperature in the specimen can hardly change and there are no compressive EAS in the first hours [42].

4) **Figure 8-11 (d, g)** shows that the temperature increase simply accelerates the development of elastic modulus and tensile strength in the first days but compromises them at 28 days. This is because high temperature negatively influences the hydration process [368]. In the TCM model, this effect is originally considered by the MC 2010 formulas.



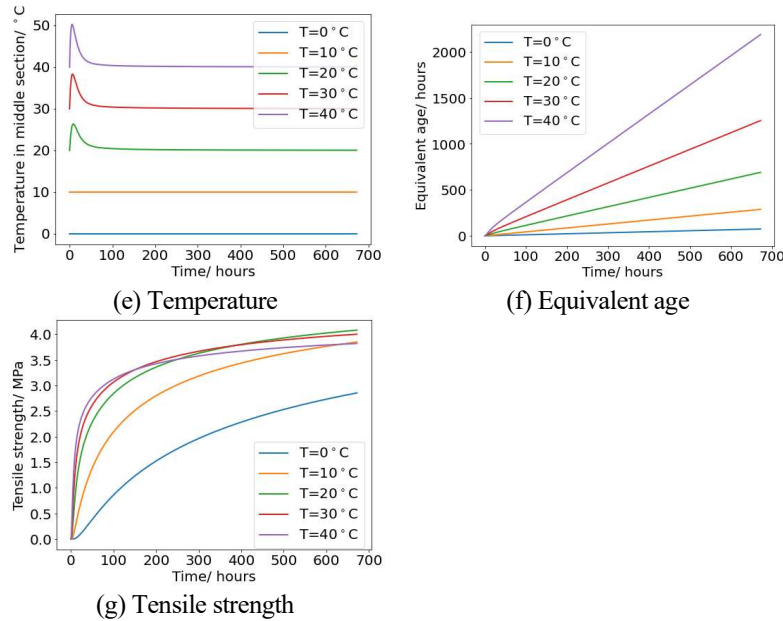


**Figure 8-11** Case study of the TCM model: (a) EAS evolution; (b) Incremental creep strain  $-xx$  component; (c) Autogenous shrinkage; (d) Effective elastic modulus; (e) Temperature development in specimen; (f) Equivalent age; (g) Tensile strength.

### 8.5.2 Data correlation

This section investigates the meaning of the first PC and then presents the correlation between the first 5 PCs and the input parameters. The PCA procedure described in the Section 8.4.1.2 shows that the first 5 PCs can express the original EAS vector produced by the TCM model with high accuracy (with a MSE lower than 0.0005618). Moreover, the first PC occupies over 98% of the variance ratio and can be considered as a significant variable that represent the EAS vector. However, although the PCA procedure has a clear mathematical meaning, what the first PC exactly represents is unknown a-priori. To this end, this study conducts a parametric study on the first PC. First, this study assumes the first PC equals to 0, 1, 2, 3, ..., 100, and conducts an inverse PCA (inverse of Eq (8-18)) to transform this first PC to a 672-by-1 EAS vector. Note that all 101 sets of inverse PCA are in a good order as shown in [Figure 8-12](#), but only 6 results are selected to show here to make the pattern clearer and more intuitive.

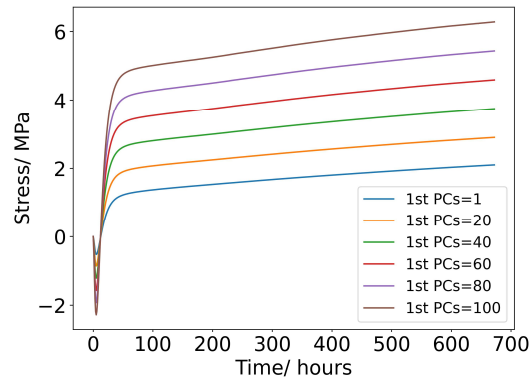


**Figure 8-12 Random cases for comparing PCA and original EAS vector. X axes represent the time (hours). Y axes represent stress (MPa).**

The results show that the first PC represents the global magnitude of the whole EAS vector, irrespective whether the specimen is in compression or in tension. Compared with other indexes like “zero-stress temperature” [369,370], “peak of compressive stress” [371], and “peak of tensile stress” [230], which are mostly based on a single observation at a single time point, the first PC represents an overall characteristic of the whole EAS vector and can be regarded as a global index for evaluating the EAS evolution.

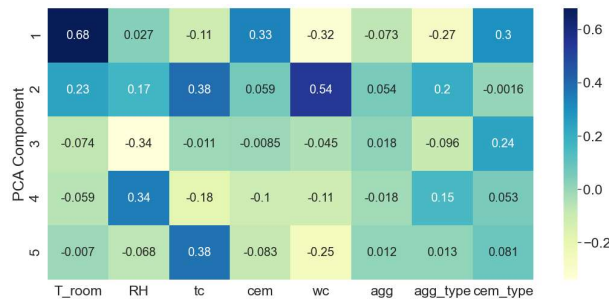


**Figure 8-13 Correlation matrix between PCs and input variables**

**Figure 8-13** shows the correlation matrix between the first 5 PCs and the input parameters calculated over the 1000 samples of the OSEL. As described before, the first PC occupies the 98% variance ratio among all PCs and represents the global magnitude of the EAS vector. Therefore, the correlation between the first PC and input parameters can reveal the influence of various factors on the EAS evolution. The first row of the correlation matrix stands for the correlation between the first PC and the input parameters. A positive correlation coefficient means that increase of the corresponding parameter can increase the first PC, which means that it increases the overall EAS magnitude. In other words, the corresponding

parameter has a positive contribution to the EAS evolution. By analyzing the correlations at the first row of the correlation matrix, the following is observed:

- 1) Environmental temperature has the highest positive contribution to the EAS evolution, which is not surprising since temperature not only influences the hydration speed, but also accounts for a higher heat release in the first hours. Fast hydration accelerates the development of shrinkage and elastic modulus, and finally accelerates the EAS evolution, as shown in the section 8.5.1. High heat release increases the thermal deformation and can greatly increase both the compressive and the tensile stress.
- 2) Parameters “cement amount” and “cement type” also have positive contributions to the EAS evolution. High cement amount and cement type indicates more heat release, which can increase EAS. Note that cement type 1, 2, 3 represent cement class ranging from low strength/ slow hydration to high strength/ rapid hydration.
- 3) Parameters w/c ratio, a/c ratio, and aggregate type all have a negative contribution to the EAS evolution. This is in accordance with common understanding of the physical process: Increasing w/c and aggregate type can result in concrete with lower strength and lower elastic modulus, and therefore slow down the EAS evolution. Although the increase of w/c may result in more drying shrinkage after curing, the contribution of w/c to EAS magnitude remains negative because the decrease of elastic modulus and autogenous shrinkage plays a more significant role in this process. Increasing the a/c can reduce the amount of cement paste which is the shrinking phase, and increase the extent of internal restraint, which causes a further decrease of the overall shrinkage.
- 4) Parameter “time of curing” has a negative contribution since longer curing indicates less drying shrinkage and therefore can cause less EAS.
- 5) The correlation of RH is low, because the influence of RH is complex. According to the material model, increasing RH can result in a decrease of creep and drying shrinkage. Lower creep means lower stress relaxation, and therefore higher EAS. However, lower drying shrinkage can reduce EAS, which in fact should also depend on the time of curing. The change of RH can induce counteracting effects among various concrete behaviors, so that its influence is not monotonic, at least in the TCM model.

Based on the meaning of the first five PCs and the correlation analysis of over 1000 data samples, this section illustrates that the TCM model proposed in this chapter can generate reasonable EAS results given different input parameters.

### 8.5.3 Training history

This section presents the model performance during the learning steps. To evaluate the prediction performance of the model, this study employs a cross-validation procedure: AEL model will use OSEL's database as testing set, and OSEL will use AEL's database as testing set. In this way, both AEL and OSEL have to be tested by 1000 unseen samples. Note that, in Machine Learning practice, in general the size of the testing set is 10~ 40% of the training set, while this study uses the same size of the training set. In this sense, a big testing set poses a more challenging task for the ML model, and can better reflect the model performance. Mean Square Error (MSE), Mean Absolute Error (MAE) and Coefficient of Determination ( $R^2$ ) are used as the metrics, as follows:

$$R^2 = 1 - \frac{\sum_{i=1}^n (y_i - \hat{y}_i)^2}{\sum_{i=1}^n (y_i - \bar{y})^2} \quad (8-26)$$

$$RMSE = \frac{1}{n} \sum_{i=1}^n (y_i - \hat{y}_i)^2 \quad (8-27)$$

$$MAE = \frac{1}{n} \sum_{i=1}^n |y_i - \hat{y}_i| \quad (8-28)$$

where  $y_i$  is the EAS vector of  $i^{\text{th}}$  sample point output by the TCM model;  $\hat{y}_i$  is the EAS vector predicted by AEL or OSEL model for  $i^{\text{th}}$  sample;  $\bar{y}$  is the mean value of the EAS vector. Note that both AEL and OSEL model give the output of EAS in the form of 5-by-1 PCA component, so that an inverse PCA procedure is needed before measuring the performance.

After the training of AEL and OSEL model is finished, a step-by-step analysis is carried out to check their learning history. At each analysis step, the number of samples used for training both models are increased, and a cross validation procedure is conducted, shown in **Figure 8-14**. The results show that, as the learning step increases, the number of samples used for training also increases, which improves the performance of both models. AEL outperforms OSEL during the whole training history, irrespective of the metrics is used. To achieve a certain accuracy, the number of samples required for AEL is less than 50% of that required for OSEL. For example, the AEL achieves a MSE of 0.125 MPa based on around 200 samples, while for OSEL achieving the same MSE takes more than 800 samples. This validates the efficiency of the AEL method, which is significant for surrogate modelling for an expensive model like the TCM model. Although

the gap between the AEL and OSEL is stable over the whole training history, it is not very large. The OSEL still obtains good accuracy, with a  $R^2$  close to 0.95 when 1000 samples are used in the training process. Such a good training performance can be attributed to the sample space created by LHS and robustness of the LGBM predictor.

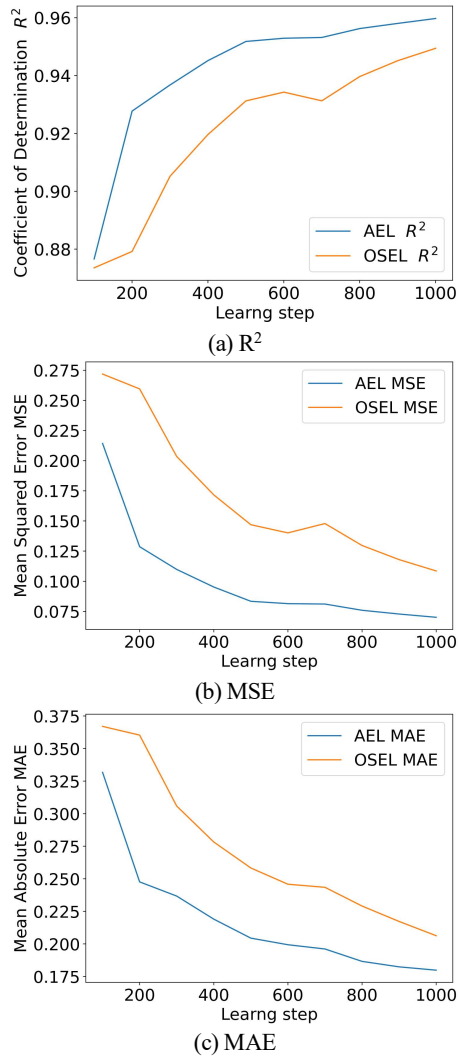


**Figure 8-14 Training history of the AEL and OSEL model: (a) Coefficient of determination; (b) Mean squared error; (c) Mean absolute error.**

The training history shows the advantages of AEL over OSEL. To further consolidate this conclusion and gain a deeper understanding of how AEL works, the final AEL database which is built by a progressive sampling

process guided by uncertainty-based query (see section 8.4.2) is shown in **Figure 8-15**. Comparing the AEL sampling results with the database of OSEL created by one-shot LHS sampling (see **Figure 8-8**), it is found that the AEL sampling puts more attention on the boundaries of the variables, while the OSEL assumes an even-distribution of all the variables and values them equally. The difference can be attributed to the uncertainty-based query in the AEL process, which results in preference for samples with higher uncertainty (i.e., higher variance). Using the variance of the GP as a measure of uncertainty, the uncertainty-based query continuously looks for the samples with high uncertainty (variance), imports them to run the TCM model, and adds the results to the training set of the LGBM model.

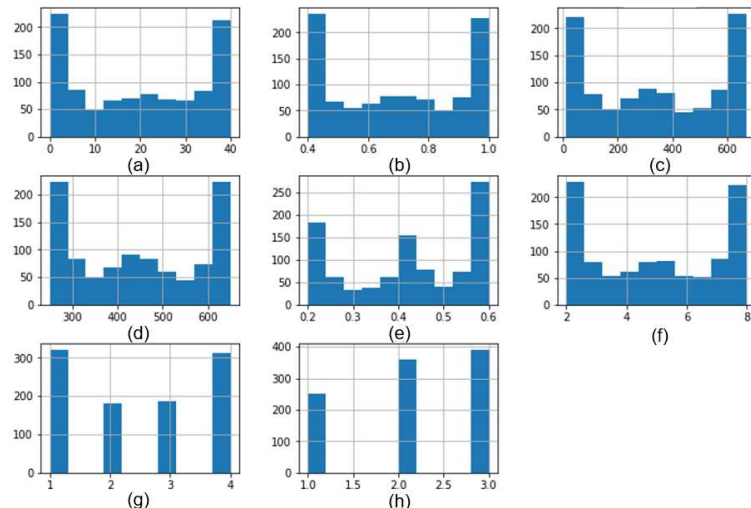


**Figure 8-15** AEL Sampling results of uncertainty-based query: (a) Temperature (°C); (b) Relative Humidity (%); (c) Time of curing (hours); (d) Cement amount (kg/m<sup>3</sup>); (e) w/c ratio; (f) a/c ratio; (g) Aggregate type; (h) Cement type. The Y axes presents the number of samples.

The uncertainty-based query of the AEL results in a consistent change of the distribution of uncertainty (variance) in the sample space at different learning iterations, as shown in **Figure 8-16**. At 10<sup>th</sup> learning step, the whole sample space is close to unknown, therefore over 28000 samples have the variance higher than 0.9 and the other 2000 samples have variance between 0.8 and 0.9. As the AEL progresses, the sample with the highest variance is used to run the TCM model and then train the LGBM and GP. This sampling strategy directly causes a decrease of the maximum variance and a shift of overall variance distribution from high to low value: 1) After 500 learning iterations, the maximum variance decreases to 0.9 from 1, and the variance range shifts to (0.44, 0.90) from (0.7, 1.0); 2) After 970

learning iterations, the maximum variance decreases to 0.76, and the variance range shifts to (0.32, 0.76). The evolution of variance distribution also shows that the decrease of maximum variance and the shift of variance range become slower as the learning iteration increases.

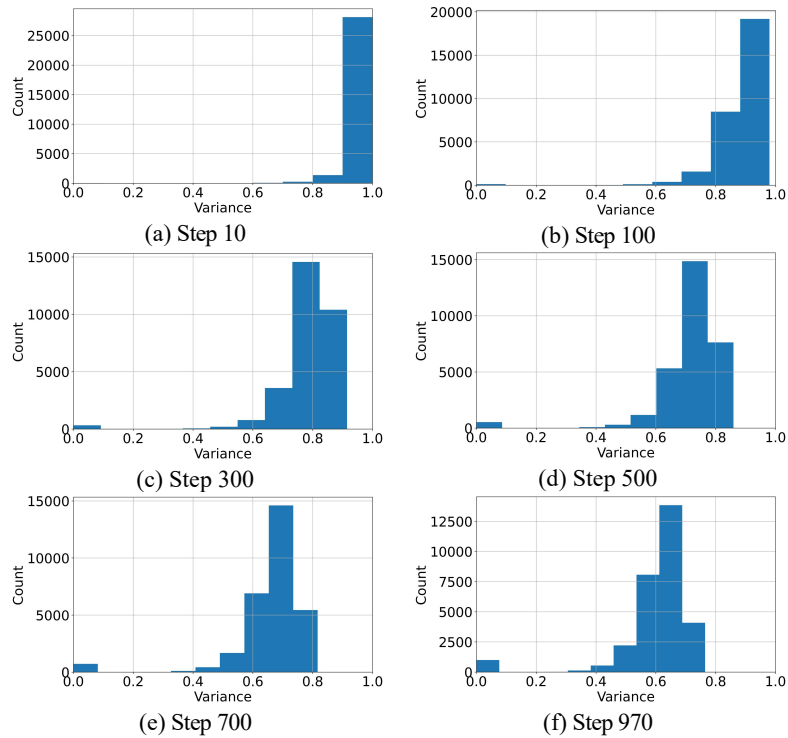


**Figure 8-16** Variance histogram at different learning iterations: (a) Step 10; (b) Step 100; (c) Step 300; (d) Step 500; (e) Step 700; (f) Step 970.

### 8.5.4 Testing

Following the cross-validation described in section 8.5.3, in which the AEL model uses OSEL's database as testing set, and OSEL uses AEL's database as testing set, the testing results of the AEL and OSEL are shown in [Figure 8-17](#). The red line is a perfect-prediction line, and the data aligning on the red line means that the AEL or OSEL prediction (X-axis) is equal to the TCM modelling results (Y-axis). The testing results show that both AEL and OSEL can obtain high  $R^2$  and low MSE and MAE, with the majority of testing samples around the perfect-prediction line. AEL results show smaller deviation from the perfect-prediction line, which indicates better performance. This is in accordance with the results of all three metrics, as shown in the training history of Section 8.5.3. More specifically, the OSEL prediction at high-stress conditions shows a significant deviation from the

perfect-prediction line, which indicates AEL's advantage at the sample space boundary. This advantage is due to the uncertainty-based query which puts preference in the boundary of sample variables, as shown in [Figure 8-15](#). Although the advantage of AEL over OSEL shown here is obvious, it should also be noted that the cross-validation procedure that uses the AEL's dataset as OSEL's testing set exposes the weakness of OSEL to a higher extent. Therefore, the advantages of AEL over OSEL shown here may be overestimated.

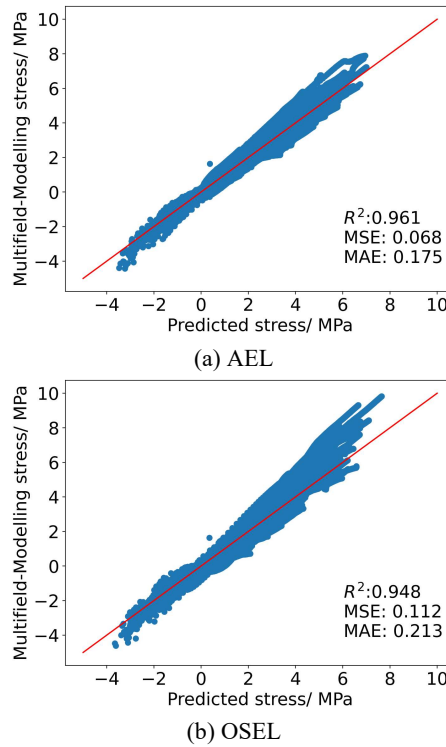


Figure 8-17 Testing results of AEL and OSEL: (a) AEL; (b) OSEL

## 8.6 Conclusions

To accurately predict the early-age stress (EAS) evolution of concrete, an Active Ensemble Learning (AEL) method is proposed to efficiently construct a surrogate model of a Thermo-Chemo-Mechanical (TCM) model. Based on the rigorous theoretical basis, the TCM model is built to simulate the aging material properties and behaviors of concrete, which together result in the evolution of EAS under restrained condition. The AEL framework incorporates Principal Component Analysis (PCA), Gaussian

Process (GP), and Light Gradient Boosting Machine (LGBM). To evaluate the efficiency and precision of AEL framework, One-Shot Ensemble Learning (OSEL) is also conducted as comparison. Overall, based on this study, the following conclusions can be drawn:

- 1) The dimensionality of the EAS vector can be effectively reduced by PCA, with the first principal component (PC) occupying a variance ratio of over 98%. The parametric study finds that the first PC represents the magnitude of the EAS vector, which means that the first PC can be used as a global index for evaluating the EAS evolution.
- 2) The case study and correlation analysis for the first PC together prove the applicability of the proposed TCM model. Based on Fourier's law, Arrhenius's equation, Rate-type creep law, and the built material model, the TCM model is able to simulate the hydration reaction, heat transfer, and viscoelastic stress evolution. By analyzing the results over 1000 samples, it is found that ambient temperature is the most significant factor that can increase the EAS magnitude. The influence of the other parameters (i.e., w/c, a/c, aggregate type, cement type, cement amount, relative humidity and time of curing) is also quantified by their correlation coefficients.
- 3) The AEL framework built in this study outperforms the traditional Machine Learning routine OSEL with higher R2 (i.e., 0.961 versus 0.948) lower MSE (0.068 versus 0.112) and lower MAE (0.175 versus 0.213). Based on the uncertainty-based query, the AEL keeps putting attention on the uncertain samples, which are mostly located at the boundary of the sampling space. The active learning process guided by the uncertainty-based query results in consistent improvement of the uncertainty (variance) distribution, and greatly improves the prediction accuracy of EAS at extreme conditions.
- 4) To achieve a certain accuracy, the AEL framework only needs a small sample size, which is less than 50% of the OSEL. This is a great advantage in efficiency, because running the TCM model is computationally expansive, and obtaining a large dataset through TCM modelling is difficult.
- 5) The proposed AEL method can effectively build a surrogate of the multi-field model to allow for more efficient optimization and reliability analysis of the structural design to prevent EAC. It is suggested that the further improvement concentrates on the learning function of the AEL process which can achieve more efficient global sampling and prediction.

# 9. RETROSPECTION, CONCLUSIONS AND RECOMMENDATIONS

*This chapter reflects on the work of the whole thesis, synthesizes the findings of the main chapters to draw conclusions, and provides recommendations for future work.*

## 9.1 RETROSPECTION

Early-age cracking (EAC) is a common issue in cementitious materials, posing a threat to the functionality, durability, and aesthetics of engineering structures like dams, tunnels, and underground garages. This thesis set out to develop new experimental and modeling techniques to tackle the EAC problem, with a particular focus on EAC resulting from AD (AD). AD arises from the hydration reactions of cementitious materials. Consequently, the risk of AD-induced EAC is intrinsic to cementitious systems, unlike thermal and drying deformation, which can be prevented through external measures like active cooling and sealing.

While AD serves as an indicator for evaluating the AD-induced EAC risk, early-age stress (EAS), which can be tested through a Temperature-Stress Testing Machine (TSTM), offers a more straightforward index for EAC analysis. Thus, this thesis initiated preliminary work with standard TSTM tests, focusing on the AD-induced EAS evolution of high-volume slag concrete, as presented in chapters 3 and 4. A finite element model built on the rate-type creep law using the input of a continuous Kelvin chain, in combination with Bayesian inverse modelling of aging creep, was developed to simulate EAS evolution. However, the complexity of the TSTM system made the tests labor-intensive, hindering extensive and comprehensive applications of such testing methods. Furthermore, it was specifically noted that when quantifying the EAS evolution, creep/relaxation becomes a crucial input for the model.

The preliminary study (chapters 3 and 4) inspired subsequent work on the development of a more efficient TSTM (chapters 5 and 6) and models (chapter 7) for simulating the stress relaxation during EAS evolution. Building on the principles of the standard TSTM, a Mini-TSTM was developed, which enables more efficient tests of various early-age behaviors and properties related to EAC issues, including AD, elastic modulus, creep compliance, and the coefficient of thermal expansion. Comprehensive validation tests were conducted to demonstrate the reliability and applicability of the developed Mini-TSTM. In addition, the effects of curing temperature on AD and EAS in ordinary cement paste, which remained unclear in current literature, were investigated through Mini-TSTM tests. One issue that arose during the development of the Mini-TSTM was an observed variation in the measured early age AD in nominally identical cement paste specimens, but with cements coming from different batches. However, a good match between the EAS and AD tested in the same batch, which was analyzed both qualitatively and quantitatively,

validated the applicability of the developed setup. By the statistical and theoretical analysis of the viscoelastic model, it was also found that such variation of early age AD only causes negligible differences in EAS.

Based on the testing results of the Mini-TSTM, four different numerical modelling schemes for the stress relaxation process were established and examined. It was found that numerically solving the Volterra integral of creep compliance function can lead to negative relaxation modulus and cause significant error in EAS prediction. Accordingly, the rate-type creep law with Maxwell-chain was found to be optimal for stress relaxation, which directly uses relaxation modulus calculated from the tested creep compliance as input. The predicted EAS showed a good match with the results of Mini-TSTM tests, which validated the proposed model.

Chapter 8 extended the aforementioned efforts to a more general scenario by establishing a thermo-chemo-mechanical (TCM) multifield model, coupling heat transport, hydration reaction, and viscoelasticity to simulate the EAS evolution. A material model was built based on the Model Code 2010 (MC2010) to provide input of AD, drying shrinkage, and creep for the TCM model. It must be noted that some limitations of the MC2010 were passed on to the TCM model, such as the lack of theoretical consideration of autogenous expansion and the temperature effects on AD. Then, an active machine learning model comprising mainly Principal Component Analysis (PCA), Gaussian Process (GP), and Light Gradient Boosting Machine (LGBM), was established as a surrogate for the TCM model, significantly enhancing the efficiency of EAS prediction based on the input of mixture and environmental parameters.

In summary, the work has led to efficient and reliable testing and modeling methods, contributing to the understanding of EAC issues in cementitious systems.

## 9.2 CONCLUSIONS

To better address the EAC issues, this thesis develops new experimental and modelling techniques. main conclusions of this thesis are as below:

*The developed Mini-TSTM is an efficient testing system for early-age behaviors and properties that are related to EAC analysis.* In view of the complexity of standard TSTM which is labor-intensive, a small and light Mini-TSTM was built, enabling more efficient tests of not only EAS and AD but also elastic modulus, creep and coefficient of thermal expansion. The design of the Mini-TSTM addressed several issues in standard TSTM tests,

including pre-test installation and post-test disassembling, continuous control for full-restraint condition, LVDT installation, and friction between the specimen and the supporting table. Comprehensive tests on two types of cement paste (CEM I 42.5N and CEM III B 42.5 N) were conducted to validate the applicability and reliability of the developed setup. Using the tested AD and creep as input, a theoretical viscoelastic model was established to predict the EAS with good accuracy, offering further validation of the Mini-TSTM.

*The autogenous expansion is often an important part of AD and may not be neglected when quantifying the EAS evolution.* Many studies of AD only focus on the shrinkage part, which is induced by the self-desiccation effects and directly causes the EAC. However, the AD of both Portland and high-volume slag cement paste/ concrete is initially characterized by a substantial autogenous expansion, as confirmed by multiple standard TSTM tests in chapter 3 and Mini-TSTM tests in chapter 5 and 6. The extensive TSTM tests show the effects of different cementitious materials, water to cement ratios, and temperatures on the expansion behavior. In addition, multiple microscale tests including X-Ray Diffraction, Environmental Scanning Electron Microscopy, and Mercury Intrusion Porosimetry revealed that production of ettringite and calcium hydroxide causes the expansion behavior of high-volume slag and Portland cement paste/ concrete, respectively. The autogenous expansion causes compressive stress in the beginning, delays the occurrence of tensile stress and therefore is favorable for EAC prevention.

*Higher temperature increases the risk of AD-induced EAC.* The Mini-TSTM tests in chapter 6 show that the AD of Portland cement paste can be viewed as a four-stage process, including the initial deformation, autogenous expansion, plateau of slow deformation, and autogenous shrinkage. Although the EAS in the first three stages is low, due to low elastic modulus and high relaxation, the first three stages can delay the occurrence of tensile stress induced by the autogenous shrinkage in the last stage. Increasing the temperature will shorten the duration of the first three stages and increase the rate of autogenous shrinkage in the last stage, directly leading to EAC.

*The maturity concept cannot predict the AD (and AD-induced EAS) at different temperatures.* This conclusion is supported by the testing results of chapter 6. The main reasons are: 1) the effects of temperature on the production of expansive products in the first three stages are clearly not considered by the maturity concept; and 2) the assumption that temperature only influences the hydration rate is invalid considering the self-desiccation process, because the temperature influences not only the

hydration rate but also the porosity, relative humidity, and surface tension. However, the maturity concept can be successfully used for predicting the early-age elastic modulus and relaxation modulus at different temperatures, which can be used for prediction of EAS given the AD at different temperatures as input.

*Proposed numerical models for simulating stress relaxation are able to compute the EAS evolution with good accuracy.* Four different numerical/analytical models for simulating the stress relaxation were built and their performance was evaluated using the Mini-TSTM. The conversion of relaxation modulus from measured creep data is an important step in the EAS modelling. Numerically solving the Volterra integral of creep compliance function can achieve such conversion, but for young concrete with a steep aging creep function, it causes negative relaxation modulus and directly compromises the prediction accuracy of EAS. Accordingly, an analytical method was applied herein, which is based on the definition of relaxation test, to obtain the relaxation modulus from creep test. For one-dimensional (1D) analysis, the relaxation modulus can be directly used as input in the numerical scheme of stress superposition to calculate the EAS. For three-dimensional (3D) analysis, a series of time-dependent Maxwell chains can be firstly fitted using the obtained relaxation modulus and then used as input for a finite element model with rate-type creep law. The final assessment showed that such method obtained good accuracy in both 1D and 3D analysis.

*The proposed active ensemble learning scheme can be used to build a surrogate of the complex multifield model to form an efficient tool for EAS prediction.* A Thermo-Chemo-Mechanical (TCM) model was first built to provide data for the machine learning approach. Based on Fourier's law, Arrhenius's equation, Rate-type creep law, and the built material model, the TCM model couples the hydration reaction, heat transfer, and viscoelasticity. The TCM model can simulate the evolving properties (i.e., viscoelasticity), behaviors (i.e., thermal, autogenous and drying deformation), and EAS. Then, by incorporating the PCA, GP, and LGBM, an active ensemble learning model was efficiently trained with an uncertainty-guided data sampling strategy. The GP model quantifies the variance of the sampling space and delivered the most uncertain data point to the TCM model as the input, which then was used to train the AEL model. The AEL method substantially reduced the number of samples that is needed to train the machine learning model and achieve good prediction accuracy of EAS in the end.

### 9.3 RECOMMENDATIONS FOR FUTURE RESEARCH

This thesis focused on developing new experimental and numerical modelling techniques for assessing the EAC issues. The aforementioned works can benefit the resolution of EAC issues and give following recommendations for future research works:

First, the EAC issues of novel materials (such as alkali-activated materials, ultra-high performance cementitious materials, strain-hardening cementitious composites, and limestone calcine clay cement) should be investigated comprehensively using the Mini-TSTM setup. The early-age properties and behaviors including the AD, thermal deformation, coefficients of thermal expansion, creep, elastic modulus, and EAS can all be tested and assessed by the developed Mini-TSTM, offering a more comprehensive and systematic understanding of the EAC risk of these materials.

In addition, studies focused on more fundamental aspects of very early-age creep of Portland cement should be carried out. This thesis demonstrated that the early-age creep compliance function, which was extracted by the load-controlled Mini-TSTM tests, is essential for predicting the EAS. Unlike long-term creep, early-age creep is controlled by a very steep aging function and is closely related to the hydration process of the cementitious material. A theoretical model of the evolution of early-age creep, which needs to couple the hydration reaction and viscoelasticity, should be developed to assist the EAS prediction for the aim of EAC control.

Furthermore, the built TCM model still needs improvements, including more refined consideration of AD, drying deformation, and creep compliance. Current TCM model employed the Model Code 2010 (MC2010) and maturity concepts for these effects, which may lack theoretical consideration in some aspects, and some formulas are often proven to be inappropriate. For example, the formula of AD in MC 2010 does not take the autogenous expansion into account. Future improvement for the TCM model needs to enhance the current formulas of various properties and behaviors (i.e., AD, drying deformation, creep compliance, coefficient of thermal deformation, etc.) with more theoretical considerations.

Data-driven approaches are promising design and optimization tools for EAC prevention. Other than the active ensemble learning approach developed in this thesis, future study could investigate the use of time-series prediction methods, such as transformers and recurrent neural networks. Besides, graphical neural networks or physics-informed neural

---

networks are also promising tools to build more efficient and accurate model for prediction tasks. By combining the prior knowledge of the EAC mechanisms and testing data of TSTM test, a better EAS prediction model may also be built.

## REFERENCE

- [1] I. Maruyama, P. Lura, Properties of early-age concrete relevant to cracking in massive concrete, *Cem Concr Res.* 123 (2019) 105770. <https://doi.org/10.1016/j.cemconres.2019.05.015>.
- [2] Md. Safiuddin, A. Kaish, C.-O. Woon, S. Raman, Early-Age Cracking in Concrete: Causes, Consequences, Remedial Measures, and Recommendations, *Applied Sciences.* 8 (2018) 1730. <https://doi.org/10.3390/app8101730>.
- [3] A. Bentur, K. Kovler, Evaluation of early age cracking characteristics in cementitious systems, *Mater Struct.* 36 (2003) 183–190. <https://doi.org/10.1007/BF02479556>.
- [4] B. Klemczak, A. Żmij, Reliability of standard methods for evaluating the early-age cracking risk of thermal-shrinkage origin in concrete walls, *Constr Build Mater.* 226 (2019) 651–661. <https://doi.org/10.1016/j.conbuildmat.2019.07.167>.
- [5] J. Xin, Y. Liu, G. Zhang, Z. Wang, J. Wang, N. Yang, Y. Qiao, Evaluation of early-age thermal cracking resistance of high w/b, high volume fly ash (HVFA) concrete using temperature stress testing machine, *Case Studies in Construction Materials.* 16 (2022) e00825. <https://doi.org/10.1016/j.cscm.2021.e00825>.
- [6] D. Huang, P. Chen, H. Peng, Y. Yang, Q. Yuan, M. Su, A review and comparison study on drying shrinkage prediction between alkali-activated fly ash/slag and ordinary Portland cement, *Constr Build Mater.* 305 (2021) 124760. <https://doi.org/10.1016/j.conbuildmat.2021.124760>.
- [7] N.P. Tran, C. Gunasekara, D.W. Law, S. Houshyar, S. Setunge, A. Cwirzen, A critical review on drying shrinkage mitigation strategies in cement-based materials, *Journal of Building Engineering.* 38 (2021) 102210. <https://doi.org/10.1016/j.jobe.2021.102210>.
- [8] J. Yang, Q. Wang, Y. Zhou, Influence of Curing Time on the Drying Shrinkage of Concretes with Different Binders and Water-to-Binder Ratios, *Advances in Materials Science and Engineering.* 2017 (2017) 1–10. <https://doi.org/10.1155/2017/2695435>.
- [9] Z. Hu, C. Shi, Z. Cao, Z. Ou, D. Wang, Z. Wu, L. He, A review on testing methods for autogenous shrinkage measurement of cement-based

- materials, *J Sustain Cem Based Mater.* 2 (2013) 161–171. <https://doi.org/10.1080/21650373.2013.797937>.
- [10] L. Wu, N. Farzadnia, C. Shi, Z. Zhang, H. Wang, Autogenous shrinkage of high performance concrete: A review, *Constr Build Mater.* 149 (2017) 62–75. <https://doi.org/10.1016/j.conbuildmat.2017.05.064>.
- [11] L. Yang, C. Shi, Z. Wu, Mitigation techniques for autogenous shrinkage of ultra-high-performance concrete – A review, *Compos B Eng.* 178 (2019) 107456. <https://doi.org/10.1016/j.COMPOSITESB.2019.107456>.
- [12] X. Zhang, Z. Liu, F. Wang, Autogenous shrinkage behavior of ultra-high performance concrete, *Constr Build Mater.* 226 (2019) 459–468. <https://doi.org/10.1016/j.conbuildmat.2019.07.177>.
- [13] B. Zhang, H. Zhu, P. Feng, P. Zhang, A review on shrinkage-reducing methods and mechanisms of alkali-activated/geopolymer systems: Effects of chemical additives, *Journal of Building Engineering.* 49 (2022) 104056. <https://doi.org/10.1016/j.jobe.2022.104056>.
- [14] A. Darquennes, S. Staquet, B. Espion, Determination of time-zero and its effect on AD evolution, *European Journal of Environmental and Civil Engineering.* 15 (2011) 1017–1029. <https://doi.org/10.1080/19648189.2011.9695290>.
- [15] J.R.T. Filho, M.A.P.G. de Araújo, D. Snoeck, N. De Belie, Discussing different approaches for the time-zero as start for autogenous shrinkage in cement pastes containing superabsorbent polymers, *Materials.* 12 (2019). <https://doi.org/10.3390/ma12182962>.
- [16] M. Wyrzykowski, Z. Hu, S. Ghourchian, K. Scrivener, P. Lura, Corrugated tube protocol for autogenous shrinkage measurements: review and statistical assessment, *Mater Struct.* 50 (2017) 57. <https://doi.org/10.1617/s11527-016-0933-2>.
- [17] S. Tang, D. Huang, Z. He, A review of autogenous shrinkage models of concrete, *Journal of Building Engineering.* 44 (2021) 103412. <https://doi.org/10.1016/j.jobe.2021.103412>.
- [18] C. Schröfl, K.A. Erk, W. Siriwatwechakul, M. Wyrzykowski, D. Snoeck, Recent progress in superabsorbent polymers for concrete, *Cem Concr Res.* 151 (2022) 106648. <https://doi.org/10.1016/j.cemconres.2021.106648>.

- [19] Y. Mao, J. Liu, C. Shi, Autogenous shrinkage and drying shrinkage of recycled aggregate concrete: A review, *J Clean Prod.* 295 (2021) 126435. <https://doi.org/10.1016/j.jclepro.2021.126435>.
- [20] A.E. Klausen, T. Kanstad, The effect of shrinkage reducing admixtures on drying shrinkage, AD , and early age stress development of concrete, *Structural Concrete.* 22 (2021). <https://doi.org/10.1002/suco.201900583>.
- [21] P. Zhan, Z. He, Application of shrinkage reducing admixture in concrete: A review, *Constr Build Mater.* 201 (2019) 676–690. <https://doi.org/10.1016/j.conbuildmat.2018.12.209>.
- [22] W. Zhang, H. Lin, M. Xue, S. Wang, J. Ran, F. Su, J. Zhu, Influence of shrinkage reducing admixtures on the performance of cementitious composites: A review, *Constr Build Mater.* 325 (2022) 126579. <https://doi.org/10.1016/j.conbuildmat.2022.126579>.
- [23] G.M. Moelich, P.J. Kruger, R. Combrinck, Mitigating early age cracking in 3D printed concrete using fibres, superabsorbent polymers, shrinkage reducing admixtures, B-CSA cement and curing measures, *Cem Concr Res.* 159 (2022) 106862. <https://doi.org/10.1016/j.CEMCONRES.2022.106862>.
- [24] H. Zhu, Y. Hu, R. Ma, J. Wang, Q. Li, Concrete thermal failure criteria, test method, and mechanism: A review, *Constr Build Mater.* 283 (2021) 122762. <https://doi.org/10.1016/j.conbuildmat.2021.122762>.
- [25] J. Xin, G. Zhang, Y. Liu, Z. Wang, Z. Wu, Evaluation of behavior and cracking potential of early-age cementitious systems using uniaxial restraint tests: A review, *Constr Build Mater.* 231 (2020) 117146. <https://doi.org/10.1016/j.CONBUILDMAT.2019.117146>.
- [26] S. Staquet, B. Delsaute, A. Darquennes, B. Espion, DESIGN OF A REVISITED TSTM SYSTEM FOR TESTING CONCRETE SINCE SETTING TIME UNDER FREE AND RESTRAINT CONDITIONS, 2012.
- [27] D.H. Nguyen, V.T. Nguyen, P. Lura, V.T.N. Dao, Temperature-stress testing machine – A state-of-the-art design and its unique applications in concrete research, *Cem Concr Compos.* 102 (2019) 28–38. <https://doi.org/10.1016/j.CEMCONCOMP.2019.04.019>.
- [28] A. E. Klausen, Early age crack assessment of concrete structures, experimental determination of decisive parameters, Ph.D. thesis, NTNU, 2016.

- [29] Y. Liu, A.K. Schindler, Finite-Element Modeling of Early-Age Concrete Stress Development, *Journal of Materials in Civil Engineering*. 32 (2020) 04019338. [https://doi.org/10.1061/\(asce\)mt.1943-5533.0002988](https://doi.org/10.1061/(asce)mt.1943-5533.0002988).
- [30] American Concrete Institute., ACI Committee 209--Creep and Shrinkage., Guide for modeling and calculating shrinkage and creep in hardened concrete, American Concrete Institute, 2008.
- [31] P. Lura, O.M. Jensen, K. Van Breugel, Autogenous shrinkage in high-performance cement paste: An evaluation of basic mechanisms, *Cem Concr Res.* 33 (2003) 223–232. [https://doi.org/10.1016/S0008-8846\(02\)00890-6](https://doi.org/10.1016/S0008-8846(02)00890-6).
- [32] L. Barcelo, M. Moranville, B. Clavaud, Autogenous shrinkage of concrete: a balance between autogenous swelling and self-desiccation, *Cem Concr Res.* 35 (2005) 177–183. <https://doi.org/10.1016/j.cemconres.2004.05.050>.
- [33] J. Carette, S. Staquet, Unified modelling of the temperature effect on the ADs of cement-based materials, *Cem Concr Compos.* 94 (2018) 62–71. <https://doi.org/10.1016/j.cemconcomp.2018.08.008>.
- [34] J. Carette, S. Joseph, Ö. Cizer, S. Staquet, Decoupling the autogenous swelling from the self-desiccation deformation in early age concrete with mineral additions: Micro-macro observations and unified modelling, *Cem Concr Compos.* 85 (2018) 122–132. <https://doi.org/10.1016/j.cemconcomp.2017.10.008>.
- [35] K. Orosz, H. Hedlund, A. Cwirzen, Effects of variable curing temperatures on AD of blended cement concretes, *Constr Build Mater.* 149 (2017) 474–480. <https://doi.org/10.1016/j.conbuildmat.2017.05.143>.
- [36] M.N. Amin, J.-S. Kim, T.T. Dat, J.-K. Kim, Improving test methods to measure early age autogenous shrinkage in concrete based on air cooling, *The IES Journal Part A: Civil & Structural Engineering.* 3 (2010) 244–256. <https://doi.org/10.1080/19373260.2010.522314>.
- [37] S. Staquet, B. Delsaute, A. Darquennes, B. Espion, Design of a revisited TSTM system for testing concrete since setting time under free and restraint conditions, in: *CONCRACK 3 – RILEM-JCI International Workshop on Crack Control of Mass Concrete and Related Issues Concerning Early-Age of Concrete Structures*, Paris, France, 2012.

- [38] M.H. Zhang, C.T. Tam, M.P. Leow, Effect of water-to-cementitious materials ratio and silica fume on the autogenous shrinkage of concrete, *Cem Concr Res.* 33 (2003) 1687–1694. [https://doi.org/10.1016/S0008-8846\(03\)00149-2](https://doi.org/10.1016/S0008-8846(03)00149-2).
- [39] Ø. Bjøntegaard, E.J. Sellevold, Interaction between thermal dilation and AD in high performance concrete, *Mater Struct.* 34 (2001) 266–272. <https://doi.org/10.1007/BF02482205>.
- [40] M. Viviani, B. Glisic, I.F.C. Smith, Separation of thermal and AD at varying temperatures using optical fiber sensors, *Cem Concr Compos.* 29 (2007) 435–447. <https://doi.org/10.1016/j.cemconcomp.2007.01.005>.
- [41] L. Li, V. Dao, P. Lura, AD and coefficient of thermal expansion of early-age concrete: Initial outcomes of a study using a newly-developed Temperature Stress Testing Machine, *Cem Concr Compos.* 119 (2021) 103997. <https://doi.org/10.1016/j.cemconcomp.2021.103997>.
- [42] P. Lura, K. van Breugel, I. Maruyama, Effect of curing temperature and type of cement on early-age shrinkage of high-performance concrete, *Cem Concr Res.* 31 (2001) 1867–1872. [https://doi.org/10.1016/S0008-8846\(01\)00601-9](https://doi.org/10.1016/S0008-8846(01)00601-9).
- [43] H. Huang, G. Ye, Examining the “time-zero” of autogenous shrinkage in high/ultra-high performance cement pastes, *Cem Concr Res.* 97 (2017) 107–114. <https://doi.org/10.1016/j.CEMCONRES.2017.03.010>.
- [44] Y. Ma, X. Yang, J. Hu, Z. Zhang, H. Wang, Accurate determination of the “time-zero” of autogenous shrinkage in alkali-activated fly ash/slag system, *Compos B Eng.* 177 (2019) 107367. <https://doi.org/10.1016/j.COMPOSITESB.2019.107367>.
- [45] O. Mejlhede Jensen, P. Freiesleben Hansen, A dilatometer for measuring AD in hardening portland cement paste, *Mater Struct.* 28 (1995) 406–409. <https://doi.org/10.1007/BF02473076>.
- [46] T. Lu, Z. Li, H. Huang, Effect of supplementary materials on the autogenous shrinkage of cement paste, *Materials.* 13 (2020) 1–15. <https://doi.org/10.3390/ma13153367>.
- [47] M. Sun, P. Visintin, T. Bennett, The effect of specimen size on autogenous and total shrinkage of ultra-high performance concrete (UHPC), *Constr Build Mater.* 327 (2022) 126952. <https://doi.org/10.1016/j.CONBUILDMAT.2022.126952>.

- [48] A.E. Klausen, T. Kanstad, Ø. Bjøntegaard, E.J. Sellevold, The effect of curing temperature on AD of fly ash concretes, *Cem Concr Compos.* 109 (2020) 103574. <https://doi.org/10.1016/j.cemconcomp.2020.103574>.
- [49] F. Hansen, P., J. Pedersen, Maturity computer for controlled curing and hardening of concrete, *Nordisk Betong.* 1 (1977) 19–34.
- [50] O.M. Jensen, P.F. Hansen, Influence of temperature on AD and relative humidity change in hardening cement paste, *Cem Concr Res.* 29 (1999) 567–575. [https://doi.org/10.1016/S0008-8846\(99\)00021-6](https://doi.org/10.1016/S0008-8846(99)00021-6).
- [51] C. Jiang, Y. Yang, Y. Wang, Y. Zhou, C. Ma, Autogenous shrinkage of high performance concrete containing mineral admixtures under different curing temperatures, *Constr Build Mater.* 61 (2014) 260–269. <https://doi.org/10.1016/J.CONBUILDMAT.2014.03.023>.
- [52] H.-W. Reinhardt, M. Stegmaier, Influence of heat curing on the pore structure and compressive strength of self-compacting concrete (SCC), *Cem Concr Res.* 36 (2006) 879–885. <https://doi.org/10.1016/j.cemconres.2005.12.004>.
- [53] A. Loukili, D. Chopin, A. Khelidj, J.-Y. Le Touzo, A new approach to determine autogenous shrinkage of mortar at an early age considering temperature history, *Cem Concr Res.* 30 (2000) 915–922. [https://doi.org/10.1016/S0008-8846\(00\)00241-6](https://doi.org/10.1016/S0008-8846(00)00241-6).
- [54] I. Chu, S.H. Kwon, M.N. Amin, J.-K. Kim, Estimation of temperature effects on autogenous shrinkage of concrete by a new prediction model, *Constr Build Mater.* 35 (2012) 171–182. <https://doi.org/10.1016/j.conbuildmat.2012.03.005>.
- [55] D. Shen, J. Jiang, J. Shen, P. Yao, G. Jiang, Influence of curing temperature on autogenous shrinkage and cracking resistance of high-performance concrete at an early age, *Constr Build Mater.* 103 (2016) 67–76. <https://doi.org/10.1016/J.CONBUILDMAT.2015.11.039>.
- [56] I. Maruyama, A. Teramoto, Temperature dependence of autogenous shrinkage of silica fume cement pastes with a very low water–binder ratio, *Cem Concr Res.* 50 (2013) 41–50. <https://doi.org/10.1016/j.cemconres.2013.03.017>.
- [57] E. Tazawa, S. Miyazawa, Influence of cement and admixture on autogenous shrinkage of cement paste, *Cem Concr Res.* 25 (1995) 281–287. [https://doi.org/10.1016/0008-8846\(95\)00010-0](https://doi.org/10.1016/0008-8846(95)00010-0).

- [58] K.M. Lee, H.K. Lee, S.H. Lee, G.Y. Kim, Autogenous shrinkage of concrete containing granulated blast-furnace slag, *Cem Concr Res.* 36 (2006) 1279–1285. <https://doi.org/10.1016/j.CEMCONRES.2006.01.005>.
- [59] D.P. Bentz, O.M. Jensen, K.K. Hansen, J.F. Olesen, H. Stang, C.-J. Haecker, Influence of Cement Particle-Size Distribution on Early Age Autogenous Strains and Stresses in Cement-Based Materials, *Journal of the American Ceramic Society.* 84 (2001) 129–135. <https://doi.org/10.1111/j.1151-2916.2001.tb00619.x>.
- [60] D.P. Bentz, E.J. Garboczi, C.J. Haecker, O.M. Jensen, Effects of cement particle size distribution on performance properties of Portland cement-based materials, *Cem Concr Res.* 29 (1999) 1663–1671. [https://doi.org/10.1016/S0008-8846\(99\)00163-5](https://doi.org/10.1016/S0008-8846(99)00163-5).
- [61] M. Bouasker, N.E.H. Khalifa, P. Mounanga, N. Ben Kahla, Early-age deformation and autogenous cracking risk of slag–limestone filler-cement blended binders, *Constr Build Mater.* 55 (2014) 158–167. <https://doi.org/10.1016/j.conbuildmat.2014.01.037>.
- [62] E. Ghafari, S.A. Ghahari, H. Costa, E. Júlio, A. Portugal, L. Durães, Effect of supplementary cementitious materials on autogenous shrinkage of ultra-high performance concrete, *Constr Build Mater.* 127 (2016) 43–48. <https://doi.org/10.1016/j.CONBUILDMAT.2016.09.123>.
- [63] C. Van Bunderen, R. Snellings, L. Vandewalle, Ö. Cizer, Early-age hydration and AD of cement paste containing flash calcined dredging sediments, *Constr Build Mater.* 200 (2019) 104–115. <https://doi.org/10.1016/j.conbuildmat.2018.12.090>.
- [64] Q.D. Nguyen, S. Afroz, Y. Zhang, T. Kim, W. Li, A. Castel, Autogenous and total shrinkage of limestone calcined clay cement (LC3) concretes, *Constr Build Mater.* 314 (2022) 125720. <https://doi.org/10.1016/j.conbuildmat.2021.125720>.
- [65] Z. Li, M. Nedeljković, B. Chen, G. Ye, Mitigating the autogenous shrinkage of alkali-activated slag by metakaolin, *Cem Concr Res.* 122 (2019) 30–41. <https://doi.org/10.1016/j.cemconres.2019.04.016>.
- [66] Z. Li, T. Lu, X. Liang, H. Dong, G. Ye, Mechanisms of autogenous shrinkage of alkali-activated slag and fly ash pastes, *Cem Concr Res.* 135 (2020). <https://doi.org/10.1016/j.cemconres.2020.106107>.

- [67] Z. Liu, W. Hansen, Aggregate and slag cement effects on autogenous shrinkage in cementitious materials, *Constr Build Mater.* 121 (2016) 429–436. <https://doi.org/10.1016/j.conbuildmat.2016.06.012>.
- [68] T. Lu, Z. Li, H. Huang, Restraining effect of aggregates on autogenous shrinkage in cement mortar and concrete, *Constr Build Mater.* 289 (2021) 123166. <https://doi.org/10.1016/j.CONBUILDMAT.2021.123166>.
- [69] Y. Chen, J. Wei, H. Huang, W. Jin, Q. Yu, Application of 3D-DIC to characterize the effect of aggregate size and volume on non-uniform shrinkage strain distribution in concrete, *Cem Concr Compos.* 86 (2018) 178–189. <https://doi.org/10.1016/j.cemconcomp.2017.11.005>.
- [70] P. Gao, Y. Chen, H. Huang, Z. Qian, E. Schlangen, J. Wei, Q. Yu, Effect of coarse aggregate size on non-uniform stress/strain and drying-induced microcracking in concrete, *Compos B Eng.* 216 (2021). <https://doi.org/10.1016/j.compositesb.2021.108880>.
- [71] S. Zhutovsky, K. Kovler, A. Bentur, Efficiency of lightweight aggregates for internal curing of high strength concrete to eliminate autogenous shrinkage, *Mater Struct.* 35 (2002) 97–101. <https://doi.org/10.1007/BF02482108>.
- [72] A. Bentur, S. Igarashi, K. Kovler, Prevention of autogenous shrinkage in high-strength concrete by internal curing using wet lightweight aggregates, *Cem Concr Res.* 31 (2001) 1587–1591. [https://doi.org/10.1016/S0008-8846\(01\)00608-1](https://doi.org/10.1016/S0008-8846(01)00608-1).
- [73] B. Akcay, M.A. Tasdemir, Optimisation of using lightweight aggregates in mitigating AD of concrete, *Constr Build Mater.* 23 (2009) 353–363. <https://doi.org/10.1016/j.conbuildmat.2007.11.015>.
- [74] Y. Zhuang, D. Zheng, Z. Ng, T. Ji, X. Chen, Effect of lightweight aggregate type on early-age autogenous shrinkage of concrete, *Constr Build Mater.* 120 (2016) 373–381. <https://doi.org/10.1016/j.conbuildmat.2016.05.105>.
- [75] M. Valcuende, E. Marco, C. Parra, P. Serna, Influence of limestone filler and viscosity-modifying admixture on the shrinkage of self-compacting concrete, *Cem Concr Res.* 42 (2012) 583–592. <https://doi.org/10.1016/j.cemconres.2012.01.001>.
- [76] W. Zhang, H. Lin, M. Xue, S. Wang, J. Ran, F. Su, J. Zhu, Influence of shrinkage reducing admixtures on the performance of

- cementitious composites: A review, *Constr Build Mater.* 325 (2022) 126579. <https://doi.org/10.1016/j.conbuildmat.2022.126579>.
- [77] J. Zhang, Y. Ma, H. Zhao, H. Sun, J. Liu, Mitigating autogenous shrinkage of cement paste with novel shrinkage-reducing polycarboxylate superplasticizer, *Mater Struct.* 55 (2022) 231. <https://doi.org/10.1617/s11527-022-02066-9>.
- [78] H. Zhao, Y. Xiang, J. Liu, Z. Zhang, R. Jia, T. Yao, H. Li, W. Xu, Q. Tian, Effects of reinforcement on AD of early-age concrete containing CaO-based expansion agent, *Constr Build Mater.* 320 (2022) 126197. <https://doi.org/10.1016/j.conbuildmat.2021.126197>.
- [79] S. Feng, J. Lyu, H. Xiao, J. Feng, Application of cellulose fibre in ultra-high-performance concrete to mitigate autogenous shrinkage, *J Sustain Cem Based Mater.* (2022) 1–14. <https://doi.org/10.1080/21650373.2022.2119618>.
- [80] D. Shen, C. Wen, P. Zhu, Y. Wu, J. Yuan, Influence of Barchip fiber on early-age autogenous shrinkage of high strength concrete, *Constr Build Mater.* 256 (2020) 119223. <https://doi.org/10.1016/j.conbuildmat.2020.119223>.
- [81] D. Sirtoli, M. Wyrzykowski, P. Riva, S. Tortelli, M. Marchi, P. Lura, Shrinkage and creep of high-performance concrete based on calcium sulfoaluminate cement, *Cem Concr Compos.* 98 (2019) 61–73. <https://doi.org/10.1016/j.cemconcomp.2019.02.006>.
- [82] D. Sirtoli, M. Wyrzykowski, P. Riva, P. Lura, Autogenous and drying shrinkage of mortars based on Portland and calcium sulfoaluminate cements, *Mater Struct.* 53 (2020) 126. <https://doi.org/10.1617/s11527-020-01561-1>.
- [83] H. Zhao, H. Liu, Y. Wan, R. Maria Ghantous, J. Li, Y. Liu, Y. Ni, J. Guan, Mechanical properties and AD behavior of early-age concrete containing pre-wetted ceramsite and CaO-based expansive agent, *Constr Build Mater.* 267 (2021). <https://doi.org/10.1016/j.conbuildmat.2020.120992>.
- [84] J. Justs, M. Wyrzykowski, D. Bajare, P. Lura, Internal curing by superabsorbent polymers in ultra-high performance concrete, *Cem Concr Res.* 76 (2015) 82–90. <https://doi.org/10.1016/j.cemconres.2015.05.005>.
- [85] D. Snoeck, O.M. Jensen, N. De Belie, The influence of superabsorbent polymers on the autogenous shrinkage properties of cement pastes with supplementary cementitious materials, *Cem Concr Res.* 74

- (2015) 59–67.  
<https://doi.org/10.1016/J.CEMCONRES.2015.03.020>.
- [86] Y. Chen, M. Liang, Y. Zhang, Z. Li, B. Šavija, E. Schlangen, O. Çopuroğlu, Can superabsorbent polymers be used as rheology modifiers for cementitious materials in the context of 3D concrete printing?, *Constr Build Mater.* 371 (2023) 130777. <https://doi.org/10.1016/j.conbuildmat.2023.130777>.
- [87] M.H. Lai, S.A.M. Binhowimal, A.M. Griffith, L. Hanzic, Q. Wang, Z. Chen, J.C.M. Ho, Shrinkage design model of concrete incorporating wet packing density, *Constr Build Mater.* 280 (2021) 122448. <https://doi.org/10.1016/j.conbuildmat.2021.122448>.
- [88] M.H. Hubler, R. Wendner, Z.P. Bažant, Statistical justification of Model B4 for drying and autogenous shrinkage of concrete and comparisons to other models, *Mater Struct.* 48 (2015) 797–814. <https://doi.org/10.1617/s11527-014-0516-z>.
- [89] K. Sakata, T. Shimomura, Recent Progress in Research on and Code Evaluation of Concrete Creep and Shrinkage in Japan, *Journal of Advanced Concrete Technology.* 2 (2004) 133–140. <https://doi.org/10.3151/jact.2.133>.
- [90] W. Raphael, R. Faddoul, F. Geara, A. Chateauneuf, Improvements to the Eurocode 2 shrinkage model for concrete using a large experimental database, *Structural Concrete.* 13 (2012) 174–181. <https://doi.org/10.1002/suco.201100029>.
- [91] B. Hilloulin, V.Q. Tran, Using machine learning techniques for predicting autogenous shrinkage of concrete incorporating superabsorbent polymers and supplementary cementitious materials, *Journal of Building Engineering.* 49 (2022) 104086. <https://doi.org/10.1016/j.jobe.2022.104086>.
- [92] L. Bal, F. Buyle-Bodin, Artificial neural network for predicting drying shrinkage of concrete, *Constr Build Mater.* 38 (2013) 248–254. <https://doi.org/10.1016/J.CONBUILDMAT.2012.08.043>.
- [93] C. Pichler, R. Lackner, H.A. Mang, A multiscale micromechanics model for the autogenous-shrinkage deformation of early-age cement-based materials, *Eng Fract Mech.* 74 (2007) 34–58. <https://doi.org/10.1016/j.engfracmech.2006.01.034>.
- [94] O. Bernard, F.-J. Ulm, E. Lemarchand, A multiscale micromechanics-hydration model for the early-age elastic properties of cement-

- based materials, *Cem Concr Res.* 33 (2003) 1293–1309. [https://doi.org/10.1016/S0008-8846\(03\)00039-5](https://doi.org/10.1016/S0008-8846(03)00039-5).
- [95] M. Pathirage, D.P. Bentz, G. Di Luzio, E. Masoero, G. Cusatis, The ONIX model: a parameter-free multiscale framework for the prediction of self-desiccation in concrete, *Cem Concr Compos.* 103 (2019) 36–48. <https://doi.org/10.1016/j.cemconcomp.2019.04.011>.
- [96] G. Di Luzio, G. Cusatis, Hygro-thermo-chemical modeling of high-performance concrete. II: Numerical implementation, calibration, and validation, *Cem Concr Compos.* 31 (2009) 309–324. <https://doi.org/10.1016/j.CEMCONCOMP.2009.02.016>.
- [97] G. Di Luzio, G. Cusatis, Hygro-thermo-chemical modeling of high performance concrete. I: Theory, *Cem Concr Compos.* 31 (2009) 301–308. <https://doi.org/10.1016/J.CEMCONCOMP.2009.02.015>.
- [98] H. Zhao, J. Liu, X. Yin, Y. Wang, D. Huang, A multiscale prediction model and simulation for autogenous shrinkage deformation of early-age cementitious materials, *Constr Build Mater.* 215 (2019) 482–493. <https://doi.org/10.1016/j.conbuildmat.2019.04.225>.
- [99] E.A.B. Koenders, K. van Breugel, Numerical modelling of autogenous shrinkage of hardening cement paste, *Cem Concr Res.* 27 (1997) 1489–1499. [https://doi.org/10.1016/S0008-8846\(97\)00170-1](https://doi.org/10.1016/S0008-8846(97)00170-1).
- [100] K. van Breugel, Numerical simulation of hydration and microstructural development in hardening cement-based materials (I) theory, *Cem Concr Res.* 25 (1995) 319–331. [https://doi.org/10.1016/0008-8846\(95\)00017-8](https://doi.org/10.1016/0008-8846(95)00017-8).
- [101] G. Ye, K. van Breugel, A.L.A. Fraaij, Three-dimensional microstructure analysis of numerically simulated cementitious materials, *Cem Concr Res.* 33 (2003) 215–222. [https://doi.org/10.1016/S0008-8846\(02\)00889-X](https://doi.org/10.1016/S0008-8846(02)00889-X).
- [102] T. Shimomura, K. Maekawa, Analysis of the drying shrinkage behaviour of concrete using a micromechanical model based on the micropore structure of concrete, *Magazine of Concrete Research.* 49 (1997) 303–322. <https://doi.org/10.1680/mac.1997.49.181.303>.
- [103] A. Aili, M. Vandamme, J.-M. Torrenti, B. Masson, Is long-term autogenous shrinkage a creep phenomenon induced by capillary

- effects due to self-desiccation?, *Cem Concr Res.* 108 (2018) 186–200. <https://doi.org/10.1016/j.cemconres.2018.02.023>.
- [104] P. Gao, G. Ye, H. Huang, Z. Qian, E. Schlangen, J. Wei, Q. Yu, Incorporating elastic and creep deformations in modelling the three-dimensional autogenous shrinkage of cement paste, *Cem Concr Res.* 160 (2022) 106907. <https://doi.org/10.1016/j.cemconres.2022.106907>.
- [105] E. Schlangen, E.J. Garboczi, Fracture simulations of concrete using lattice models: Computational aspects, *Eng Fract Mech.* 57 (1997) 319–332. [https://doi.org/10.1016/S0013-7944\(97\)00010-6](https://doi.org/10.1016/S0013-7944(97)00010-6).
- [106] L. Huang, Z. Chen, H. Ye, A mechanistic model for the time-dependent autogenous shrinkage of high performance concrete, *Constr Build Mater.* 255 (2020). <https://doi.org/10.1016/j.conbuildmat.2020.119335>.
- [107] Z. Hu, M. Wyrzykowski, K. Scrivener, P. Lura, Prediction of autogenous shrinkage of cement pastes as poro-visco-elastic deformation, *Cem Concr Res.* 126 (2019). <https://doi.org/10.1016/j.cemconres.2019.105917>.
- [108] T. Lu, Z. Li, K. van Breugel, Modelling of autogenous shrinkage of hardening cement paste, *Constr Build Mater.* 264 (2020). <https://doi.org/10.1016/j.conbuildmat.2020.120708>.
- [109] P. Klug, F. Wittmann, Activation energy and activation volume of creep of hardened cement paste, *Materials Science and Engineering.* 15 (1974) 63–66. [https://doi.org/10.1016/0025-5416\(74\)90030-5](https://doi.org/10.1016/0025-5416(74)90030-5).
- [110] Z. Li, T. Lu, Y. Chen, B. Wu, G. Ye, Prediction of the autogenous shrinkage and microcracking of alkali-activated slag and fly ash concrete, *Cem Concr Compos.* 117 (2021). <https://doi.org/10.1016/j.cemconcomp.2020.103913>.
- [111] Z.P. Bažant, M. Jirásek, *Creep and Hygrothermal Effects in Concrete Structures*, Springer Netherlands, Dordrecht, 2018. <https://doi.org/10.1007/978-94-024-1138-6>.
- [112] Z.P. Bazant, S.T. Wu, Rate-type creep law of aging concrete based on Maxwell chain ER(t, r), (1974).
- [113] fib, *fib Model Code for Concrete Structures 2010*, Wiley-VCH Verlag GmbH & Co. KGaA, Weinheim, Germany, 2013. <https://doi.org/10.1002/9783433604090>.

- [114] American Concrete Institute Committee 209 (ACI), Prediction of Creep, Shrinkage, and Temperature Effects in Concrete Structures, ACI: Farmington Hills, MI, USA, 1992.
- [115] B. Brussels, Concrete Tests—Test Specimens—Part 2: Making and Curing of Test Specimens for Strength Tests; ISO/TC 71/SC 1 Test Methods for Concrete; , International Organization for Standardization, Geneva, Switzerland, 1986.
- [116] EN, EN 1992-1-1 Eurocode 2: Design of Concrete Structures—Part 1-1: General Rules and Rules for Buildings, CEN, Brussels, Belgium, 2002.
- [117] AASHTO, AASHTO LRFD Bridge Design Specifications, American Association of State Highway and Transportation Officials, Washington DC, 2012.
- [118] M.A. Rashid, M.A. Mansur, P. Paramasivam, Correlations between Mechanical Properties of High-Strength Concrete, *Journal of Materials in Civil Engineering*. 14 (2002) 230–238. [https://doi.org/10.1061/\(ASCE\)0899-1561\(2002\)14:3\(230\)](https://doi.org/10.1061/(ASCE)0899-1561(2002)14:3(230)).
- [119] F.P. Zhou, F.D. Lydon, B.I.G. Barr, Effect of coarse aggregate on elastic modulus and compressive strength of high performance concrete, *Cem Concr Res*. 25 (1995) 177–186. [https://doi.org/10.1016/0008-8846\(94\)00125-1](https://doi.org/10.1016/0008-8846(94)00125-1).
- [120] A.M. Neville, *Properties of concrete-5th edition*, 2011.
- [121] D. Geng, N. Dai, X. Jin, E. Miao, Comparison of calculating methods and applications of different concrete maturity, *J Phys Conf Ser*. 2011 (2021) 012022. <https://doi.org/10.1088/1742-6596/2011/1/012022>.
- [122] V. Waller, L. d'Aloia, F. Cussigh, S. Lecrux, Using the maturity method in concrete cracking control at early ages, *Cem Concr Compos*. 26 (2004) 589–599. [https://doi.org/10.1016/S0958-9465\(03\)00080-5](https://doi.org/10.1016/S0958-9465(03)00080-5).
- [123] H. Beushausen, T. Dittmer, The influence of aggregate type on the strength and elastic modulus of high strength concrete, *Constr Build Mater*. 74 (2015) 132–139. <https://doi.org/10.1016/J.CONBUILDMAT.2014.08.055>.
- [124] C. Boulay, S. Staquet, B. Delsaute, J. Carette, M. Crespini, O. Yazoghli-Marzouk, É. Merliot, S. Ramanich, How to monitor the modulus of elasticity of concrete, automatically since the earliest age?,

- Materials and Structures/Materiaux et Constructions. 47 (2014) 141–155. <https://doi.org/10.1617/s11527-013-0051-3>.
- [125] J. Carette, S. Staquet, Monitoring and modelling the early age and hardening behaviour of eco-concrete through continuous non-destructive measurements: Part II. Mechanical behaviour, *Cem Concr Compos.* 73 (2016) 1–9. <https://doi.org/10.1016/j.cemconcomp.2016.07.003>.
- [126] G. Constantinides, F.J. Ulm, The effect of two types of C-S-H on the elasticity of cement-based materials: Results from nanoindentation and micromechanical modeling, *Cem Concr Res.* 34 (2004) 67–80. [https://doi.org/10.1016/S0008-8846\(03\)00230-8](https://doi.org/10.1016/S0008-8846(03)00230-8).
- [127] P.D. Tennis, H.M. Jennings, A model for two types of calcium silicate hydrate in the microstructure of Portland cement pastes, *Cem Concr Res.* 30 (2000) 855–863. [https://doi.org/10.1016/S0008-8846\(00\)00257-X](https://doi.org/10.1016/S0008-8846(00)00257-X).
- [128] X. Chen, D. Hou, Y. Han, X. Ding, P. Hua, Clustering analysis of grid nanoindentation data for cementitious materials, *J Mater Sci.* 56 (2021) 12238–12255. <https://doi.org/10.1007/s10853-021-05848-8>.
- [129] L. Sorelli, G. Constantinides, F.J. Ulm, F. Toutlemonde, The nano-mechanical signature of Ultra High Performance Concrete by statistical nanoindentation techniques, *Cem Concr Res.* 38 (2008) 1447–1456. <https://doi.org/10.1016/J.CEMCONRES.2008.09.002>.
- [130] W.R.L. Da Silva, J. Němeček, P. Štemberk, Methodology for nanoindentation-assisted prediction of macroscale elastic properties of high performance cementitious composites, *Cem Concr Compos.* 45 (2014) 57–68. <https://doi.org/10.1016/J.CEMCONCOMP.2013.09.013>.
- [131] Y. Li, Y. Li, R. Wang, Quantitative evaluation of elastic modulus of concrete with nanoindentation and homogenization method, *Constr Build Mater.* 212 (2019) 295–303. <https://doi.org/10.1016/j.conbuildmat.2019.04.002>.
- [132] Z. Hu, M. Wyrzykowski, M. Griffa, K. Scrivener, P. Lura, Young's modulus and creep of calcium-silicate-hydrate compacts measured by microindentation, *Cem Concr Res.* 134 (2020). <https://doi.org/10.1016/j.cemconres.2020.106104>.
- [133] W. Wilson, L. Sorelli, A. Tagnit-Hamou, Unveiling micro-chemo-mechanical properties of C-(A)-S-H and other phases in blended-

- cement pastes, *Cem Concr Res.* 107 (2018) 317–336. <https://doi.org/10.1016/j.CEMCONRES.2018.02.010>.
- [134] L. Göbel, C. Bos, R. Schwaiger, A. Flohr, A. Osburg, Micromechanics-based investigation of the elastic properties of polymer-modified cementitious materials using nanoindentation and semi-analytical modeling, *Cem Concr Compos.* 88 (2018) 100–114. <https://doi.org/10.1016/j.cemconcomp.2018.01.010>.
- [135] G. Fang, Q. Wang, M. Zhang, Micromechanical analysis of interfacial transition zone in alkali-activated fly ash-slag concrete, *Cem Concr Compos.* 119 (2021) 103990. <https://doi.org/10.1016/j.cemconcomp.2021.103990>.
- [136] Z. Luo, W. Li, Y. Gan, X. He, A. Castel, D. Sheng, Nanoindentation on micromechanical properties and microstructure of geopolymers with nano-SiO<sub>2</sub> and nano-TiO<sub>2</sub>, *Cem Concr Compos.* 117 (2021). <https://doi.org/10.1016/j.cemconcomp.2020.103883>.
- [137] Y. Sun, J.-X. Lu, C.S. Poon, Strength degradation of seawater-mixed alite pastes: an explanation from statistical nanoindentation perspective, *Cem Concr Res.* 152 (2022) 106669. <https://doi.org/10.1016/j.cemconres.2021.106669>.
- [138] W. Wilson, J.M. Rivera-Torres, L. Sorelli, A. Durán-Herrera, A. Tagnit-Hamou, The micromechanical signature of high-volume natural pozzolan concrete by combined statistical nanoindentation and SEM-EDS analyses, *Cem Concr Res.* 91 (2017) 1–12. <https://doi.org/10.1016/j.CEMCONRES.2016.10.004>.
- [139] B. Šavija, H. Zhang, E. Schlangen, Micromechanical testing and modelling of blast furnace slag cement pastes, *Constr Build Mater.* 239 (2020). <https://doi.org/10.1016/j.conbuildmat.2019.117841>.
- [140] H. Zhang, B. Šavija, M. Luković, E. Schlangen, Experimentally informed micromechanical modelling of cement paste: An approach coupling X-ray computed tomography and statistical nanoindentation, *Compos B Eng.* 157 (2019) 109–122. <https://doi.org/10.1016/j.COMPOSITESB.2018.08.102>.
- [141] H. Zhang, B. Šavija, S.C. Figueiredo, E. Schlangen, Experimentally validated multi-scale modelling scheme of deformation and fracture of cement paste, *Cem Concr Res.* 102 (2017) 175–186. <https://doi.org/10.1016/j.CEMCONRES.2017.09.011>.
- [142] H. Zhang, Y. Xu, Y. Gan, Z. Chang, E. Schlangen, B. Šavija, Microstructure informed micromechanical modelling of hydrated

- cement paste: Techniques and challenges, *Constr Build Mater.* 251 (2020) 118983. <https://doi.org/10.1016/j.CONBUILDMAT.2020.118983>.
- [143] K.M. Lee, J.H. Park, A numerical model for elastic modulus of concrete considering interfacial transition zone, *Cem Concr Res.* 38 (2008) 396–402. <https://doi.org/10.1016/j.CEMCONRES.2007.09.019>.
- [144] S. Krishnya, Y. Yoda, Y. Elakneswaran, A two-stage model for the prediction of mechanical properties of cement paste, *Cem Concr Compos.* 115 (2021) 103853. <https://doi.org/10.1016/j.CEMCONCOMP.2020.103853>.
- [145] A. Princigallo, P. Lura, K. Van Breugel, G. Levita, Early development of properties in a cement paste: A numerical and experimental study, *Cem Concr Res.* 33 (2003) 1013–1020. [https://doi.org/10.1016/S0008-8846\(03\)00002-4](https://doi.org/10.1016/S0008-8846(03)00002-4).
- [146] V. Šmilauer, Z. Bittnar, Microstructure-based micromechanical prediction of elastic properties in hydrating cement paste, *Cem Concr Res.* 36 (2006) 1708–1718. <https://doi.org/10.1016/j.cemconres.2006.05.014>.
- [147] S. Liang, Y. Wei, Z. Wu, Multiscale modeling elastic properties of cement-based materials considering imperfect interface effect, *Constr Build Mater.* 154 (2017) 567–579. <https://doi.org/10.1016/j.conbuildmat.2017.07.196>.
- [148] L. Charpin, Y. Le Pape, É. Coustabeau, É. Toppani, G. Heinfling, C. Le Bellego, B. Masson, J. Montalvo, A. Courtois, J. Sanahuja, N. Reviron, A 12 year EDF study of concrete creep under uniaxial and biaxial loading, *Cem Concr Res.* 103 (2018) 140–159. <https://doi.org/10.1016/j.cemconres.2017.10.009>.
- [149] M. Irfan-ul-Hassan, B. Pichler, R. Reihnsner, Ch. Hellmich, Elastic and creep properties of young cement paste, as determined from hourly repeated minute-long quasi-static tests, *Cem Concr Res.* 82 (2016) 36–49. <https://doi.org/10.1016/j.cemconres.2015.11.007>.
- [150] B. Delsaute, C. Boulay, S. Staquet, Creep testing of concrete since setting time by means of permanent and repeated minute-long loadings, *Cem Concr Compos.* 73 (2016) 75–88. <https://doi.org/10.1016/j.CEMCONCOMP.2016.07.005>.
- [151] M. Ausweger, E. Binder, O. Lahayne, R. Reihnsner, G. Maier, M. Peyerl, B. Pichler, Early-age evolution of strength, stiffness, and non-aging

- creep of concretes: Experimental characterization and correlation analysis, *Materials*. 12 (2019). <https://doi.org/10.3390/ma12020207>.
- [152] H. Huang, R. Garcia, S.S. Huang, M. Guadagnini, K. Pilakoutas, A practical creep model for concrete elements under eccentric compression, *Materials and Structures/Materiaux et Constructions*. 52 (2019). <https://doi.org/10.1617/s11527-019-1432-z>.
- [153] B. Delsaute, J.M. Torrenti, S. Staquet, Modeling basic creep of concrete since setting time, *Cem Concr Compos*. 83 (2017) 239–250. <https://doi.org/10.1016/j.cemconcomp.2017.07.023>.
- [154] M. Wyrzykowski, K. Scrivener, P. Lura, Basic creep of cement paste at early age - the role of cement hydration, *Cem Concr Res*. 116 (2019) 191–201. <https://doi.org/10.1016/j.cemconres.2018.11.013>.
- [155] S. Liang, Y. Wei, Methodology of obtaining intrinsic creep property of concrete by flexural deflection test, *Cem Concr Compos*. 97 (2019) 288–299. <https://doi.org/10.1016/j.cemconcomp.2019.01.003>.
- [156] Y. Wei, J. Huang, S. Liang, Measurement and modeling concrete creep considering relative humidity effect, *Mech Time Depend Mater*. 24 (2020) 161–177. <https://doi.org/10.1007/s11043-019-09414-3>.
- [157] M. Farah, F. Grondin, S.Y. Alam, A. Loukili, Experimental approach to investigate creep-damage bilateral effects in concrete at early age, *Cem Concr Compos*. 96 (2019) 128–137. <https://doi.org/10.1016/j.cemconcomp.2018.11.022>.
- [158] A. Dabarera, L. Li, V. Dao, Experimental evaluation and modelling of early-age basic tensile creep in high-performance concrete, *Materials and Structures/Materiaux et Constructions*. 54 (2021). <https://doi.org/10.1617/s11527-021-01722-w>.
- [159] H. Zhu, Q. Li, Y. Hu, R. Ma, Double feedback control method for determining early-age restrained creep of concrete using a temperature stress testing machine, *Materials*. 11 (2018). <https://doi.org/10.3390/ma11071079>.
- [160] Y. Li, J. Chen, L. Wen, J. Wang, K. Li, Investigation of the Nonlinear Creep of Concrete with Different Initial Defect Rates under Continuous Compression with Acoustic Emission Technology,

- Journal of Materials in Civil Engineering. 33 (2021) 04020441.  
[https://doi.org/10.1061/\(asce\)mt.1943-5533.0003550](https://doi.org/10.1061/(asce)mt.1943-5533.0003550).
- [161] Z. Zhao, K. Wang, D.A. Lange, H. Zhou, W. Wang, D. Zhu, Creep and thermal cracking of ultra-high volume fly ash mass concrete at early age, *Cem Concr Compos.* 99 (2019) 191–202.  
<https://doi.org/10.1016/j.cemconcomp.2019.02.018>.
- [162] Z. Hu, A. Hilaire, M. Wyrzykowski, P. Lura, K. Scrivener, Visco-elastic behavior of blended cement pastes at early ages, *Cem Concr Compos.* 107 (2020) 103497.  
<https://doi.org/10.1016/j.cemconcomp.2019.103497>.
- [163] Z. He, P. Zhan, S. Du, B. Liu, W. Yuan, Creep behavior of concrete containing glass powder, *Compos B Eng.* 166 (2019) 13–20.  
<https://doi.org/10.1016/j.compositesb.2018.11.133>.
- [164] C. Gu, Y. Wang, F. Gao, Y. Yang, T. Ni, J. Liu, X. Lou, J. Chen, Early age tensile creep of high performance concrete containing mineral admixtures: Experiments and modeling, *Constr Build Mater.* 197 (2019) 766–777.  
<https://doi.org/10.1016/j.conbuildmat.2018.11.218>.
- [165] B. Delsaute, J.M. Torrenti, S. Staquet, Prediction of the basic creep of concrete with high substitution of Portland cement by mineral additions at early age, *Structural Concrete.* 22 (2021) E563–E580.  
<https://doi.org/10.1002/suco.201900313>.
- [166] M. Briffaut, F. Benboudjema, J.M. Torrenti, G. Nahas, Concrete early age basic creep: Experiments and test of rheological modelling approaches, *Constr Build Mater.* 36 (2012) 373–380.  
<https://doi.org/10.1016/j.conbuildmat.2012.04.101>.
- [167] D. Shen, J. Jiang, W. Wang, J. Shen, G. Jiang, Tensile creep and cracking resistance of concrete with different water-to-cement ratios at early age, *Constr Build Mater.* 146 (2017) 410–418.  
<https://doi.org/10.1016/j.conbuildmat.2017.04.056>.
- [168] X. Zheng, T. Ji, S.M. Easa, B. Zhang, Z. Jiang, Tensile basic creep behavior of lightweight aggregate concrete reinforced with steel fiber, *Constr Build Mater.* 200 (2019) 356–367.  
<https://doi.org/10.1016/j.conbuildmat.2018.12.138>.
- [169] R. V. Silva, J. de Brito, R.K. Dhir, Comparative analysis of existing prediction models on the creep behaviour of recycled aggregate concrete, *Eng Struct.* 100 (2015) 31–42.  
<https://doi.org/10.1016/j.engstruct.2015.06.004>.

- [170] L. Zhu, J.-J. Wang, X. Li, G.-Y. Zhao, X.-J. Huo, Experimental and numerical study on creep and shrinkage effects of ultra high-performance concrete beam, *Compos B Eng.* 184 (2020) 107713. <https://doi.org/10.1016/j.compositesb.2019.107713>.
- [171] Z. Zhao, H. Zhang, B. Fang, Y. Sun, Y. Zhong, T. Shi, Tensile Creep Model of Slab Concrete Based on Microprestress-Solidification Theory, *Materials.* 13 (2020) 3157. <https://doi.org/10.3390/ma13143157>.
- [172] L. Li, A.G.P. Dabarera, V. Dao, Basic tensile creep of concrete with and without superabsorbent polymers at early ages, *Constr Build Mater.* 320 (2022) 126180. <https://doi.org/10.1016/j.conbuildmat.2021.126180>.
- [173] Z.P. Bažant, G. Cusatis, L. Cedolin, Temperature Effect on Concrete Creep Modeled by Microprestress-Solidification Theory, *J Eng Mech.* 130 (2004) 691–699. [https://doi.org/10.1061/\(ASCE\)0733-9399\(2004\)130:6\(691\)](https://doi.org/10.1061/(ASCE)0733-9399(2004)130:6(691)).
- [174] M. Liang, Z. Chang, Z. Wan, Y. Gan, E. Schlangen, B. Šavija, Interpretable Ensemble-Machine-Learning models for predicting creep behavior of concrete, *Cem Concr Compos.* 125 (2022) 104295. <https://doi.org/10.1016/j.cemconcomp.2021.104295>.
- [175] G. De Schutter, Applicability of degree of hydration concept and maturity method for thermo-visco-elastic behaviour of early age concrete, *Cem Concr Compos.* 26 (2004) 437–443. [https://doi.org/10.1016/S0958-9465\(03\)00067-2](https://doi.org/10.1016/S0958-9465(03)00067-2).
- [176] J. Frech-Baronet, L. Sorelli, J.P. Charron, New evidences on the effect of the internal relative humidity on the creep and relaxation behaviour of a cement paste by micro-indentation techniques, *Cem Concr Res.* 91 (2017) 39–51. <https://doi.org/10.1016/j.cemconres.2016.10.005>.
- [177] P. Yu, Y.H. Duan, Q.X. Fan, S.W. Tang, Improved MPS model for concrete creep under variable humidity and temperature, *Constr Build Mater.* 243 (2020) 118183. <https://doi.org/10.1016/j.conbuildmat.2020.118183>.
- [178] D.S. Atrushi, *Tensile and Compressive Creep of Early Age Concrete: Testing and Modelling*, 2003.
- [179] P. Rossi, J.L. Tailhan, F. Le Maou, Comparison of concrete creep in tension and in compression: Influence of concrete age at loading

- and drying conditions, *Cem Concr Res.* 51 (2013) 78–84. <https://doi.org/10.1016/j.cemconres.2013.04.001>.
- [180] A.E. Klausen, T. Kanstad, Ø. Bjøntegaard, E. Sellevold, Comparison of tensile and compressive creep of fly ash concretes in the hardening phase, *Cem Concr Res.* 95 (2017) 188–194. <https://doi.org/10.1016/j.cemconres.2017.02.018>.
- [181] Y. Wei, Z. Wu, J. Huang, S. Liang, Comparison of Compressive, Tensile, and Flexural Creep of Early-Age Concretes under Sealed and Drying Conditions, *Journal of Materials in Civil Engineering*. 30 (2018) 04018289. [https://doi.org/10.1061/\(asce\)mt.1943-5533.0002495](https://doi.org/10.1061/(asce)mt.1943-5533.0002495).
- [182] Q. Zhang, R. Le Roy, M. Vandamme, B. Zuber, Long-term creep properties of cementitious materials: Comparing microindentation testing with macroscopic uniaxial compressive testing, *Cem Concr Res.* 58 (2014) 89–98. <https://doi.org/10.1016/j.cemconres.2014.01.004>.
- [183] Y. Wei, S. Liang, X. Gao, Indentation creep of cementitious materials: Experimental investigation from nano to micro length scales, *Constr Build Mater.* 143 (2017) 222–233. <https://doi.org/10.1016/j.conbuildmat.2017.03.126>.
- [184] S. Mallick, M.B. Anoop, K. Balaji Rao, Early age creep of cement paste - Governing mechanisms and role of water-A microindentation study, *Cem Concr Res.* 116 (2019) 284–298. <https://doi.org/10.1016/j.cemconres.2018.12.004>.
- [185] S. Mallick, M.B. Anoop, K.B. Rao, Creep of cement paste containing fly ash - An investigation using microindentation technique, *Cem Concr Res.* 121 (2019) 21–36. <https://doi.org/10.1016/j.cemconres.2019.04.006>.
- [186] S. Liang, Y. Wei, New insights into creep and creep recovery of hardened cement paste at micro scale, *Constr Build Mater.* 248 (2020). <https://doi.org/10.1016/j.conbuildmat.2020.118724>.
- [187] S. Liang, Y. Wei, Effects of water-to-cement ratio and curing age on microscopic creep and creep recovery of hardened cement pastes by microindentation, *Cem Concr Compos.* 113 (2020) 103619. <https://doi.org/10.1016/j.cemconcomp.2020.103619>.
- [188] J. Li, W. Zhang, P.J.M. Monteiro, Preferred orientation of calcium aluminosilicate hydrate compacts: Implications for creep and

- indentation, *Cem Concr Res.* 143 (2021) 106371. <https://doi.org/10.1016/j.cemconres.2021.106371>.
- [189] M. Vandamme, F.-J. Ulm, Nanoindentation investigation of creep properties of calcium silicate hydrates, *Cem Concr Res.* 52 (2013) 38–52. <https://doi.org/10.1016/j.cemconres.2013.05.006>.
- [190] Y. Gan, M. Vandamme, H. Zhang, Y. Chen, E. Schlangen, K. van Breugel, B. Šavija, Micro-cantilever testing on the short-term creep behaviour of cement paste at micro-scale, *Cem Concr Res.* 134 (2020). <https://doi.org/10.1016/j.cemconres.2020.106105>.
- [191] P. Suwanmaneechot, A. Aili, I. Maruyama, Creep behavior of C-S-H under different drying relative humidities: Interpretation of microindentation tests and sorption measurements by multi-scale analysis, *Cem Concr Res.* 132 (2020). <https://doi.org/10.1016/j.cemconres.2020.106036>.
- [192] Y. Li, Y. Liu, Z. Wang, H. Li, J. Mu, Effect of phases on the creep properties of cement paste based on indentation test and homogenization scheme, *Constr Build Mater.* 317 (2022) 125957. <https://doi.org/10.1016/j.conbuildmat.2021.125957>.
- [193] Z.P. Bazant, E. Osman, Double power law for basic creep of concrete, *Matériaux et Construction.* 9 (1976) 3–11.
- [194] J.M. Torrenti, R. Le Roy, Analysis of some basic creep tests on concrete and their implications for modeling, *Structural Concrete.* 19 (2018) 483–488. <https://doi.org/10.1002/suco.201600197>.
- [195] G. De Schutter, L. Taerwe, Fictitious degree of hydration method for the basic creep of early age concrete, 2000.
- [196] W. Jiang, G. De Schutter, Y. Yuan, Degree of hydration based prediction of early age basic creep and creep recovery of blended concrete, *Cem Concr Compos.* 48 (2014) 83–90. <https://doi.org/10.1016/j.cemconcomp.2013.10.012>.
- [197] W. Wang, J. Gong, New relaxation function and age-adjusted effective modulus expressions for creep analysis of concrete structures, *Eng Struct.* 188 (2019) 1–10. <https://doi.org/10.1016/j.engstruct.2019.03.009>.
- [198] L. Bal, F. Buyle-Bodin, Artificial neural network for predicting creep of concrete, *Neural Comput Appl.* 25 (2014) 1359–1367. <https://doi.org/10.1007/s00521-014-1623-z>.

- [199] A.H. Gandomi, S. Sajedi, B. Kiani, Q. Huang, Genetic programming for experimental big data mining: A case study on concrete creep formulation, *Autom Constr.* 70 (2016) 89–97. <https://doi.org/10.1016/j.autcon.2016.06.010>.
- [200] K. Li, Y. Long, H. Wang, Y.-F. Wang, Modeling and Sensitivity Analysis of Concrete Creep with Machine Learning Methods, *Journal of Materials in Civil Engineering*. 33 (2021) 04021206. [https://doi.org/10.1061/\(asce\)mt.1943-5533.0003843](https://doi.org/10.1061/(asce)mt.1943-5533.0003843).
- [201] M. Liang, Y. Gan, Z. Chang, Z. Wan, E. Schlangen, B. Šavija, Microstructure-informed deep convolutional neural network for predicting short-term creep modulus of cement paste, *Cem Concr Res.* 152 (2022) 106681. <https://doi.org/10.1016/j.cemconres.2021.106681>.
- [202] Z.R. Bažant, G.H. Li, Comprehensive database on concrete creep and shrinkage, *ACI Mater J.* 105 (2008). <https://doi.org/10.14359/20206>.
- [203] M.H. Hubler, R. Wendner, Z.P. Bažant, Comprehensive database for concrete creep and shrinkage: Analysis and recommendations for testing and recording, *ACI Mater J.* 112 (2015) 547–558. <https://doi.org/10.14359/51687452>.
- [204] I. Carol, Z.P. Bažant, Viscoelasticity with Aging Caused by Solidification of Nonaging Constituent, *J Eng Mech.* 119 (1993) 2252–2269. [https://doi.org/10.1061/\(ASCE\)0733-9399\(1993\)119:11\(2252\)](https://doi.org/10.1061/(ASCE)0733-9399(1993)119:11(2252)).
- [205] B. Hedegaard, Creep and Shrinkage Modeling of Concrete Using Solidification Theory, *Journal of Materials in Civil Engineering*. 32 (2020) 04020179. [https://doi.org/10.1061/\(asce\)mt.1943-5533.0003256](https://doi.org/10.1061/(asce)mt.1943-5533.0003256).
- [206] B.P. Zdenek Bazant, S. Prasannan, S. Member, SOLIDIFICATION THEORY FOR CONCRETE CREEP. II: VERIFICATION AND APPLICATION, n.d.
- [207] A. Hilaire, F. Benboudjema, A. Darquennes, Y. Berthaud, G. Nahas, Analysis of concrete creep in compression, tension and bending: Numerical modeling, in: *Mechanics and Physics of Creep, Shrinkage, and Durability of Concrete: A Tribute to Zdenek P. Bazant - Proceedings of the 9th Int. Conf. on Creep, Shrinkage, and Durability Mechanics, CONCREEP 2013*, American Society of Civil

- Engineers (ASCE), 2013: pp. 348–355.  
<https://doi.org/10.1061/9780784413111.041>.
- [208] B.D. Hedegaard, C.K. Shield, C.E. W. French, Smeared-Bar Model for Viscoelastic Analysis of Uncracked Reinforced Concrete Structures, *Journal of Structural Engineering*. 141 (2015) 04014167.  
[https://doi.org/10.1061/\(asce\)st.1943-541x.0001124](https://doi.org/10.1061/(asce)st.1943-541x.0001124).
- [209] Z.P. Bažant, Y. Xi, Continuous Retardation Spectrum for Solidification Theory of Concrete Creep, *J Eng Mech*. 121 (1995) 281–288.  
[https://doi.org/10.1061/\(ASCE\)0733-9399\(1995\)121:2\(281\)](https://doi.org/10.1061/(ASCE)0733-9399(1995)121:2(281)).
- [210] M. Jirásek, P. Havlásek, Accurate approximations of concrete creep compliance functions based on continuous retardation spectra, *Comput Struct*. 135 (2014) 155–168.  
<https://doi.org/10.1016/J.COMPSTRUC.2014.01.024>.
- [211] Z.P. Bazant, Y. Xi, S. Baweja, Continuous retardation spectrum for solidification theory of aging creep of concrete, *Proceedings of Engineering Mechanics*. 2 (1995).
- [212] Q. Yu, P. Bažant, R. Wendner, Improved Algorithm for Efficient and Realistic Creep Analysis of Large Creep-Sensitive Concrete Structures, *ACI Struct J*. 109 (2012).  
<https://doi.org/10.14359/51684044>.
- [213] G. Di Luzio, L. Cedolin, C. Beltrami, Tridimensional Long-Term Finite Element Analysis of Reinforced Concrete Structures with Rate-Type Creep Approach, *Applied Sciences*. 10 (2020) 4772.  
<https://doi.org/10.3390/app10144772>.
- [214] T. Honorio, B. Bary, F. Benboudjema, Multiscale estimation of ageing viscoelastic properties of cement-based materials: A combined analytical and numerical approach to estimate the behaviour at early age, *Cem Concr Res*. 85 (2016) 137–155.  
<https://doi.org/10.1016/j.cemconres.2016.03.010>.
- [215] Y. Li, Y. Liu, Y. Li, Y. Li, R. Wang, Evaluation of concrete creep properties based on indentation test and multiscale homogenization method, *Cem Concr Compos*. 123 (2021) 104135.  
<https://doi.org/10.1016/J.CEMCONCOMP.2021.104135>.
- [216] A. Aili, M. Vandamme, J.M. Torrenti, B. Masson, A viscoelastic poromechanical model for shrinkage and creep of concrete, *Cem Concr Res*. 129 (2020) 105970.  
<https://doi.org/10.1016/J.CEMCONRES.2019.105970>.

- [217] T. Mori, K. Tanaka, Average stress in matrix and average elastic energy of materials with misfitting inclusions, *Acta Metallurgica*. 21 (1973) 571–574. [https://doi.org/10.1016/0001-6160\(73\)90064-3](https://doi.org/10.1016/0001-6160(73)90064-3).
- [218] R. Hill, A self-consistent mechanics of composite materials, *J Mech Phys Solids*. 13 (1965) 213–222. [https://doi.org/10.1016/0022-5096\(65\)90010-4](https://doi.org/10.1016/0022-5096(65)90010-4).
- [219] M. Königsberger, T. Honório, J. Sanahuja, B. Delsaute, B.L.A. Pichler, Homogenization of nonaging basic creep of cementitious materials: A multiscale modeling benchmark, *Constr Build Mater*. 290 (2021) 123144. <https://doi.org/10.1016/j.conbuildmat.2021.123144>.
- [220] J. Baronet, L. Sorelli, J.P. Charron, M. Vandamme, J. Sanahuja, A two-scale method to rapidly characterize the logarithmic basic creep of concrete by coupling microindentation and uniaxial compression creep test, *Cem Concr Compos*. 125 (2022). <https://doi.org/10.1016/j.cemconcomp.2021.104274>.
- [221] Z. Hu, A. Hilaire, J. Ston, M. Wyrzykowski, P. Lura, K. Scrivener, Intrinsic viscoelasticity of C-S-H assessed from basic creep of cement pastes, *Cem Concr Res*. 121 (2019) 11–20. <https://doi.org/10.1016/j.cemconres.2019.04.003>.
- [222] Y. Gan, C. Romero Rodriguez, H. Zhang, E. Schlangen, K. van Breugel, B. Šavija, Modeling of microstructural effects on the creep of hardened cement paste using an experimentally informed lattice model, *Computer-Aided Civil and Infrastructure Engineering*. 36 (2021) 560–576. <https://doi.org/10.1111/mice.12659>.
- [223] F. Lavergne, J.F. Barthélémy, Confronting a refined multiscale estimate for the aging basic creep of concrete with a comprehensive experimental database, *Cem Concr Res*. 136 (2020). <https://doi.org/10.1016/j.cemconres.2020.106163>.
- [224] V. Semianiuk, V. Tur, M.F. Herrador, M. Paredes G., Early age strains and self-stresses of expansive concrete members under uniaxial restraint conditions, *Constr Build Mater*. 131 (2017) 39–49. <https://doi.org/10.1016/j.CONBUILDMAT.2016.11.008>.
- [225] P. Lura, O.M. Jensen, J. Weiss, Cracking in cement paste induced by autogenous shrinkage, *Materials and Structures/Materiaux et Constructions*. 42 (2009) 1089–1099. <https://doi.org/10.1617/s11527-008-9445-z>.

- [226] R. Spingenschmid, *Prevention of Thermal Cracking in Concrete at Early Ages*, E&FN Spon, London, 1998.
- [227] M. Briffaut, F. Benboudjema, L. D'Aloia, Effect of fibres on early age cracking of concrete tunnel lining. Part I: Laboratory ring test, *Tunnelling and Underground Space Technology*. 59 (2016) 215–220. <https://doi.org/10.1016/j.TUST.2016.07.016>.
- [228] Y. Gao, J. Zhang, P. Han, Determination of stress relaxation parameters of concrete in tension at early-age by ring test, *Constr Build Mater*. 41 (2013) 152–164. <https://doi.org/10.1016/j.CONBUILDMAT.2012.12.004>.
- [229] D. Shen, Y. Jiao, Y. Gao, S. Zhu, G. Jiang, Influence of ground granulated blast furnace slag on cracking potential of high performance concrete at early age, *Constr Build Mater*. 241 (2020). <https://doi.org/10.1016/j.conbuildmat.2019.117839>.
- [230] D. Shen, K. Liu, C. Wen, Y. Shen, G. Jiang, Early-age cracking resistance of ground granulated blast furnace slag concrete, *Constr Build Mater*. 222 (2019) 278–287. <https://doi.org/10.1016/j.conbuildmat.2019.06.028>.
- [231] A.E. Klausen, T. Kanstad, Ø. Bjøntegaard, Hardening concrete exposed to realistic curing temperature regimes and restraint conditions: Advanced testing and design methodology, *Advances in Materials Science and Engineering*. 2019 (2019). <https://doi.org/10.1155/2019/9071034>.
- [232] R. Springenschmid, R. Breitenbücher, M. Mangold, Development of the cracking frame and the temperature-stress testing machine, in: *Proceedings of the International RILEM Symposium, Munich, Germany, 1994*: pp. 137–144.
- [233] S. Igarashi, A. Bentur, K. Kovler, Autogenous shrinkage and induced restraining stresses in high-strength concretes, *Cem Concr Res*. 30 (2000) 1701–1707. [https://doi.org/10.1016/S0008-8846\(00\)00399-9](https://doi.org/10.1016/S0008-8846(00)00399-9).
- [234] Ø. Bjøntegaard, *Thermal dilation and AD as driving forces to self-induced stresses in high performance concrete*, Ph.D. thesis, Norwegian University of Science and Technology (NTNU), 1999.
- [235] S.J. Lokhorst, *Deformational Behaviour of Concrete Influenced by Hydration Related Changes of the Microstructure*, Delft University of Technology, 2001.

- [236] G. Ou, Z. Lin, T. Kishi, The practical application of a self-developed temperature stress testing machine in development of expansive concrete blended with calcium sulfoaluminate additives, *Cem Concr Res.* 164 (2023) 107045. <https://doi.org/10.1016/j.cemconres.2022.107045>.
- [237] Z. Li, S. Zhang, X. Liang, G. Ye, Cracking potential of alkali-activated slag and fly ash concrete subjected to restrained autogenous shrinkage, *Cem Concr Compos.* 114 (2020). <https://doi.org/10.1016/j.cemconcomp.2020.103767>.
- [238] M. Azenha, F. Kanavaris, D. Schlicke, A. Jędrzejewska, F. Benboudjema, T. Honorio, V. Šmilauer, C. Serra, J. Forth, K. Riding, B. Khadka, C. Sousa, M. Briffaut, L. Lacarrière, E. Koenders, T. Kanstad, A. Klausen, J.M. Torrenti, E.M.R. Fairbairn, Recommendations of RILEM TC 287-CCS: thermo-chemo-mechanical modelling of massive concrete structures towards cracking risk assessment, *Materials and Structures/Materiaux et Constructions.* 54 (2021) 135. <https://doi.org/10.1617/s11527-021-01732-8>.
- [239] H. Zhu, Y. Hu, Q. Li, R. Ma, Restrained cracking failure behavior of concrete due to temperature and shrinkage, *Constr Build Mater.* 244 (2020) 118318. <https://doi.org/10.1016/j.conbuildmat.2020.118318>.
- [240] J. Xin, Y. Liu, G. Zhang, Z. Wang, N. Yang, Y. Qiao, J. Wang, Comparison of thermal cracking potential evaluation criteria for mass concrete structures, *Mater Struct.* 54 (2021) 243. <https://doi.org/10.1617/s11527-021-01840-5>.
- [241] A.E. Klausen, T. Kanstad, Ø. Bjøntegaard, The cracking risk of hardening concrete exposed to realistic curing temperature regimes and restraint conditions – Experimental investigations of important parameters, *Constr Build Mater.* 338 (2022) 127662. <https://doi.org/10.1016/j.CONBUILDMAT.2022.127662>.
- [242] A. Darquennes, S. Staquet, M.P. Delplancke-Ogletree, B. Espion, Effect of AD on the cracking risk of slag cement concretes, *Cem Concr Compos.* 33 (2011) 368–379. <https://doi.org/10.1016/j.cemconcomp.2010.12.003>.
- [243] A. Darquennes, S. Staquet, B. Espion, Behaviour of slag cement concrete under restraint conditions, *European Journal of*

- Environmental and Civil Engineering. 15 (2011) 787–798.  
<https://doi.org/10.1080/19648189.2011.9693365>.
- [244] M. Liang, Z. Chang, Y. Zhang, H. Cheng, S. He, E. Schlangen, B. Šavija, AD induced- stress evolution in high-volume GGBFS concrete: Macro-scale behavior and micro-scale origin, *Constr Build Mater.* 370 (2023) 130663.  
<https://doi.org/10.1016/j.conbuildmat.2023.130663>.
- [245] A. Markandeya, N. Shanahan, D.M. Gunatilake, K.A. Riding, A. Zayed, Influence of slag composition on cracking potential of slag-portland cement concrete, *Constr Build Mater.* 164 (2018) 820–829.  
<https://doi.org/10.1016/j.conbuildmat.2017.12.216>.
- [246] G.M. Ji, T. Kanstad, Bjøntegaard, Calibration of Material Models against TSTM Test for Crack Risk Assessment of Early-Age Concrete Containing Fly Ash, *Advances in Materials Science and Engineering.* 2018 (2018).  
<https://doi.org/10.1155/2018/1069181>.
- [247] A.Z. Bendimerad, B. Delsaute, E. Rozière, S. Staquet, A. Loukili, Advanced techniques for the study of shrinkage-induced cracking of concrete with recycled aggregates at early age, *Constr Build Mater.* 233 (2020) 117340.  
<https://doi.org/10.1016/j.conbuildmat.2019.117340>.
- [248] L. Wang, G. Li, X. Li, F. Guo, S. Tang, X. Lu, A. Hanif, Influence of reactivity and dosage of MgO expansive agent on shrinkage and crack resistance of face slab concrete, *Cem Concr Compos.* 126 (2022) 104333.  
<https://doi.org/10.1016/j.cemconcomp.2021.104333>.
- [249] Z.P. Bažant, S.-S. Kim, Nonlinear Creep of Concrete—Adaptation and Flow, *Journal of the Engineering Mechanics Division.* 105 (1979) 429–446. <https://doi.org/10.1061/JMCEA3.0002483>.
- [250] F. Wittmann, *Bestimmung physikalischer Eigenschaften des Zementsteins*, 1974.
- [251] K. Van Breugel, *Relaxation of Young Concrete*, 1980.
- [252] Y. Wei, S. Liang, W. Guo, W. Hansen, Stress prediction in very early-age concrete subject to restraint under varying temperature histories, *Cem Concr Compos.* 83 (2017) 45–56.  
<https://doi.org/10.1016/j.cemconcomp.2017.07.006>.

- [253] Z. Li, X. Liang, C. Liu, M. Liang, K. van Breugel, G. Ye, Thermal deformation and stress of alkali-activated slag concrete under semi-adiabatic condition: Experiments and simulations, *Cem Concr Res.* 159 (2022) 106887. <https://doi.org/10.1016/j.cemconres.2022.106887>.
- [254] M. Liang, Z. Chang, S. He, Y. Chen, Y. Gan, E. Schlangen, B. Šavija, Predicting early-age stress evolution in restrained concrete by thermo-chemo-mechanical model and active ensemble learning, *Computer-Aided Civil and Infrastructure Engineering.* 37 (2022) 1809–1833. <https://doi.org/10.1111/mice.12915>.
- [255] M. Liang, Z. Li, S. He, Z. Chang, Y. Gan, E. Schlangen, B. Šavija, Stress evolution in restrained GGBFS concrete due to AD : bayesian optimization of aging creep, *Constr Build Mater.* 324 (2022) 126690. <https://doi.org/10.1016/j.conbuildmat.2022.126690>.
- [256] O. Boukendakdji, E.H. Kadri, S. Kenai, Effects of granulated blast furnace slag and superplasticizer type on the fresh properties and compressive strength of self-compacting concrete, *Cem Concr Compos.* 34 (2012) 583–590. <https://doi.org/10.1016/j.cemconcomp.2011.08.013>.
- [257] S.J. Barnett, M.N. Soutsos, S.G. Millard, J.H. Bungey, Strength development of mortars containing ground granulated blast-furnace slag: Effect of curing temperature and determination of apparent activation energies, *Cem Concr Res.* 36 (2006) 434–440. <https://doi.org/10.1016/j.cemconres.2005.11.002>.
- [258] J.M. Khatib, J.J. Hibbert, Selected engineering properties of concrete incorporating slag and metakaolin, *Constr Build Mater.* 19 (2005) 460–472. <https://doi.org/10.1016/j.conbuildmat.2004.07.017>.
- [259] M.A. Megat Johari, J.J. Brooks, S. Kabir, P. Rivard, Influence of supplementary cementitious materials on engineering properties of high strength concrete, *Constr Build Mater.* 25 (2011) 2639–2648. <https://doi.org/10.1016/j.conbuildmat.2010.12.013>.
- [260] X.Y. Wang, H.S. Lee, K.B. Park, J.J. Kim, J.S. Golden, A multi-phase kinetic model to simulate hydration of slag–cement blends, *Cem Concr Compos.* 32 (2010) 468–477. <https://doi.org/10.1016/j.cemconcomp.2010.03.006>.
- [261] V. Kocaba, E. Gallucci, K.L. Scrivener, Methods for determination of degree of reaction of slag in blended cement pastes, *Cem Concr Res.*

- 42 (2012) 511–525.  
<https://doi.org/10.1016/J.CEMCONRES.2011.11.010>.
- [262] X.Y. Wang, H.S. Lee, Modeling the hydration of concrete incorporating fly ash or slag, *Cem Concr Res.* 40 (2010) 984–996.  
<https://doi.org/10.1016/J.CEMCONRES.2010.03.001>.
- [263] A. Darquennes, M.I.A. Khokhar, E. Rozière, A. Loukili, F. Grondin, S. Staquet, Early age deformations of concrete with high content of mineral additions, *Constr Build Mater.* 25 (2011) 1836–1847.  
<https://doi.org/10.1016/J.CONBUILDMAT.2010.11.077>.
- [264] Y. Wei, W. Hansen, Early-age strain–stress relationship and cracking behavior of slag cement mixtures subject to constant uniaxial restraint, *Constr Build Mater.* 49 (2013) 635–642.  
<https://doi.org/10.1016/J.CONBUILDMAT.2013.08.061>.
- [265] P. Lura, J. Couch, O.M. Jensen, J. Weiss, Early-age acoustic emission measurements in hydrating cement paste: Evidence for cavitation during solidification due to self-desiccation, *Cem Concr Res.* 39 (2009) 861–867.  
<https://doi.org/10.1016/j.cemconres.2009.06.015>.
- [266] Y. Zhang, S. Zhang, Y. Chen, O. Çopuroğlu, The effect of slag chemistry on the reactivity of synthetic and commercial slags, *Constr Build Mater.* 335 (2022) 127493.  
<https://doi.org/10.1016/J.CONBUILDMAT.2022.127493>.
- [267] R.J. Flatt, G.W. Scherer, Thermodynamics of crystallization stresses in DEF, *Cem Concr Res.* 38 (2008) 325–336.  
<https://doi.org/10.1016/J.CEMCONRES.2007.10.002>.
- [268] Modelling of autogenous shrinkage of cement paste, (n.d.).
- [269] K. Scrivener, R. Snellings, B. Lothenbach, A practical guide to microstructural analysis of cementitious materials, n.d.
- [270] S. Diamond, Mercury porosimetry: An inappropriate method for the measurement of pore size distributions in cement-based materials, *Cem Concr Res.* 30 (2000) 1517–1525.  
[https://doi.org/10.1016/S0008-8846\(00\)00370-7](https://doi.org/10.1016/S0008-8846(00)00370-7).
- [271] C. Gallé, Effect of drying on cement-based materials pore structure as identified by mercury intrusion porosimetry, *Cem Concr Res.* 31 (2001) 1467–1477.  
[https://doi.org/10.1016/S0008-8846\(01\)00594-4](https://doi.org/10.1016/S0008-8846(01)00594-4).

- [272] R. Kumar, B. Bhattacharjee, Study on some factors affecting the results in the use of MIP method in concrete research, *Cem Concr Res.* 33 (2003) 417–424. [https://doi.org/10.1016/S0008-8846\(02\)00974-2](https://doi.org/10.1016/S0008-8846(02)00974-2).
- [273] J. Zhao, D. Wang, P. Yan, Design and experimental study of a ternary blended cement containing high volume steel slag and blast-furnace slag based on Fuller distribution model, *Constr Build Mater.* 140 (2017) 248–256. <https://doi.org/10.1016/j.conbuildmat.2017.02.119>.
- [274] K. Meinhard, R. Lackner, Multi-phase hydration model for prediction of hydration-heat release of blended cements, *Cem Concr Res.* 38 (2008) 794–802. <https://doi.org/10.1016/j.cemconres.2008.01.008>.
- [275] Y. Choi, R.L. Yuan, Experimental relationship between splitting tensile strength and compressive strength of GFRC and PFRC, *Cem Concr Res.* 35 (2005) 1587–1591. <https://doi.org/10.1016/j.cemconres.2004.09.010>.
- [276] M.F.M. Zain, H.B. Mahmud, A. Ilham, M. Faizal, Prediction of splitting tensile strength of high-performance concrete, *Cem Concr Res.* 32 (2002) 1251–1258. [https://doi.org/10.1016/S0008-8846\(02\)00768-8](https://doi.org/10.1016/S0008-8846(02)00768-8).
- [277] P. Virtanen, R. Gommers, T.E. Oliphant, M. Haberland, T. Reddy, D. Cournapeau, E. Burovski, P. Peterson, W. Weckesser, J. Bright, S.J. van der Walt, M. Brett, J. Wilson, K.J. Millman, N. Mayorov, A.R.J. Nelson, E. Jones, R. Kern, E. Larson, C.J. Carey, Í. Polat, Y. Feng, E.W. Moore, J. VanderPlas, D. Laxalde, J. Perktold, R. Cimrman, I. Henriksen, E.A. Quintero, C.R. Harris, A.M. Archibald, A.H. Ribeiro, F. Pedregosa, P. van Mulbregt, A. Vijaykumar, A. Pietro Bardelli, A. Rothberg, A. Hilboll, A. Kloeckner, A. Scopatz, A. Lee, A. Rokem, C.N. Woods, C. Fulton, C. Masson, C. Häggström, C. Fitzgerald, D.A. Nicholson, D.R. Hagen, D. v. Pasechnik, E. Olivetti, E. Martin, E. Wieser, F. Silva, F. Lenders, F. Wilhelm, G. Young, G.A. Price, G.-L. Ingold, G.E. Allen, G.R. Lee, H. Audren, I. Probst, J.P. Dietrich, J. Silterra, J.T. Webber, J. Slavič, J. Nothman, J. Buchner, J. Kulick, J.L. Schönberger, J.V. de Miranda Cardoso, J. Reimer, J. Harrington, J.L.C. Rodríguez, J. Nunez-Iglesias, J. Kuczynski, K. Tritz, M. Thoma, M. Newville, M. Kümmerer, M. Bolingbroke, M. Tartre, M. Pak, N.J. Smith, N. Nowaczyk, N. Shebanov, O. Pavlyk, P.A. Brodtkorb, P. Lee, R.T. McGibbon, R. Feldbauer, S. Lewis, S. Tygier, S. Sievert, S. Vigna,

- S. Peterson, S. More, T. Pudlik, T. Oshima, T.J. Pingel, T.P. Robitaille, T. Spura, T.R. Jones, T. Cera, T. Leslie, T. Zito, T. Krauss, U. Upadhyay, Y.O. Halchenko, Y. Vázquez-Baeza, SciPy 1.0: fundamental algorithms for scientific computing in Python, *Nat Methods*. 17 (2020) 261–272. <https://doi.org/10.1038/s41592-019-0686-2>.
- [278] J. Xin, G. Zhang, Y. Liu, Z. Wang, Z. Wu, Evaluation of behavior and cracking potential of early-age cementitious systems using uniaxial restraint tests: A review, *Constr Build Mater*. 231 (2020). <https://doi.org/10.1016/j.conbuildmat.2019.117146>.
- [279] M. Gesoğlu, E. Güneyisi, T. Özturan, Effects of end conditions on compressive strength and static elastic modulus of very high strength concrete, *Cem Concr Res*. 32 (2002) 1545–1550. [https://doi.org/10.1016/S0008-8846\(02\)00826-8](https://doi.org/10.1016/S0008-8846(02)00826-8).
- [280] H. M. Rietveld, A Profile Refinement Method for Nuclear and Magnetic Structures, *J Appl Crystallogr*. 2 (1969) 65–71.
- [281] N. Doebelin, R. Kleeberg, Profex: A graphical user interface for the Rietveld refinement program BGMN, *J Appl Crystallogr*. 48 (2015). <https://doi.org/10.1107/S1600576715014685>.
- [282] V. Baroghel-Bouny, P. Mounanga, A. Khelidj, A. Loukili, N. Rafaï, AD s of cement pastes, *Cem Concr Res*. 36 (2006) 123–136. <https://doi.org/10.1016/j.cemconres.2004.10.020>.
- [283] V. Šmilauer, P. Havlásek, T. Gasch, A. Delaplace, D.E.M. Bouhjiti, F. Benboudjema, M. Briffaut, F. Kanavaris, M. Azenha, Hygro-mechanical modeling of restrained ring test: COST TU1404 benchmark, *Constr Build Mater*. 229 (2019) 116543. <https://doi.org/10.1016/j.CONBUILDMAT.2019.07.269>.
- [284] Z.P. Bazant, L. Panula, Practical prediction of time-dependent deformations of concrete Part I: Shrinkage (1), n.d.
- [285] K. Kuder, D. Lehman, J. Berman, G. Hannesson, R. Shogren, Mechanical properties of self consolidating concrete blended with high volumes of fly ash and slag, *Constr Build Mater*. 34 (2012) 285–295. <https://doi.org/10.1016/j.conbuildmat.2012.02.034>.
- [286] International Federation for Structural Concrete (fib), *Fib Model Code for Concrete Structures 2010*, Ernst & Sohn, Wiley, Berlin, Germany, 2013.

- [287] CSA Technical Committee, Reinforced Concrete Design, A23.3-04, Design of Concrete Structures, Canadian Standards Association: Rexdale, ON, Canada, 2004.
- [288] EN, EN 1992-1-1 Eurocode 2: Design of Concrete Structures—Part 1-1: General Rules and Rules for Buildings, CEN, Brussels, Belgium, 2005.
- [289] Z.P. Bažant, Creep and Shrinkage in Concrete Structures; Mathematical Modeling of Creep and Shrinkage of Concrete, John Wiley and Sons, New York, NY, USA, 1982.
- [290] R. Mahnken, E. Stein, The identification of parameters for viscoplastic models via finite-element methods and gradient methods, *Model Simul Mat Sci Eng.* 2 (1994) 597–616. <https://doi.org/10.1088/0965-0393/2/3A/013>.
- [291] J. Kajberg, G. Lindkvist, Characterisation of materials subjected to large strains by inverse modelling based on in-plane displacement fields, *Int J Solids Struct.* 41 (2004) 3439–3459. <https://doi.org/10.1016/j.ijsolstr.2004.02.021>.
- [292] A. Tarantola, Inverse Problem Theory, Methods for Data Fitting and Model Parameter Estimation, Elsevier Publisher B.V, New York, USA, 1987.
- [293] C.Edward. Rasmussen, C.K.I. Williams, Gaussian processes for machine learning, MIT Press, 2006.
- [294] J. Mockus, V. Tiesis, A. Zilinskas, The application of Bayesian methods for seeking the extremum, *Towards Global Optimization* . 2 (1978) 117–129.
- [295] D.R. Jones, A taxonomy of global optimization methods based on response surfaces, *Journal of Global Optimization.* 21 (2001) 345–383. <https://doi.org/10.1023/A:1012771025575>.
- [296] A. Wilson, R. Adams, Gaussian Process Kernels for Pattern Discovery and Extrapolation, *Proceedings of the 30th International Conference on Machine Learning PMLR.* 28 (2013) 1067–1075.
- [297] D.R. Jones, M. Schonlau, W.J. Welch, Efficient Global Optimization of Expensive Black-Box Functions, *Journal of Global Optimization.* 13 (1998) 455–492. <https://doi.org/10.1023/A:1008306431147>.
- [298] A.A. Chiniforush, M. Gharehchaei, A. Akbar Nezhad, A. Castel, F. Moghaddam, L. Keyte, D. Hocking, S. Foster, Numerical simulation of risk mitigation strategies for early-age thermal cracking and DEF

- in concrete, *Constr Build Mater.* 322 (2022) 126478. <https://doi.org/10.1016/j.CONBUILDMAT.2022.126478>.
- [299] D. Gawin, F. Pesavento, B.A. Schrefler, Hygro-thermo-chemo-mechanical modelling of concrete at early ages and beyond. Part I: hydration and hygro-thermal phenomena, *Int J Numer Methods Eng.* 67 (2006) 299–331. <https://doi.org/10.1002/nme.1615>.
- [300] J.R. van Bokhorst, Early-age cracking of concrete A study into the influence of stress relaxation on early-age cracking of concrete structures under imposed deformations, n.d. <http://repository.tudelft.nl/>.
- [301] Y. Gao, J. Zhang, P. Han, Determination of stress relaxation parameters of concrete in tension at early-age by ring test, *Constr Build Mater.* 41 (2013) 152–164. <https://doi.org/10.1016/j.conbuildmat.2012.12.004>.
- [302] K. van Breugel, *Simulation of hydration and Formation of Structure in Hardening Cement-Based Materials*, TU Delft, 1991.
- [303] Methods for Calculating Activation Energy for Portland Cement, *ACI Mater J.* 104 (2007). <https://doi.org/10.14359/18499>.
- [304] Pietro Lura, *AD and Internal Curing of Concrete*, Delft University of Technology, 2003.
- [305] A. Bentur, M. Ish-Shalom, Properties of type K expansive cement of pure components II. Proposed mechanism of ettringite formation and expansion in unrestrained paste of pure expansive component, *Cem Concr Res.* 4 (1974) 709–721. [https://doi.org/10.1016/0008-8846\(74\)90043-X](https://doi.org/10.1016/0008-8846(74)90043-X).
- [306] P.K. Mehta, Mechanism of expansion associated with ettringite formation, *Cem Concr Res.* 3 (1973) 1–6. [https://doi.org/10.1016/0008-8846\(73\)90056-2](https://doi.org/10.1016/0008-8846(73)90056-2).
- [307] V. Baroghel-Bouny, P. Mounanga, A. Khelidj, A. Loukili, N. Rafai, *AD s of cement pastes*, *Cem Concr Res.* 36 (2006) 123–136. <https://doi.org/10.1016/j.cemconres.2004.10.020>.
- [308] C. Jiang, Y. Yang, Y. Wang, Y. Zhou, C. Ma, Autogenous shrinkage of high performance concrete containing mineral admixtures under different curing temperatures, *Constr Build Mater.* 61 (2014) 260–269. <https://doi.org/10.1016/j.conbuildmat.2014.03.023>.
- [309] P. Mounanga, V. Baroghel-Bouny, A. Loukili, A. Khelidj, *AD s of cement pastes: Part I. Temperature effects at early age and micro-*

- macro correlations, *Cem Concr Res.* 36 (2006) 110–122. <https://doi.org/10.1016/j.cemconres.2004.10.019>.
- [310] S. Poyet, Experimental investigation of the effect of temperature on the first desorption isotherm of concrete, *Cem Concr Res.* 39 (2009) 1052–1059. <https://doi.org/10.1016/j.cemconres.2009.06.019>.
- [311] J.M. de Burgh, S.J. Foster, Influence of temperature on water vapour sorption isotherms and kinetics of hardened cement paste and concrete, *Cem Concr Res.* 92 (2017) 37–55. <https://doi.org/10.1016/j.cemconres.2016.11.006>.
- [312] A.A. Almusallam, Effect of environmental conditions on the properties of fresh and hardened concrete, *Cem Concr Compos.* 23 (2001) 353–361. [https://doi.org/10.1016/S0958-9465\(01\)00007-5](https://doi.org/10.1016/S0958-9465(01)00007-5).
- [313] J.I. Escalante-García, J.H. Sharp, Effect of temperature on the hydration of the main clinker phases in portland cements: part i, neat cements, *Cem Concr Res.* 28 (1998) 1245–1257. [https://doi.org/10.1016/S0008-8846\(98\)00115-X](https://doi.org/10.1016/S0008-8846(98)00115-X).
- [314] B. Lothenbach, F. Winnefeld, C. Alder, E. Wieland, P. Lunk, Effect of temperature on the pore solution, microstructure and hydration products of Portland cement pastes, *Cem Concr Res.* 37 (2007) 483–491. <https://doi.org/10.1016/j.cemconres.2006.11.016>.
- [315] K.O. Kjellsen, R.J. Detwiler, O.E. GjØrv, Development of microstructures in plain cement pastes hydrated at different temperatures, *Cem Concr Res.* 21 (1991) 179–189. [https://doi.org/10.1016/0008-8846\(91\)90044-I](https://doi.org/10.1016/0008-8846(91)90044-I).
- [316] P. Turcry, A. Loukili, L. Barcelo, J.M. Casabonne, Can the maturity concept be used to separate the autogenous shrinkage and thermal deformation of a cement paste at early age?, *Cem Concr Res.* 32 (2002) 1443–1450. [https://doi.org/10.1016/S0008-8846\(02\)00800-1](https://doi.org/10.1016/S0008-8846(02)00800-1).
- [317] G. Di Luzio, G. Cusatis, Solidification–microprestress–microplane (SMM) theory for concrete at early age: Theory, validation and application, *Int J Solids Struct.* 50 (2013) 957–975. <https://doi.org/10.1016/J.IJSOLSTR.2012.11.022>.
- [318] Z.P. Bažant, S. Baweja, Creep and Shrinkage Prediction Model for Analysis and Design of Concrete Structures: Model B3, 2000. [www.fsv.cvut.cz/kristek](http://www.fsv.cvut.cz/kristek).

- [319] R.H. Byrd, J.C. Gilbert, J. Nocedal, A trust region method based on interior point techniques for nonlinear programming, *Math Program.* 89 (2000) 149–185. <https://doi.org/10.1007/PL00011391>.
- [320] R.H. Byrd, M.E. Hribar, J. Nocedal, An Interior Point Algorithm for Large-Scale Nonlinear Programming, *SIAM Journal on Optimization.* 9 (1999) 877–900. <https://doi.org/10.1137/S1052623497325107>.
- [321] T.F. Coleman, Y. Li, An Interior Trust Region Approach for Nonlinear Minimization Subject to Bounds, *SIAM Journal on Optimization.* 6 (1996) 418–445. <https://doi.org/10.1137/0806023>.
- [322] T.F. Coleman, Y. Li, On the convergence of interior-reflective Newton methods for nonlinear minimization subject to bounds, *Math Program.* 67 (1994) 189–224. <https://doi.org/10.1007/BF01582221>.
- [323] P.E. Gill, W. Murray, M. H. Wright, *Practical Optimization*, Academic Press, London, 1981.
- [324] S.P. Han, A globally convergent method for nonlinear programming, *J Optim Theory Appl.* 22 (1977) 297–309. <https://doi.org/10.1007/BF00932858>.
- [325] M.J.D. Powell, A fast algorithm for nonlinearly constrained optimization calculations, in: 1978: pp. 144–157. <https://doi.org/10.1007/BFb0067703>.
- [326] M.J.D. Powell, THE CONVERGENCE OF VARIABLE METRIC METHODS FOR NONLINEARLY CONSTRAINED OPTIMIZATION CALCULATIONS, in: *Nonlinear Programming 3*, Elsevier, 1978: pp. 27–63. <https://doi.org/10.1016/B978-0-12-468660-1.50007-4>.
- [327] R.A. Waltz, J.L. Morales, J. Nocedal, D. Orban, An interior algorithm for nonlinear optimization that combines line search and trust region steps, *Math Program.* 107 (2006) 391–408. <https://doi.org/10.1007/s10107-004-0560-5>.
- [328] M. Cervera, J. Oliver, T. Prato, Thermo-Chemo-Mechanical Model for Concrete. II: Damage and Creep, *J Eng Mech.* 125 (1999) 1028–1039. [https://doi.org/10.1061/\(ASCE\)0733-9399\(1999\)125:9\(1028\)](https://doi.org/10.1061/(ASCE)0733-9399(1999)125:9(1028)).

- [329] M. Cervera, J. Oliver, T. Prato, Thermo-Chemo-Mechanical Model for Concrete. I: Hydration and Aging, *J Eng Mech.* 125 (1999) 1018–1027. [https://doi.org/10.1061/\(ASCE\)0733-9399\(1999\)125:9\(1018\)](https://doi.org/10.1061/(ASCE)0733-9399(1999)125:9(1018)).
- [330] R. Lackner, H.A. Mang, Chemoplastic material model for the simulation of early-age cracking: From the constitutive law to numerical analyses of massive concrete structures, *Cem Concr Compos.* 26 (2004) 551–562. [https://doi.org/10.1016/S0958-9465\(03\)00071-4](https://doi.org/10.1016/S0958-9465(03)00071-4).
- [331] H. Zhao, K. Jiang, R. Yang, Y. Tang, J. Liu, Experimental and theoretical analysis on coupled effect of hydration, temperature and humidity in early-age cement-based materials, *Int J Heat Mass Transf.* 146 (2020) 118784. <https://doi.org/10.1016/j.ijheatmasstransfer.2019.118784>.
- [332] H. Zhao, K. Jiang, B. Hong, R. Yang, W. Xu, Q. Tian, J. Liu, Experimental and Numerical Analysis on Coupled Hygro-Thermo-Chemo-Mechanical Effect in Early-Age Concrete, *Journal of Materials in Civil Engineering.* 33 (2021) 04021064. [https://doi.org/10.1061/\(ASCE\)MT.1943-5533.0003666](https://doi.org/10.1061/(ASCE)MT.1943-5533.0003666).
- [333] M.R. Rajashekhar, B.R. Ellingwood, A new look at the response surface approach for reliability analysis, *Structural Safety.* 12 (1993) 205–220. [https://doi.org/10.1016/0167-4730\(93\)90003-J](https://doi.org/10.1016/0167-4730(93)90003-J).
- [334] S. Lai, M. Serra, Concrete strength prediction by means of neural network, *Constr Build Mater.* 11 (1997) 93–98. [https://doi.org/10.1016/S0950-0618\(97\)00007-X](https://doi.org/10.1016/S0950-0618(97)00007-X).
- [335] F. Kang, J. Li, Displacement Model for Concrete Dam Safety Monitoring via Gaussian Process Regression Considering Extreme Air Temperature, *Journal of Structural Engineering.* 146 (2020) 05019001. [https://doi.org/10.1061/\(ASCE\)ST.1943-541X.0002467](https://doi.org/10.1061/(ASCE)ST.1943-541X.0002467).
- [336] A. Karbassi, B. Mohebi, S. Rezaee, P. Lestuzzi, Damage prediction for regular reinforced concrete buildings using the decision tree algorithm, *Comput Struct.* 130 (2014) 46–56. <https://doi.org/10.1016/j.compstruc.2013.10.006>.
- [337] J. Zhang, G. Ma, Y. Huang, J. sun, F. Aslani, B. Nener, Modelling uniaxial compressive strength of lightweight self-compacting concrete using random forest regression, *Constr Build Mater.* 210

- (2019) 713–719.  
<https://doi.org/10.1016/j.conbuildmat.2019.03.189>.
- [338] G. Bayar, T. Bilir, A novel study for the estimation of crack propagation in concrete using machine learning algorithms, *Constr Build Mater.* 215 (2019) 670–685.  
<https://doi.org/10.1016/j.CONBUILDMAT.2019.04.227>.
- [339] A. Marani, A. Jamali, M.L. Nehdi, Predicting Ultra-High-Performance Concrete Compressive Strength Using Tabular Generative Adversarial Networks, *Materials.* 13 (2020) 4757.  
<https://doi.org/10.3390/ma13214757>.
- [340] T. Han, A. Siddique, K. Khayat, J. Huang, A. Kumar, An ensemble machine learning approach for prediction and optimization of modulus of elasticity of recycled aggregate concrete, *Constr Build Mater.* 244 (2020) 118271.  
<https://doi.org/10.1016/J.CONBUILDMAT.2020.118271>.
- [341] O.B. Olalusi, P. Spyridis, Machine learning-based models for the concrete breakout capacity prediction of single anchors in shear, *Advances in Engineering Software.* 147 (2020) 102832.  
<https://doi.org/10.1016/J.ADVENGSOFT.2020.102832>.
- [342] R. Solhmirzaei, H. Salehi, V. Kodur, M.Z. Naser, Machine learning framework for predicting failure mode and shear capacity of ultra high performance concrete beams, *Eng Struct.* 224 (2020) 111221.  
<https://doi.org/10.1016/J.ENGSTRUCT.2020.111221>.
- [343] E. Gomaa, T. Han, M. ElGawady, J. Huang, A. Kumar, Machine learning to predict properties of fresh and hardened alkali-activated concrete, *Cem Concr Compos.* 115 (2021) 103863.  
<https://doi.org/10.1016/J.CEMCONCOMP.2020.103863>.
- [344] M.C. Kang, D.Y. Yoo, R. Gupta, Machine learning-based prediction for compressive and flexural strengths of steel fiber-reinforced concrete, *Constr Build Mater.* 266 (2021) 121117.  
<https://doi.org/10.1016/J.CONBUILDMAT.2020.121117>.
- [345] M. Su, Q. Zhong, H. Peng, S. Li, Selected machine learning approaches for predicting the interfacial bond strength between FRPs and concrete, *Constr Build Mater.* 270 (2021) 121456.  
<https://doi.org/10.1016/J.CONBUILDMAT.2020.121456>.
- [346] A. Tomar, H. V. Burton, Active learning method for risk assessment of distributed infrastructure systems, *Computer-Aided Civil and*

- Infrastructure Engineering. 36 (2021) 438–452. <https://doi.org/10.1111/mice.12665>.
- [347] Y. Yuan, F.T.K. Au, D. Yang, J. Zhang, Active learning structural model updating of a multisensory system based on Kriging method and Bayesian inference, *Computer-Aided Civil and Infrastructure Engineering*. (2022). <https://doi.org/10.1111/mice.12822>.
- [348] Z.P. Bažant, J. Chern, Strain Softening with Creep and Exponential Algorithm, *J Eng Mech*. 111 (1985) 391–415. [https://doi.org/10.1061/\(ASCE\)0733-9399\(1985\)111:3\(391\)](https://doi.org/10.1061/(ASCE)0733-9399(1985)111:3(391)).
- [349] D. Gawin, F. Pesavento, B.A. Schrefler, Hygro-thermo-chemo-mechanical modelling of concrete at early ages and beyond. Part II: shrinkage and creep of concrete, *Int J Numer Methods Eng*. 67 (2006) 332–363. <https://doi.org/10.1002/nme.1636>.
- [350] F.-J. Ulm, O. Coussy, Modeling of Thermochemomechanical Couplings of Concrete at Early Ages, *J Eng Mech*. 121 (1995) 785–794. [https://doi.org/10.1061/\(ASCE\)0733-9399\(1995\)121:7\(785\)](https://doi.org/10.1061/(ASCE)0733-9399(1995)121:7(785)).
- [351] S.J. Pantazopoulou, R.H. Mills, Microstructural Aspects of the Mechanical Response of Plain Concrete, *ACI Mater J*. 92 (1995) 605–616. <https://doi.org/10.14359/9780>.
- [352] Z.P. Bazant, M.F. Kaplan, *Concrete at high temperatures: material properties and mathematical models*, 1996.
- [353] D.P. Bentz, A review of early-age properties of cement-based materials, *Cem Concr Res*. 38 (2008) 196–204. <https://doi.org/10.1016/J.CEMCONRES.2007.09.005>.
- [354] J.D. Hoffman, J.D. Hoffman, S. Frankel, *Numerical Methods for Engineers and Scientists*, CRC Press, 2018. <https://doi.org/10.1201/9781315274508>.
- [355] B. Stute, V. Krupp, E. von Lieres, Performance of iterative equation solvers for mass transfer problems in three-dimensional sphere packings in COMSOL, *Simul Model Pract Theory*. 33 (2013) 115–131. <https://doi.org/10.1016/j.simpat.2012.10.004>.
- [356] T. Chen, C. Guestrin, XGBoost, in: *Proceedings of the 22nd ACM SIGKDD International Conference on Knowledge Discovery and Data Mining*, ACM, New York, NY, USA, 2016: pp. 785–794. <https://doi.org/10.1145/2939672.2939785>.

- [357] Z. Wan, Y. Xu, B. Šavija, On the Use of Machine Learning Models for Prediction of Compressive Strength of Concrete: Influence of Dimensionality Reduction on the Model Performance, *Materials*. 14 (2021) 713. <https://doi.org/10.3390/ma14040713>.
- [358] M. Batog, Z. Giergiczny, Influence of mass concrete constituents on its properties, *Constr Build Mater*. 146 (2017) 221–230. <https://doi.org/10.1016/j.conbuildmat.2017.04.085>.
- [359] Y. Lee, M.-S. Choi, S.-T. Yi, J.-K. Kim, Experimental study on the convective heat transfer coefficient of early-age concrete, *Cem Concr Compos*. 31 (2009) 60–71. <https://doi.org/10.1016/j.cemconcomp.2008.09.009>.
- [360] B. Klemczak, M. Batog, Z. Giergiczny, A. Žmij, Complex Effect of Concrete Composition on the Thermo-Mechanical Behaviour of Mass Concrete, *Materials*. 11 (2018) 2207. <https://doi.org/10.3390/ma11112207>.
- [361] W.-L. Loh, On Latin hypercube sampling, *The Annals of Statistics*. 24 (1996) 2058–2080. <https://doi.org/10.1214/aos/1069362310>.
- [362] N. Halko, P.G. Martinsson, J.A. Tropp, Finding Structure with Randomness: Probabilistic Algorithms for Constructing Approximate Matrix Decompositions, *SIAM Review*. 53 (2011) 217–288. <https://doi.org/10.1137/090771806>.
- [363] B.J. Bichon, M.S. Eldred, L.P. Swiler, S. Mahadevan, J.M. McFarland, Efficient Global Reliability Analysis for Nonlinear Implicit Performance Functions, *AIAA Journal*. 46 (2008) 2459–2468. <https://doi.org/10.2514/1.34321>.
- [364] B. Echard, N. Gayton, M. Lemaire, AK-MCS: An active learning reliability method combining Kriging and Monte Carlo Simulation, *Structural Safety*. 33 (2011) 145–154. <https://doi.org/10.1016/j.strusafe.2011.01.002>.
- [365] A.J. Myles, R.N. Feudale, Y. Liu, N.A. Woody, S.D. Brown, An introduction to decision tree modeling, *J Chemom*. 18 (2004) 275–285. <https://doi.org/10.1002/cem.873>.
- [366] G. Ke, Q. Meng, T. Finley, T. Wang, W. Chen, W. Ma, Q. Ye, T.Y. Liu, LightGBM: A highly efficient gradient boosting decision tree, in: *Adv Neural Inf Process Syst*, 2017: pp. 3149–3157.

- [367] I. Maruyama, P. Lura, Properties of early-age concrete relevant to cracking in massive concrete, *Cem Concr Res.* 123 (2019) 105770. <https://doi.org/10.1016/j.cemconres.2019.05.015>.
- [368] J.K. Kim, Y.H. Moon, S.H. Eo, Compressive strength development of concrete with different curing time and temperature, *Cem Concr Res.* 28 (1998) 1761–1773. [https://doi.org/10.1016/S0008-8846\(98\)00164-1](https://doi.org/10.1016/S0008-8846(98)00164-1).
- [369] A. Dabarera, L. Li, P. Lura, V. Dao, Assessing the zero-stress temperature in high performance concrete at early age, *Cem Concr Compos.* 127 (2022) 104384. <https://doi.org/10.1016/j.cemconcomp.2021.104384>.
- [370] J.H. Yeon, S. Choi, M.C. Won, Evaluation of zero-stress temperature prediction model for Portland cement concrete pavements, *Constr Build Mater.* 40 (2013) 492–500. <https://doi.org/10.1016/j.conbuildmat.2012.10.013>.
- [371] D.P. Bentz, G. Sant, J. Weiss, Early-Age Properties of Cement-Based Materials. I: Influence of Cement Fineness, *Journal of Materials in Civil Engineering.* 20 (2008) 502–508. [https://doi.org/10.1061/\(ASCE\)0899-1561\(2008\)20:7\(502\)](https://doi.org/10.1061/(ASCE)0899-1561(2008)20:7(502)).

## SUMMARY

Since the introduction of cementitious materials, shrinkage-induced early-age cracking (EAC) has emerged as a significant issue that negatively influences the function, durability, and aesthetics of concrete structures like dams, tunnels, and underground garages. This thesis aims to develop new experimental and modelling techniques that help resolve this long-lasting issue, with a particular emphasis on the EAC induced by AD (AD). Unlike the thermal and drying deformation which are induced by heat and moisture transport, respectively, the AD is an intrinsic behavior caused by the self-desiccation of the hydration of cementitious materials. The AD-induced EAC risk is especially high when it comes to modern (or future) cementitious materials, such as high-performance concrete, ultra-high-performance concrete, and alkali-activated slag concrete.

The early-age stress (EAS) evolution is a straightforward index to evaluate the EAC risk. The Temperature Stress Testing Machine (TSTM) is a powerful tool for testing not only the AD-induced EAS but also the evolution of elastic modulus and creep under different temperatures. This thesis describes research on TSTM tests of the EAS evolution of high-volume slag concrete. By combining the TSTM tests with X-Ray Diffraction, Environmental Scanning Electron Microscopy, and Mercury Intrusion Porosimetry, this thesis unveiled the macro and microscale mechanisms of AD and AD-induced EAS in high-volume slag concrete. Furthermore, a Bayesian Inverse Modelling technique based on the rate-type creep law with Kelvin chain was developed to predict the EAS evolution as measured in the standard TSTM test. Both experimental and modelling results from the standard TSTM tests emphasized creep/relaxation's significant influence on EAS evolution. Moreover, the complexity of standard TSTM test makes it very labor-intensive, urging the need to develop a more efficient testing system to allow for more efficient tests.

Based on the major principles of the standard TSTM, a Mini-TSTM has been developed herein, which can be vertically installed in universal testing machine and allows for more efficient tests of many EAC-related behaviors and properties of cementitious materials, including EAS, AD, elastic modulus, creep, and coefficient of thermal expansion. Comprehensive validation of the built Mini-TSTM was done by testing the AD, EAS, creep,

elastic modulus, and coefficient of thermal expansion of two types of cement paste (CEM I 42.5N and CEM III B 42.5 N). Using the tested AD, creep and elastic modulus as input, a simple viscoelastic model was built to predict the EAS with good accuracy, offering further validation of the designed Mini-TSTM. This model also highlighted that early AD measurement variations negligibly influence EAS due to the low elastic modulus and high creep/relaxation. Furthermore, the Mini-TSTM was used to investigate the influence of temperature on AD and AD-induced EAS. It was found that the AD of Portland cement paste is a four-stage process including the initial deformation, autogenous expansion, plateau of slow deformation, and autogenous shrinkage. Increasing the temperature will cause higher AD-induced EAC risk, by shortening the duration of the first three stages and increasing the shrinkage rate in the last stage. Furthermore, the applicability of maturity concept was found to be problematic in prediction of AD in different temperatures. But the maturity concept can still be used to predict the early-age creep and elastic modulus, which helps for predicting the EAS if the AD at different temperature is known.

Based on the Mini-TSTM tests, a numerical modelling scheme for simulating stress relaxation was proposed to compute the EAS evolution with good accuracy. It was found that numerically solving the Volterra integral of creep compliance function can lead to negative relaxation modulus, especially when considering the fast evolution of creep properties in the early-age. This can lead to substantial error when predicting the EAS. Accordingly, an analytical solution based on the definition of relaxation test was used in this study, which directly enabled the conversion of relaxation modulus from creep compliance. Using the relaxation modulus as input, a finite element model with time-dependent Maxwell chains and rate-type creep law was built to predict the EAS with good accuracy.

In order to develop a numerical tool for more general scenarios, this thesis also developed a Thermo-Chemo-Mechanical (TCM) model which couples the hydration reaction, heat transfer, and viscoelasticity. Based on Fourier's law, Arrhenius's equation, Rate-type creep law, and a material model built mainly on Model Code 2010, the TCM model is able to simulate the evolving properties (i.e., viscoelasticity), behaviors (i.e., thermal, autogenous and drying deformation), and EAS. Further statistical analysis on 1000 random samples revealed that the temperature plays the most important role in EAS evolution. Meanwhile, data-driven approaches were also employed to build more efficient tools for EAS prediction. On top of the TCM model, an active ensemble learning (AEL) model was established as a

surrogate for the TCM model. The AEL model comprises the Principal Component Analysis (PCA) for dimension reduction, Gaussian Process (GP) for uncertainty quantification, and Light Gradient Boosting Machine (LGBM) for EAS prediction. Using an uncertainty-guided data sampling and training strategy, the AEL method can train the surrogate of TCM model with less data samples and make more accurate and efficient EAS prediction.

Overall, efficient and reliable experimental and modelling techniques for EAC analysis have been developed in this thesis, including a Mini-TSTM, a refined stress relaxation model, and an AEL model built on top of a TCM model, which can help the resolution of EAC issues in the application of cementitious materials.

## SAMENVATTING

Sinds de introductie van cementgebonden materialen zijn door krimp veroorzaakte scheuren in jong beton (EAC) een belangrijk probleem geworden. Het heeft dat een negatieve invloed heeft op het functioneren, de duurzaamheid en esthetiek van betonconstructies zoals dammen, tunnels en ondergrondse garages. Dit proefschrift heeft tot doel nieuwe experimentele en modelleringstechnieken te ontwikkelen die dit langdurige probleem helpen oplossen, met een bijzondere nadruk op de EAC veroorzaakt door autogene vervorming (AD). In tegenstelling tot de thermische en uitdrogingsvervorming die worden veroorzaakt door respectievelijk warmte- en vochttransport, is AD een intrinsiek gedrag dat wordt veroorzaakt door de zelfuitdroging van de hydratatie van cementachtige materialen. Het door AD veroorzaakte EAC-risico is vooral hoog als het gaat om moderne (of toekomstige) cementgebonden materialen, zoals hoogwaardig beton, ultrahoogwaardig beton en alkalisch geactiveerd slakkenbeton.

Het verloop van de spanning in jong beton (EAS) is een eenvoudige index om het EAC-risico te evalueren. De "Temperature Stress Testing Machine" (TSTM) is een krachtig hulpmiddel voor het testen van niet alleen de AD-geïnduceerde EAS, maar ook het verloop van de elasticiteitsmodulus en kruip onder verschillende temperaturen. Dit proefschrift beschrijft onderzoek voor TSTM-testen van de EAS-evolutie van beton gemaakt met cement met een hoog slakgehalte. Een combinatie van TSTM-testen, röntgendiffractie, elektronenmicroscopie en kwikporosimetrie, zijn gebruikt om meer inzicht te krijgen in de mechanismen op macro- en microschaal van AD en AD-geïnduceerde EAS in beton met cement met een hoog slakgehalte. Bovendien werd een "Bayesian Inverse Modelling" techniek ontwikkeld, gebaseerd op de "rate-type" kruipwet met een Kelvinketen, om de EAS-evolutie te voorspellen zoals gemeten in de standaard TSTM-test. Zowel experimentele als modelleringsresultaten van de standaard TSTM-tests benadrukten de significante invloed van kruip/relaxatie op de EAS-evolutie. Bovendien maakt de complexiteit van de standaard TSTM-test deze zeer arbeidsintensief, wat de noodzaak benadrukt om een efficiënter testsysteem te ontwikkelen om efficiëntere tests mogelijk te maken.

Gebaseerd op de belangrijkste principes van de standaard TSTM is in dit proefschrift een Mini-TSTM ontwikkeld, die verticaal kan worden geïnstalleerd in een universele testmachine en efficiëntere tests mogelijk maakt van veel EAC-gerelateerd gedrag en eigenschappen van cementachtige materialen, waaronder EAS, AD, elasticiteitsmodulus, kruip en thermische uitzettingscoëfficiënt. Uitgebreide validatie van de gebouwde Mini-TSTM werd uitgevoerd door het testen van de AD, EAS, kruip, elastische modulus en thermische uitzettingscoëfficiënt van twee soorten cementpasta (CEM I 42,5N en CEM III B 42,5 N). Met behulp van de geteste AD-, kruip- en elastische modulus als invoer werd een eenvoudig visco-elastisch model gebouwd om de EAS met goede nauwkeurigheid te voorspellen, wat verdere validatie van de ontworpen Mini-TSTM biedt. Dit model benadrukte ook dat vroege AD-metingsvariaties de EAS verwaarloosbaar beïnvloeden vanwege de lage elasticiteitsmodulus en de hoge kruip/relaxatie. Bovendien werd de Mini-TSTM gebruikt om de invloed van temperatuur op AD en AD-geïnduceerde EAS te onderzoeken. Er werd vastgesteld dat de AD van Portland-cementpasta een proces in vier fasen is, inclusief de initiële vervorming, autogene uitzetting, plateau van langzame vervorming en autogene krimp. Het verhogen van de temperatuur zal een hoger AD-geïnduceerd EAC-risico veroorzaken, door de duur van de eerste drie fasen te verkorten en de krimpsnelheid in de laatste fase te verhogen. Bovendien bleek de toepasbaarheid van het “maturity-concept” problematisch te zijn bij het voorspellen van AD bij verschillende temperaturen. Maar het “maturity-concept” kan nog steeds worden gebruikt om de kruip en de elasticiteitsmodulus op jonge leeftijd te voorspellen, wat helpt bij het voorspellen van de EAS als de AD bij verschillende temperaturen bekend is.

Gebaseerd op de Mini-TSTM-tests werd een numeriek modelleringschema voor het simuleren van spanningsrelaxatie voorgesteld om de EAS-evolutie met goede nauwkeurigheid te berekenen. Er werd ontdekt dat het numeriek oplossen van de Volterra-integraal van de kruipfunctie kan leiden tot een negatieve relaxatiemodulus, vooral als rekening wordt gehouden met de snelle evolutie van kruip-eigenschappen op jonge leeftijd. Dit kan tot aanzienlijke fouten leiden bij het voorspellen van de EAS. Dienovereenkomstig werd in dit onderzoek een analytische oplossing gebruikt, gebaseerd op de definitie van de relaxatietest, die direct de conversie van de relaxatiemodulus uit de kruip mogelijk maakte. Met behulp van de relaxatiemodulus als invoer werd een eindige-elementenmodel met tijdsafhankelijke Maxwell-ketens en “rate-type” kruipwet gebouwd om de EAS met goede nauwkeurigheid te voorspellen.

Om een numeriek hulpmiddel voor meer algemene scenario's te ontwikkelen, werd in dit proefschrift ook een Thermo-Chemo-Mechanisch (TCM) model ontwikkeld dat de hydratatiereactie, warmteoverdracht en visco-elasticiteit koppelt. Gebaseerd op de wet van Fourier, de vergelijking van Arrhenius, de "rate-type" kruipwet en een materiaalmodel dat voornamelijk is gebouwd op Model Code 2010, is het TCM-model in staat de zich ontwikkelende eigenschappen (dat wil zeggen visco-elasticiteit), gedrag (dat wil zeggen thermische, autogene en drogingskrimp) en EAS te simuleren. Verdere statistische analyse van 1000 willekeurige monsters onthulde dat de temperatuur de belangrijkste rol speelt in de EAS-evolutie. Ook werden datagestuurde benaderingen gebruikt om efficiëntere tools voor EAS-voorspelling te bouwen. Bovenop het TCM-model werd een actief ensemble-leermodel (AEL) opgesteld als surrogaat voor het TCM-model. Het AEL-model omvat de Principal Component Analysis (PCA) voor dimensiereductie, Gaussian Process (GP) voor onzekerheidskwantificering en Light Gradient Boosting Machine (LGBM) voor EAS-voorspelling. Met behulp van een op onzekerheid gebaseerde databemonsterings- en trainingsstrategie kan de AEL-methode het surrogaat van het TCM-model trainen met minder datamonsters en een nauwkeurigere en efficiëntere EAS-voorspelling doen.

Samengevat zijn in dit proefschrift efficiënte en betrouwbare experimentele en modelleringstechnieken voor EAC-analyse ontwikkeld, waaronder een Mini-TSTM, een verfijnd spanningsrelaxatiemodel en een AEL-model gekoppeld aan een TCM-model, dat kan helpen bij het oplossen van EAC-problemen bij de toepassing van cementgebonden materialen.

## ACKNOWLEDGEMENTS

As I approach the culmination of my PhD studies at the Delft University of Technology's Microlab, I find myself reflecting on the journey with immense gratitude. This chapter of my academic career has been profoundly shaped not only by my own endeavors but significantly by the support and camaraderie of my supervisors, colleagues, friends, and family.

Everything related to my PhD stemmed from the email I received from my promotor, Prof. Erik Schlangen, in January 2020, when I was still confused about my academic future. He offered me the opportunity to firmly pursue my true research interests. On the first day I arrived, he led me into the Microlab, showed me around the testing facilities, and introduced me to colleagues. Since then, he has always been around to guide me through my research journey. He is not only a smart and experienced researcher but also open-minded and encouraging supervisor. When I struggled with research questions, he was always open to discussion in his office, next to the coffee machine, or simply in the corridor. He has a unique ability to keep academic discussions engaging by infusing them with his sense of humor, yet he remains formal and provides succinct insights. His example leads me to believe in the significant influence of supervisors on the PhD student and set me a great example for my future research and teaching career. I am really grateful for having his supervision and guidance.

I am also very grateful for having my promotor and daily supervisor, Dr. Branko Šavija. Branko is a very energetic researcher, a constructive supervisor, and a kind and humorous friend. His prompt responses to my requests for meetings and paper reviews, coupled with his consistent presence to offer suggestions and support, have been invaluable. His keen sensitivity to the latest advancements in our field and enthusiasm for sharing innovative research ideas inspire me and enrich my research work. In addition, he is a caring and humorous friend and has brought me a lot of laughter and encouragement, lightening the rigors of research. I deeply appreciate his supervision and guidance, which have been pillars of support throughout my research journey.

Besides my promotors, I would like to acknowledge the chairperson and all of my committee members: Prof. Chris Kleijn, Prof. Klaas van Breugel, Prof. Max Hendriks, Prof. Eddie Koenders, Dr. Stéphanie Staquet, and Dr. Ya Wei for taking the time to review the draft of this work.

I extend my heartfelt thanks to my master's supervisor, Prof. Chuan He, for his invaluable assistance, support, and guidance along my research journey. His mentorship was crucial in advancing my research to its current stage. I am also grateful to Prof. Kun Feng, my daily supervisor during my master's studies, for establishing a solid foundation in my research skills. Their contributions have been fundamental to my academic progress.

I extend my special thanks to my wonderful officemates at the office 6.21: Yu Chen, Patrick Holthuizen, and Anne Linde van Overmeir. Conversing with you about all aspects of life and work has always been a source of joy and relief. Your friendship, fun moments, and invaluable advice have greatly enriched my PhD journey. I consider myself fortunate to have shared this experience with you.

I extend my profound gratitude to a group of senior colleagues and close friends within the Microlab, who have given me consistent support and advice for both life and work, since the beginning of my PhD journey: Yidong Gan, Yading Xu, Yu Chen, Ze Chang, Shan He, Yu Zhang, and Zhi Wan. We have closely collaborated on many novel research ideas that lead to interesting findings. Their qualities, expertise, and bright minds greatly enriched my PhD journey. Beyond research works, they are close friends who make a great part of my PhD life. I am very lucky to have them in my PhD journey.

I extend my special appreciation to my esteemed colleagues and cherished friends: Dr. Guang Ye, Prof. Henk Jonkers, Dr. Oğuzhan Çopuroğlu, Dr. Mladena Luković, Dr. Muhammad Fotouhi, Prof. Giovanni Di Luzio, Zhiwei Qian, Hua Dong, Zhengxian Yang, Tianshi Lu, Jiayi Chen, Xuliang Hou, Bei Wu, Leyang Lyu, Yibing Zuo, Yong Zhang, Hongzhi Zhang, Shi Xu, Wenjuan Lyu, Shizhe Zhang, Zhenming Li, Marija Nedeljković, Hao Huang, Claudia Romero Rodriguez, Bart Hendrix, Albina Kostuchenko, Stefan Chaves Figueiredo, Boyu Chen, Luiz Miranda de Lima Junior, Zhiyuan Xu, Fernando Mendonca Filho, Irving Alfredo Flores Beltran, Emanuele Rossi, Xuhui Liang, Yun Chen, Lu Cheng, Xingliang Yao, Yitao Huang, Shozab Mustafa, Ameya Kamat, Chen Liu, Hu Shi, Guilherme da Silva Munhoz, Yu Zeng, Jinbao Xie, Wen Zhou, Aliakbar Ghaderiaram, Farnaz Aghabeyk, Mayank Gupta, Rowin Bol, Max Veeger, Zhaozeng Meng, Yufei Zhang, Dautse Heimovaara, and Jeannette van den Bos. Your friendship, the countless coffee breaks, parties, and all the wonderful moments we've shared have granted me the most beautiful and precious memories of my time at TU Delft.

I owe special thanks to Maiko van Leeuwen and Ton Blom for their invaluable assistance in various mechanical tests and for their help with concrete casting in both the micro- and marco-labs. Additionally, my gratitude extends to Maiko for his efforts in fostering camaraderie through the organization of beer parties at PSOR and BBQs at his home.

My heartfelt thanks go to Kees van Beek for his kind support throughout my PhD journey. His wealth of ideas on technical details significantly shaped the Mini-TSTM's design, and his assistance in resolving numerous practical challenges was invaluable. His kindness, patience, support, and expertise have been indispensable, making me exceedingly fortunate to have him as part of my journey. I am also deeply grateful to Jeroen Koning for his assistance in the design and manufacturing of the Mini-TSTM setup. His contributions were crucial to the smooth completion of my PhD.

My sincere appreciation goes to Fred Schilperoort, Arjan Thijssen, Paul Vermeulen, John van den Berg, and Leon Roessen for their professional assistance in all aspects of laboratory work. Their expertise and support were indispensable. I also wish to recognize Iris Batterham, Jacqueline Berghenhenegouwen, Jaap Meijer, Iris Nederhof-van Woggelum, and Sandra Schuchmann-Hagman for their invaluable help with various day-to-day issues. Their kindness and support played a crucial role in facilitating my research activities.

I am deeply thankful for the friendships I've formed in the Netherlands. My heartfelt gratitude extends to Hanting Ye, Yubao Zhou, Xinling Yue, Hao Cheng, Pei He, Tianlong Jia, Zhanchong Shi, Fanxiang Xu, Langzi Chang, Xinrui Zhang, Zichao Li, and Shuaiqi Yuan. Your support and camaraderie have been invaluable to me. I consider myself incredibly fortunate to have shared this journey with you, cherishing the memories we've created at every lunch and dinner party.

Finally, and most importantly, I must express my deepest gratitude to my parents and grandparents. Their unwavering support and silent love have filled my life with vibrant colors and endowed me with the courage to pursue my dreams. Their sacrifices and belief in me have been the constant source of my strength. I am eternally committed to making them proud in all my endeavors.

Minfei Liang  
Delft, March 2024

## LIST OF PUBLICATIONS

### Journal Publications

1. **Liang, M.**, Luzio, G. Di, Schlangen, E., & Šavija, B. (2024). *Experimentally informed modeling of the early-age stress evolution in cementitious materials using exponential conversion from creep to relaxation*. [Computer-Aided Civil and Infrastructure Engineering](#).
2. **Liang, M.**, Liu, C., Liang, X., Chang, Z., Schlangen, E., & Šavija, B. (2024). *Effects of temperature on autogenous deformation and early-age stress evolution in cement pastes with low water to cement ratio*. [Construction and Building Materials](#), 411, 134752.
3. **Liang, M.**, Xie, J., He, S., Chen, Y., Schlangen, E., & Šavija, B. (2024). *Autogenous deformation-induced stress evolution in cementitious materials considering viscoelastic properties: A review of experiments and models*. [Developments in the Built Environment](#), 17, 100356.
4. **Liang, M.**, Chang, Z., Holthuizen, P., Chen, Y., He, S., Schlangen, E., & Šavija, B. (2023). *Efficiently Assessing the Early-Age Cracking Risk of Cementitious Materials with A Mini Temperature Stress Testing Machine*. (Under Review)
5. **Liang, M.**, He, S., Gan, Y., Zhang, H., Chang, Z., Schlangen, E., & Šavija, B. (2023). *Predicting micromechanical properties of cement paste from backscattered electron (BSE) images by computer vision*. [Materials & Design](#), 229, 111905.
6. **Liang, M.**, Zhang, Y., He, S., Chen, Y., Schlangen, E., & Šavija, B. (2023). *On the chemo-mechanical evolution process of high-volume slag cement paste*. [Construction and Building Materials](#), 400, 132891.
7. **Liang, M.**, Chang, Z., Zhang, Y., Cheng, H., He, S., Schlangen, E., & Šavija, B. (2023). *Autogenous deformation induced-stress evolution in high-volume GGBFS concrete: Macro-scale behavior and micro-scale origin*. [Construction and Building Materials](#) 370, 130663.
8. **Liang, M.**, Chang, Z., He, S., Chen, Y., Gan, Y., Schlangen, E., & Šavija, B. (2022). *Predicting early-age stress evolution in restrained concrete by thermo - chemo - mechanical model and active ensemble learning*. [Computer-Aided Civil and Infrastructure Engineering](#), 37(14), 1809–1833.
9. **Liang, M.**, Chang, Z., Wan, Z., Gan, Y., Schlangen, E., & Šavija, B. (2022). *Interpretable Ensemble-Machine-Learning models for predicting creep behavior of concrete*. [Cement and Concrete Composites](#), 125, 104295.

10. **Liang, M.**, Gan, Y., Chang, Z., Wan, Z., Schlangen, E., & Šavija, B. (2022). *Microstructure-informed deep convolutional neural network for predicting short-term creep modulus of cement paste*. *Cement and Concrete Research*, *152*, 106681.
11. **Liang, M.**, Li, Z., He, S., Chang, Z., Gan, Y., Schlangen, E., & Šavija, B. (2022). *Stress evolution in restrained GGBFS concrete due to autogenous deformation: Bayesian optimization of aging creep*. *Construction and Building Materials*, *324*, 126690.
12. **Liang, M.**, Feng, F., He, C., Li, Y., An, L., Guo, W. (2020). A meso-scale model toward concrete water permeability regarding aggregate permeability. *Construction and Building Materials* *261*, 120547
13. Zhou, Y., **Liang, M.**, & Yue, X. (2024). *Deep residual learning for acoustic emission source localization in A steel-concrete composite slab*. *Construction and Building Materials*, *411*, 134220.
14. Chang, Z., **Liang, M.**, Chen, Y., Schlangen, E., & Šavija, B. (2023). *Does early age creep influence buildability of 3D printed concrete? Insights from numerical simulations*. *Additive Manufacturing*, *77*, 103788.
15. Chen, Y., **Liang, M.**, Zhang, Y., Li, Z., Šavija, B., Schlangen, E., & Çopuroğlu, O. (2023). *Can superabsorbent polymers be used as rheology modifiers for cementitious materials in the context of 3D concrete printing?* *Construction and Building Materials*, *371*, 130777.
16. Chang, Z., **Liang, M.**, Xu, Y., Wan, Z., Schlangen, E., & Šavija, B. (2023). *Early-age creep of 3D printable mortar: Experiments and analytical modelling*. *Cement and Concrete Composites*, *138*, 104973.
17. Chang, Z., **Liang, M.**, He, S., Schlangen, E., & Šavija, B. (2023). *Lattice modelling of early-age creep of 3D printed segments with the consideration of stress history*. *Materials & Design*, *234*, 112340.
18. Zhang, Y., **Liang, M.**, Gan, Y., & Çopuroğlu, O. (2022a). *Effect of MgO content on the quantitative role of hydrotalcite-like phase in a cement-slag system during carbonation*. *Cement and Concrete Composites*, *134*, 104765.
19. Zhang, Y., **Liang, M.**, Gan, Y., & Çopuroğlu, O. (2022b). *Micro-Mechanical Properties of Slag Rim Formed in Cement-Slag System Evaluated by Nanoindentation Combined with SEM*. *Materials*, *15*(18), 6347.
20. Chang, Z., **Liang, M.**, Xu, Y., Schlangen, E., & Šavija, B. (2022). *3D concrete printing: Lattice modeling of structural failure considering damage and deformed geometry*. *Cement and Concrete Composites*, *133*, 104719.

21. He, S., Chen, Y., **Liang, M.**, Yang, E.-H., & Schlangen, E. (2023). *Distribution of porosity surrounding a microfiber in cement paste*. [Cement and Concrete Composites](#), *142*, 105188.
22. Chang, Z., Zhang, H., **Liang, M.**, Schlangen, E., & Šavija, B. (2022). *Numerical simulation of elastic buckling in 3D concrete printing using the lattice model with geometric nonlinearity*. [Automation in Construction](#), *142*, 104485.
23. Gan, Y., Zhang, H., **Liang, M.**, Zhang, Y., Schlangen, E., van Breugel, K., & Šavija, B. (2022). *Flexural strength and fatigue properties of interfacial transition zone at the microscale*. [Cement and Concrete Composites](#), *133*, 104717.
24. Gan, Y., Zhang, H., **Liang, M.**, Schlangen, E., van Breugel, K., & Šavija, B. (2021). *A numerical study of fatigue of hardened cement paste at the microscale*. [International Journal of Fatigue](#), *151*, 106401.
25. Xie, J., Xu, Y., Meng, Z., **Liang, M.**, Wan, Z., Šavija, B. (2024). *Peanut shaped auxetic cementitious cellular composite (ACCC)*. [Construction and Building Materials](#), *419*, 135539.
26. Wan, Z., Xu, Y., Chang, Z., **Liang, M.**, & Šavija, B. (2024). *Automatic enhancement of vascular configuration for self-healing concrete through reinforcement learning approach*. [Construction and Building Materials](#), *411*, 134592.
27. Chen, Y., Zhang, Y., He, S., **Liang, M.**, Zhang, Y., Schlangen, E., & Çopuroğlu, O. (2023). *Rheology control of limestone calcined clay cement pastes by modifying the content of fine-grained metakaolin*. [Journal of Sustainable Cement-Based Materials](#), *12*(9), 1126–1140.
28. He, S., Mustafa, S., Chang, Z., **Liang, M.**, Schlangen, E., & Luković, M. (2023). *Ultra-thin Strain Hardening Cementitious Composite (SHCC) layer in reinforced concrete cover zone for crack width control*. [Engineering Structures](#), *292*, 116584.
29. Li, Z., Liang, X., Liu, C., **Liang, M.**, van Breugel, K., & Ye, G. (2022). *Thermal deformation and stress of alkali-activated slag concrete under semi-adiabatic condition: Experiments and simulations*. [Cement and Concrete Research](#), *159*, 106887.

### Conference Proceedings

1. **Liang, M.**, Schlangen, E., & Šavija, B. (2023). *Bayesian Inverse Modelling of Early-Age Stress Evolution in GGBFS Concrete Due to Autogenous Deformation and Aging Creep*. In RILEM International Conference on Numerical Modeling Strategies for Sustainable Concrete Structures.

2. Schlangen, E., **Liang, M.**, & Savija, B. (2023). *The Influence of Autogenous Shrinkage and Creep on the Risk of Early Age Cracking*. In RILEM RILEM International Conference on Numerical Modeling Strategies for Sustainable Concrete Structure.
3. He, S., **Liang, M.**, Yang, E., & Schlangen, E. (2023). *A New Method to Quantitatively Characterize the Porosity of Fiber/Matrix Interfacial Transition Zone (ITZ) via Longitudinal Cross-Sections*. In International Conference on Strain-Hardening Cement-Based Composites.

## CURRICULUM VITAE

### MINFEI LIANG



11-04-1994 Born in Fujian, China.

#### EDUCATION

Sep. 2013 – July. 2017	B.SC student Civil Engineering Southwest Jiaotong University, China
Sep. 2017 – July. 2020	M.SC student Bridge and Tunnel Engineering Southwest Jiaotong University, China
Oct. 2020 – Present	PhD. candidate Civil Engineering and Geosciences Delft University of Technology, The Netherlands